

**DOCTOR OF PHILOSOPHY**

**Effects of Ti6Al4V powder recycling in electron and laser beam powder bed fusion additive manufacturing**

Soundarapandiyan, Gowtham

*Award date:*  
2022

*Awarding institution:*  
Coventry University

[Link to publication](#)

**General rights**

Copyright and moral rights for the publications made accessible in the public portal are retained by the authors and/or other copyright owners and it is a condition of accessing publications that users recognise and abide by the legal requirements associated with these rights.

- Users may download and print one copy of this thesis for personal non-commercial research or study
- This thesis cannot be reproduced or quoted extensively from without first obtaining permission from the copyright holder(s)
- You may not further distribute the material or use it for any profit-making activity or commercial gain
- You may freely distribute the URL identifying the publication in the public portal

**Take down policy**

If you believe that this document breaches copyright please contact us providing details, and we will remove access to the work immediately and investigate your claim.

---

# **Effects of Ti6Al4V powder recycling in electron and laser beam powder bed fusion additive manufacturing**

---

A thesis submitted to Coventry University  
for the Degree of PhD

by

Gowtham Soundarapandiyan

July 2021



Centre for Materials and Manufacturing Engineering  
Faculty of Engineering, Environment and Computing  
Coventry University



## Certificate of Ethical Approval

Applicant:

Gowtham Soundarapandiyam

Project Title:

A study on Ti6Al4V Powder Degradation and its Effect on Component Integrity in Powder Bed Fusion Additive Manufacturing

This is to certify that the above named applicant has completed the Coventry University Ethical Approval process and their project has been confirmed and approved as Low Risk

Date of approval:

23 September 2020

Project Reference Number:

P110113

## Abstract

Recycling of the unused surplus powder after laser beam powder fusion (LB-PBF) and electron beam powder bed fusion (EB-PBF) processes improve process efficiency. However, some of the recycled powder particles may have different physical and chemical characteristics due to degradation during part manufacturing, recovery, powder handling, and reuse that can affect the quality of the build parts. Therefore, it is important to understand the properties of the recycled powder, especially when it is used for manufacturing safety critical parts for aerospace applications. The present work aims to highlight different types and mechanisms of Ti6Al4V powder degradation, as a consequence of powder recycling, and its subsequent impact on the build properties.

The first part of the thesis presents an evaluation of the evolution of powder properties up to 10 build cycles using a simulated powder recycling strategy that enabled minimal virgin powder top-up in EB-PBF process. The results show heterogeneous powder degradation, with the powder particles located near the melt zone suffering maximum degradation. Degradation in the powder physical characteristics caused an increase in the fraction of lack-of-fusion defects in the specimens produced from the recycled powder. However, post-thermal treatment processes, hot isostatic pressing (HIPing) + solution treatment + ageing appears to be promising in eliminating the lack-of-fusion defects in the recycled builds. Due to the reactive nature of the Ti6Al4V alloy, an increase in the oxygen (O) content was unavoidable and therefore, the recycled powder showed an 0.02 wt.% increased O content compared to the virgin powder. However, since the O content in the recycled powder stayed within the maximum limit (0.13 wt.%), only a slight increase in the material yield and tensile strength (by 10 MPa) with negligible changes in ductility were observed.

Normally, in industry, the recycled powder is often blended or topped-up with virgin powder during recycling to maintain the build volume. The recycled powder particles present in the blend that have different physical and chemical properties compared to the virgin powder may cause localised inhomogeneity in the build properties. The change in powder physical characteristics with recycling are marginal and so the subsequent impact on part properties can be restored by performing additional post-thermal treatments.

Therefore, the second part of this thesis presents an investigation on the effects of blending a high and low O content Ti6Al4V powder on the build properties using in situ and ex situ experiments in the LB-PBF process. A small batch of Ti6Al4V powder (virgin powder) with O content of 0.12 wt.% was artificially oxidised to 0.40 wt.% (oxidised powder). The oxidised powder was blended with virgin powder in a suitable ratio such that the blended powder had 0.20 wt.% O. Due to problems during manufacture which resulted in large lack-of-fusion defects, the mechanical properties were more significantly influenced by the process-related defects than the O content in the powder feedstock. Therefore, to further understand the effects of powder oxidation, in situ X-ray imaging experiments were conducted in a miniature LB-PBF process replicator on powders with two different O levels, 0.12 wt.%, and 0.40 wt.%. The results indicated that the high O content powder particles had a positive effect in reducing the number of melt ejections, surface roughness and defect population in the build parts.

\*\*\*\*\*

## Preface

This PhD thesis is based on the work conducted from January 2018 to June 2021. Majority of the experiments were carried out in National Structural Integrity Research Centre (NSIRC) at TWI Ltd (Cambridge, UK). Other essential experiments were conducted at University of Sheffield (Sheffield, UK), TWI Ltd (Rotherham, UK), Research Complex at Harwell (Oxford, UK) and Diamond Light Source (Oxford, UK) through collaborations. This PhD program was sponsored by Lloyd's Register Foundation (LRF) and Coventry University. The research work has been conducted under the supervision of Professor Michael E. Fitzpatrick (Faculty of Engineering, Environment and Computing, Coventry University, Coventry, UK), Professor Bo Chen (School of Engineering, Leicester University, Leicester, UK), Dr Carol Johnston (Fatigue Integrity Management, TWI Ltd, Cambridge, UK) and Dr Raja Khan (Thermal Processing Technologies, TWI Ltd, Cambridge, UK).

Some parts of this thesis has been disseminated in the form of journal papers, posters and oral presentations in research symposium, local and international conferences.

### List of journal papers

- (i) **Gowtham Soundarapandiyan**, Carol Johnston, Raja H.U. Khan, Chu Lun Alex Leung, Peter D. Lee, Everth Hernández-Nava Bo Chen, Michael E. Fitzpatrick, '*The effects of powder reuse on the mechanical response of electron beam additively manufactured Ti6Al4V parts*', Additive Manufacturing, 46, 102101, 2021. <https://doi.org/10.1016/j.addma.2021.102101>.
- (ii) **Gowtham Soundarapandiyan**, Carol Johnston, Raja Khan, Bo Chen, Michael Fitzpatrick, '*A technical review of the challenges of powder recycling in the laser powder bed fusion additive manufacturing process*', Journal of Engineering, 1-7, 2021. <https://doi.org/10.1049/tje2.12013>.
- (iii) **Gowtham Soundarapandiyan**, Raja Khan, Carol Johnston, Bo Chen, Michael Fitzpatrick. '*Effect of post-processing thermal treatments on electron-beam powder bed-fused Ti6Al4V*.' Material Design & Processing Communications, 3(4):e168, 2020. <https://doi.org/10.1002/mdp2.168>.

- (iv) **Gowtham Soundarapandiyan**, Chu Lun Alex Leung, Carol Johnston, Phil McNutt, Alisha Bhatt, Peter D. Lee, Bo Chen, Michael E. Fitzpatrick, '*Effect of Ti6Al4V powder oxidation in laser beam additive manufacturing process*', Scripta Materialia. (Pending submission).

### List of conference presentations

- (i) **Gowtham Soundarapandiyan**, Chu Lun Alex Leung, Carol Johnston, Raja H.U. Khan, Alisha Bhatt, Peter D. Lee, Bo Chen, Michael E. Fitzpatrick, '*Effect of Powder Feedstock Blending on the Structural Integrity of Laser Powder Bed Fused Ti6Al4V Components*'. ASTM-International Conference on Additive Manufacturing (ASTM-ICAM 2020), Virtual, 16-20<sup>th</sup> November 2020. (Oral presentation).
- (ii) **Gowtham Soundarapandiyan**, Chu Lun Alex Leung, Carol Johnston, Raja H.U. Khan, Alisha Bhatt, Peter D. Lee, Bo Chen, Michael E. Fitzpatrick, '*Effect of powder oxygen content in laser additive manufacturing: Revealed by in-situ high speed X-ray imaging*'. EEC & IFTC research symposium, Virtual, 11<sup>th</sup> November 2020. (Oral presentation).
- (iii) **Gowtham Soundarapandiyan**, Carol Johnston, Raja Khan, Bo Chen, Michael Fitzpatrick, '*Ti6Al4V Powder Degradation in Electron beam Powder Bed Fusion Additive Manufacturing*'. NSIRC Annual Conference, Virtual, 21<sup>st</sup> July 2020. (Oral presentation).
- (iv) **Gowtham Soundarapandiyan**, Raja Khan, Carol Johnston, Bo Chen, Michael Fitzpatrick, '*Effect of post-thermal treatment on the structural integrity of EB-PBF Ti6Al4V material*'. European Conference on Structural Integrity of Additively Manufactured Materials (ESIAM19), Trondheim, Norway, 9-11<sup>th</sup> September 2019. (Oral presentation).
- (v) **Gowtham Soundarapandiyan**, Carol Johnston, Raja Khan, Bo Chen, Michael Fitzpatrick, '*Degradation in Recycled Ti6Al4V powder in Electron Beam Powder Bed Fusion Additive Manufacturing*'. European Conference on Structural Integrity of Additively Manufactured Materials (ESIAM19), Trondheim, Norway, 9-11<sup>th</sup> September 2019. (Poster presentation).
- (vi) **Gowtham Soundarapandiyan**, Raja Khan, Carol Johnston, Bo Chen, Michael Fitzpatrick, '*Effect of Post-Thermal Treatments on the Mechanical Properties of EB-PBF Ti6Al4V*'. NSIRC Annual Conference, TWI Ltd, Cambridge, UK, 1-2<sup>nd</sup> July 2019. (Oral presentation).

- (vii) **Gowtham Soundarapandiyan**, Carol Johnston, Raja Khan, Bo Chen, Michael Fitzpatrick '*Understanding the Effects of Powder Reuse in EBM using Plasma Atomised Gr5 Ti6Al4V Powder*'. NSIRC Annual Conference, TWI Ltd, Cambridge, UK, 2-3<sup>rd</sup> July 2018. (Poster presentation).

### **Other publications**

- (i) Alisha Bhatt, Chu Lun Alex Leung, **Gowtham Soundarapandiyan**, Sebastian Marussi, Saurabh Shah, Robert Atwood, Peter D. Lee, '*The effects of Surface Roughness on Ti-6Al-4V with varying process parameters unveiled by In-situ X-ray imaging*', TMS 2021 Annual Meeting & Exhibition, Virtual, March 14-18<sup>th</sup>, 2021. (Poster presentation).
- (ii) David T. Rees, Chu Lun Alex Leung, **Gowtham Soundarapandiyan**, Sebastian Marussi, Saurabh Shah, Robert Atwood, Gavin Baxter, Martyn Jones, Peter D. Lee, '*Synchrotron imaging of the influence of oxidation with aging on cracking phenomena during laser powder bed fusion of CM247*', TMS 2021 Annual Meeting & Exhibition, Virtual, March 14-18<sup>th</sup>, 2021. (Poster presentation).
- (iii) Alisha Bhatt, Chu Lun Alex Leung, **Gowtham Soundarapandiyan**, Sebastian Marussi, Saurabh Shah, Robert Atwood, Peter D. Lee, '*Quantifying Surface Roughness in AM Ti-6Al-4V Using In-situ X-ray imaging*', Acta Materialia. (Pending submission).
- (iv) David T. Rees, Chu Lun Alex Leung, **Gowtham Soundarapandiyan**, Joe Elambasseril, Sebastian Marussi, Saurabh Shah, Shashidhara Marathe, Milan Brandt, Mark Easton, Peter D. Lee, '*Synchrotron imaging of the cracking in laser powder bed fused CM247*', Additive Manufacturing. (Pending submission).

\*\*\*\*\*

## Acknowledgements

I am indebted to a number of individuals in the academia and industrial circles who assisted me in several ways throughout my PhD programme. Firstly, I would like to thank Coventry University, NSIRC and TWI Ltd for facilitating this research. This research was made possible by the sponsorship and support of the Lloyd's Register Foundation, a charitable organisation that helps to protect life and property by supporting engineering-related education, public engagement and the application of research.

I am highly thankful to my academic supervisor, *Prof. Michael E. Fitzpatrick* from Coventry University for his continuous support and guidance. He was always available and stood by my side whenever I faced any administrative or technical issue. I am grateful to my co-supervisor *Prof. Bo Chen* from Leicester University. His knowledge, vision and constructive criticisms greatly improved my research plan and writing skills. I would like to express my immense gratitude to my industrial supervisor *Dr Carol Johnston* for being an immediate go-to person whenever I faced an obstacle in experimentations. Her continuous motivation, involvement, guidance and making herself available whenever I needed greatly benefited me in channelling this PhD in the correct direction. I am very grateful to my second industrial supervisor *Dr Raja Khan* for helping me with various aspects of this PhD. He gave me the opportunity to discover the world of powder metallurgy. His knowledge, experience and training profoundly helped me to perform powder characterisations and related data analysis.

Heartiest thanks to my peers at TWI Ltd for providing me the required training and guidance in performing several material characterisations. Special thanks to *Dr. Michael Dodge* for training me on EBSD technique and sharing his expertise on fractography study. Thanks to *Dr. Shiela Stevens* for training me to operate the SEM, *Mr. Ben Robinson* for performing surface roughness measurements on the builds made during the beamtime, *Dr Kostas Georgilas* for training me on several powder characterisation techniques and *Mrs. Sally Day* for performing XRD and oxygen content measurements on my powders and AM builds. My sincere thanks to the technicians at TWI Ltd namely, *Mr. Ashley Spencer*, *Mr. Ramin Taheri*, *Mrs. Diane Shaw*, *Mr. Jerry Godden* and *Mr. Phillip Cossey* for training me on metallography specimen preparation and performing mechanical tests and *Mr. Tomaso Maccio* for manufacturing LB-PBF builds. I would also like to thank *Mr. Markus Young* for his support in scheduling mechanical tests. My sincere thanks to

*Dr. Phil McNutt, Dr. Alexandre Sabard, and Mr. Damian Whiteman* for helping me with the powder heat treatment experiment. Without their help, it would not have been possible to prepare powder samples for the beamtime experiments.

My warm regards to University of Sheffield for providing us the powder feedstock for the EB-PBF powder recycling study and *Dr. Everth Hernández-Nava* from University of Sheffield for conducting powder recycling trials and fabricating EB-PBF builds using ARCAM Q10 plus EB-PBF machine from virgin and recycled powder.

I am very grateful for the strong and fruitful collaboration with *Prof. Peter D. Lee* and his research team: *Dr. Chu Lun Alex Leung, Miss. Alisha Bhatt, Dr. Lorna Sinclair, Mr. David T. Rees, Dr. Samuel J Clark and Dr. Yuze Huang*, based at Research complex at Harwell for their support and technical discussions during the beamtime and most-importantly for providing the LB-PBF process replicator which helped us to conduct the study on the effects of powder oxidation on AM builds. Special thanks to *Dr. Chu Lun Alex Leung* for winning the beamtime proposal, performing image flat field image correction and denoising. Thanks to *Dr Saurabh Shah* for performing X-ray CT scans using the facilities at Research complex at Harwell. A special mention must be given to their exceptional planning and prioritising my work during the lockdown due to COVID-19 pandemic outbreak, which would have otherwise had serious implication on my PhD progress.

I would like to thank my colleagues turned friends, *Dr. Dibakor Boruah, Mr. Emre Akgun, Mr. Mehran Shahriarifar, Mr. Sameera Weeratunga, Dr. Jazeel Chukkan, Mr. Usama Javid, Mr. Afnan Islam, Dr. Kuveshni Govender, Dr. Sulochana Subramanian, Miss. Nagu Sathappan and Dr. Xu Liu* for providing me a joyful learning environment.

Outside academia, I want to thank *Prof. Devendranath Ramkumar* from VIT University, India for his morale support. I would like to express my immense gratitude to my parents and sister for their constant love and support and lastly my beloved wife for her sacrifice, patience and encouragement which helped me to complete this PhD research.

\*\*\*\*\*

## List of abbreviations

AM	Additive manufacture
AGA	Argon gas atomisation
AMS	Aerospace Material Specifications
AR	Aspect ratio
ASTM	American Society for Testing and Materials
BCC	Body-centered cubic
BJ3D	Binder jet 3D printing
BSE	Backscattered electron
CAD	Computer aided design
CSAM	Cold spray additive manufacture
CW	Continuous wave
DED	Directed energy deposition
EB-PBF	Electron beam powder bed fusion
EBSD	Electron backscatter diffraction
EDS	Energy dispersive spectroscopy
EL	Elongation
ELI	Extra low interstitial
FCC	Face-centered cubic
FEG-SEM	Field emission gun scanning electron microscopy
FFC	Flat-field correction
Fps	Frames per second
GA	Gas atomisation
GMAW	Gas metal arc welding
GTA	Gas tungsten arc
HAGB	High-angle grain boundary
HCF	High cycle fatigue
HCP	Hexagonal close-packed
HDH	Hydride-dehydride
HIP	Hot isostatic press
HR	Hausner ratio
ICP	Inductive coupled plasma spectroscopy

IGF	Inert gas fusion
IPF	Inverse pole figure
ISOPR	In situ and operando process replicator
LAGB	Low-angle grain boundary
LB-PBF	Laser beam powder bed fusion
LENS	Lasers engineered net shaping
LMD	Laser metal deposition
NIST	National Institute of Standards and Technology
PA	Plasma atomisation
PAD	Plasma arc deposition
PBF	Powder bed fusion
PREP	Plasma rotating electrode process
PRS	Powder recovery system
PSD	Particle size distribution
SE	Secondary electron
SEM	Scanning electron microscopy
SLS	Selective laser sintering
SSS	Solid solution strengthen
STA	Solution treatment and aging
STL	Standard tessellation language
TIG	Tungsten inert gas
UTS	Ultimate tensile strength
WAAM	Wire arc additive manufacture
XCT	X-ray computed tomography
XPS	X-ray photoelectron spectroscopy
XRD	X-ray diffraction
YS	Yield stress

## List of figures

<b>Figure 1.1</b> a) Unconsumed powder during LB-PBF process; b) cost breakdown in powder bed AM processes (after [22]).	2
<b>Figure 2.1</b> Main topics discussed in this chapter.	5
<b>Figure 2.2</b> Unit cell of (a) $\alpha$ phase with HCP crystal structure of lattice parameters $a= 0.295$ nm, $c= 0.468$ nm, highlighting some of the densely packed planes; (b) $\beta$ phase with BCC crystal structure of lattice parameter $a= 0.332$ at $900^{\circ}\text{C}$ , highlighting one of six densely packed $\{110\}$ planes (after [1]).	7
<b>Figure 2.3</b> Schematic showing the effect of alloying elements on titanium phase transformation (after [4]).	8
<b>Figure 2.4</b> Titanium alloys classification revealing $\alpha$ , $\alpha+\beta$ and $\beta$ alloys region (after [1]).	8
<b>Figure 2.5</b> Pseudo-phase diagram of Thermo-Calc prediction of $\alpha_2$ phase formation in Ti-4V-10 alloy (after [29]).	11
<b>Figure 2.6</b> Effects of cooling rate on Ti6Al4V material microstructure: (a) $\alpha'$ , (b) $\alpha'+\alpha_m$ and (c) $\alpha+\beta$ Widmanstätten structure (after [28]).	12
<b>Figure 2.7</b> Optical microscopy image of cross-section of Ti6Al4V alloy oxidised at (a) $600^{\circ}\text{C}$ (b) $700^{\circ}\text{C}$ and (c) $850^{\circ}\text{C}$ revealing $\alpha$ -case formed over the surface (after [31]).	13
<b>Figure 2.8</b> Changes in $\alpha$ -case depth at varying oxidation time and temperatures (after [32]).	13
<b>Figure 2.9</b> (a) Low cycle fatigue (LCF) of Ti-6242 alloy at 0.4% and 0.3% strain rate (after [33]); (b) Variation of Vickers microhardness of Ti6Al4V from surface containing $\alpha$ -case to the parent material (after [32]).	14
<b>Figure 2.10</b> Ti6Al4V phase transformation at different cooling rates (after [28]).	15
<b>Figure 2.11</b> Effect of cooling rates on (a) tensile properties of Ti6242, Ti6Al4V and IMI834 alloys, and (b) fatigue properties of Ti6Al4V alloy (after [1]).	18
<b>Figure 2.12</b> Effect of O content on mechanical properties of cp-Ti and Ti6Al4V (after [34]).	18

<b>Figure 2.13</b> Tensile elongation values of Ti6Al4V material manufactured by (a) powder metallurgy and (b) additive manufacturing processes with varying O content (after [35]). .....	19
<b>Figure 2.14</b> AM components used in commercial aircrafts: (a) bracket connector, (b) engine fuel nozzle, and (c) airfoil with cooling channels (after [40]).	20
<b>Figure 2.15</b> Classification of AM processes based on material processing capability (after [44]).	23
<b>Figure 2.16</b> (a) Schematic of electron beam powder bed fusion additive manufacturing system; (b) ARCAM machine and build chamber.	27
<b>Figure 2.17</b> Thermal camera images recorded during Layer 3 powder consolidation of Ti6Al4V EB-PBF process, revealing (a) deposited powder layer, (b) preheat 1 scan lines, (c) preheat 2 scan lines, (d) contour melting performed by MultiBeam™ technology, (e) hatch melting, (f) post-heating (author's own results).	29
<b>Figure 2.18</b> (a) Schematic of LB-PBF process; (b) Realiser 125 LB-PBF system build chamber.	30
<b>Figure 2.19</b> Schematics showing track morphology (a) continuous wave mode, (b and c) effect of time interval between pulses in modulated wave laser [63].	31
<b>Figure 2.20</b> Schematic of laser beam energy (a) absorption and (b) reflection during laser-powder interaction of LB-PBF process (after [70]).	32
<b>Figure 2.21</b> Schematic of (a) conduction mode of melting, (b) keyhole mode, and (c) multiple reflections by the keyhole walls in laser beam welding (after [75]).	33
<b>Figure 2.22</b> Effect of surface active elements on surface tension gradient; (a and b) negative surface tension gradient causing centrifugal convection; (b and c) positive surface tension gradient causing inward centripetal flow (after [78]). .....	34
<b>Figure 2.23</b> SEM image of powder morphology: (a) virgin powder; (b) type-I, (c) type-II and (d) type-III spatter particles (after [92]).	36
<b>Figure 2.24</b> SEM micrograph of (a) GA and (b) PA powder (author's own results).	39

<b>Figure 2.25</b> Gas entrapment in powder particles visualised using (a) optical microscope (author's own result), and (b) X-ray computed tomography (XCT) (after [100]).	45
<b>Figure 2.26</b> Schematic shows sequence of events causing gas entrapment in powder particles in atomisation process (after [122]).	46
<b>Figure 2.27</b> SEM (backscattered electron (BSE) mode) and EDS/EDX revealing Ti6Al4V particles with maraging steel powder at (a and d) 0.5%, (b and c) 1%, and (c and f) 2.5% contaminants. Ti6Al4V particles are coloured blue (after [125]).	47
<b>Figure 2.28</b> Optical micrographs of Ti6Al4V processed by EB-PBF (a) as-fabricated and (b) HIPed condition; and Ti6Al4V produced by LB-PBF process (c) as-fabricated and (d) HIPed condition (after [55]).	51
<b>Figure 3.1</b> Powder sampling and manufacturing strategy used to fabricate test coupons following virgin and recycled conditions.	57
<b>Figure 3.2</b> Morphologi 4-ID (Malvern Panalytical), 2D particle imaging.	59
<b>Figure 3.3</b> Malvern Panalytical Mastersizer 3000 system used for PSD measurement.	61
<b>Figure 3.4</b> Test set-up for (a) Hall flow and apparent density, and (b) tap density measurements.	62
<b>Figure 3.5</b> (a) CAD model of build layout; dimensions of (b) tensile, (c) Charpy impact V-notch, and (d) fatigue specimens.	64
<b>Figure 3.6</b> Powder heat treatment furnace used for powder oxidation.	68
<b>Figure 3.7</b> Schematic of in situ and operando process replicator that can be installed in X-ray imaging synchrotron beamlines (after [67]).	70
<b>Figure 4.1</b> SEM image of EB-PBF Ti6Al4V (a-c) virgin and (d-f) recycled powders. Yellow arrows point the common features such as satellites, elongations, irregularly shaped particles, agglomerates, and particles with open porosities present in (a) and (d). Blue arrows point fine particles (b and c) in virgin powder. Red arrows point to the craters (e) and concave sites (f) in recycled powder.	76
<b>Figure 4.2</b> SEM BSE image of EB-PBF Ti6Al4V (a and b) near-melt zone and (c) away-melt zone powder morphology.	76

<b>Figure 4.3</b> Quantitative powder shape and size analysis: (a) Illustration of classified 2D particle radiographs, the number below each radiograph corresponds to their circularity value, (b) shape analysis results of virgin, recycled, and near-melt zone powders; PSD of (c) virgin vs recycled and (d) away-melt zone vs near-melt zone powders measured by laser diffraction.....	77
<b>Figure 4.4</b> (a) Optical microscopy and (b) SEM BSE image of virgin powder cross-section revealing entrapped powder porosity. ....	78
<b>Figure 4.5</b> SEM BSE image of EB-PBF Ti6Al4V (a and b) virgin, (c) away-melt zone, (d and e) near-melt zone and (f and g) recycled powder particle microstructure.....	80
<b>Figure 4.6</b> Orientation maps of virgin (a) and near-melt zone (b) powder particles based on the IPF. (c) Band contrast map of the same virgin (d) and near-melt zone (e) powder particle with HAGB (red, $\theta > 15^\circ$ ) and LAGB (blue, $1.5^\circ < \theta < 15^\circ$ ).....	81
<b>Figure 4.7</b> Phase maps of EB-PBF Ti6Al4V (a) virgin and (b) near-melt zone powder particles. Blue region- HCP; red region- BCC; black region- zero solutions. ....	81
<b>Figure 4.8</b> Ti6Al4V EB-PBF sieve residue: SEM image of powder particles, (a) hard-sintered, (b) unbroken soft-sintered (red circle), and (c) agglomerated melt ejection; (d) the microstructure of a melt ejection that fell over a powder particle (indicated by the black circle); high magnification images of the (d1) powder particle and (d2) melt ejection regions; (e) orientation map with inset IPF and (f) band contrast map with HAGB (red) and LAGB (blue) of a melt ejection that fell over two powder particles. ....	82
<b>Figure 4.9</b> SEM SE image of (a) virgin and (b) recycled builds in build direction (note the difference in the scale bar length). Up-arrow indicates the build direction. The inset images show the presence of $\alpha_{GB}$ , $\alpha$ and $\beta$ . ....	83
<b>Figure 4.10</b> Fatigue life and SEM images of example fracture surfaces of EB-PBF Ti6Al4V specimens produced from virgin and recycled powder: (a) HCF results, (b) macrograph of virgin specimen, (c) embedded small pores, (d) crack initiation from a surface pore; (e) macrograph of recycled specimen, (f) embedded large spherical pore, (g) crack initiation from a lack-of-fusion defect.....	85
<b>Figure 4.11</b> Fatigue fracture surface of virgin EB-PBF Ti6Al4V specimen that failed after 114,111 cycles. Lack-of-fusion defects and gas pores embedded in the fracture surface are highlighted.....	86

- Figure 4.12** Pore quantification in virgin and recycled Ti6Al4V test specimen using X-ray computed tomography. 3D rendered images of pores overlaid on (a) virgin and (b) recycled test specimens. Z axis corresponds to the build direction. Defect (c) volume fraction, (d) porosity percentage and (e) sphericity as a function of pore equivalent diameter. ....87
- Figure 5.1** SEM micrograph of Ti6Al4V EB-PBF builds in SE mode: virgin specimen (a) as-built and (c) post-thermally treated condition; recycled specimen (b) as-built and (d) post-thermally treated condition (note the difference in the scale bar length).....98
- Figure 5.2** Optical micrograph of Ti6Al4V EB-PBF virgin build (a) as-built and (c) post-thermally treated condition; recycled build (b) as-built and (d) post-thermally treated condition. Red circles highlight spherical gas pores while yellow arrows point lack-of-fusion defects. ....99
- Figure 5.3** Stress-strain plot of the virgin and recycled EB-PBF Ti6Al4V specimens in the as-built and post-thermally treated condition ..... 102
- Figure 5.4** High cycle fatigue properties of virgin and recycled builds in the as-built and post-thermally treated conditions. (a) Uniaxial HCF test; fatigue fracture surfaces of virgin (b) as-built and (d) post-thermally treated condition; fatigue fracture surfaces of recycled (c) as-built and (e) post-thermally treated condition..... 104
- Figure 6.1** SEM BSE image of (a) virgin and (b) oxidised powder; (c) PSD of virgin and oxidised powder. .... 108
- Figure 6.2** SEM image of (a) virgin and (b) oxidised powder particle cross-sections with corresponding EDX/EDS line scan of (c) virgin and (d) oxidised powder particles..... 109
- Figure 6.3** Tensile stress-strain curves of virgin and blended specimens..... 111
- Figure 6.4** SEM SE image of LB-PBF Ti6Al4V tensile fracture surfaces of virgin (a) specimen 1, (b) specimen 2 and blended (c) specimen 1, (d) specimen 2. The scale bars for all the macro surfaces are the same..... 111
- Figure 6.5** Fatigue life and SEM images of fracture surfaces of LB-PBF Ti6Al4V specimens produced from virgin and blended powder: (a) HCF results; (b) virgin specimen that failed from a surface pore, (b1); (c) virgin specimen that failed from a lack-of-fusion

defect, (c1); (d) blended specimen that failed from a surface pore, (d1); (e) blended specimen that failed from a lack-of-fusion defect, (e1). ..... 112

**Figure 6.6** Dynamic X-ray images showing laser-Ti6Al4V powder interaction and spatter formation at 150 W and 50 mms<sup>-1</sup> in the virgin condition at (a) Layer 1, (b) Layer 2, (c) Layer 5 and (d) Layer 10. The scale bars in all the radiographs are 500 μm. The spatter contours are marked by red-dashed circle; Contours of melt tracks, unmelted powder and the depression regions are marked by red, blue and yellow-dashed line respectively. 116

**Figure 6.7** Dynamic X-ray images showing laser-Ti6Al4V powder interaction and spatter formation at 150 W and 50 mms<sup>-1</sup> in the oxidised condition at (a) Layer 1, (b) Layer 2, (c) Layer 5 and (d) Layer 10. The scale bars in all the radiographs are 500 μm. .... 117

**Figure 6.8** Spatter quantity in virgin and oxidised condition. .... 118

**Figure 6.9** (a) Radiograph of Layer 7 virgin build produced using 150 W laser power and 50 mms<sup>-1</sup> scan speed showing unmelted spatter (red circle); (b) radiograph of Layer 2 virgin build formed using 100 W laser power and 50 mms<sup>-1</sup> scan speed showing spatter induced surface roughness and porous spatter. The scale bar in both a and b measured 1 mm. Powder bed contamination by droplet spatters: spatter solidified/sintered over (c) single powder particle, (d and e) cluster of particles to form agglomerates, and (f) spherical 'super-ball' spatter. .... 120

**Figure 6.10** Melt track surface profiles of builds produced by (a) virgin and (b) oxidised powder from layers 1 to 6; (c) average surface roughness in virgin and oxidised builds; effect of layer roughness on powder spreading in (d) virgin and (e) oxidised condition. .... 123

**Figure 6.11** Defect quantification in virgin and oxidised Ti6Al4V builds produced by ISOPR using XCT technique. 3D rendered images of pores overlaid on (a) virgin and (b) oxidised builds. (c) Percentage of porosity and its (d) sphericity as a function of pore equivalent diameter. .... 124

**Figure 6.12** SEM SE image of (a) virgin and (b) oxidised build microstructures. White arrow indicate build direction. Note the difference in scale bar length. .... 125

## List of tables

<b>Table 2.1</b> Chemical composition of Ti6Al4V as per ASTM B265.....	15
<b>Table 2.2</b> Standard terminologies used in AM as per ISO/ASTM 52900.....	21
<b>Table 2.3</b> Classification of powder flow behaviour based on the HR values [105].....	43
<b>Table 3.1</b> Particle shape parameters used for classification of spherical, satellites, irregular, and fine Ti6Al4V EB-PBF powder particles for quantitative powder shape analysis. ....	60
<b>Table 3.2</b> Chemical composition (wt.%) of Ti6Al4V powder. ....	66
<b>Table 4.1</b> Al, V and O content of EB-PBF Ti6Al4V powders in virgin, recycled, near-melt and away-melt zone conditions, and the builds.....	75
<b>Table 4.2</b> Mechanical properties of virgin and recycled EB-PBF Ti6Al4V builds. ASTM F3001- minimum tensile properties of ELI Ti6Al4V specimen in X-Y direction (perpendicular to build direction) produced by powder bed fusion AM. ....	84
<b>Table 5.1</b> Static mechanical properties of Ti6Al4V EB-PBF virgin and recycled material in the as-built and post-thermally treated condition. ....	102
<b>Table 6.1</b> Tensile properties of virgin and blended LB-PBF Ti6Al4V builds. ....	110

# Table of Contents

<b>Abstract</b> .....	<b>iv</b>
<b>Preface</b> .....	<b>vi</b>
<b>Acknowledgements</b> .....	<b>ix</b>
<b>List of abbreviations</b> .....	<b>xi</b>
<b>List of figures</b> .....	<b>xiii</b>
<b>List of tables</b> .....	<b>xix</b>
<b>1 Introduction</b> .....	<b>1</b>
1.1 Background and motivation for research .....	1
1.2 Research aim .....	3
1.3 Research objectives .....	3
1.4 Thesis structure .....	4
<b>2 Literature review</b> .....	<b>5</b>
2.1 Introduction.....	5
2.2 Titanium metallurgy .....	6
2.2.1 Background .....	6
2.2.2 Crystal structure .....	6
2.2.3 Titanium alloys and classification .....	7
2.2.4 Phase transformation .....	10
2.2.5 Hardening mechanism .....	12
2.2.6 Oxidation .....	12
2.3 Ti6Al4V .....	14
2.3.1 Background .....	14
2.3.2 Heat treatment.....	15
2.3.3 Microstructure .....	17
2.3.4 Influence of microstructure on mechanical properties .....	17
2.4 Additive manufacturing.....	20
2.4.1 Introduction .....	20
2.4.2 Process chain.....	22

---

2.4.3	Classifications in additive manufacturing.....	22
2.5	Powder bed fusion .....	24
2.5.1	Electron beam powder bed fusion (EB-PBF) process .....	24
2.5.2	Laser beam powder bed fusion (LB-PBF) process.....	29
2.6	Raw materials .....	37
2.6.1	Powder production.....	38
2.6.2	Powder characteristics.....	39
2.6.3	Powder recycling.....	47
2.7	Effects of powder recycling- Ti6Al4V alloy .....	48
2.7.1	Evolution of powder properties with powder recycling.....	48
2.7.2	Evolution of build properties with powder recycling .....	50
2.8	Summary .....	54
2.9	Knowledge gaps .....	55
<b>3</b>	<b>Experimental methodology .....</b>	<b>56</b>
3.1	Introduction.....	56
3.2	Part-1: Electron beam powder bed fusion.....	56
3.2.1	Overview .....	56
3.2.2	Powder feedstock material .....	56
3.2.3	Experimental approach.....	56
3.2.4	Manufacturing parameters.....	58
3.2.5	Powder characterisation .....	58
3.2.6	Post-thermal treatment .....	63
3.2.7	Part characterisation.....	63
3.3	Part-2: Laser beam powder bed fusion.....	66
3.3.1	Overview .....	66
3.3.2	Powder feedstock.....	66
3.3.3	Experimental approach.....	66
3.3.4	Powder preparation and blending.....	67

3.3.5	Powder characterisation .....	68
3.3.6	Mechanical test specimen manufacture .....	69
3.3.7	Mechanical test specimen characterisation .....	69
3.3.8	Real-time synchrotron imaging using process replicator.....	69
3.3.9	Image processing.....	71
3.3.10	Spatter and roughness measurement.....	71
3.3.11	X-ray computed tomography.....	72
3.3.12	Microstructure and microhardness .....	72
<b>4</b>	<b>Effects of powder recycling in electron beam powder bed fusion .....</b>	<b>73</b>
4.1	Introduction.....	73
4.2	Effects of recycling on powder properties .....	75
4.2.1	Powder chemical composition.....	75
4.2.2	Powder morphology and particle size distribution.....	75
4.2.3	Powder cross-section analysis.....	78
4.2.4	Sieve residue.....	82
4.3	Effects of recycling on build properties.....	83
4.4	Discussion .....	87
4.4.1	Evolution of powder characteristics .....	87
4.4.2	Evolution of build properties .....	92
4.5	Chapter conclusions .....	94
<b>5</b>	<b>Response of virgin and recycled EB-PBF builds to post-thermal treatment... 96</b>	
5.1	Introduction.....	96
5.2	Effects of post-thermal treatment on the virgin and recycled build microstructure and defects.....	98
5.3	Effects of post-thermal treatment on the virgin and recycled build Mechanical properties .....	100
5.4	Chapter conclusions .....	104
<b>6</b>	<b>Effects of powder recycling in laser beam powder bed fusion .....</b>	<b>106</b>
6.1	Introduction.....	106
6.2	Powder characteristics.....	108

---

6.3	Mechanical properties of builds produced from virgin and blended powder	110
6.4	Real-time monitoring of multi-layer build formation using virgin and oxidised powder in LB-PBF process	113
6.4.1	Multilayer build formation	113
6.4.2	Spatter formation	114
6.4.3	Spatter quantification	118
6.5	Effects of spatter on build properties and powder recycling	119
6.6	Morphology of melt tracks produced using virgin and oxidised powder	121
6.7	Analysis of defects in the builds produced from virgin and oxidised powder	123
6.8	Microstructure and hardness of melt tracks produced from virgin and oxidised powder	124
6.9	Chapter conclusions	125
<b>7</b>	<b>Conclusions and future work</b>	<b>127</b>
7.1	Research summary	127
7.2	Key research findings	128
7.2.1	Evolution of powder properties with recycling in the EB-PBF process	128
7.2.2	Evolution of build properties with recycling in the EB-PBF process	129
7.2.3	Effects of high O Ti6Al4V powder particles in the LB-PBF process	129
7.3	Limitations of the current study	129
7.4	Outlook for future research	130
	<b>References</b>	<b>133</b>
	<b>Appendix A</b>	<b>149</b>
	<b>Appendix B</b>	<b>152</b>
	<b>Appendix C</b>	<b>153</b>

# 1 Introduction

## 1.1 Background and motivation for research

Titanium alloys are used in a wide range of diversified applications including biomedical, aerospace, automotive, nuclear, energy and marine industries [1]. Although a large number of titanium alloys are available in the market, Ti6Al4V covers 50% of the whole titanium production, and is therefore the most popular titanium alloy [2]. Ti6Al4V is used in several parts of modern aircraft structures (*e.g.* fan blades, engine parts, airframe components, *etc.*) owing to its high strength to weight ratio, low density, high fatigue, corrosion and oxidation resistance (up to  $\sim 400^{\circ}\text{C}$ ) [3,4].

Although there is an increasing demand for the use of Ti6Al4V components in aerospace, fabricating them using conventional routes (*e.g.* casting, forging, *etc.*) and subsequent machining leads to high material wastages, thereby increasing the buy-to-fly ratio (mass of the material used for producing the part to mass of the finished part) [5]. In addition, the alloy has low thermal conductivity, high oxygen reactivity, and strain hardening behaviour that makes it challenging to be processed by conventional manufacturing routes [6]. Additive manufacturing (AM) processes like laser and electron beam powder bed fusion offer a viable solution by restricting the material quantity requirements necessary to achieve the desired part geometry and thereby reducing the buy-to-fly ratio [7]. Other benefits include fewer manufacturing steps, less tooling requirements, shorter lead time and higher design freedom [8]. Therefore, customized complex functional engineering parts made of difficult to machine materials like Ti6Al4V can be manufactured at reduced costs [9–12].

The principle of operation in both EB-PBF and LB-PBF processes is fairly similar: the powder particles are melted and fused by a laser or electron beam pass-by-pass and layer upon layer fashion based on the input computer aided design (CAD) data [13–16]. Commonly mentioned benefits of using powder as a feedstock material in an AM process are its ability to be recycled for subsequent build cycles [17], serving as support structures, especially in EB-PBF process [18] and powder blending to produce multi-material AM builds with various compositions [19]. A key issue in employing AM components in aerospace industries is the consistency in part properties. On one hand, the performance of the AM machines and process control (*e.g.* power, scan speed, layer

thickness hatch spacing, *etc.*) have a strong influence on build properties [20]. On the other hand, the physical and chemical properties of the powder feedstock play a vital role in producing components with reproducible properties for demanding applications [21]. Hence, it is important to understand the connection between the properties of the individual powder particles and the bulk powder behaviour which contributes to the configuration of each powder layer. The quality of the powder layers, which are influenced by powder spreadability, packing behaviour, chemical composition and cleanliness, determines the quality of the components built. Hence, detailed understanding of the powder intrinsic and extrinsic properties and its evolution throughout the entire build regime is crucial to produce components with predictable properties.

Principally, the volume of the powder consumed during the manufacturing process depends entirely on the size of the components fabricated relative to the build volume of the AM machine. Sometimes the volume of the component could be significantly less than the volume of the powder present on the build platform, as illustrated in Figure 1.1a. Since, the material costs in powder bed AM constitute up to 20% (Figure 1.1b) of the total manufacturing costs, reusing the unmelted powder becomes an interesting option to improve process efficiency.

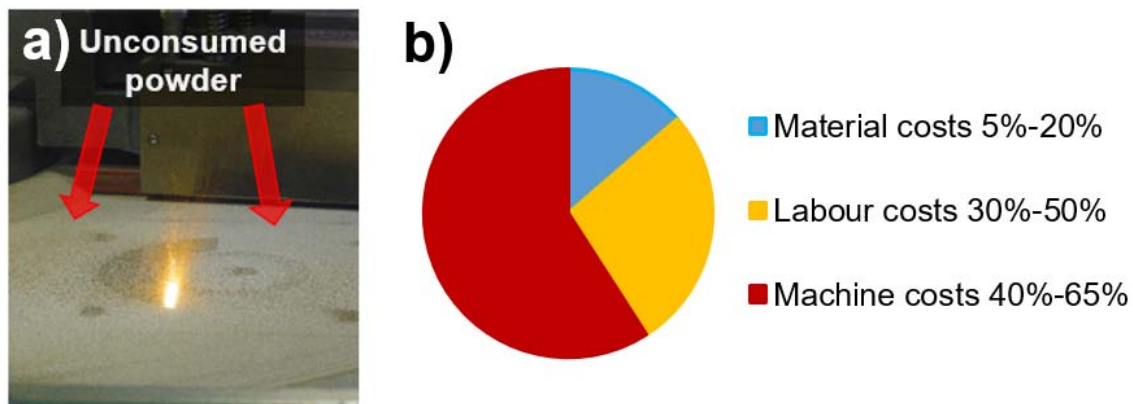


**Figure 1.1** a) Unconsumed powder during LB-PBF process; b) cost breakdown in powder bed AM processes (after [22]).

However some of the recycled powder particles may have different physical and chemical properties owing to the degradation during recycling, which can affect the bulk powder behaviour. Excessive variations in powder characteristics between the builds can cause heterogeneity in powder layer properties. This can increase the volume of defects

in the components leading to poor mechanical performance and undesired surface finish and thereby can lead to inconsistencies in the build properties when using recycled powder [23]. Hence, manufacturers are often reluctant to use recycled powder to manufacture high value parts for safety critical aerospace applications. Therefore, there is a natural interest to understand the effects of powder recycling and its impact on the parts thus fabricated.

## **1.2 Research aim**

In view of the above factors, the current study is aimed to address the effects of recycling Ti6Al4V powder in LB-PBF and EB-PBF processes, which are the two most popular metal powder bed-based AM processes used for manufacturing aerospace components of intricate geometry. Hopefully, the findings of this research will provide a better understanding of the challenges in powder recycling and enable development of suitable standards for the application of recycled powder in manufacturing safety critical parts for aerospace industries.

The research problem is addressed using three facets. The first facet covers the effects of powder recycling on powder and component properties in the EB-PBF process. In the second facet, the response of additional post-thermal treatments on the recycled EB-PBF build properties compared to the virgin builds are presented. The final facet demonstrates the effects of powder blending during recycling in the LB-PBF process, with attention given to the powder chemical changes, especially oxidation. The results reported provide a better understanding of the challenges in using recycled powder for fabrication of industrial aerospace components.

## **1.3 Research objectives**

The thesis aim has been divided into the following objectives:

- (i) To identify the changes in powder properties with recycling and how the changes in individual powder particles affect bulk powder behaviour.
- (ii) To correlate the changes in powder characteristics with recycling to its corresponding impact on build properties.
- (iii) To evaluate the effect of post-thermal treatment on the mechanical and microstructural properties of the builds produced from recycled powder.

- (iv) To investigate the impact of powder oxidation on melt pool dynamics, spatter, defects, surface roughness and the potential effects of blending the virgin and recycled powder with different oxygen contents on the mechanical properties.

## 1.4 Thesis structure

In the view of addressing the above objectives, following this introduction chapter, Chapter 2 provides a background of titanium alloys, EB-PBF and LB-PBF processes, properties of Ti6Al4V material processed by EB-PBF and LB-PBF processes, and powder feedstock properties. Also, previous studies performed on Ti6Al4V powder recycling are reviewed and the current research gaps are highlighted. The experimental approach and the characterisation techniques employed in this study to assess powder recyclability are described in Chapter 3.

In Chapter 4, the effects of powder recycling and their impact on build properties in EB-PBF process are presented. The effects of preheat scans, the heterogeneity in powder property changes within the same build, effects of powder recovery, sieving, and multiple reuse on microstructure, defect population, static and dynamic mechanical properties are discussed (Research objective 1 and 2).

Chapter 5 presents the response of virgin and recycled EB-PBF builds to post-thermal treatments. The builds are tested and compared in terms of their microstructure and mechanical properties in the as-manufactured and heat treated condition (Research objective 3).

In Chapter 6, powder blending during powder recycling in LB-PBF process are demonstrated, with an emphasis on powder chemical changes, such as powder oxidation. Real time X-ray imaging experiments reveal the effects of powder oxidation on laser-matter interaction, surface roughness evolution and defect population (Research objective 4).

Chapter 7 summarises the key findings of this research and also provides possibilities of future work that could arise out of this presented work.

\*\*\*\*\*

## 2 Literature review

### 2.1 Introduction

This review was conducted with an aim to develop a theoretical framework and understanding of the relevant areas, identify the knowledge gaps and build-up an experimental strategy to investigate the challenges of recycling Ti6Al4V powder in powder bed fusion additive manufacturing process. This review chapter focuses on some of the key topics shown in Figure 2.1 that are relevant to the current research. To begin with, this chapter introduces the fundamentals of titanium metallurgy; powder bed fusion AM process with emphasis on LB-PBF and EB-PBF processes; the powder feedstock requirements and its influence on build quality. Afterwards, the advantages and challenges in powder recycling, previous research work conducted and the current knowledge gaps are discussed.

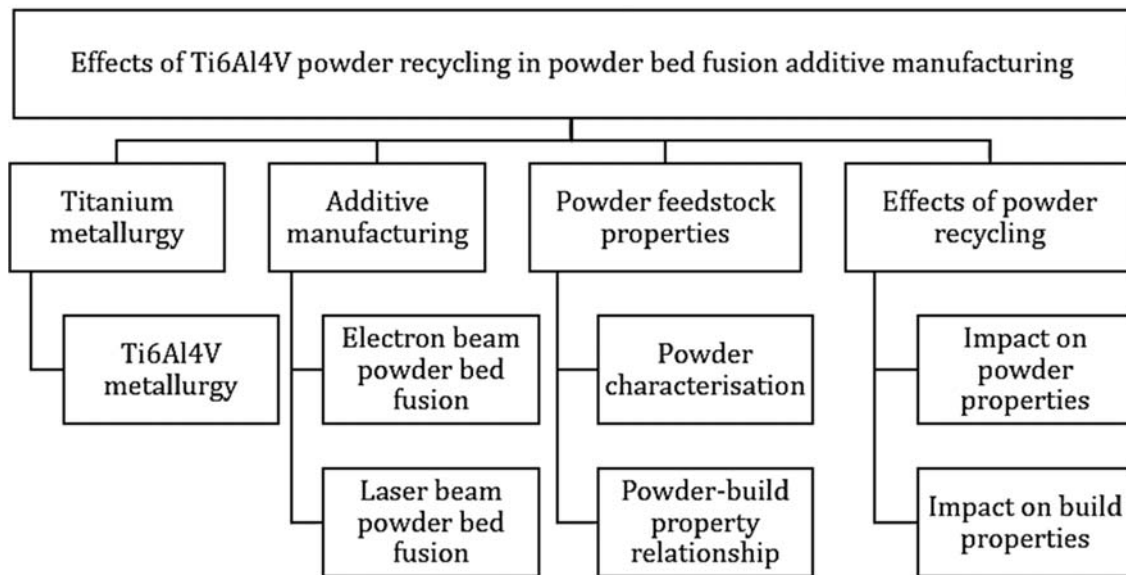


**Figure 2.1** Main topics discussed in this chapter.

---

Some parts of this chapter has been published as a review article entitled '*A technical review of the challenges of powder recycling in the laser powder bed fusion additive manufacturing process*', Journal of Engineering, 1-7, Soundarapandiyam *et al.* 2021.

## 2.2 Titanium metallurgy

### 2.2.1 Background

Titanium is one of the light alloy elements that has a wide range of diversified applications in defence, aerospace, automobile, oil and gas, sports, marine, medical industries due to its high strength, low density and corrosion resistance over its competing materials like steel and aluminium [1,24,25]. The material can be processed into products using several manufacturing routes including casting, forging, powder metallurgy and advanced manufacturing techniques like AM [6,26,27]. Titanium is highly reactive with oxygen and is therefore melted and cast in a vacuum or inert environment. Upon exposure to air, it forms a metal oxide layer on its surface at room temperature. At high temperatures, the oxide layer breaks and oxygen diffuses through the oxide layer causing alloy embrittlement, restricting titanium application to temperatures below 600°C [1]. It also has poor machinability that can result in high tool wear and poor part surface quality. This is due to its work hardening behaviour and low thermal conductivity, modulus and hardness. Therefore special cutting tools and coolants are often used while machining titanium. These factors increase the costs of the material and limiting titanium only to high value applications [27].

### 2.2.2 Crystal structure

Titanium can crystallise adopting different crystal structures depending on the temperature range. Commercially pure titanium (cp-Ti), at room temperature exists in a hexagonal close packed structure (HCP) referred to as  $\alpha$  titanium. At elevated temperatures of about 882°C, referred to as the  $\beta$  transus temperature, it undergoes allotropic transformation to body-centered cubic structure (BCC), referred as  $\beta$  titanium. The  $\beta$  transus temperature depends on the purity of the metal *i.e.* the alloy content. Figure 2.2 shows schematically the  $\alpha$  and  $\beta$  phase crystal structure in titanium with the lattice parameters and densely packed planes [4].

Due to the HCP structure of pure titanium, deformation can occur by twinning and activation of slip systems through dislocations. However, when solute content is high, for example in  $\alpha+\beta$  alloys, twinning deformation is suppressed. Only three slip systems are available in the HCP structure while BCC has twelve slip systems and therefore the ease of plastic deformation is higher in BCC than HCP. Also, the energy required to cause the dislocations to glide on the slip plane is higher in the HCP than BCC structure as the length



and  $\beta$  phases and have less effect on the  $\beta$  transus temperature and therefore are referred to as neutral elements [4]. Figure 2.3 shows schematically the effect of alloying elements on the phase diagram.

This item has been removed due to 3rd Party Copyright. The unabridged version of the thesis can be found in the Lanchester Library, Coventry University.

**Figure 2.3** Schematic showing the effect of alloying elements on titanium phase transformation (after [4]).

Excessive addition of alloying elements can result in alloy embrittlement. The influence of  $\alpha$  and  $\beta$  stabilisers on the properties of titanium alloys is expressed empirically as  $[Al]_{eq.} = [Al] + 0.17 [Zr] + 0.33 [Sn] + 10 [O]$ . Titanium alloys are classified based on the pseudo-binary phase diagram shown in Figure 2.4 [1].

This item has been removed due to 3rd Party Copyright. The unabridged version of the thesis can be found in the Lanchester Library, Coventry University.

**Figure 2.4** Titanium alloys classification revealing  $\alpha$ ,  $\alpha+\beta$  and  $\beta$  alloys region (after [1]).

### 2.2.3.1 $\alpha$ alloys

The alloys in this group are mainly made by substitutional and interstitial  $\alpha$  stabilising elements with a small concentration of  $\beta$  stabilisers. In addition, limited quantities of V, Fe and Mo are also alloyed to improve the material strength. Alloys of different grades are developed by varying the concentration of the alloying elements [1]. The properties of the alloys are generated by the HCP structure and the processing techniques employed.  $\alpha$  titanium alloys cannot be strengthened by heat treatment due to limited phase transformation. The alloys possess high creep and corrosion resistance but poor ductility and forgeability [27].

### 2.2.3.2 Near $\alpha$ alloys

These alloys are developed for high temperature applications and consists of a relatively higher concentration of  $\beta$  stabilisers (up to 2%) and they exhibit a combination of high creep resistance, strength and better forgeability than  $\alpha$  alloys [25].

### 2.2.3.3 $\alpha+\beta$ alloys

$\alpha+\beta$  alloys are blend of one or more alpha favouring and beta favouring alloying elements which moves the alloy composition away from the alpha solvus boundary. The alloys exhibit an excellent balance of ductility, strength and fatigue properties but possess low creep resistance than the near  $\alpha$  alloys that limit their applications to below 400°C. The presence of sufficient amount of  $\beta$  stabilising elements retains the  $\beta$  phase at room temperature. Different types of microstructures are attainable by adjusting the concentration of the alloying elements, the processing method and the heat treatment conditions to meet the properties required for the application [4]. As can be seen in Figure 2.4, based on the rate of solidification, the microstructure may be  $\alpha+\beta$  for slow cooling or martensitic for rapid cooling (due to the diffusionless transformation). The  $M_s$  line represents the martensitic start temperature. Ti6Al4V is the most popular alloy in this group which has a composition close to the near  $\alpha$  alloys with 6 wt.% Al (which can vary between 5.5% to 6.75%) acting as the  $\alpha$  stabilising element and 4 wt.% V (which can vary between 3.5% to 4.5%) that acts as the  $\beta$  stabilising element [1].

### 2.2.3.4 $\beta$ alloys

$\beta$  alloys consists of sufficiently high quantities of  $\beta$  stabilising elements to retain the BCC structure at room temperature. This offers the ability to cold-form the alloy in the soft  $\beta$  phase condition and subsequently increase hardenability by aging heat-treatments. The

alloys exhibit high ductility and toughness, which are achieved due to the low concentration of oxygen and carbon [26].

## 2.2.4 Phase transformation

Upon cooling, the BCC  $\beta$  phase transforms to the HCP  $\alpha$  phase following either the martensitic (diffusionless) or by the diffusion and growth transformation mechanism.

### 2.2.4.1 Martensite transformation

The martensite transformation is observed when alloys are subjected to high cooling rates. This results in the activation of shear systems causing transition from BCC ( $\beta$ ) $\rightarrow$ HCP ( $\alpha$ ) crystal structure [1]. Ahmed *et al.* [28] reported that at high cooling rates above  $425^\circ\text{C/s}^{-1}$ , the microstructure consisted of fully acicular morphology of  $\alpha'$  in Ti6Al4V alloy (Figure 2.6a). At slightly lower cooling rates between  $425^\circ\text{C}$  and  $20^\circ\text{C}$ , nucleation and growth of  $\alpha$  phase occurred at the  $\beta$  grain boundaries and the grain boundary  $\alpha$  had a HCP structure, which was relatively blocky and contained high dislocation density, similar to  $\alpha'$ . This type of transformation are referred to as massive transformations and the resultant martensite is called massive martensite microstructure (Figure 2.6b). It can be seen in Figure 2.6a and b that the acicular martensite structure consists of needle-like discrete  $\alpha$  plates, while massive martensite consists of isolated packets comprising fine parallel  $\alpha$  plates of the same orientation. Increasing the alloy content causes distortion of the HCP structure to form orthorhombic phase referred to as  $\alpha''$ . The  $M_s$  depends on the concentration of the alloying elements.  $\alpha$  stabilisers increase  $M_s$  while it decreases with increasing  $\beta$  stabilising elements [1].

During phase transformation ( $\beta\rightarrow\alpha$ ) in binary Ti-Al alloys, some transient secondary phases can also form.  $\alpha_2$  ( $\text{Ti}_3\text{Al}$ ) is one of those secondary phases that has received significant concern due to its deleterious effect on material elongation and stress-corrosion cracking [26]. The  $\alpha_2$  phase is hence favoured in titanium alloys that are used at high temperatures, where stress-corrosion cracking is not a major factor. Yan *et al.* [29] demonstrated that the increase in the O content of Ti6Al4V alloy stimulated the precipitation and the increase in volume fraction of  $\alpha_2$  phase in the material. Furthermore, oxygen favoured stabilisation of  $\alpha_2$  phase. Thermo-Calc prediction has shown that for alloy containing 1 wt.% O, the precipitation of  $\alpha_2$  in the  $\alpha$  phase occurred at about  $500^\circ\text{C}$  when the cooling rate was  $10^\circ\text{C}/\text{min}^{-1}$  (Figure 2.5). Microstructure investigation performed by the same authors have shown that clusters of  $\text{Ti}_3\text{Al}$  ( $\alpha_2$ )

precipitates were present in the  $\alpha$  phase regions of Ti6Al4V alloy containing 0.49 wt.% O. Furthermore, a steep decline in the material elongation with increasing O content was observed. This limits the maximum O content in the Ti6Al4V material to 0.2 wt.% in aerospace applications. However, it has been reported in [26] that material strength can be increased by 15-35 MPa with the formation of  $\alpha_2$ . The effect of increase in O content on Ti6Al4V material properties is discussed further in Section 2.3.4.

This item has been removed due to 3rd Party Copyright.  
The unabridged version of the thesis can be found in the  
Lanchester Library, Coventry University.

**Figure 2.5** Pseudo-phase diagram of Thermo-Calc prediction of  $\alpha_2$  phase formation in Ti-4V-10 alloy (after [29]).

#### 2.2.4.2 Diffusional transformation

Diffusional transformation occurs by slow cooling the alloy from the  $\beta$  phase through the  $\alpha+\beta$  to the  $\alpha$  phase field. At low cooling rates, nucleation of the  $\alpha$  phase begins at the  $\beta$  grain boundary which further grows to form continuous  $\alpha$  plates over the grain boundary  $\beta$ , referred to as grain boundary  $\alpha$  ( $\alpha_{GB}$ ). With continued cooling,  $\alpha$  plates start to nucleate from  $\alpha_{GB}$  or  $\beta$  grain boundary and grow into the  $\beta$  grain matrix until they meet another  $\alpha$  plate nucleated from a different site on the grain boundary [26]. The resulting structure consists of a series of  $\alpha$  plates separated by a retained  $\beta$  matrix as shown in Figure 2.6c. The resulting microstructure is termed a lamellar microstructure. Further, an increase or decrease in the cooling rate affects the width of the  $\alpha$  plates. At high solidification rates, new  $\alpha$  plates nucleate from the previously formed  $\alpha$  plates and grow in a direction perpendicular to the previously formed  $\alpha$  plate, resulting in a basket-weave like structure, referred to as a Widmanstätten structure [1].

This item has been removed due to 3rd Party Copyright. The unabridged version of the thesis can be found in the Lanchester Library, Coventry University.

**Figure 2.6** Effects of cooling rate on Ti6Al4V material microstructure: (a)  $\alpha'$ , (b)  $\alpha'+\alpha_m$  and (c)  $\alpha+\beta$  Widmanstätten structure (after [28]).

### 2.2.5 Hardening mechanism

Hardenability is the ability to tailor the properties of an alloy to achieve the required hardness level. It can be achieved by solid solution strengthening (SSS), grain boundary hardening and precipitation hardening [1]. Grain boundary hardening can be achieved by increasing the cooling rate and attaining a fine lamellar structure or inducing a martensitic transformation. However, the increase in hardness by martensite formation is only marginal in Ti alloys compared to steels, where the high hardness level is caused by the lattice distortion to a tetragonal structure [26].

SSS in the  $\alpha$  phase is caused by substitutional elements like Al, Zr and Sn and interstitial elements like O and N, and in the  $\beta$  phase, solute elements like V, Nb, Mo, Fe and Cr contribute to SSS. These elements dissolve in both the phases of the Ti alloy either by substitution with Ti atoms or interstitially in the crystal structure and offer resistance to the motion of dislocations during plastic deformation, thereby increasing the yield strength of the material [26]. Precipitation hardening is achieved by the precipitation of new phase from super saturated solid solution. For example, in Ti-Al alloys, intermetallic phase,  $Ti_3Al$  or  $\alpha_2$  is formed at high solute contents which improves material strength and creep resistance. The properties of the alloys are also influenced by the morphology and dispersion of the precipitates. Precipitation is generally achieved by subsequent homogenisation and aging treatments after rapid cooling. These precipitates interact and hinder the dislocation glide causing dislocation pile-ups which in turn leads to material strengthening [4].

### 2.2.6 Oxidation

Titanium alloys have a high affinity with oxygen. Oxidation occurs instantaneously on the surface of titanium upon exposure to air. The formed oxide layer,  $TiO_2$ , prevents the metal

from further oxidation at room temperature [30]. Guleryuz *et al.* [31] demonstrated that the natural oxide layer degraded at high temperatures and oxygen diffused through the scale resulting in the growth of the oxide layer inwards at the metal/oxide interface due to the affinity of Ti alloys with O. Furthermore, since oxygen has a high solubility in the  $\alpha$  phase, an  $\alpha$ -rich layer stabilised by O, referred as ' $\alpha$  case' formed adjacent to the natural oxide layer. Figure 2.7 shows the optical microscopy image of Ti6Al4V alloy cross-section. It can be seen that the thickness of the  $\alpha$ -case increases with increase in temperature of oxidation. In addition, Gaddam *et al.* [32] demonstrated that the  $\alpha$  case thickness also increases with increase in oxidation time and the rate of oxidation is quicker at higher temperatures, as shown in Figure 2.8. The  $\alpha$ -case is generally recognised as a hard and brittle layer that can lower the fatigue resistance and fracture toughness of the material. In the same study [32], the authors have shown that the  $\alpha$  case formed on the Ti6Al4V alloy had higher microhardness than the parent material (Figure 2.9b). In [33], it was demonstrated that the low cycle fatigue life of Ti-6242 alloy decreased with increase in  $\alpha$ -case depth (Figure 2.9a).

This item has been removed due to 3rd Party Copyright. The unabridged version of the thesis can be found in the Lanchester Library, Coventry University.

**Figure 2.7** Optical microscopy image of cross-section of Ti6Al4V alloy oxidised at (a) 600°C (b) 700°C and (c) 850°C revealing  $\alpha$ -case formed over the surface (after [31]).

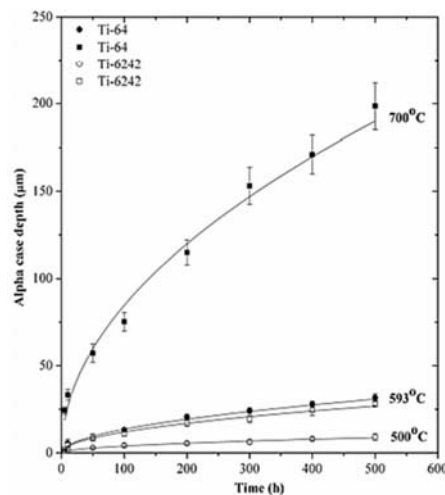


**Figure 2.8** Changes in  $\alpha$ -case depth at varying oxidation time and temperatures (after [32])

Therefore, oxidation is a major limiting factor for high temperature application of titanium. Nevertheless, alloy additions including Mo, Nb, Si, Cr, Al *etc.* are introduced to reduce the diffusion of O. These elements form a more thermally stable oxide layer that prevents further diffusion of O. For example, Al forms  $\alpha$ -Al<sub>2</sub>O<sub>3</sub> which is relatively more stable and dense than TiO<sub>2</sub> and so results in a mixed TiO<sub>2</sub> + Al<sub>2</sub>O<sub>3</sub> layer beneath the primary surface oxide layer of TiO<sub>2</sub> [1].

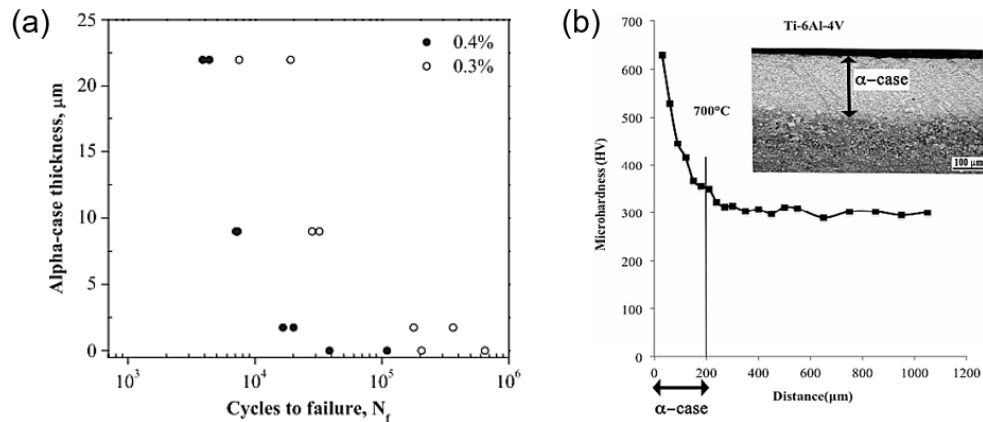


**Figure 2.9** (a) Low cycle fatigue (LCF) of Ti-6242 alloy at 0.4% and 0.3% strain rate (after [33]); (b) Variation of Vickers microhardness of Ti6Al4V from surface containing  $\alpha$ -case to the parent material (after [32]).

## 2.3 Ti6Al4V

### 2.3.1 Background

Ti6Al4V belongs to the  $\alpha+\beta$  group of titanium alloys, and exhibits an excellent balance of ductility, strength and fatigue properties. Today, there are more than 100 titanium alloys, out of which 50% of the applications are covered by Ti6Al4V [26]. Two commercial grades of Ti6Al4V, Grade 5 and Grade 23 are available in the market in the as-cast, wrought and powder forms and are generally used in the annealed or solution treated and aged conditions. The chemical composition of the alloy is shown in Table 2.1. The 6 wt.% Al acts as the stabilising element of the  $\alpha$  phase and 4 wt.% V acts as the  $\beta$  stabilising element. The main difference between Grade 5 and Grade 23 is that the O level can be up to 0.20 wt.% in Grade 5 while in Grade 23 only a maximum O content of 0.13 wt.% is allowed. Grade 23 (also referred to as 'extra low interstitial', ELI) offers high damage tolerance and high fracture toughness but lower strength in comparison to Grade 5 and is widely used in biomedical applications for producing neck, knee, hip, spine *etc.* implants [25].  $\alpha$  phase is predominant at room temperature but at elevated

temperatures of about 995°C ( $\beta$  transus), the alloy undergoes allotropic transformation to single  $\beta$  phase [1]. The alloy is processed and heat treated in the  $\alpha+\beta$  or  $\beta$  phase field and subsequently either slow or fast cooled to achieve the required properties. Therefore, the properties of the alloy depend on the microstructure developed during solidification, processing and subsequent heat treatment practices employed [26].

**Table 2.1** Chemical composition of Ti6Al4V as per ASTM B265.

Grade	Al	V	Fe	O	N	C	H	Ti
5	5.5- 6.75	3.5-4.5	≤0.4	≤0.2	≤0.05	≤0.10	≤0.015	Bal.
23	5.5-6.5	3.5-4.5	≤0.25	≤0.13	≤0.03	≤0.08	≤0.013	Bal.

### 2.3.2 Heat treatment

Ti6Al4V is a heat treatable alloy and therefore the microstructure can be tailored to achieve the properties for the required applications. Heat treatments are performed for stress relieving to remove residual stress, and to improve material ductility, toughness, fatigue life and strength. Figure 2.10 shows the different types of transformations that can occur by varying the cooling rates in Ti6Al4V. It can be seen that the martensite transformation during cooling from the  $\beta$  phase can occur at cooling rates from 18°Cs<sup>-1</sup> to 425°Cs<sup>-1</sup> and the corresponding  $M_s$  ranges from 575°C to 800°C depending on the concentration of the alloy contents present in the material [25].

This item has been removed due to 3rd Party Copyright. The unabridged version of the thesis can be found in the Lanchester Library, Coventry University.

**Figure 2.10** Ti6Al4V phase transformation at different cooling rates (after [28]).

### 2.3.2.1 Annealing treatment

Annealing treatment is performed to improve the fracture toughness, ductility and fatigue properties of the material. There are different types of annealing treatments.

**Stress relief annealing treatment** is used to reduce the residual stresses developed in the material during the manufacturing process. The material is heated and held in the  $\alpha+\beta$  field, followed by slow cooling in air. For Ti6Al4V it is generally conducted in the temperature range of 480-650°C. In the case of  $\beta$  annealing, the material is heated to the  $\beta$  phase region, isothermally held and cooled in air, or furnace or water quenched. Long dwell time and slow cooling rate can lead to coarsening of  $\alpha$  colony size, lamellar  $\alpha$  and  $\alpha_{GB}$  which can affect the mechanical properties.  $\beta$  annealing improves fracture toughness but reduces strength of the material [1].

**Mill annealing treatment** is performed on wrought material and is referred to as incomplete annealing as the microstructure of the material in the wrought-state is preserved. For Ti6Al4V, the material is heated to 700-800°C, isothermally held and air cooled [4].

**Recrystallisation annealing** is performed to alleviate dislocation pile-ups developed due to cold or hot-working processes and improve fracture toughness of the material. In this heat treatment, the alloy is heated to the upper end of the  $\alpha+\beta$  field, isothermally held and furnace cooled [4].

### 2.3.2.2 Solution treatment and aging (STA)

The process comprises solution treatment of the alloy in the  $\beta/\alpha+\beta$  field followed by quenching and aging. Quenching the alloy results in the formation of  $\alpha'$  microstructure. As mentioned earlier, only a marginal increase in hardness is achieved as a result of this transformation ( $\beta \rightarrow \alpha'$ ) as both  $\alpha$  and  $\alpha'$  have the same crystal structure and lattice parameters, unlike in steels. The marginal increase in hardness is achieved as a result of dislocation pile-ups due to rapid cooling. Aging leads to decomposition of  $\alpha' \rightarrow \alpha+\beta$  ( $\beta$  isomorphous) or  $\beta$  intermetallic compound ( $\beta$  eutectoid) depending on the alloy content. STA treated alloys offer superior strength but reduced ductility and fracture toughness than the annealed condition. To improve ductility, in some cases, overaging is performed but strength is then compromised [25].

### 2.3.3 Microstructure

Ti6Al4V alloy can develop mainly three types of microstructure: lamellar, equiaxed and bimodal depending on the processing conditions. Bimodal and equiaxed microstructures are a product of thermomechanical processes [1]. Since the focus of this work is on additive manufacture, only lamellar microstructure, their morphology and impact on the mechanical properties are discussed.

#### 2.3.3.1 Lamellar

Lamellar structure is formed as a result of slow cooling from the  $\beta$  transus that leads to diffusion and growth of  $\alpha$  plates along the  $\beta$  grain boundaries and into the matrix as shown in Figure 2.6c. The size of  $\alpha$  colonies, width of lamellae  $\alpha$  and  $\alpha_{GB}$  are determined by the processing temperature and cooling rate. The width of  $\alpha$  plates and the size of  $\alpha$  colonies reduce with increasing cooling rate. High cooling rates lead to martensite transformation. In the slow cooled materials, the width of the lamellae  $\alpha$  can be equal to  $\alpha_{GB}$  width. For martensite structures, further annealing treatment is generally performed in the  $\alpha+\beta$  field to transform  $\alpha' \rightarrow$  fine  $\alpha+\beta$  [26].

### 2.3.4 Influence of microstructure on mechanical properties

The lamellar microstructural features that can impact the mechanical properties are  $\alpha$  colony size,  $\beta$  grain size, thickness of  $\alpha$  lamellae and  $\alpha_{GB}$  and volume fraction of  $\alpha$  and  $\beta$  phases. By adjusting these features, a broad range of mechanical properties can be achieved. A reduction in  $\alpha$  colony size and  $\alpha$  lamellae thickness increases yield stress and material ductility. Lutjering *et al.* [1] stated that  $\alpha$  colony size is the most vital factor that influences mechanical properties of Ti6Al4V alloys. The size of  $\alpha$  colonies inside the  $\beta$  grain is determined by the cooling rate. This is because the effective slip length for a dislocation glide is determined by the  $\alpha$  colony size. At a high rate of cooling, the  $\alpha$  colony size decreases and the slip length reduces and thereby increases the yield stress (YS) as per Hall-Petch relationship. Figure 2.11a shows the impact on yield strength and elongation at varying cooling rates. It can be seen that there is a gradual increase in the yield stress caused by the decrease in  $\alpha$  colony size and lamellae  $\alpha$  followed by steep increase caused due to the formation of martensite structure. Similarly, in the case of high cycle fatigue (HCF), it can be seen in Figure 2.11b that it has the same trend as yield strength with increasing cooling rate. Ductility tends to reach a peak and then starts to decline. This is because the fracture mode changes from the transcrystalline to

intercrystalline dimple mode at high cooling rates. The slope of decline in elongation depends on the strength difference between the matrix and the  $\alpha_{GB}$ .

This item has been removed due to 3rd Party Copyright. The unabridged version of the thesis can be found in the Lanchester Library, Coventry University.

**Figure 2.11** Effect of cooling rates on (a) tensile properties of Ti6242, Ti6Al4V and IMI834 alloys, and (b) fatigue properties of Ti6Al4V alloy (after [1]).

In addition to cooling rate, concentration of alloying elements that are present as a solid solution also influences mechanical properties. For instance, Oh *et al.* [34] demonstrated that the increase in interstitial O content tends to increase the yield strength and ultimate tensile strength (UTS) and reduce material elongation in wrought cp-Ti and Ti6Al4V alloys, as shown in Figure 2.12. Similarly, in Ti6Al4V materials manufactured by powder metallurgy and additive manufacturing processes, Yan *et al.* [35] demonstrated that elongation of the material decreased with increasing oxygen content (Figure 2.13a). In addition, AM materials comprised of  $\alpha'$  microstructure displayed much lower ductility compared to the material containing  $\alpha+\beta$  microstructure for the given O content as highlighted in Figure 2.13b.

This item has been removed due to 3rd Party Copyright. The unabridged version of the thesis can be found in the Lanchester Library, Coventry University.

**Figure 2.12** Effect of O content on mechanical properties of cp-Ti and Ti6Al4V (after [34]).

This item has been removed due to 3rd Party Copyright. The unabridged version of the thesis can be found in the Lanchester Library, Coventry University.

**Figure 2.13** Tensile elongation values of Ti6Al4V material manufactured by (a) powder metallurgy and (b) additive manufacturing processes with varying O content (after [35]).

## 2.4 Additive manufacturing

### 2.4.1 Introduction

Started initially as a tool for producing models and prototype parts, AM presently is one of the prominent advanced manufacturing techniques for manufacturing functional engineering components for several industrial applications [36]. According to the American Society for Testing and Materials (ASTM), AM is defined as “a process of joining materials to make objects from 3D model data, usually layer upon layer, as opposed to subtractive manufacturing methodologies” [37]. Commercial AM machines that are available in the market today generally follow the same working principle but with variation in the method of layer deposition, material forms (wire, powder, sheet, *etc.*), heat source and layer consolidation mechanisms. These factors determine the economics of the process and the properties of the parts. AM processes can be used on a broad range of materials including metals, polymers, ceramics and composites to produce the desired components. The standard terminologies used in AM according to ISO/ASTM 52900 are listed in Table 2.2. Only the terminologies relevant to the current work are mentioned.

AM offers huge benefits as it produces customised parts of complex geometry seamlessly from the CAD model. It also reduces the number of processing stages, resources and offers the ability to predict the amount of time required to fabricate a component [8,13]. The oldest application of AM was in construction and nowadays AM technologies are used to produce products for several industrial sectors [38]. Among them, the aerospace industry is one of the key sectors using AM techniques due to its unique benefits including a lower buy-to-fly ratio, weight reduction, and the ability to repair damaged components and develop customised parts [39,40]. Figure 2.14 shows some examples of AM components that are used in commercial aircrafts.

This item has been removed due to 3rd Party Copyright. The unabridged version of the thesis can be found in the Lanchester Library, Coventry University.

**Figure 2.14** AM components used in commercial aircrafts: (a) bracket connector, (b) engine fuel nozzle, and (c) airfoil with cooling channels (after [40]).

**Table 2.2** Standard terminologies used in AM as per ISO/ASTM 52900.

<b>Terminology</b>	<b>Definition</b>
3D printer	The machine used to fabricate the part by 3D printing method.
AM machine	Part of AM system that includes the manufacturing machine, control software and its accessories.
Bounding box	Cuboid box that spans maximum extents on the 3D part surface.
Build chamber	Enclosed chamber of the AM machine within which parts are fabricated.
Build cycle	Process cycle in which one or more parts are built in the build chamber.
Build envelope	Largest dimensions in the x-, y- and z-axes inside the build space.
Build orientation	Orientation of the part in the build platform which is represented by the machine co-ordinate system.
Build platform	Base surface over which the parts are built and supported until completed.
Build surface	Surface over which fresh layer is deposited. It could refer to build platform or previously deposited layer.
Build volume	Maximum usable volume of the build chamber.
Fusion	Joining two or more material into one.
Layer	Material spread or deposited.
Machine coordinate system	3D coordinate system that is defined by a fixed point in the build platform.
Overflow region	Region in the powder bed fusion AM machine where excess powder is collected.
Part	Functional material produced by fusion of the deposited materials which could be a product or a section of a product.
Part cake	Lightly bound powder surrounding the fabricated part.
Part location	Location of the part specified by the coordinate system in the build volume.
Powder batch	Virgin, used or blended powder feedstock that is used for fabrication.
Powder bed	Build region of an AM machine in which the powder particles are selectively fused.
Powder bed fusion	Process in which the energy source selectively fuses the powder materials in the powder bed.
Powder blend	Thorough mixing of different powders.
Powder lot	Powder produced under controlled and traceable condition from a single powder fabrication cycle.
Process parameters	Operation parameters and settings.
STL	Standard Tessellation Language- file format of the CAD data that is communicated to the AM machine which describes the part surface geometry as triangular tessellations.
Used powder	Powder that has passed through the AM machine at least for one build cycle.
Virgin powder	Unused new powder.

### 2.4.2 Process chain

The processing steps in AM involve development of the CAD model to the production and application of the 3D part. Most AM processes involve the following steps of processing sequence [38].

**Step 1 conceptualisation and CAD model:** Conceptualisation involves generating the idea of the product geometry and its intended function which could be narrative or representative drawings. 3D CAD software with user interface or reverse engineering technologies from the existing models can be used to generate the design [41]. The developed design is then converted to standard tessellation language (STL) file format. Following that, the data is transferred from the computer to the designated AM machine.

**Step 2 Machine set-up:** This step involves ensuring the energy source, feedstock delivery system and other machine hardware are positioned correctly, and checking the process settings required to produce the build. Most AM machines have default process settings or settings used on previous builds available. If no modification is necessary, the build process can be executed, however, non-optimised process parameters can result in poor build quality [41].

**Step 3 Fabrication:** The computer controlled layer-wise fabrication is performed until the required product is finished. User verification of the process conditions like energy input level, chamber environment conditions and feedstock deposition might be needed in the initial stages of the build.

**Step 4 Removal and cleaning:** After the part fabrication is complete, the part is removed from the build platform along with any support structures. Cleaning methods depend on the type of AM process used. For example, EB-PBF process uses a specialised blasting operation to remove the sintered powder from the part.

**Step 5 Post treatment:** Post treating of the parts such as surface enhancement, hot-isostatic pressing and heat treatments may be essential in some cases to meet the required properties for certain applications [38].

### 2.4.3 Classifications in additive manufacturing

Several metal AM processes are currently available which can be grouped based on material processing capabilities, feedstock material form, delivery method and binding agents. Figure 2.15 shows an AM classification based on material processing capabilities.

It can be seen that a broad range of materials can be processed by AM techniques. Commonly used feedstock in metal AM processes are in the form of wire, powder and sheets [42,43].

As highlighted by Herzog *et al.* [13], some processes like directed energy deposition (DED) use more than one type of feedstock material forms (powder and wire). The feedstock material in DED is chosen based on the application requirements. For example, wire feedstock can provide higher build rate but the surface quality is generally low compared to powder DED. The method of feedstock delivery can also differ. For instance, in powder bed fusion (PBF), the powder is spread over a build platform and the energy source binds the particles; whereas in DED, the powder is blown towards the energy source [13].

This item has been removed due to 3rd Party Copyright. The unabridged version of the thesis can be found in the Lanchester Library, Coventry University.

**Figure 2.15** Classification of AM processes based on material processing capability (after [44]).

Several binding agents are used depending on the type of AM process, including thermal sources from laser beam (selective laser sintering (SLS), LB-PBF, laser metal deposition (LMD), lasers engineered net shaping (LENS), *etc.*), electron beam (EB-PBF and wire-fed electron beam AM (EBAM)), plasma beam (plasma arc deposition, PAD), heat from arc (wire arc AM, WAAM), frictional energy (additive friction stir deposition, AFSD), kinetic energy (cold spray AM, CSAM), and chemical binders (ink jet printing, IJP), binder jet 3D printing, BJ3D) [45]. Among the different AM techniques, LB-PBF and EB-PBF which are variants of PBF process are the focus of this work and therefore will be further discussed in the following sections.

## 2.5 Powder bed fusion

Powder bed fusion refers to AM processes that produce a bed containing millions of powder particles that are selectively fused to fabricate the desired component. In all PBF processes, the powder is spread in layers using a coater and fused selectively in the regions of interest [8,10,13]. Variants arise in the mechanism of fusion. For instance, in the LB-PBF and EB-PBF processes, the particles are fully melted and fused using thermal energy; whereas in SLS, the particles are partially melted and fused. The classification can further be divided based on the type of energy beam: LB-PBF and SLS use a laser beam while EB-PBF use an electron beam [10,46,47]. This work covers only EB-PBF and LB-PBF techniques that are described in the following sections.

Any material that can be melted and solidified can be processed using the PBF AM technique. A wide range of materials can be processed including thermoplastics, calcium hydroxyapatite, pre-alloyed metal powders, coated metal powders, and much more. Application of metal PBF parts is increasing rapidly in biomedical and aerospace industries owing to its inherent advantage of manufacturing complex geometrical parts with excellent part properties [38]. However, the build rate in PBF is relatively low in comparison to other AM processes like DED and also suffers size constraints, *i.e.* only small to medium sized parts can be manufactured as the component size is limited by the machine chamber volume. Therefore, machine manufacturers like ARCAM are currently focusing on increasing the powder bed size for manufacturing larger components. Some of the key advantages of the PBF process are: (i) ability to manufacture complex functional parts, (ii) high process efficiency, (iii) better surface quality, and (iv) ability to manufacture overhang structures.

### 2.5.1 Electron beam powder bed fusion (EB-PBF) process

#### 2.5.1.1 Introduction

The EB-PBF process is a variant of the PBF process that uses the kinetic energy of electrons to fuse powder particles in the region of interest in a layer-by-layer fashion to produce the required 3D component. The technology was developed by Chalmers University and commercialised by ARCAM AB, Sweden [38]. EB-PBF uses a beam of electrons that travels near to the light speed to create the thermal energy necessary to locally melt the particles. The use of electrons limits the application of EB-PBF systems to only electrically conductive powders [48]. Additionally, like any other electron beam-

based system, EB-PBF process operates in vacuum to prevent beam disturbances by gas atoms. This increases the initial capital cost for establishing the EB-PBF system which is a factor that limits the application of the EB-PBF technique [38]. Variables such as powder feedstock properties and beam parameters must be checked before initiating the build process to produce a defect free part. Machine manufacturers like ARCAM provide pre-set default build themes. These settings can be manipulated to a certain extent based on the user requirements or for conducting research [41].

#### 2.5.1.2 *Electron beam melting*

The electron beam that is used to melt and fuse the particles is generated by an electrically heated filament (the cathode). Cathode materials have a high melting point to prevent them from melting, and low work function to produce the electrical discharge at low voltages [45]. The work function of a material determines the voltage required to remove an electron from its surface. Gibson *et al.* [38] stated that the efficiency of electron beam generation is higher than producing a laser beam due to the lower amount of heat loss during electron discharge at the cathode. Upon applying sufficient voltage, the discharged electrons from the cathode propel towards a positively charged, perforated anode, forming a beam of electrons. Current and voltage are the key parameters that control the power of the electron beam. An increase in voltage increases the speed of the electrons in the beam, while an increase in current increases the density of electrons in the beam [48]. The electron beam is focused and deflected by the magnetic field generated by a set of four magnets present in the electron beam column (Figure 2.16a). Beam manipulations such as transverse speed and focus are controlled by adjusting the magnetic field. Electron beams can be moved at higher speeds than a laser beam. However, at excessive speeds non-melting or partial melting of the powder particles can occur leading to defects in the parts produced [45]. This high-speed beam translation technique is used to pre-sinter the powder bed prior to melting to reduce charging, as will be explained in Section 2.5.1.3.

**Advantage of EB-PBF process are:** (i) high geometric freedom, (ii) requires less tooling, (iii) produces less material waste as the unused powder can be recycled after each build, (iv) faster build rate than LB-PBF as higher penetration can be achieved with the electron beam. This is because less reflection of the electron beam by the powder particles occurs compared to laser-powder interaction. In addition, the electron beam can be deflected at relatively high speeds such that it can create multiple melt pools

simultaneously [45], (v) better efficiency in electron beam generation compared to the laser beam [38], (vi) use of vacuum environment reduces contaminations like powder and melt pool oxidation during melting and preheating, (vii) requires minimal support structures as the powder bed is preheated and the sintered powder bed can support cantilever features of the part [18], (viii) due to relatively slow cooling rate, residual stresses development in the material is reduced [49].

**Limitations of EB-PBF process are:** (i) only electrically conductive materials can be processed [38], (ii) use of vacuum environment can accelerate the evaporation of light elements present in the alloy [50], (iii) high capital investment is required, (iv) the volume of the part that can be manufactured is limited by the size of the build chamber, (v) lower part resolution compared to the parts fabricated by LB-PBF process.

When the electron beam hits the powder particles, it interacts with the electron cloud of the metal atoms present in the particles. If the electron beam power is high enough, it will penetrate deeper without any deflection by the free electrons until decelerated by the atomic lattice [48]. The lattice vibration generates thermal energy necessary to melt the powder particles. Electron beams are generally used in a more diffuse state than the laser beam to avoid excessive local charge build-up. Therefore, the heat affected area and melt pool volume are larger in comparison to LB-PBF process [38].

### 2.5.1.3 Process description

A schematic of the EB-PBF system along with the machine chamber is shown in Figure 2.16. The key components of the machine include beam generation from the electron gun, beam control using electromagnetic coil and the process chamber where powder melting occurs. The hopper acts as the powder reservoir that feeds the powder onto the build table, which is then spread onto the start plate and over the build platform by a raker. The raker moves between the two hoppers in the transverse direction and thereby fetching the powder that flows out of the hopper baffles. Selective melting is then performed based on the set process parameters (*i.e.* power, speed, *etc.*). The energy absorption of the powder particles depends on the conductivity of the alloy, the process settings and the condition of the powder feedstock.

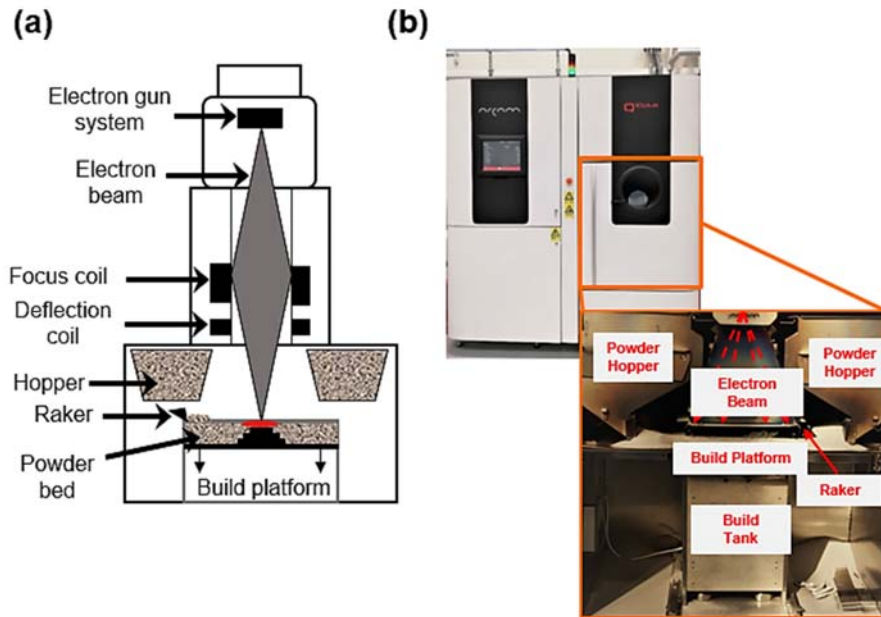


**Figure 2.16** (a) Schematic of electron beam powder bed fusion additive manufacturing system; (b) ARCAM machine and build chamber.

The EB-PBF process involves four steps to produce a consolidated layer: (i) Powder spreading, (ii) preheating, (iii) melting and (iv) post-heating [51–53], as shown by the thermal camera image in Figure 2.17. The process starts by beam-heating of the start plate to a pre-set temperature (which depends on the alloy), followed by lowering the start plate to a distance that is equal to the pre-set layer height. A thin layer of powder is then deposited over the substrate plate by means of a raking mechanism (Figure 2.17a).

**Powder spreading:** Powder deposition is an important factor that can influence the quality of the parts built, and the quality of the deposited layer depends on the properties of the powder. Internal particle defects or non-desirable powder physical/chemical properties can affect part properties, which will be discussed later in Section 2.6.2.

**Preheating:** When electron beam is imparted over a layer of loose powder particles, the charges can get accumulated due to low electrical conductivity of the powder bed. This leads to electrostatic repulsion between the powder particles. In extreme cases, particles are ejected from the build platform, commonly referred to as ‘powder smoke’. Powder smoking leads to failure of the build. The phenomenon of powder smoking has been studied extensively in [48]. The authors have reported that coarser particle size, high scan speed and high temperature powder bed can suppress smoking behaviour. Furthermore, it has been reported that presence of oxide layer on the particle surface

inhibited charge distribution, and thereby acted as electrically insulate overlayer .This caused accumulation of charges. It has been reported by the same authors that increasing the temperature of the powder bed by preheating the powder bed before melting using defocused electron beam at high scanning speeds decrease the resistivity of the oxide layer and reduce powder smoking.

Powder bed preheating also reduces the residual stress development in the part by reducing the thermal gradients during solidification [49,54]. Due to the slow rate of cooling in EB-PBF compared to LB-PBF, the microstructure developed in the EB-PBF parts is different than the LB-PBF parts as demonstrated in [55] where the Ti6Al4V EB-PBF parts had  $\alpha+\beta$  microstructure while LB-PBF parts had predominantly  $\alpha'$  microstructure.

Preheating is applied to both the start plate and the deposited powder layer. Preheating enables sintering of the powder particles, and this improves the conductivity of the powder bed. Optimum preheat temperature must be maintained. A high preheat temperature leads to melting of powder particles, which affects powder recyclability and also results in poor part surface quality. Low preheat temperature leads to charge build-up. Preheating of the powder bed is performed in two stages, commonly referred to as preheat 1 and preheat 2 among ARCAM users. Preheat 1 is applied to the entire build layer, and is intended to raise and maintain the temperature of the entire powder layer by a series of scan lines that is defined by line offset and line order (Figure 2.17b). Preheat 2 is then applied, generally using the same parameters as preheat 1 but only over the area which will be melted with a few millimetres offset to the CAD contour, to maintain the heat input and enhance particle sintering (Figure 2.17c). A defocused electron beam at high scanning speeds are used in both preheats. The high beam speed does not impart a significant number of electrons to melt the particles. Therefore the energy input is reduced enough to sinter the particles [56].

**Melting:** Following preheat, selective melting is performed in two steps. Contour regions of the part are melted using a multibeam mode, where the beam is deflected at high speeds over the part contours to produce multiple melt pools at the same time (Figure 2.17d). After that, hatch melting fills the inner regions of the part geometry by a single beam mode using a focused electron beam at relatively low scanning speed [57] (Figure 2.17e).

**Post-heating:** After melting, post-heating is performed over the entire build area, to normalise the powder bed temperature gradient for the next layer [52], (Figure 2.17f). The build platform then descends by a distance corresponding to the layer height, a fresh layer of powder is spread and the process continues [53].

The powder bed is then allowed to cool and the machine is vented. The sintered powder bed containing the part is blasted with compressed air in the powder recovery system (PRS). The PRS chamber is filled with argon to prevent powder contamination. The unused powder and the desired part are then recovered. The unused powder can be sieved and recycled for use in subsequent builds.

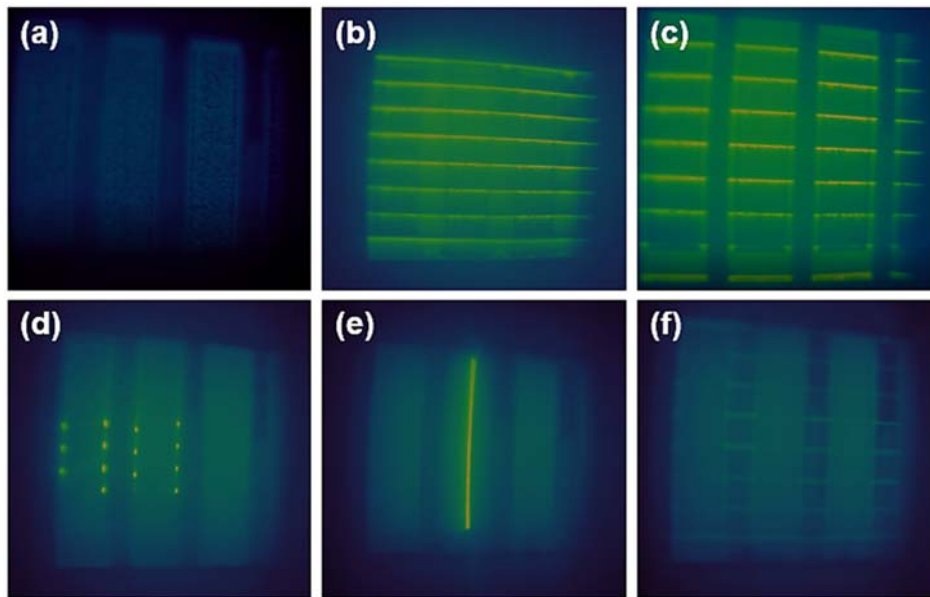


**Figure 2.17** Thermal camera images recorded during Layer 3 powder consolidation of Ti6Al4V EB-PBF process, revealing (a) deposited powder layer, (b) preheat 1 scan lines, (c) preheat 2 scan lines, (d) contour melting performed by MultiBeam™ technology, (e) hatch melting, (f) post-heating (*author's own results*).

### 2.5.2 Laser beam powder bed fusion (LB-PBF) process

The principle of the LB-PBF process is similar to EB-PBF, but a laser is used as the heat source. The laser beam scans the powder bed in predefined regions using optical mirrors which deflect the laser to different areas in the powder layer based on the CAD geometry [6,15,58]. Figure 2.18 shows the schematic of the LB-PBF process and the LB-PBF machine chamber. The laser, with a pre-set power and scan speed or exposure time is focused through the optical window over the deposited powder layer. The laser beam is transmitted, absorbed or reflected by the powder particles. Melting of the powder particles initiates when sufficient laser energy is absorbed by the powder particles,

creating a melt pool that grows by consuming or wetting the surrounding powder particles. After the laser beam spot moves away, rapid solidification occurs and a track bead is formed [6,59]. Argon gas is continuously flushed into the chamber during the build to prevent oxidation of melt pool and powder feedstock [58]. The properties of the consolidated component depends on some of the key variables including laser power, scanning speed, hatch distance, layer thickness and powder properties [6,60,61].

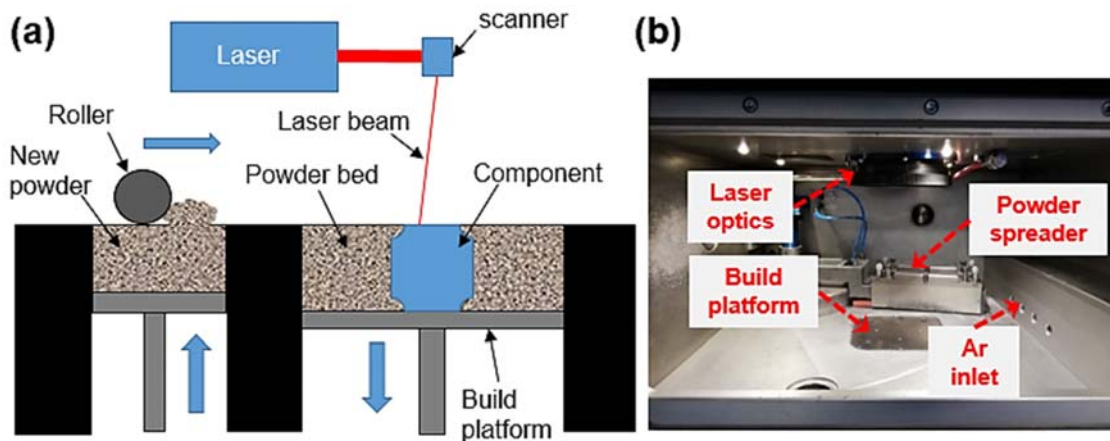


**Figure 2.18** (a) Schematic of LB-PBF process; (b) Realiser 125 LB-PBF system build chamber.

In LB-PBF process, Yb-fiber and Nd:YAG lasers that can provide short wavelengths are employed to improve manufacturing precision. Both the lasers can be operated in a pulsed and continuous wave mode [62]. In the case of pulsed wave mode, the output power is delivered in pulse durations at a pre-set repetition rate. While in continuous wave mode, the laser energy is delivered continuously independent of time. The laser beam is irradiated back and forth across the powder bed surface. In this scan strategy, the scan lines are overlapped such that each successive scan track re-melts the previously scanned track and the layer underneath, as shown schematically in Figure 2.19a. Whereas in the modulate laser scan strategy, the laser diode is switched on and off rapidly by controlling the current supplied to the diode. Therefore, a series of circles overlapping each other is formed (Figure 2.19b). With the decrease in time interval between the pulse duration, the exposure elongates and eventually resulting in continuous exposure when time gap is eliminated (Figure 2.19c).

This item has been removed due to 3rd Party Copyright. The unabridged version of the thesis can be found in the Lanchester Library, Coventry University.

**Figure 2.19** Schematics showing track morphology (a) continuous wave mode, (b and c) effect of time interval between pulses in modulated wave laser [63].

### 2.5.2.1 Melt pool formation

Due to the highly dynamic nature of the LB-PBF process, investigating the physical phenomena of laser-matter interaction and powder consolidation have been reported to be complex [64,65]. However, in recent years, several simulation and *operando* studies have been conducted that improved the understanding of the physics behind melt pool formation, kinetics of the molten pool and spatter mechanisms [59,65–69].

When a laser-beam is focussed over the layer of powder particles during the LB-PBF process, the absorbed energy is either consumed, leading to particle melting and vaporisation, or lost due to conduction, convection and radiation, as shown schematically in Figure 2.20a. Therefore, to effectively melt the powder particles, the absorbed energy should be greater than the energy consumed and heat losses as shown in equation 2.1 [70].

$$Q_a \geq Q_{melting} + Q_{vaporisation} + Q_{heat\ loss} \quad (2.1)$$

where,  $Q_a$  is absorbed energy,  $Q_{melting}$  and  $Q_{vaporisation}$  is energy consumed for melting and vaporisation respectively, and  $Q_{heat\ loss}$  is energy lost due to conduction in the powder bed and the substrate, convection in the melt pool and radiation between powder bed and LB-PBF machine chamber environment.

This item has been removed due to 3rd Party Copyright. The unabridged version of the thesis can be found in the Lanchester Library, Coventry University.

**Figure 2.20** Schematic of laser beam energy (a) absorption and (b) reflection during laser-powder interaction of LB-PBF process (after [70]).

In addition, the existence of gaps in the powder layer can lead to multiple reflections of the laser beam, enhancing laser absorptivity (Figure 2.20b). Furthermore, the optical properties of the material and presence of multi-layer oxides over the powder particle surface can further influence laser absorptivity [71].

When sufficient laser beam energy is absorbed by the powder particles, the powder melts and forms an initial melt pool. The process of melting occurs in two stages: the conduction mode and keyhole mode of melting, as shown schematically in Figure 2.21. The conduction mode of melting occurs at low laser energy density by heat conduction. The melt pool thus formed is broad and shallow, *i.e.* has a low aspect ratio (Figure 2.21a). At higher energy densities, the conduction mode of melting changes to keyhole mode when the surface temperature of the melt pool reaches the boiling point (Figure 2.21b). Therefore, metal vaporisation occurs at the surface of the melt pool which creates a vapour cavity that in turn exerts a strong recoil pressure normal to the surface of the melt pool. The recoil pressure drives the melt pool to the bottom of the vapour channel, leading to a thin layer of liquid at the beam spot leading to the formation of a keyhole [72]. The keyhole thus formed moves along the scan direction.

The laser beam has a Gaussian energy distribution, therefore, the highest temperature is realised at the regions exposed to the centre of the beam [65]. Furthermore, Fabbro *et al.* [73] have shown that the laser absorptivity is higher in keyhole mode of melting due to multiple reflections of the beam at the walls of the keyhole, enabling higher melt pool penetration (Figure 2.21c). However, the gaseous keyhole is unstable and sometimes the surrounding liquid may not have sufficient time to fill the keyhole during rapid solidification which leads to gas pores, as discussed by

Leung *et al.* in [67]. The aspect ratio of the keyhole depends on the process parameters and layer thickness used [74].

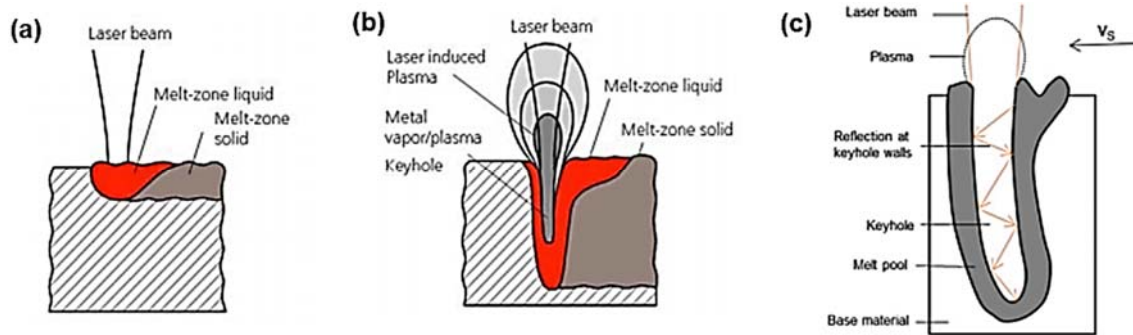


**Figure 2.21** Schematic of (a) conduction mode of melting, (b) keyhole mode, and (c) multiple reflections by the keyhole walls in laser beam welding (after [75]).

### 2.5.2.2 Melt pool growth

When the melt pool is formed, capillary motion of the melt pool wets the substrate and the surrounding powder particles. The surface tension, driven by the temperature gradients in the melt pool, drives the melt flow around the beam spot [72]. The surface tension, which is a function of temperature, is negative in most metal alloys, *i.e.* lower at the beam spot than at the melt pool boundaries. The melt pool is pushed downward due to strong recoil pressure, then flows backwards from the hot keyhole region towards high surface tension regions that are at lower temperature. When the temperature drops at the centre of the melt pool, as the laser moves away, the surface tension increases and the melt flows back to the centre. This creates a melt flow convection pattern. Such surface tension induced flow is called Marangoni convection, reported as a key factor for melt pool growth [68]. When the laser moves away from the keyhole, the temperature begins to drop, the vapour pressure decreases and surface tension increases, which causes the keyhole walls to collapse [65].

In addition, powder entrainment into the melt pool, caused by inward flow of the ambient air induced by the metal vapour jet at the keyhole region has also been reported to promote melt pool growth [64]. However, particle entrainment into the melt pool can create powder denudation in the region around the melt pool [76,77]. Therefore, sometimes, due to the lack of particles to melt at the laser-front, the laser beam moves ahead and creates a new melt bead, which due to backward flow caused by Marangoni effects, merges with the previous melt track [69], which further confirms that surface tension driven Marangoni flow is the key factor that drives the melt pool growth.

### 2.5.2.2.1 Influence of oxides

Lu *et al.* [78] reported that melt bead penetration increased in SS304 alloy due to the presence of surface active elements such as oxides in gas metal arc welding (GMAW). A similar phenomenon was observed by Shi *et al.* [79] in hybrid laser-tungsten inert gas (TIG) welding in TA15 titanium alloy. The presence of the surface active elements can alter the surface tension gradient from negative to positive. This subsequently changes the melt pool flow direction from outward centripetal to inward centrifugal flow, as shown schematically in Figure 2.22, proposed by Heiple *et al.* [80] for laser welding. This was demonstrated to also be the case in the LB-PBF process by Leung *et al.* [69] using *operando* X-ray imaging technique. Therefore, in addition to powder physical properties and process parameters, the chemical properties of the powder layer can also influence powder layer consolidation. In some cases, the solute atoms can dissolve in the melt pool creating a solid solution. For instance, in Ti6Al4V, oxygen atoms can dissolve up to 0.33 wt.% without forming precipitates [29]. In such cases, the surface tension remained unchanged but, the viscosity of the melt increased as demonstrated in [81].

This item has been removed due to 3rd Party Copyright. The unabridged version of the thesis can be found in the Lanchester Library, Coventry University.

**Figure 2.22** Effect of surface active elements on surface tension gradient; (a and b) negative surface tension gradient causing centrifugal convection; (b and c) positive surface tension gradient causing inward centripetal flow (after [78]).

### 2.5.2.3 Spatter formation

During the LB-PBF process, it is common to notice bright ejections from the melting area, similar to any laser manufacturing process such as drilling or welding [82–84]. The ejections could be solid (powder) or molten droplets (melt pool ejections) [85]. Melt ejections occur from the molten pool [86]. Yin *et al.* [87] concluded that the recoil force generated due to rapid vaporisation at the melt pool surface was the main cause of droplet spatter ejection and it occurred when the recoil pressure exceeds the surface tension of the melt pool [15]. In addition, Leung *et al.* [69] observed pore bursting during laser re-melting which led to further increase in the number of melt ejections.

Powder spatter occurs from the region surrounding the beam spot [86]. It is caused by the entrainment of powder particles in the vapour plume. Hot spatter occurs if the entrained particles interact directly with the laser heat source and cold spatter occurs when powder particles have not been irradiated by the laser beam during ejection [88]. Furthermore, Young *et al.* [89] observed agglomerated powder spatters, *i.e.* spatters and powder particles tended to coalesce during ejection. Two types of agglomerated powder spatters have been observed: (i) liquid-liquid and (ii) liquid-solid agglomerated powder spatters. Liquid-liquid spatters formed when two neighbouring droplet spatters collide and form a larger spatter. Liquid-solid spatter formed when the droplet spatter collided with the unfused powder particles in the powder bed or ejected powder spatter and produced a larger spatter, as also reported by Nassar *et al.* [90].

The formation of the spatters is highly dependent on the input energy density, which is a function of laser power ( $P$ ), scan speed ( $V$ ), layer thickness and hatch spacing ( $h$ ) as shown by the equation (2.2) [88].

$$IED = \frac{P}{vht} \quad (2.2)$$

In terms of spatter particle distribution, increased numbers of spatter particles have been found in the region closer to the melting area [91]. Wang *et al.* [92] classified spatter particles based on their morphology as shown in Figures 2.23b–d and speculated their trajectories. Type-I spatter (Figure 2.23b) ejected from the melt pool and had sufficient time to solidify as a smooth spherical particle before falling back in the powder bed. Type-II spatter (Figure 2.23c) collided with the other fine spatters or condensate before falling into the powder bed, resulting in the sintering of fines on the particle surface. Type-III spatter (Figure 2.23d) ejected from the laser front, had a shorter flight

path and bombarded with the unfused particles in the powder bed in the half-molten condition resulting in the formation of an irregular shape. These non-spherical particles can significantly affect the powder flow and packing behaviour by creating local voids in the powder bed that can result in lack-of-fusion defects in the built parts [93].

This item has been removed due to 3rd Party Copyright. The unabridged version of the thesis can be found in the Lanchester Library, Coventry University.

**Figure 2.23** SEM image of powder morphology: (a) virgin powder; (b) type-I, (c) type-II and (d) type-III spatter particles (after [92]).

Spatter particles have different phase and chemical composition compared to virgin powder. For example, in 316L and 304L stainless steel, it has been reported that the  $\delta$ -ferrite content was high compared to the virgin powder. Oxides of manganese and silicon were also observed on the spatter particle surfaces [94,95]. As the spatters have different surface chemistry and size distribution, their attenuation of the laser beam was different. This resulted in unmelted particles becoming embedded inside the part [36] and on the part surfaces [96]. Similarly, Esmailizadeh *et al.* [97] reported an increase in defect density and surface roughness of parts manufactured from spatter-rich regions of the powder bed.

As spatter particles can cause potential deterioration to the part and powder properties, efficient reduction and removal methods should be employed. Argon gas flow used during the process can carry the spatter particles and condensate outside the powder bed. However, large-size spatters are hard to remove as they possess relatively high inertia resulting in high gravitational forces acting on them. For efficient prevention

of spatters from falling back into the powder bed, Ladewig *et al.* [98] made some key recommendations: (a) homogenous gas flow at a high velocity close to the build surface is required, and care must be taken to avoid disturbing the powder layer, as it may affect the powder-layer density; (b) upward turbulence in the flow should be kept to a minimum as this could disturb the laser beam. In addition, Khairallah [99] proposed preheating the powder bed using a lower laser energy density before selective melting (similar to the approach used in EB-PBF process) that would sinter the powder particles, restrict their mobility and reduce the number of spatter particles.

## 2.6 Raw materials

Alloys in powder forms are used in metal PBF processes. Several types of powders with broad range of particle sizes, shapes and chemistries are employed. The use of metal in powder form has some inherent advantages, like recyclability, serving as a support structure to the built part (in EB-PBF) and the ability to be blended with different alloy powders [17–19]. Safety precautions need to be followed while handling powders which requires specialised handling tools, PPEs and storage conditions. The properties of the final part and the set-up of process parameters depends to a large extent on the properties of the initial powder feedstock used. Therefore, a thorough understanding of the powder characteristics required to achieve the desired part properties is essential [100]. Several conferences, research organisations, such as the National Institute of Standards and Technology (NIST), and international standards organisations like ASTM and ISO are focusing on increasing the awareness of the importance of powder feedstock, development of standards for qualification and establishment of feedstock-parameter-structure-properties relationship [101].

The properties of the powder feedstock depend on the type of powder manufacturing process employed. Metal powders can be produced by several techniques including electrolysis, solid state reduction, chemical processing, atomisation, hydride-dehydride process (HDH), *etc.* Among them, the atomisation method using gas (gas atomisation, GA) or plasma (plasma atomisation, PA) is commonly employed for producing pre-alloyed spherical powders of Ti6Al4V for applications in LB-PBF and EB-PBF processes [27].

## 2.6.1 Powder production

In the current work, GA powder was used to conduct the reuse cycles and manufacture test coupons. Since in some places the properties of PA powder have been compared with the GA powder, only GA and PA powder production methods and the characteristics of the resultant powder are discussed in the following sections.

### 2.6.1.1 Gas atomisation

The process initiates by induction melting of the pre-alloyed ingot in a vacuum or inert environment. The melt is then transferred to a tundish to regulate liquid metal flow or directly bottom poured via a nozzle into the atomising chamber. The liquid metal stream that free-falls inside the chamber is disintegrated into droplets, by high pressure inert gas jets. The droplets then rapidly solidify into spherical particles as they drop to the bottom of the atomiser. Use of inert gas prevents the liquid metal stream from oxidation especially when reactive materials like titanium alloys are used. This method is used to produce powders with a size range up to 500  $\mu\text{m}$  [102]. Figure 2.24a shows an example of gas atomised powder. As can be seen, the resultant powder consists of mostly spherical particles. However some fractions of non-spherical particles, including satellites and agglomerates which can affect the powder flow are also found. Chen *et al.* [100] found high fractions of gas porosity entrapped within GA powder particles, which can affect part density [103]. Section 2.6.2.5 covers the gas entrapment mechanism and characterisation methods in more detail.

### 2.6.1.2 Plasma atomisation

In this process, pre-alloyed wire is fed to plasma torches which melt and break the wire into droplets that solidify into spherical powder particles as they drop to the bottom of the atomiser [27]. This method is used to produce powders of size range between 25 and 250  $\mu\text{m}$ . The powders produced using this technique have better sphericity, fewer satellites and low porosity compared to GA powders [100,104]. Figure 2.24b shows an example SEM micrograph of plasma atomised powder.

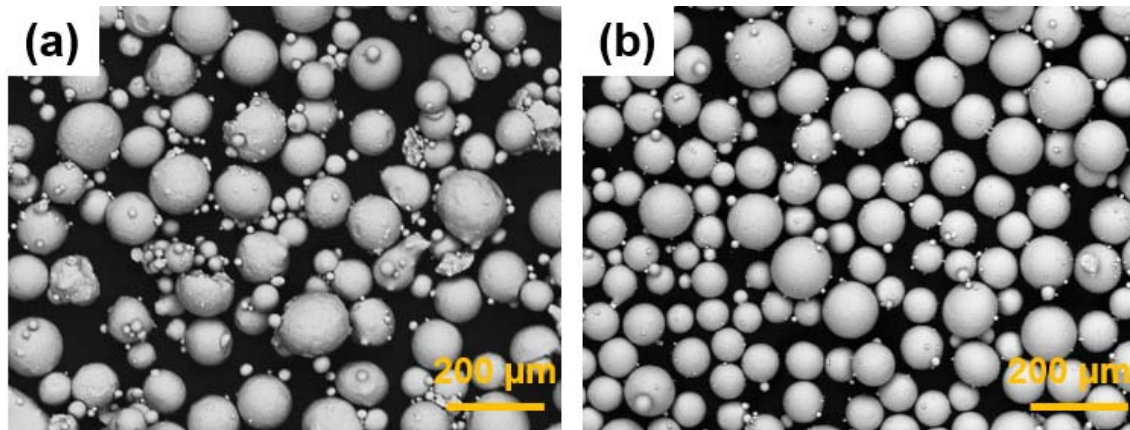


**Figure 2.24** SEM micrograph of (a) GA and (b) PA powder (*author's own results*).

### 2.6.2 Powder characteristics

The components produced by metal PBF processes are generally comprised of thousands of layers made by fusion of millions of powder particles. The individual powder particle properties determine the performance of the bulk powder behaviour and the subsequent part properties [105]. Hence, it is important to understand the connection between the properties at the individual particle level and bulk powder levels to produce components with predictable properties. In the following sections, some of the key powder intrinsic and extrinsic properties, characterisation methods and their potential impact on part quality are discussed.

#### 2.6.2.1 Powder morphology and its effect on powder flow and packing behaviour

Powder morphology refers to the physical characteristics of the powder particles such as shape, size and surface roughness. Powder morphology is studied by imaging methods using optical and electron microscopy techniques. The image thus acquired can be used for qualitative and quantitative analysis. Recently, automated 2D imaging machines are available that can capture images of thousands of powder particles in a short span of time with minimum post-image processing requirements to estimate particle shapes. Particle shape parameters like powder size, sphericity, convexity, elongation *etc.* can then be determined empirically.

In the LB-PBF and EB-PBF processes, spherical powders are used as they offer better flow and packing behaviour. The sphericity and smoothness of the powder particles depends to a large extent on the powder manufacturing techniques employed. As can be seen in Figure 2.24, the powder particles produced by GA process have relatively rough surfaces with a higher fraction of non-spherical particles like satellites

and agglomerates, compared to PA powder. Sun *et al.* [106] reported an increase in surface roughness of PA powder with recycling.

Non-spherical powder particles can result in degradation in powder flow and packing efficiency [105]. The presence of satellite and agglomerated particles can have a negative effect on the density of the powder layers. Nan *et al.* [107] demonstrated through particle based simulation that non-spherical particles experience high frictional forces during layer spreading as they formed a large contact area with the build surface. These large frictional forces resulted in jamming during layer spreading which led to voids in the powder layers. The authors hypothesise that these voids present in the powder layer might lead to lack-of-fusion defects in the parts manufactured. The authors also demonstrated that increase in blade height, *i.e.* the distance between the blade and the substrate plate, reduced jamming and provided a denser layer. Similar observations were made by Ahmed *et al.* [108]. However, with this approach of increasing layer height, the part resolution might have to be compromised.

#### 2.6.2.2 Particle size distribution and its effect on powder flow and packing behaviour

Particle size distribution (PSD) is a vital parameter that determines the process settings, powder flow, powder layer and part density [61]. Powder PSD is usually reported as a number or volume of particles over a list of size ranges.  $D_v x$  means that x percentage of particles of the total volume are higher or lower than the particular particle diameter. For example, if  $D_v 10$  is 45  $\mu\text{m}$ , it means that 10% of the particles are smaller than  $\text{Ø}45 \mu\text{m}$ . On the other hand, if  $D_v 90$  is 105  $\mu\text{m}$ , it means that 10% of the particles have diameter larger than 105  $\mu\text{m}$ . Powder PSD in AM is commonly measured using three methods: imaging, sieve analysis and laser diffraction.

**Imaging technique:** Imaging based methods are one of the conventional techniques that can be used for any powder morphology. The process includes imaging using microscopy, processing (which includes contrast enhancement, segmentation *etc.*) and measurement. The method can be used for both qualitative and quantitative analysis. This method is highly reliable and accurate, however the image processing is often tedious and time-consuming [105]. Currently, automatic feature analysis machines like Morphologi (Malvern Instruments) that are capable of analysing thousands of particles are available. Current limitation in these latest machines is that they analyse the particles in only two dimensions and also initial capital cost is high.

**Sieve analysis:** Is one of the traditional methods that has been used by powder metallurgy industries to determine PSD. It involves the use of stacked sieves, with increasing mesh size from the bottom to the top. The powder is introduced into the vibrating sieve stack at the top, and particles corresponding to their sizes are retained by the mesh. The mass of powder in each sieve mesh is measured and the size distribution is calculated [109]. This is a standardised technique (ASTM B214) that is relatively fast, simple and requires less skilled labour. However, there are some drawbacks. The PSD is obtained based on the difference between the mesh sizes, if a higher resolution measurement is required, it increases the cost as additional sieves need to be incorporated to reduce the bin size. In addition, when fine powder particles are used, the particles tend to agglomerate leading to inaccurate measurements [105].

**Laser diffraction technique:** A widely used light scattering based technique in which a diffraction pattern is obtained by passing laser light through a medium (liquid or dry) containing powder particles. The photodetectors capture the diffraction pattern and convert them into electrical signals. The electrical signals are processed using special algorithms based on Mie's or Rayleigh's theory or a combination of both to provide the size distribution data [110]. The corresponding standard is ASTM B822. The key advantages include quantitative significance that can provide statistical rigour, there is no requirement for post processing the data, and it is less time consuming. However, one of the limitations of this technique is that it assumes all the particles are spheres and therefore errors may occur when non-spherical powder particles are analysed [105]. However, since in EB-PBF and LB-PBF metal AM based processes, powder consists of mostly spherical particles, this is a minor problem.

Therefore, weighing the pros and cons of these techniques, laser diffraction is the most robust method currently available for estimation of PSD for metal PBF powders.

PSD plays a huge role in determining the powder flow behaviour [94]. Therefore, there are limits on the maximum and minimum particle sizes that can be used in the PBF process to produce dense components. The presence of fine particles in the powder can promote particle cohesion, as fine particles have high surface energies and therefore have a higher tendency to agglomerate which thereby results in poor powder flowability [111]. Employing coarse powder particles can improve powder flow behaviour but has a negative effect on the packing density of the powder bed [112]. Close packing of uniformly sized spheres can provide 74% packing density (face centered cubic (FCC))

crystal structure). Powell *et al.* [113] have demonstrated that packing density of the powder bed increased substantially when particles of different sizes were used. This is because fine particles filled the gaps formed between the coarse particles. It is also possible that the presence of fine particles in the powder layer can absorb more energy because they have a higher surface area to volume ratio and therefore could produce enhanced particle sintering by localised melting during preheating in the EB-PBF process. However, employing powder with a wide PSD can affect powder flowability [94]. This illustrates how one property could be contradictory to the other. Therefore an optimised PSD that benefits both flow and packing behaviour is used, typically 15-45  $\mu\text{m}$  for LB-PBF and 45-106  $\mu\text{m}$  for EB-PBF process for manufacturing titanium parts [102].

### 2.6.2.3 Flowability and packing behaviour

Flowability is a bulk powder characteristic that is highly dependent on the physical characteristics of individual particles and their interaction with other particles, the substrate or previously deposited layer, the spreader arm and the chamber environment [101]. Many of the methods of measuring powder flow, that were developed for powder metallurgy applications, are being used in AM, including Hall (ASTM B213) and Carney (ASTM B964) flowmeter funnels, Hausner ratio (HR) as described in ASTM D7481, angle of repose (ASTM B213), *etc.* [101,114]. Furthermore, in recent years, rheometers have also been used for evaluating the flow behaviour of cohesive powders and have been reported to provide promising results [115]. In the current work only Hall and the Hausner ratio have been used to evaluate and compare powder flow behaviour. Therefore, a brief description of those two methods are described below.

**The Hall flowmeter** is relatively cheap, simple and rapid tool used to evaluate and compare the flow properties of powders. A specific powder mass (50 g) is made to free-fall through a funnel with an orifice of specific diameter under the influence of gravity. The time taken for the entire powder mass to exit the orifice is measured [101]. Spierings *et al.* [114] after reviewing several powder flow measurement methods considered that compared to other flow measurement techniques, Hall flow measurements could provide reliable values for flow behaviour in AM powders.

**The Hausner ratio** is an empirical value of the ratio of tap density to apparent density. The relationship between HR values and its corresponding flow behaviour are shown in Table 2.3.  $\text{HR} < 1.25$  are considered as free-flowing powders. It has been stated in [114] that HR does not correlate well with the AM processing conditions. Vock *et al.* [101] stated

that HR can only be used as a comparative method rather than deriving quantitative conclusions.

**Table 2.3** Classification of powder flow behaviour based on the HR values [105].

Hausner ratio	Flow description
1.00-1.11	Excellent
1.12-1.18	Good
1.19-1.25	Fair
1.26-1.34	Passable
1.35-1.45	Poor
1.46-1.59	Very poor
>1.60	Non-Flowable

Powder packing behaviour is another major bulk powder property that can also impact the build properties. Powder packing behaviour in the powder bed is usually estimated by measuring either apparent or tap (ASTM B527) densities. In some cases, both measurements are considered. Apparent density is measured using different methods such as Hall flowmeter (ASTM B212), Carney flowmeter (ASTM B417), Arnold meter (ASTM B703) and Scott volumeter (ASTM B329). Some studies have also used simulation and imaging techniques to predict and monitor particle packing behaviour [108,116]. However, these imaging techniques cannot be applied in an industrial setting due to a lack of suitable standards.

A thin, homogenous, dense layer of uniform thickness is desired in a PBF process to produce components without defects. Spherical powder with optimum PSD is therefore essential. Liu *et al.* [117] investigated the effect of PSD on LB-PBF part density and mechanical properties. The authors concluded that process parameter optimisation is essential for different PSDs and powder with wide PSD provided a highly dense part with smooth surfaces.

In addition to using powder with optimum properties, powder layer quality can also be improved by optimising the spreader blade parameters. For instance, Haeri *et al.* [116] observed an improvement in layer spreading with change of blade design. A roller-type powder spreader showed better performance in producing a dense layer than a blade-type spreader. In addition, Yao *et al.* [118] reported that a 15° tilt in the blade-type spreader can improve powder spreadability and high blade speed results in more patchy areas. The authors concluded that a medium blade speed can provide a more uniform powder layer. Ahmed *et al.* [108] have reported that increasing the height between the powder layer and the spreader improves powder layer quality. Overall,

powder bed quality depends on the particle dynamics near the spreader and therefore, powder physical properties like morphology and size distribution have a significant effect on the dynamics of spreading.

#### 2.6.2.4 Chemical composition

Similar to any part manufacturing process, the chemical composition of the raw material becomes the basic essential property that needs to be evaluated to meet chemical requirements of the desired part. In AM, a broad range of techniques that are employed in other manufacturing processes are used to measure chemical composition, including X-ray photoelectron spectroscopy (XPS) [94], energy dispersive spectroscopy (EDS/EDX) [119], inductive coupled plasma spectroscopy (ICP) [69], inert gas fusion (IGF) [5], *etc.*

Chemical composition of the powders and the parts produced have also been reported to change with powder reuse [50]. Monitoring the change in chemical properties is crucial to predict the mechanical properties of the final part. For example, at high interstitial powder O content, Popov *et al.* [23] observed an increase in yield and tensile strength at the expense of reduction in elongation of Ti6Al4V parts manufactured by the EB-PBF process.

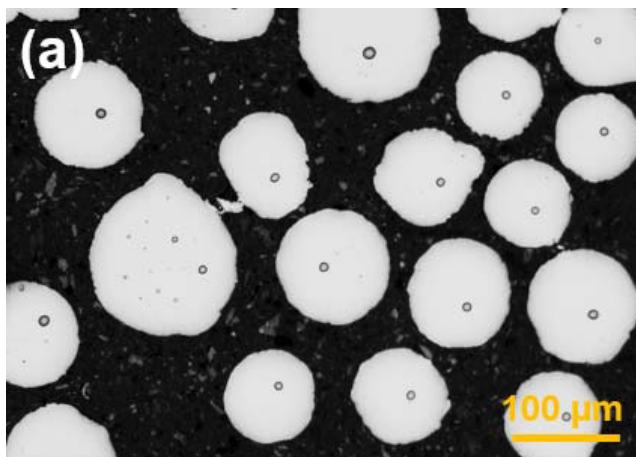
Gruber *et al.* [119] found selective oxidation of Al on the surfaces of IN718 powder particles with recycling in the EB-PBF process. The so-formed Al oxides continued to grow with increasing powder reuse. Similarly, in the LB-PBF process, Gasper *et al.* [120] observed Al<sub>2</sub>O<sub>3</sub> oxides on the surface of IN718 powder spatter particles. When these spatter particles fall back into the powder bed, they can lead to local increase in the powder O levels and can cause chemical inhomogeneity in the powder layer. However, neither study addressed the influence of Al<sub>2</sub>O<sub>3</sub> oxides on the part properties.

Leung *et al.* [69] investigated the effects of maraging steel O content on molten pool dynamics in LB-PBF process using real time X-ray imaging. The authors found that the Marangoni convection reversed with increase in the oxide content of the melt pool due to the change in surface tension gradient from negative to positive. Furthermore, the presence of oxides in the melt pool acted as nucleation sites for pores. The authors did not extend their study to investigate the effects of change in melt flow direction on mechanical properties of the parts. Mills *et al.* [121] have reported an increased number of dimples/humps on the gas tungsten arc (GTA)/TIG welded surface when the Marangoni convection reversed and so a similar effect is possible in LB-PBF process, which could lead to a rougher surface. Therefore, melt pool convection demands

attention from the perspective of part surface roughness and its effect on mechanical properties, particularly fatigue performance. Overall, understanding the composition and the chemical state of the alloying elements in the new and recycled powder used in AM can be useful to predict part properties.

#### 2.6.2.5 Powder purity

**Gas porosity:** In addition to the voids present in the powder layer due to inconsistencies in spreading, internal defects in the powder particles can also contribute to porosity in the built parts [5]. Figure 2.25 shows the presence of pores inside the powder particles. Microscopy and X-ray imaging techniques are useful tools for analysing powder porosity. The sources of these porosity were reported to be inert gas entrapment during the atomisation process [103]. It can be seen in Figure 2.25a that coarser particles have a higher number of gas pores in comparison to the smaller particles. Similar observations have been reported by Chen *et al.* [100]. The authors also compared powder porosity in GA, PA and plasma rotating electrode process (PREP) powders. They found that the GA powder had the highest volume of porosity (0.2%), followed by PA (0.12%) and PREP (0.08%) powder. Powder porosity generally has a spherical morphology, possibly due to the high pressure inside the liquid droplet acting on the gas bubble. A simple schematic of the gas entrapment process during gas atomisation is shown in Figure 2.26. When the gas jet strikes the molten droplet, it stretches in a direction perpendicular to the direction of the jet stream. This is followed by shredding of smaller droplets from the periphery regions. Upon reaching high surface tension during cooling, the droplet collapses on itself, entrapping some gas bubbles inside [122].



This item has been removed due to 3rd Party Copyright. The unabridged version of the thesis can be found in the Lanchester Library, Coventry University.

**Figure 2.25** Gas entrapment in powder particles visualised using (a) optical microscope (*author's own result*), and (b) X-ray computed tomography (XCT) (after [100]).

This item has been removed due to 3rd Party Copyright. The unabridged version of the thesis can be found in the Lanchester Library, Coventry University.

**Figure 2.26** Schematic shows sequence of events causing gas entrapment in powder particles in atomisation process (after [122]).

**Foreign element contamination:** Powder purity is a critical factor when it comes to safety-critical, high-performance applications like aerospace, defence and space parts. Powder purity is not often reported in studies. As PBF is a layer-by-layer manufacturing process, when a foreign element is introduced in any one layer during manufacturing, it can become sealed-in by the subsequent layers.

There are several sources from which contaminants can be introduced into the powder. Some of the sources of contamination are: (i) Wear of refractory elements from atomiser nozzles [104] and crucibles [123] during gas atomisation, (ii) partially solidified powder particles impinging on stainless steel walls of the atomiser can pick up iron during gas atomisation, (iii) improper cleaning of the atomiser, when changing the alloy, can lead to powder cross-contamination, (iv) cross-contamination could also occur when the same AM machine is used for processing different powder alloys, (v) in the PA process, tungsten nozzles used in the plasma torches can wear-out, creating tungsten inclusions in the powder. As tungsten particles possess a higher melting temperature than most of the commonly used AM powders such titanium, stainless steel or aluminium, they can remain unmelted and create inclusions in the manufactured part which act as preferred sites for crack initiation [124]. Santeccchia *et al.* [125] demonstrated that SEM and EDS techniques can be used to detect powder contamination (Figure 2.27).

Since the presence of foreign contaminants in the part can cause deleterious effects on part properties, it is important to assess the potential contamination sources and check powder purity alongside other characterisation techniques before application in AM.

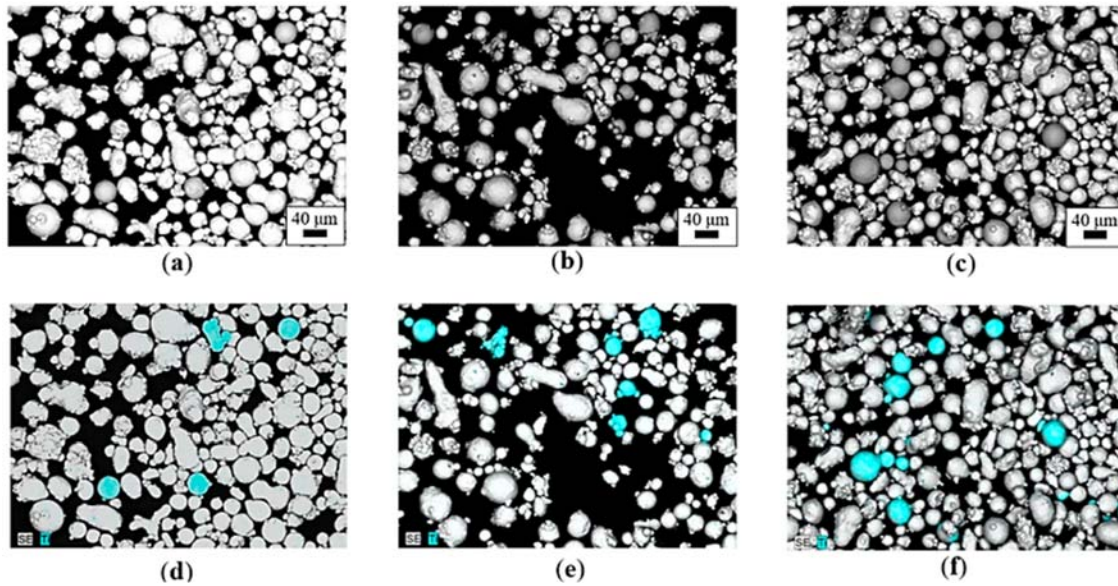


**Figure 2.27** SEM (backscattered electron (BSE) mode) and EDS/EDX revealing Ti6Al4V particles with maraging steel powder at (a and d) 0.5%, (b and c) 1%, and (c and f) 2.5% contaminants. Ti6Al4V particles are coloured blue (after [125]).

### 2.6.3 Powder recycling

In PBF AM techniques like LB-PBF and EB-PBF, it is not possible to feed the precise volume of powder required to manufacture the part. For example, it is not possible to produce a 2 cm<sup>3</sup> part by feeding 2 cm<sup>3</sup> of powder into the AM machine, because the powder must be spread across the entire build plate and a minimum powder bed volume requirement needs to be met. Therefore, the entire build plate is filled with powder regardless of the component size. The area of the build plate depends on the machine used. In some cases, less than 50% of the powder bed volume is utilised to produce the part while the remaining powder is left unconsumed [113].

A widely followed technique is recovery and recycling of the unconsumed, left-out powder in the build chamber. Petrovic *et al.* [126] have stated that about 95% of the unconsumed powder can be reused in the subsequent builds. Hence, recycling unconsumed metal powders can provide huge economic and environmental benefits [127].

During powder recycling, the unconsolidated powder is recovered from the build chamber, sieved and stored or incorporated into the next build. As described previously, powder characteristics are prone to changes based on manufacturing, handling and storage conditions [50]. Therefore, suitable precautions need to be taken to ensure powder degradation through mechanisms such as oxidation and contamination are

prevented or controlled by following established recovery, handling and storage methods.

However, currently there are no specific standards to regulate recycling methodology, and hence powder recycling is mostly carried out based on user experience. Therefore, the type and degree of change in powder and part properties varies between different industries [113].

Evolution of recycled powder properties also depends on powder chemistry, applied process parameters and the volume of powder bed utilised to produce the component [58]. It is important to understand the evolution of physical and chemical powder characteristics with reuse so that the parts can be produced with consistent predictable properties [88]. In the past few years, a number of studies have looked at the effects of Ti6Al4V powder recycling in both LB-PBF and EB-PBF process as summarised in Appendix A. The observed changes in powder and subsequent part properties with recycling are summarised in the following sections.

## **2.7 Effects of powder recycling- Ti6Al4V alloy**

### **2.7.1 Evolution of powder properties with powder recycling**

#### *2.7.1.1 Chemical composition*

As previously described, Ti6Al4V has a high affinity with oxygen [4], and there are various sources through which oxygen could be incorporated into the powder. A major source is humidity in the atmosphere. This occurs when the powder particles absorb moisture on their surface upon exposure to humidity, which then breaks down into oxygen due to the high temperature inside the AM machine chamber. The dissociated oxygen is then picked up by the powder particles [106,128]. In the EB-PBF process, Cao *et al.* [129] observed an increase in the oxide layer thickness after 10 times of powder reuse. Supporting that, Tang *et al.* [50] observed that the bulk powder O content increased after 22 reuse times. However, the O content stayed within the maximum limit of 0.2 wt.% suggested in ASTM F2924 for AM Ti6Al4V. Similar observations have also been reported in both EB-PBF [126,130] and LB-PBF [131–133] processes. However, Sun *et al.* [106] and Popov *et al.* [23] have reported the O content to exceed 0.3 wt.% in Ti6Al4V powder recycled for 30 and 69 build cycles. Additionally in the LB-PBF process, Wang *et al.* [92] and Gasper *et al.* [120] observed surface oxidation to occur in spatters formed during the melting of CoCr and IN718 powders respectively. This occurred because the melt ejections, being at high

temperatures, are more reactive than the rest of the powder particles and therefore they reacted with the residual oxygen left in the chamber [92]. Although, no literature has investigated the O content of Ti6Al4V spatters formed during LB-PBF process, it is possible that spatter oxidation could occur since the alloy is highly oxidising at elevated temperatures [1]. When these oxidised spatters fall back into the powder bed, they can lead to local increase in the O content of the powder bed.

#### 2.7.1.2 Powder morphology

Deterioration in powder shapes can occur during part manufacturing and recovery. However, powder morphological changes have been reported to be marginal in all of the studies. Sun *et al.* [106] and Tang *et al.* [50] reported Ti6Al4V plasma atomised powder surface deformation with reuse in the EB-PBF process as a result of the recovery process in the PRS chamber, where particles tend to collide with each other. Denti *et al.* [134] reported powder agglomerations increased in the Ti6Al4V powder recycled for 100 cycles in the LB-PBF process. The authors speculated that it was due to the effect of heat from the melt pool on the neighbouring particles that led to particle sintering. The other possibility may be that ejections from the melt pool were deposited onto the powder bed forming agglomerates. However, some studies have also reported no changes in Ti6Al4V powder morphology with recycling [126,133,135]. This is likely to be due to the lack of meticulous observation because not all the particles in the powder bed experience morphological degradation and also most of the severely affected particles are eliminated during sieving. Therefore, only the particles in the vicinity of the melt pool, exposed to spatter during LB-PBF processes, collisions during recovery and handling, and that managed to pass through the sieves, reveal deterioration or shape changes. Analysing such particles provides a better understanding of the powder degradation mechanisms. Deterioration of spherical shaped powders used in PBF can affect powder flowability and packing behaviour as discussed in Section 2.6.2.3.

#### 2.7.1.3 Size distribution

All the reported studies observed a marginal shift in the PSD curve such as Tang *et al.* [50] observed narrowing of PSD curve with increasing reuse cycles in EB-PBF process. Similarly, Carrion *et al.* [131] observed narrower PSD for powder recycled in LB-PBF process. Additionally, Ghods *et al.* [130] reported a decrease in the number of fine particles and increase in the fraction of high aspect ratio particles after recycling Ti6Al4V

powder for 30 build cycles in the EB-PBF process, which also altered the PSD curve. The decrease in fine particles improved powder flow behaviour as fine particles have greater tendency to agglomerate [111]. In powder recycled for fewer cycles, no changes were observed as reported in [128].

#### 2.7.1.4 Flowability

Tang *et al.* [50] in EB-PBF process have demonstrated that the powder flow increases with reuse. Similar observations were made in [131,136] in the LB-PBF process. All the literature refers to the narrowing of the PSD to cause improvement in powder flow but, another reason could be the decrease in the moisture content of virgin powder as result of the hot processing condition inside both EB-PBF and LB-PBF chambers.

### 2.7.2 Evolution of build properties with powder recycling

#### 2.7.2.1 Microstructure and defects

Several studies have investigated the development of Ti6Al4V microstructure in LB-PBF [24,77,137] and EB-PBF [130,138,139] processed builds. Commonly the build direction (z-plane) and the transverse direction (x-y plane) are used for analysis and comparison. Figure 2.28a and c shows the microstructure of Ti6Al4V builds produced by EB-PBF and LB-PBF processes in the transverse direction respectively (from [35]). The microstructure of the part depends on the cooling rate during the fabrication process. The mechanism of transformation into martensite and lamellar structure in titanium is described in Section 2.2.4. As shown in Figure 2.28a, the Ti6Al4V samples fabricated by EB-PBF were comprised of lamellar  $\alpha$  with retained  $\beta$  phase at their boundaries caused by diffusional transformation due to slow cooling in the heated powder bed. Figure 2.28c shows the Ti6Al4V builds produced by LB-PBF process that consisted of  $\alpha'$  microstructure developed due to large thermal gradients resulting in rapid cooling that occurred during the LB-PBF process [140]. The X-ray diffraction (XRD) measurements obtained by Thijs *et al.* [77] on Ti6Al4V LB-PBF parts showed they had a predominantly HCP structure indicating that at room temperature the LB-PBF parts exist with fully  $\alpha'$  or a mixture of  $\alpha_m + \alpha'$  microstructure with negligible  $\beta$  fraction.

Hot isostatic pressing (HIPing) is sometimes performed on parts fabricated by AM to improve component density. Although HIPing has been reported to increase the fatigue life of the components by eliminating the potential fatigue crack nucleation sites [5], it can cause significant coarsening of the  $\alpha$  laths as shown in Figure 2.28b and d, which can

reduce the strength and hardness of the parts significantly [5]. With Ti6Al4V powder recycling, Ghods *et al.* [130] and Carrion *et al.* [131] have reported no difference in microstructure between the virgin and recycled EB-PBF and LB-PBF parts.

Evidence of pores/defects in the parts fabricated by the EB-PBF and LB-PBF processes have been reported in several papers [103,140–142]. Tammam-Williams *et al.* [103] have reported two types of defect that could occur in EB-PBF parts. Gas pores are produced by the argon gas bubbles trapped inside the feedstock powder that diffuses into the melt pool during powder melting. If a gas bubble is unable to exit the melt pool during solidification, it creates small spherical voids in part. The second type of defect is referred to as lack-of-fusion defect, which arise when the electron or laser beam fails to fully consolidate powder particles. These defects have irregular morphology and can vary in size from a few  $\mu\text{m}$  to mm. Other types of defects have also been reported, for instance, Leung *et al.* [67] have shown that improper closure of the keyhole formed during laser melting can lead to keyhole pores in LB-PBF parts. Also, the ejection of melt droplets during LB-PBF process have also been hypothesised to form surface pores [69].

This item has been removed due to 3rd Party Copyright. The unabridged version of the thesis can be found in the Lanchester Library, Coventry University.

**Figure 2.28** Optical micrographs of Ti6Al4V processed by EB-PBF (a) as-fabricated and (b) HIPed condition; and Ti6Al4V produced by LB-PBF process (c) as-fabricated and (d) HIPed condition (after [55]).

Very few studies have investigated the defect morphology and volume fraction with recycling in Ti6Al4V parts produced by LB-PBF and EB-PBF processed. Tang *et al.* [50] used the Archimedes' principle to compare the density of Ti6Al4V EB-PBF parts produced from virgin and recycled powder and reported a marginal decrease in part density with recycling. In the LB-PBF process, Alamos *et al.* [143] and Denti *et al.* [134]

also used the Archimedes' method to compare the density of parts fabricated by virgin and recycled powder and reported a negligible difference. However Skalon *et al.* [132] and Seyda *et al.* [136] used a 2D imaging technique and found that the pore size increased with powder recycling in LB-PBF parts. 3D imaging technique used by Ahmed *et al.* [144] further confirmed the pore size to increase with powder reuse in 17-4 PH stainless steel LB-PBF parts. The increase in the pore size was connected to the change in powder PSD and morphology with recycling. However, neither of the studies investigated the defect morphology, which is known to vary depending on the source of defects. Also, the corresponding influence of defect size and morphology with recycling on the mechanical properties like fatigue have not been conducted.

#### 2.7.2.2 Mechanical properties

The mechanical properties of Ti6Al4V builds fabricated by EB-PBF and LB-PBF process have been investigated based on several variables including process parameters [145,146], part orientation [138,147,148], part geometry [41,149,150], location of parts in the build platform [138], layer thickness [150,151], post treatment [5,152,153], type of initial powder feedstock [117,154] and powder recycling [23,131,136].

With Ti6Al4V powder recycling in EB-PBF, Tang *et al.* [50] observed an increase in the yield and tensile strength of the material with powder reuse. The increase in material strength was attributed to the increase in the O content of the material. The interstitial elements hinder the movement of dislocations in the crystal lattice leading to increase in strength. However, the authors observed no changes in material ductility as the powder O content remained within the max. limit (0.20 wt%) but Popov *et al.* [23] reported a decrease in material elongation because the powder O content exceeded 0.3 wt.% after 69 reuse times. Furthermore, Grell *et al.* [155] demonstrated that high Ti6Al4V powder O content resulted in poor Charpy impact values of EB-PBF parts. Similar observations have been reported in LB-PBF Ti6Al4V parts in [131,132,136] where the strength and hardness increased with reuse due to increase in O content of the parts.

Although several studies are available related to fatigue properties of EB-PBF and LB-PBF Ti6Al4V parts, only two studies focused on the influence of powder recycling on the fatigue life of the parts thus fabricated. In one such study, Popov *et al.* [23] studied the effect of Ti6Al4V powder recycling in EB-PBF process on HCF properties. The tests were conducted at room temperature and cyclic loading was applied with load ratio  $R=0.1$ , a maximum stress of 675 MPa, and at a frequency of 25 Hz. The authors found that the

samples produced from the virgin powder demonstrated longer life than the samples produced from 69 times recycled powder. The authors also demonstrated that after HIPing the fatigue life of the recycled part improved significantly, and was close to that of the virgin part without HIPing. The authors correlate the reduction in fatigue life to the powder degradation such as particle surface cracking, gas pores and surface oxidation. However, the other reason for the lower fatigue life could be the change in powder PSD caused by increase in the fraction of high aspect ratio particles and reduction in the number of fine particles that resulted in the lack-of-fusion defects from where the fatigue crack nucleated in the recycled part during cyclic loading. Therefore, other bulk powder properties like flowability could have been a useful data. Hence, if the authors had performed further in-depth powder characterisation, defect population and morphology, it would have provided a better comprehensive understanding of the challenges in powder recycling. Carrion *et al.* [131] have compared the fatigue behaviour of Ti6Al4V LB-PBF parts produced from new and 15 times recycled powder using fatigue test in fully reversed ( $R=-1$ ) strain controlled condition. The authors observed no difference in the fatigue life between the virgin and recycled specimens in the as-manufactured surface condition (un-machined). In the machined condition, the parts produced from the recycled powder showed longer life, which is in contrast to the observation reported by Popov *et al.* in the EB-PBF process. The authors correlate the result to the better flow and apparent density behaviour exhibited by the 15 times reused powder compared to the virgin powder. Although, the recycled parts performed better when 15 times recycled powder was used, the properties could potentially deteriorate with increased number of reuse due to particle morphology deterioration as was reported in [23], or due to increase in spatter contamination, powder oxidation *etc.*

The degree of change in powder properties varies depending on the number of reuse times, type of process, recycling strategy, and build volume utilised, and therefore some studies report contradictory results. Furthermore, energy source (laser or electron beam), powder sintering (EB-PBF), processing temperature, layer consolidation mechanism, input energy density, spatter formation (LB-PBF), layer thickness, *etc.* also play a vital role in the evolution of powder properties [58]. Therefore, practically, it is not possible to propose the number of build cycles up to which a powder could be recycled for any alloys used in PBF process unless it is application specific that uses a particular process (EB-PBF or LB-PBF), with consistent build parameters, part geometry, reuse

strategy, and similar initial powder feedstock properties. Nevertheless, although the degree of degradation in powder and part properties could vary, understanding the nature, cause and mechanism of degradation is essential in order to estimate, predict and understand the properties of components produced from recycled powder in an industrial setting.

## 2.8 Summary

This review chapter consisted of four facets. In the first facet, an overview of titanium metallurgy that is relevant to the properties of AM processed Ti6Al4V was covered. Following that, the fundamental background of the AM process with an emphasis on EB-PBF and LB-PBF processes was discussed. The process mechanism in LB-PBF was extensively reviewed owing to its significance to the current research. Thirdly, feedstock powder characteristics, characterisation methods, and their influence on build properties were discussed. Finally, powder recycling and its effect on powder and parts built using LB-PBF and EB-PBF processes were reviewed.

Based on this comprehensive review it was found that AM offers a huge benefit for manufacturing geometrically intricate titanium parts which otherwise, using conventional methods, would be impossible or challenging to manufacture.

In PBF processes like LB-PBF and EB-PBF, the powder feedstock plays a crucial role in determining the properties of the built parts. However, a higher volume of powder is utilised than is required to manufacture the particular part. This results in significant volume of unfused powder being left-out that can be recycled to improve process efficiency.

Recycling Ti6Al4V powder changes its physical and chemical properties compared to the virgin powder properties. The key physical property changes include changes in PSD and particle shape, which affect powder flow and powder layer density. Due to the affinity of Ti6Al4V alloy with oxygen, the O content in the powder continued to increase with increasing reuse times. It is important to monitor the evolution of powder properties to understand and predict the properties of the part. Ti6Al4V Parts built using recycled powder showed increased tensile strength due to increase in O content, while other properties like defect density, morphology and fatigue behaviour need further investigation.

## 2.9 Knowledge gaps

Based on the critical review conducted on the published literature on Ti6Al4V powder recycling in LB-PBF and EB-PBF processes, the following research gaps have been identified:

- (i) Most of the literature on powder recycling tried to correlate the number of reuse times to changes in powder and part properties. No research focussed on the heterogeneity in powder degradation with respect to different locations in the powder bed. Investigating that will provide a better understanding of the mechanism of degradation. Also the effects of preheats in EB-PBF process on powder properties have not been studied.
- (ii) Very few studies have focused on the defects in recycled parts. However, those studies mostly focused on the quantification of defects while the defect morphology which plays a major factor in influencing fatigue life of the components have not been investigated.
- (iii) To the best of the author's knowledge, only two studies have investigated the fatigue properties of recycled Ti6Al4V parts. The results obtained in the two studies are contradictory to each other. Furthermore, a comprehensive study that includes detailed characterisation of powder properties and its correlation to fatigue properties is still lacking.
- (iv) After the parts are built, the recycled powder is topped-up with the virgin or previously used powder to maintain the build volume. No research has been performed to investigate the effects of powder blending on the mechanical properties of build parts.
- (v) With recycling, increasing O content has been identified as one of the major limiting factors for continued usage of powder. However, other than correlating the effects of increasing O content to mechanical properties, no other areas have been explored. For instance, Leung *et al.* [69] have shown in Invar 36 powder that increase in O content causes reverse in Marangoni flow pattern, increase in spatters and porosity. Similar studies have not been conducted for Ti6Al4V, even though O content is recognised as a crucial variable.

\*\*\*\*\*

## 3 Experimental methodology

### 3.1 Introduction

The previous chapter concluded that the powder undergoes changes in its physical and chemical characteristics due to recycling and this has subsequent impact on the properties of the parts thus fabricated. This chapter explains the methodology followed in this research to answer the objectives laid out in Chapter 1 and to address the knowledge gaps highlighted in Chapter 2. The methodology chapter has two parts, each with distinct approaches. In the first part, the approach was designed to address Objectives 1-3 and knowledge gaps 1-3. In the next part, the methods used to answer Objective 4 and knowledge gaps 4 and 5 are explained. The description of various characterisation and processing techniques are presented for both the parts.

### 3.2 Part-1: Electron beam powder bed fusion

#### 3.2.1 Overview

This part explores the effect of Ti6Al4V powder recycling in the EB-PBF process by using a simulated powder recycling strategy that was developed to reduce powder consumption and virgin powder top-up. The effects of preheat cycles, recycling and heterogeneity in powder degradation that exist within the same build cycle were studied.

#### 3.2.2 Powder feedstock material

In all of the published Ti6Al4V powder recyclability studies conducted in the EB-PBF process, powders provided by the machine manufacturer, *i.e.* PA powder has been mostly used. Therefore, no data is available in the open literature on the GA powder especially with recycling in EB-PBF process. Therefore, in this study, argon gas atomised (AGA) Ti6Al4V ELI powder supplied by Carpenter Additive, UK was employed.

#### 3.2.3 Experimental approach

The work was conducted in an ARCAM Q10 plus EB-PBF system using 35 kg of powder. A controlled and simulated recycling methodology was designed and employed. Figure 3.1 shows the manufacturing strategy adopted in this work. Virgin condition corresponds to manufacturing of four test coupons of the same geometry ( $120 \times 30 \times 30$  mm<sup>3</sup>) horizontally (length parallel to the start plate) using new powder, of which approximately 16 kg ended on the powder table, with the remaining 19 kg in the powder

hoppers, following ARCAM Q10 plus default settings. Following the virgin build, powder samples were collected from the top few layers at two regions in the powder bed: near-melt zone and away-melt zone as highlighted by red boxes in Figure 3.1. For the 'recycled' condition, the powder bed of the same build volume as the virgin condition was preheated 10 times. The amount of powder available was lower than in the virgin builds since material was consumed in the sample blocks in the virgin build (~500 g) plus additional losses (~200 g) in each machine setup due to powder handling. After each preheat cycle the sintered 'powder cake' was treated in the ARCAM powder recovery system and sieved (150  $\mu\text{m}$  mesh sieve), while the unused powder left in the hopper was vacuumed and collected separately. Prior to powder reloading, sieved powder was manually mixed with unused powder from the hopper in each build, then poured back into the hopper. Following 10 preheat cycles, the second set of similar test coupons were fabricated. The unconsumed powder from the build was then recovered and sieved. Two powder samples were then collected after the PRS: sieve residues (powder that failed to pass through the sieve) and recycled powder (powder that passed through the sieve). Specimens for tensile, Charpy impact and fatigue tests were then extracted from the test coupons manufactured in both virgin and recycled condition.

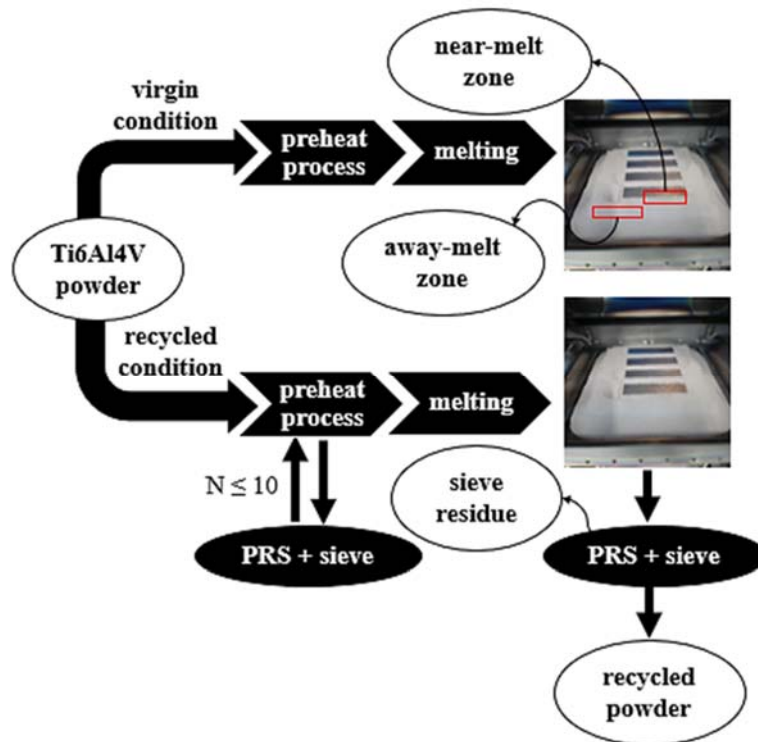


**Figure 3.1** Powder sampling and manufacturing strategy used to fabricate test coupons following virgin and recycled conditions.

### 3.2.4 Manufacturing parameters

The applied EB-PBF process parameters for both conditions were based on the standard settings in auto calculation heat model software version 5.2.23 using 50  $\mu\text{m}$  layer thickness. Prior to build, preparations included the adjustment of powder hopper baffles, raker fetching and rest positions to guarantee the free flow of particles. This was because the powder showed different flow properties to standard ARCAM PA powder. The preheat process was performed in two stages, preheat 1 and preheat 2, using a beam current of 22 and 26 mA respectively. Preheat 1 was applied over the entire build area (200  $\text{mm}^2$ ) and preheat 2 covered only the areas to be melted with 4 mm offset to the build. Both preheats were performed using a defocused beam with a focus offset of 50 mA and scanning speed of 25000  $\text{mms}^{-1}$  to reduce the energy input enough to sinter the powder particles prior to melting. The initial preheating and post-heating aimed to keep the temperature high enough to avoid powder smoke due to a decrease in powder bed temperature. Following preheats, which increased the build plate temperature to  $\sim 750^\circ\text{C}$ , melting was applied using a focused beam, 36 mA focus offset, speed index of 60 at hatch spacing of 0.2 mm.

### 3.2.5 Powder characterisation

#### 3.2.5.1 Powder chemical composition

Al and V contents of the virgin, recycled, near-melt zone and away-melt zone powders were analysed using inductively coupled plasma spectroscopy technique following ASTM E2371. The O content was measured using the IGF technique following ASTM E1409. Approximately 0.2 g of powder sample was used for analysis. The Ti6Al4V powder with nickel flux was loaded into a small graphite crucible that contained graphite powder. The crucible was then heated. Upon heating the oxygen in the sample combines with carbon in the graphite powder forming carbon monoxide, which gets further oxidised to form carbon dioxide. The carbon dioxide formed gets carried by the inert gas stream to the infrared detector. The detector analyses the sample and the result is compared to the response generated from analysing the reference sample. The oxygen in wt.% is then displayed.

#### 3.2.5.2 Powder morphology

**Qualitative analysis:** Powder morphology was studied using a Zeiss EVO LS15 SEM. Small amounts of virgin, near-melt zone, away-melt zone, recycled and sieve residue

powders were mounted on a conductive tape. Care was taken during powder mounting to avoid breaking sintered powder particles. SEM images were taken at different magnifications using the BSE detector at a working distance of 8 mm, 60  $\mu\text{m}$  aperture size and 20 keV accelerating voltage.

**Quantitative analysis:** Quantitative powder shape analysis was performed using Morphologi 4-ID equipment (Figure 3.2). Three powder samples: virgin, near-melt zone, and recycled powders were analysed. 5  $\text{mm}^3$  of powder was loaded into the sample dispersion unit (dispersion cylinder, Figure 3.2b). Then dry air was supplied at 1 bar pressure into the dispersion cylinder which distributed the powder particles over a glass plate uniformly without particle boundary overlapping. The dispersion was checked manually using the objective lens before starting the measurement. After ensuring satisfactory dispersion has been achieved, the scan area was fixed and  $\sim 10,000$  particles within the scan area were imaged using the automated-light microscope with a 10x objective lens. The dispersion and imaging parameters were the same for all the three powders analysed.

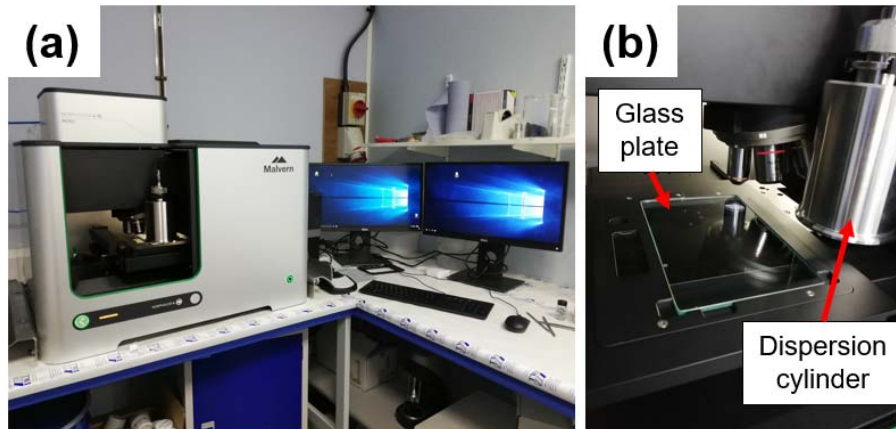


**Figure 3.2** Morphologi 4-ID (Malvern Panalytical), 2D particle imaging.

The obtained 2D grayscale projections of the individual particles were filtered and classified using Morphologi 10.20 software. The projections were initially filtered using a particle transparency parameter; particles with a mean intensity level less than 100 pixels were not analysed. The images were then classified based on the particle shape parameters defined in [156] as spherical, satellites, fines and irregular categories based on the set-limits given in Table 3.1. Circularity is calculated by:

$$C_c = \sqrt{4\pi A/P^2} \quad (3.1)$$

where  $P$  and  $A$  refer to perimeter and projected area. Convexity is defined as:

$$C_x = P_c/P \quad (3.2)$$

where  $P_c$  refers to convex hull perimeter. Finally, elongation is defined as:

$$E = 1-AR \quad (3.3)$$

where  $AR$  refers to aspect ratio, *i.e.* the ratio of Feret's minimum to maximum length.

**Table 3.1** Particle shape parameters used for classification of spherical, satellites, irregular, and fine Ti6Al4V EB-PBF powder particles for quantitative powder shape analysis.

Shape parameters	Circularity	Convexity	Elongation	Equivalent diameter / $\mu\text{m}$
Spherical	$\geq 0.984$	$\geq 0.980$	-	$\geq 25$
Satellites	0.874 to 0.985	$< 0.997$	$< 0.294$	$\geq 25$
Irregular	$< 0.874$	$< 0.997$	-	$\geq 25$
Fines	-	-	-	$< 25$

### 3.2.5.3 Particle size distribution

Laser diffraction was used to estimate the PSD using a Malvern Panalytical Mastersizer 3000 system according to ASTM B822. Figure 3.3 shows the Mastersizer 3000 system with wet unit. De-ionised water was used as the carrier for the wet dispersion method. The sample properties such as powder material (Ti6Al4V), density ( $4.41 \text{ gcm}^{-3}$ ), refractive index (2.153) *etc.* were then defined. The background was initially measured and the value did not exceed the recommended value provided by the manufacturer. No more than 25 g of powder was fed into the particle dispersion unit. The rpm of the stirrer was defined based on the user experience and manufacturer recommendation. The suspension was then circulated through the path of the laser light and a recommended 20 s circulation time elapsed before the measurements were taken. The particles that passed through the laser light inside the measurement cell created a diffraction pattern on the detector which was then automatically converted to size distribution data using Mie scattering theory. The particle size data were presented as their equivalent diameter. A total of ten iterations were performed for each powder sample. The beaker and spatula were thoroughly cleaned with acetone while the carrier tubes were flushed twice with de-ionised water and drained between each powder sample to avoid contamination.



**Figure 3.3** Malvern Panalytical Mastersizer 3000 system used for PSD measurement.

#### 3.2.5.4 Hall flow test, apparent and tap density measurement

A Hall flowmeter, supplied by LPW technologies, UK, was used to measure powder flowability as per ASTM B213. Virgin and recycled powders were analysed for flowability, apparent and tap densities. Figure 3.4a shows the experimental set-up used for Hall flow and apparent density measurements. A weighed mass of 50 g of the powder was made to flow through the funnel via an orifice of 2.5 mm into the cup. The time taken for the entire mass of powder to exit the orifice was measured using a stopwatch. A total of ten measurements were taken for each sample and the average was calculated. The funnel and cup were cleaned with acetone between each powder sample to avoid contamination. The humidity was about 44% and the temperature was  $\sim 22^{\circ}\text{C}$  throughout the twenty measurements.

Apparent density was measured using the same experimental set-up following ASTM B212. The mass of the empty density cup was first measured. The density cup is a cylindrical brass cup of known volume ( $25\text{ cm}^3$ ). The cup was placed concentric with the hall flowmeter funnel at a distance of  $\sim 25\text{ mm}$  from the bottom of the funnel (Figure 3.4a). Powder was then made to flow through the funnel via the orifice into the density cup until it filled and started to overflow. The excess powder was then carefully wiped-off and levelled without causing any vibration using a spatula. The mass of the powder-filled density cup was then measured. Apparent density was then determined by calculating the ratio of mass of powder to the volume of the density cup. Three measurements were taken per powder sample. After each measurement the density cup and the funnel were cleaned with acetone to remove any residual powder particles that may cause inaccuracies in the measurements.

Tap density of the virgin and recycled powders was measured using the tap density meter shown in Figure 3.4b following ASTM B527. The two graduated glass cylinders were thoroughly cleaned and dried. The mass of the empty cylinders was then measured. 100 g of virgin and recycled powder were filled into each glass cylinder. The glass cylinders were then mounted onto the tapping device. 3000 taps were applied at a frequency of 200 taps/min and the stroke length was 3 mm. Powder volume was measured based on readings on the graduated scale value at the tapped powder surface level. Tap density was then measured using the same method as for the apparent density.

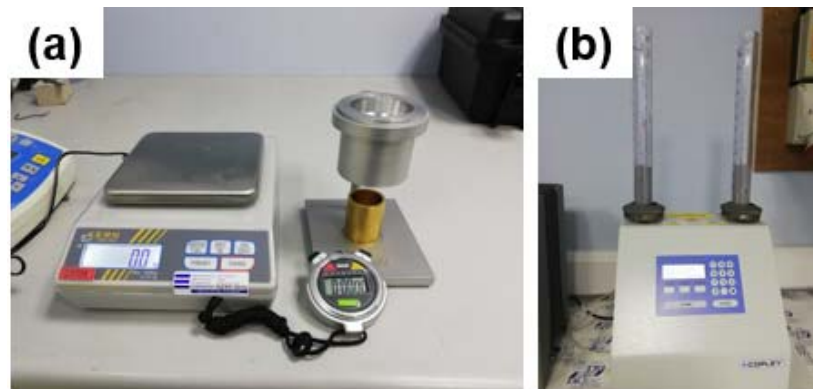


**Figure 3.4** Test set-up for (a) Hall flow and apparent density, and (b) tap density measurements.

#### 3.2.5.5 Powder cross-section analysis

All the powder samples including virgin, near-melt zone, away-melt zone, recycled and sieve residue were analysed. For metallographic examination of the powders, care was taken during mounting and polishing to ensure homogeneity in material removal. The grinding was directly performed using 2500-grit SiC paper as using coarser grits can cause detachment of particles from the bakelite. Fine polishing was then performed down to 0.25  $\mu\text{m}$  using diamond suspensions. Powder cross-sections of the virgin powder were initially examined under optical and electron microscopes to reveal the entrapped powder porosity. Following that, etching was made with Kroll's reagent (2 vol.% HF, 5 vol.%  $\text{HNO}_3$ , and 43 vol.%  $\text{H}_2\text{O}$ ) by swabbing the polished surfaces for  $\sim 20$  s to reveal the microstructure. SEM images were taken using BSE detector.

For electron backscatter diffraction (EBSD), powder samples were additionally polished with colloidal silica OP-S after 0.25  $\mu\text{m}$  diamond suspension. Powder cross-sections were analysed using a Zeiss Sigma field emission gun SEM (FEG-SEM) using AZtecHKL software. The sample was tilted to  $70^\circ$  and the detector was positioned close

to the sample to acquire the Kikuchi pattern of the particle of interest on the phosphor screen. The Kikuchi pattern obtained from each pixel was analysed by the Aztec software and the corresponding orientations and phases were determined. The phase constituents of the material were already predefined into the software, which for Ti6Al4V was HCP and BCC crystal structure. The working distance was  $\sim 2$  mm, *i.e.* the sample was positioned very close to the source to enable more electron interaction with the sample. An accelerating voltage of 30 keV, aperture size of 120  $\mu\text{m}$  and a step size of 0.3  $\mu\text{m}$  were used for all the scans performed. The data were then post-processed using ATEX software [29]. A noise reduction factor of four was applied on all EBSD maps and high-angle grain boundaries (HAGB,  $\theta > 15^\circ$ ) and low-angle grain boundaries (LAGB,  $1.5^\circ < \theta < 15^\circ$ ) were plotted over the band contrast maps.

### 3.2.6 Post-thermal treatment

Two blocks from the virgin and two from the recycled condition underwent post-thermal treatment. The four test blocks were first subjected to HIPing at 930°C with 140 MPa pressure for 4 hours in an argon atmosphere using laboratory-scale EPSI HIP equipment. It has been reported in several studies that the strength of the material decreases after HIPing due to  $\alpha$ -lath coarsening [24,141]. In order to retain the strength of the material, solution treatment and aging was then performed as per parameters recommended in AMS4999A using a vacuum furnace. The samples were solution heat treated at 927°C for 2 hours in vacuum followed by argon fast cooling until the temperature decreased below 420°C. The rapidly cooled samples were then aged under vacuum at 540°C for 4 hours followed by furnace cooling.

### 3.2.7 Part characterisation

Characterisation was performed on both the virgin and recycled test blocks in both the as-built and post-thermally treated condition. The metallographic and mechanical test specimens were extracted from the eight test blocks in the same orientation (horizontal).

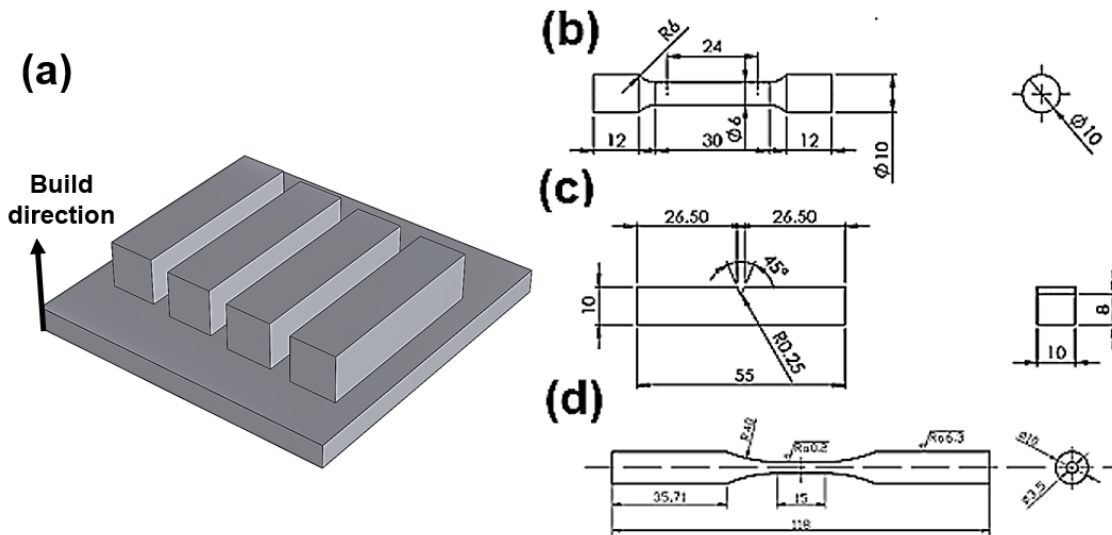


**Figure 3.5** (a) CAD model of build layout; dimensions of (b) tensile, (c) Charpy impact V-notch, and (d) fatigue specimens.

### 3.2.7.1 Microstructure

For microstructural investigation, the specimens were mounted on a conductive resin and ground with successively finer SiC abrasive paper (360- to 2500-grit). Fine polishing and etching were performed to reveal the microstructure were performed using the same method as for the powders. The microstructure in the build direction was imaged using secondary electron (SE) imaging mode in the Zeiss Sigma FEG-SEM.

### 3.2.7.2 Hardness test

Hardness testing was conducted using a Vickers microhardness tester (Zwick/Roell ZHV $\mu$ ) following ASTM E92 on as-polished samples. Six indents were made per sample at 1 kgf with a 10 s dwell time. Sufficient spacing between the indents was provided to avoid interference of the plastic deformation caused by one indent over the other. The diagonal length of the indents was measured using an optical microscope and the following standard formula was used to calculate the Vickers hardness values

$$HV = 1.8544 \times F \text{ (kgf)} / D_v^2 \text{ (mm)} \quad (3.4)$$

where  $F$  refers to load applied in kgf,  $HV$  refers to Vickers hardness number and  $D_v$  refers to the Vickers average diagonal length of the indent in mm.

### 3.2.7.3 Charpy impact test

Charpy impact testing was conducted according to ASTM E23 on a set of three V-notched specimens of dimension shown in Figure 3.5c. The machine was initially checked with a free-swing for zero indication reading of the absorbed energy. All the tests were conducted at room temperature. The specimen was positioned on the specimen supports using self-centering tongs and the pendulum was released to strike the specimen. The readings on the analogue scale were recorded.

### 3.2.7.4 Tensile test

Tensile testing was conducted on cylindrical dog-bone specimens of dimension shown in Figure 3.5b. Specimens were extracted in the horizontal direction from the virgin and recycled test blocks in both the as-built and post-thermally treated conditions. Two specimens were tested in each condition using a 100 kN capacity Instron servo-hydraulic test machine. All the tests were conducted at room temperature following ASTM E8 standard and the 0.2% proof stress, UTS and percentage of elongation were measured.

### 3.2.7.5 High cycle fatigue test

High cycle fatigue testing was performed to compare the fatigue life between the virgin and recycled parts in the as-built and post-thermally treated condition. Four specimens were tested per condition. Therefore, sixteen machined and polished (mirror surface finish,  $<0.25\ \mu\text{m}$ ) cylindrical specimens with dimensions as shown in Figure 3.5d were tested according to ASTM E466 using a 100 kN capacity Instron servo-hydraulic test machine. Cyclic loading was applied at a load ratio,  $R = 0.1$ ; a maximum stress of 600 MPa, and at a frequency of 12 Hz. All specimens were tested until complete fracture. The fracture surfaces were examined after ultrasonic surface cleaning using SE mode in SEM. The surface area of the pores on the fracture surfaces was measured using ImageJ.

### 3.2.7.6 X-ray computed tomography

X-ray computed tomography was performed at the Research Complex at Harwell, UK. The virgin and recycled test specimens ( $3 \times 3 \times 12\ \text{mm}^3$ ) in the as-built condition were analysed using a laboratory-based XCT system (Nanofocus, Phoenix|X-ray). Each XCT scan was performed at 100 kV and 140  $\mu\text{A}$  with a 0.34 mm thick copper filter, comprising 3142 radiographic projections with a 1 s exposure time per projection. These projections were reconstructed via filtered back project using the Datos|x software, resulting in an image matrix of  $990 \times 990 \times 1000$  pixels with an isotropic voxel size of  $13 \times 13 \times 13\ \mu\text{m}^3$ .

The reconstructed image volume was subsequently analysed in Avizo 8.0 (Thermofisher Scientific). Firstly, the input image volume was deblurred by 3D unsharp masking (with a radius of 5 and an edge contrast of 0.5), for contrast enhancement and image sharpening. Secondly, the filtered image was then binarised by interactive thresholding. The volume fraction, porosity (%), and sphericity measurements were performed according to [56].

### 3.3 Part-2: Laser beam powder bed fusion

#### 3.3.1 Overview

This part focuses on the effects of powder blending during Ti6Al4V powder recycling. Several powder recyclability studies including the author's recently published work [157], concluded that the Ti6Al4V powder O content increased with reuse which is consequently realised as a major factor limiting the number of times the Ti6Al4V powder can be recycled. Therefore, the aim of this part was to investigate the effects of blending high and low O content Ti6Al4V powders on build properties using in situ and ex situ experiments.

Many ex situ analyses have demonstrated the effect of O content on Ti6Al4V build properties, such as increase in strength, reduction in damage tolerance and ductility [23,158]. To further explore the potential effects of O content in AM, the current study attempted to explore the effects of powder O content on the molten pool dynamics in LB-PBF process. Given that no miniature or process monitoring facility which can study the physics of the molten pool in EB-PBF system is currently available, the study was performed in an LB-PBF system.

#### 3.3.2 Powder feedstock

Commercially available Grade 5 AGA Ti6Al4V powder supplied by TLS Technik was used to conduct the study. Table 3.2 shows the chemical composition of the powder.

**Table 3.2** Chemical composition (wt.%) of Ti6Al4V powder.

Al	V	N	C	O	Fe	Ti
6.37	3.98	0.010	0.015	0.120	0.182	Bal.

#### 3.3.3 Experimental approach

In order to avoid the extensive route to increase the powder O content by multiple reuse cycles, which consumes significant amount of time, powder volume and cost, the new AGA

powder (virgin) was artificially oxidised using a custom-built powder heat treatment furnace (designed and developed by TWI Ltd.). Based on the previously published literature, the maximum reported O content in the recycled Ti6Al4V powder was 0.33 wt.% [23]. Therefore, the aim of the artificial powder oxidation was to increase the powder O content to ~0.40 wt.%. The oxidised powder was then sieved and blended with virgin powder in suitable proportion to build test specimens for mechanical testing to investigate the effects of powder blending during recycling. To further understand the effects of powder oxidation on the melting and spatter behaviour, in situ X-ray imaging experiments were conducted in a miniature LB-PBF process replicator using virgin (0.12 wt.% O) and oxidised (0.40 wt.% O) powder.

### **3.3.4 Powder preparation and blending**

#### *3.3.4.1 Powder oxidation*

A schematic of the powder heat treatment furnace is shown in Figure 3.6. The as-received powder feedstock was poured into the vessel inside the furnace. The vessel was made of stainless steel with two parts joined together by a flange and sealed using a copper gasket. The vessel containing the powder and electroplated stirrer was rotated at 10 rpm to prevent powder sintering and ensure homogenous powder oxidation. The oxygen level in the vessel was controlled by flowing inert gas inside the vessel throughout the heat treatment cycle. The oxygen content of the vessel was monitored periodically. The temperature was monitored using a thermocouple which was inserted into the vessel of the furnace. Ar gas was initially flushed inside the vessel to remove the residual oxygen before initiating the heat treatment cycle. The powder was heated to 475°C and held for 5 h with an Ar flow rate of 0.5 l/min at 1 bar pressure, followed by furnace cooling. After oxidation, the average powder O content measured 0.40 wt.%; hereafter they will be referred as oxidised powder. The oxidised powder was sieved through a vibratory mesh of 70 µm to remove any sintered particles that may have formed during oxidation. However, no sintering occurred and all the particles managed to pass through the sieve mesh.

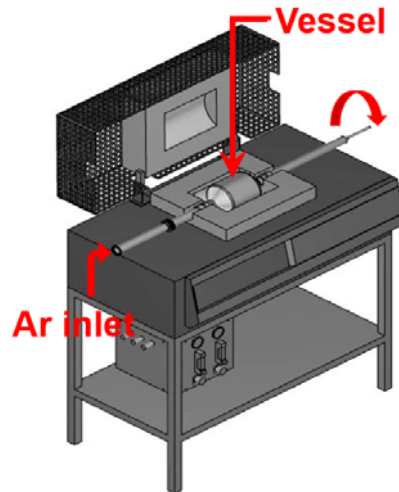


**Figure 3.6** Powder heat treatment furnace used for powder oxidation.

#### 3.3.4.2 Powder blending

Out of the 500 g of powder that was oxidised, 10 g of the oxidised powder was used in the in situ and operando process replicator (ISOPR) for real-time imaging of the laser-powder interaction. The remaining oxidised powder was blended with the virgin powder in a suitable ratio following Euler's rule of mixtures:

$$E_B = E_V V_V + E_{OP} V_{OP} \quad (3.5)$$

where  $E_B$ ,  $E_V$  and  $E_{OP}$  refer to the O content of the blended, virgin and oxidised powder respectively.  $V_V$  and  $V_{OP}$  correspond to the volume of virgin and oxidised powder respectively. The powder blending was conducted in a tumbler for 8 hours to create a 'homogenous' mix of virgin and oxidised powder. Overall, three batches of powders were used in this study- virgin, oxidised and blended with O contents of 0.12 wt.%, 0.40 wt.% and 0.20 wt.% respectively.

#### 3.3.5 Powder characterisation

The O content of the virgin, oxidised and blended powders were measured using the IGF technique. Five samples were tested in the oxidised and blended powder to verify the homogeneity in powder oxidation and blending respectively. Powder morphologies of the virgin and oxidised powders were studied using a Zeiss EVO LS15 SEM using the BSE detector. Laser diffraction was used to estimate PSD using a Malvern Panalytical Mastersizer 3000 system according to ASTM B822. Flowability of the virgin and oxidised powders was measured using Hall flow test following ASTM B213. Sample preparation for powder cross-sectional analysis was performed the same way as mentioned in Section

3.2.5.5. Imaging of particle cross-sections was performed using Zeiss Sigma FEG-SEM using BSE detector, and EDS line scan was performed across the diameter of virgin and oxidised particles to compare the distribution of elemental O within the particle and at the particle surface.

### **3.3.6 Mechanical test specimen manufacture**

Test coupons for fatigue, tensile and Charpy impact tests were produced using a Realiser 125 LB-PBF system, which consists of an Nd: YAG laser operating in pulsed wave mode. Since only 500 g of powder was oxidised and the build volume requires ~3 kg of powder, no specimens were produced using only oxidised powder. Therefore, specimens were produced using virgin (0.12 wt.% O) and blended (0.20 wt.% O) powders. Standard operating parameters followed by TWI Ltd were employed to build the specimens. The laser power was 180 W, 40  $\mu$ s exposure time with a point distance of 50  $\mu$ m and hatch distance of 80  $\mu$ m. A layer height of 60  $\mu$ m was maintained throughout the build. To compare the properties of virgin and blended builds, the process parameters used were the same for both builds.

### **3.3.7 Mechanical test specimen characterisation**

The dimensions of tensile, Charpy impact and fatigue test specimens were the same as mentioned in Section 3.2.7. Tensile testing was conducted on two specimens produced from the virgin and blended powders using a 100 kN capacity Instron servo-hydraulic test machine as per ASTM E8. Charpy impact testing was conducted on a set of three specimens manufactured from each condition according to ASTM E23. HCF testing was performed on three machined and polished (mirror surface finish, <0.25  $\mu$ m) cylindrical specimens from each condition according to ASTM E466 using a 100 kN capacity Instron servo-hydraulic test machine. Cyclic loading was applied at a load ratio,  $R = 0.1$ ; a maximum stress of 600 MPa; and at a frequency of 12 Hz. All specimens were tested until complete fracture. The fracture surfaces were examined under SEM after ultrasonic surface cleaning with acetone.

### **3.3.8 Real-time synchrotron imaging using process replicator**

The in situ and operando process replicator is a miniature portable version of a commercial LB-PBF machine that can be used to study the thermophysical phenomena in situ during powder consolidation by installing it in synchrotron X-ray imaging beamlines, and was developed by University College London, UK [67]. A schematic of the process

replicator is shown in Figure 3.7. The laser optics system comprised a 200 W Yb-doped fibre laser which operates at 1070 nm wavelength in continuous wave mode, and a series of optics including collimator, beam expander and X-Y galvanometer scanner with f-theta lens for moving and focusing the laser beam to a spot diameter of 50  $\mu\text{m}$  at a focal distance of 254 mm. The build chamber comprised a sample holder that sandwiches the substrate plate (commercially pure titanium, cp-Ti) between the two glassy carbon plates. The glassy carbon is non-reactive with the molten metal and also transparent to the X-rays, allowing more than 90% X-ray transmission at 20 – 150 keV [159]. The substrate plate was aligned with the focus point of the laser beam and perpendicular to the synchrotron X-rays.

The build chamber was initially evacuated and then backfilled with argon at 4 l/min flow rate. The powder was fed over the cp-Ti substrate using a vibratory hopper and a scraper attached to the rear end of the hopper acted as a re-coater to level the deposited powder. After each layer, the substrate plate was lowered by a distance corresponding to the pre-set layer height of 100  $\mu\text{m}$ . To investigate the effects of powder O content on the molten pool formation during LB-PBF process, 10 layers of single-line tracks of 5 mm length with laser power of 150 W and scan speed of 50  $\text{mms}^{-1}$  were produced from the virgin (0.12 wt.% O) and oxidised powders (0.40 wt.% O).

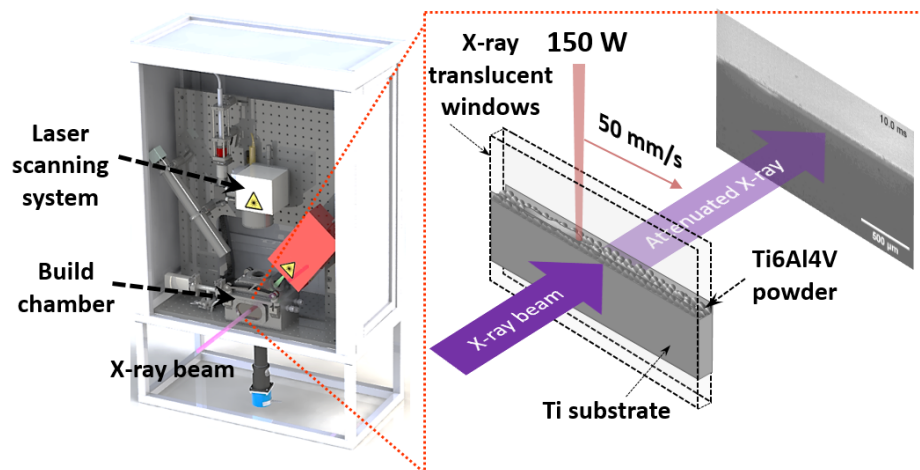


**Figure 3.7** Schematic of in situ and *operando* process replicator that can be installed in X-ray imaging synchrotron beamlines (after [67]).

The in situ imaging experiments were conducted by installing the ISOPR in the I12: JEEP beamline at Diamond Light Source, UK. The mean energy of the X-ray beam was 55 keV. The attenuated X-rays were converted to visible light using a 700  $\mu\text{m}$  thick LuAg: Ce scintillator and the radiographs were recorded with a CMOS camera (Miro 310 M, Vision

Research, US) at 5000 frames per second (fps), a 6.6  $\mu\text{m}$  pixel resolution and a field of view of 8.4 mm X 3.3 mm (width x height).

### 3.3.9 Image processing

Matlab R2020a and open source software Fiji version 1.52i were used to process and analyse the obtained radiographs. Flat-field correction equation (FFC) shown below was used initially to normalise the radiographs.

$$FFC = \frac{I_0 - Flat_{avg}}{Flat_{avg} - Dark_{avg}} \quad (3.6)$$

where  $I_0$  is the input raw image,  $FFC$  is the flat field corrected image,  $Dark_{avg}$  and  $Flat_{avg}$  are the mean of 100 dark field images and 100 flat field images respectively [67]. The radiographs were processed using the image processing toolbox available in Matlab R2020a to improve image contrast and segmentation of the melt pool boundary for surface roughness study. An example of the image processing stages is provided in Appendix B.

### 3.3.10 Spatter and roughness measurement

Spatter and surface roughness measurements were performed on the tracks formed using ISOPR from the virgin and oxidised powders. The trajectories of the droplet spatters were tracked using the manual tracking plugin available in Fiji software. Melt track roughness was measured based on the X-Y pixel coordinates along the melt track boundary. Evaluating the surface roughness using imaging techniques is not a standardised method. To validate the measurements, melt track roughness of the final track (10<sup>th</sup> layer) was compared with measurements made according to ISO4287 using a 3D profilometer (Alicona InfiniteFocusSL). The mean roughness value ( $R_a$ ) was evaluated for both the builds and compared. However, the track length relative to the surface roughness was less, *i.e.* the higher the surface roughness, the larger is the evaluation length required. Therefore, as per ISO4288, the evaluation length ( $l_n$ ) and sampling length ( $l_r$ ) should be greater than 12.5 mm and 2.5 mm respectively. However, since the length of the melt track was only 5 mm,  $l_r$  was set to 0.8 mm and  $l_n$  was set to 4 mm, which was a slight deviation from the standard. Therefore, although the  $R_a$  values calculated with this method are not technically valid, they can still be used for comparing the surface roughness between the virgin and oxidised builds.

### **3.3.11 X-ray computed tomography**

XCT was performed on builds produced from virgin and oxidised powder using a laboratory-based XCT system (Nanofocus, Phoenix|X-ray) at the Research Complex at Harwell, UK. Each XCT scan was performed at 100 kV and 140  $\mu$ A with a 0.34 mm thick copper filter, comprising 1000 radiographic projections with a 1 s exposure time per projection. These projections were reconstructed via filtered back project using the Datos|x software, resulting in an image matrix of  $588 \times 407 \times 997$  pixels with an isotropic voxel size of  $5.69 \times 5.69 \times 5.69 \mu\text{m}^3$ . The reconstructed image volume was subsequently analysed in Avizo 8.0 (Thermofisher Scientific). Firstly, the input image volume was deblurred by 3D unsharp masking (with a radius of 5 and an edge contrast of 0.5), for contrast enhancement and image sharpening. Secondly, the filtered image was then binarised by interactive thresholding. The volume fraction, porosity (%), and sphericity measurements were performed according to [56].

### **3.3.12 Microstructure and microhardness**

Microstructure and Vickers hardness of the builds produced from virgin and oxidised powders were measured following the procedures similar to that explained earlier in Section 3.2.7.1 and Section 3.2.7.2 respectively.

\*\*\*\*\*

## 4 Effects of powder recycling in electron beam powder bed fusion

### 4.1 Introduction

This chapter presents the effects of Ti6Al4V powder reuse in EB-PBF process in 10 build cycles following the systematic approach described in Chapter 3. The objectives of this chapter are to address the Objectives 1 and 2 laid out in Chapter 1 and knowledge gaps 1-3 highlighted in Chapter 2.

To the best of the author's knowledge, all of the Ti6Al4V powder recyclability studies that were previously conducted in the EB-PBF process employed plasma atomised powder. Therefore, no data are available in the open literature showing the effects of recycling relatively cheap gas atomised Ti6Al4V powder in the EB-PBF process. Therefore, argon gas atomised Ti6Al4V powder was used in this study.

Furthermore, previous studies have addressed powder degradation with recycling as a function of reuse times, while the changes in the powder properties with respect to their location in the powder bed have not been considered. This is a significant factor because the temperature gradient in the powder bed can cause inhomogeneity in the recycled powder properties. Therefore, powder particles located at two different areas in the powder bed: near-melt zone and away-melt zone regions (Figure 3.1), were investigated, in addition to the 10 times used powder. This approach also enabled an investigation of the effects of preheat cycles on powder physical and chemical properties with recycling. The changes in the powder properties at the micro-level were then correlated to the bulk powder behaviour and its influence on part properties.

The properties of the test specimens produced from the recycled powder were investigated at the micro scale using microscopy and XCT techniques to study the part microstructure and defect distribution respectively. Previous literature covered only defect density in the recycled builds, while the defect morphology, which has a strong influence on the fatigue life of the component, has not been considered. Therefore, in addition to the defect population, defect morphology in both the virgin and recycled builds has also been characterised.

Furthermore, most of the previous studies focused mainly on the influence of powder recycling on static mechanical properties [23,50]. To the best of the author's

knowledge, only two studies have investigated the fatigue response of the recycled parts, one in LB-PBF [131] and the other in EB-PBF [23]. Popov *et al.* [23] studied the effect of Ti6Al4V powder recycling in EB-PBF process on HCF properties. The authors found that the samples produced from the virgin powder demonstrated longer life than the samples produced from 69 times recycled powder. The authors correlate the reduction in fatigue life to the powder degradation such as particle surface cracking, gas pores and surface oxidation. On contrary, Carrion *et al.* [131] demonstrated the parts produced from the 15 times used powder showed longer fatigue life than the parts produced from the virgin powder. The authors correlate the result to the better flow and apparent density behaviour exhibited by the 15 times reused powder compared to the virgin powder. Although, the recycled parts performed better when 15 times recycled powder was used, the properties could potentially deteriorate with increased number of reuse due to particle morphology deterioration as was reported in [23], or due to increase in spatter contamination, powder oxidation *etc.* The results obtained in the two studies are contradictory to each other. Also, both the studies have not characterised the defect morphology and population in the recycled builds. Therefore, the current study, in addition to exploring the effects of Ti6Al4V powder recycling on static mechanical properties, also attempts to correlate their influence of defect population, morphology and their subsequent impact on high cycle fatigue behaviour.

Overall, this Chapter presents comprehensive results of the study on the effects of powder recycling on Ti6Al4V EB-PBF build properties addressing some of the current knowledge gaps.

---

Some parts of this chapter has been published as a research article entitled, '*The effects of powder reuse on the mechanical response of electron beam additively manufactured Ti6Al4V parts*', Additive Manufacturing, 46, 102101, Soundarapandiyam *et al.*, 2021.

## 4.2 Effects of recycling on powder properties

### 4.2.1 Powder chemical composition

Table 4.1 shows that the O content of the powder and the test coupon increased by 0.02 wt.% after 10 times of powder reuse, It is interesting to note that the O content of the powder particles located near to the melt zone increased by 0.04 wt.% while the powder particles located away from the melt zone showed only marginal oxidation. The powder samples from the near- and away-melt zone regions were taken after the build was completed with the virgin powder. This indicates that heterogeneity in powder oxidation arises within a build. No significant change in the Al and V contents were found between the virgin and recycled powder, except for a marginal Al loss in the near-melt zone powder. In addition, the Al content in the test coupons was found to be lower compared with the powders. This is as expected because Al is one of the light elements and its evaporation has been frequently reported during the EB-PBF process.

**Table 4.1** Al, V and O content of EB-PBF Ti6Al4V powders in virgin, recycled, near-melt and away-melt zone conditions, and the builds.

Element (wt.%)	Virgin		Near-melt zone	Away-melt zone	Recycled		ASTM F3001
	Powder	Test coupon	Powder	Powder	Powder	Test coupon	
Oxygen	0.08	0.08	0.12	0.09	0.10	0.10	0.13 max.
Aluminium	6.57	5.86	6.10	6.48	6.44	5.87	5.50-6.50
Vanadium	4.18	4.13	4.10	4.22	4.16	4.14	3.50-4.50

### 4.2.2 Powder morphology and particle size distribution

Micrographs of the virgin and recycled powders are shown in Figure 4.1a-c and d-f respectively. At lower magnification (Figure 4.1a and d), both powders look similar. Most particles are spherical with some common features generally found in AGA powders such as satellites, elongations, irregularly shaped particles, agglomerates, and particles with open pores, as indicated by yellow arrows. However, a distinct difference in the powder surface morphology can be seen at high magnification. The virgin powder, Figure 4.1b and c, contains a significant number of fine particles (indicated by blue arrows) bonded to coarser particles. By comparison, the recycled powder shows craters

(shallow depressions) and concave sites (deeper depressions) on the powder surface as indicated by red arrows in Figure 4.1e and f.

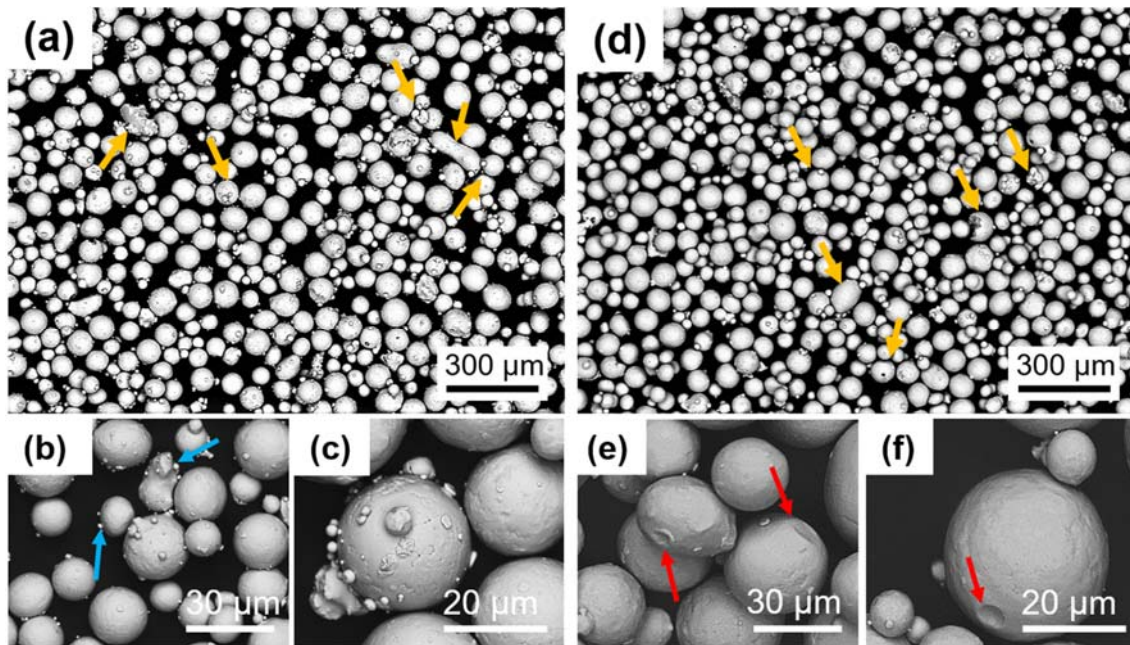


**Figure 4.1** SEM image of EB-PBF Ti6Al4V (a-c) virgin and (d-f) recycled powders. Yellow arrows point the common features such as satellites, elongations, irregularly shaped particles, agglomerates, and particles with open porosities present in (a) and (d). Blue arrows point fine particles (b and c) in virgin powder. Red arrows point to the craters (e) and concave sites (f) in recycled powder.

Morphologies of powder particles from near- and away-melt zone regions are shown in Figure 4.2. Particles close to the melt zone experience both preheats (preheat 1 and preheat 2) and are also exposed to the heat from the melt pool. Hence, some of the particles from this region may partially melt (Figure 4.2a) or fuse with one another (hard-sintering, Figure 4.2b). However, the powder particles at the edges of the powder bed are exposed to relatively less heat, and thereby exhibiting soft-sintered morphology due to the preheating ( $\sim 750^{\circ}\text{C}$ ) (Figure 4.2c).

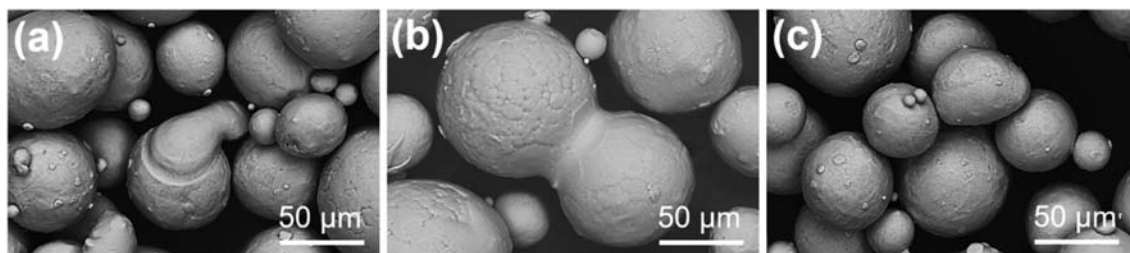


**Figure 4.2** SEM BSE image of EB-PBF Ti6Al4V (a and b) near-melt zone and (c) away-melt zone powder morphology.

Figure 4.3a shows an illustration of the 2D particle radiographs, classified using the particle shape parameters listed in Table 3.1. The percentage of particles in each class is shown in Figure 4.3b. It can be seen that the recycled powder has 26% more spherical particles than the virgin powder. In addition, the number of satellites and fine particles reduced by 10% and 30% respectively in the recycled powder. The near-melt zone powder contains a high fraction of satellites and irregular shaped particles due to sintering, and therefore has a low proportion of spherical particles.

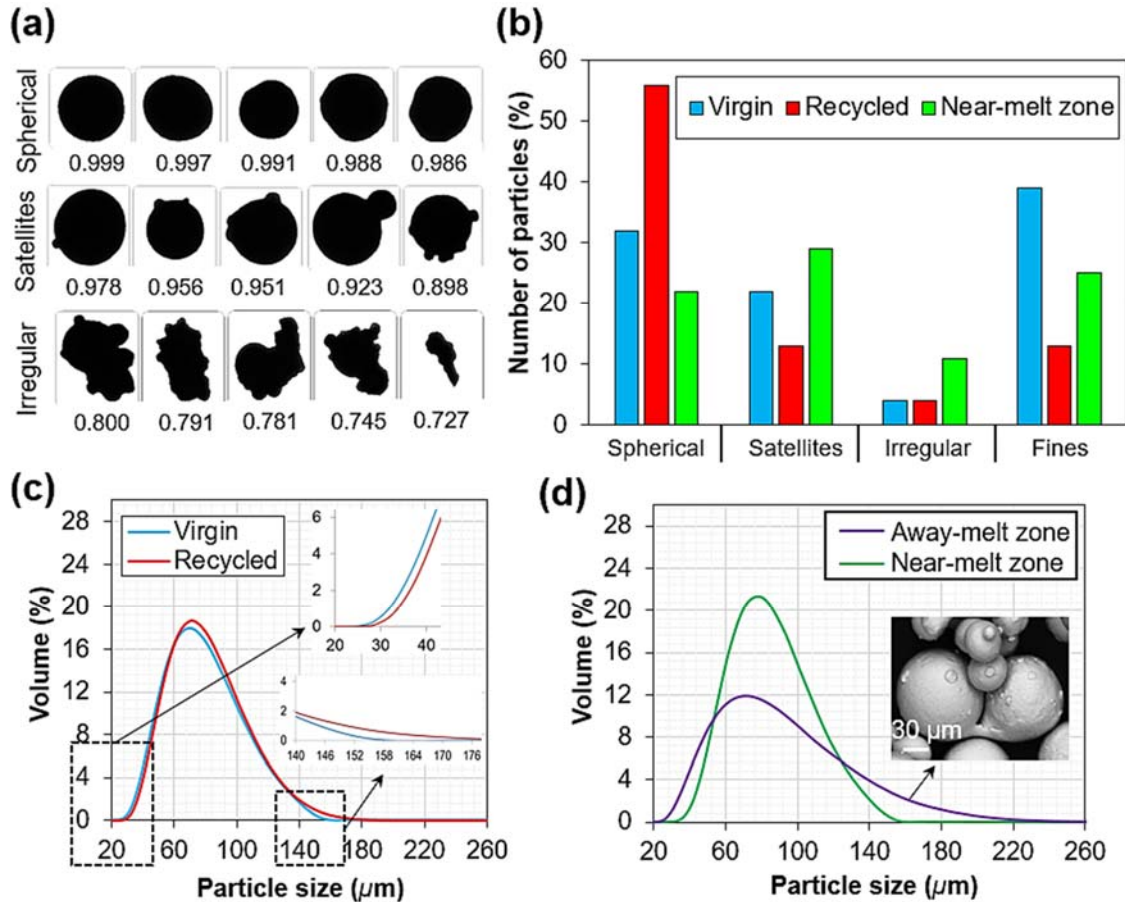


**Figure 4.3** Quantitative powder shape and size analysis: (a) Illustration of classified 2D particle radiographs, the number below each radiograph corresponds to their circularity value, (b) shape analysis results of virgin, recycled, and near-melt zone powders; PSD of (c) virgin vs recycled and (d) away-melt zone vs near-melt zone powders measured by laser diffraction.

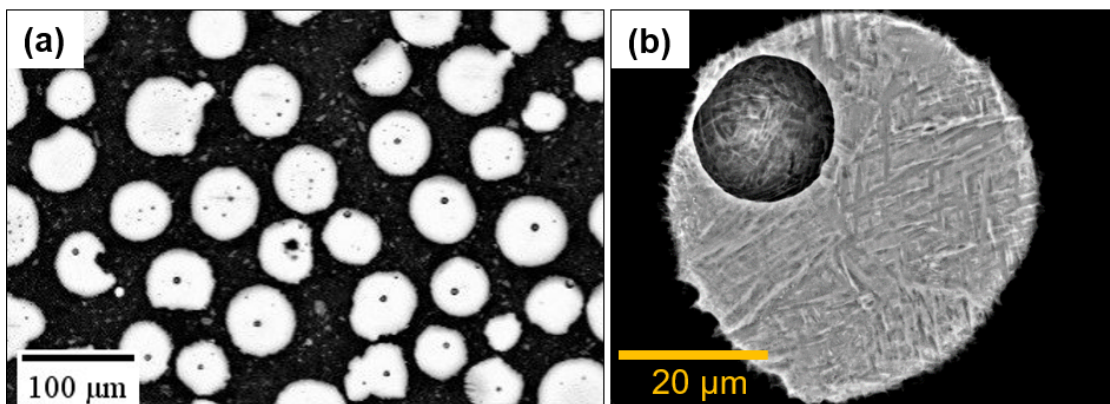
Figure 4.3c shows the PSD bell curves for the virgin and recycled powders. The respective  $D_v(10)$ ,  $D_v(50)$  and  $D_v(90)$  values are 45, 69 and 105  $\mu\text{m}$  for the virgin powder and 47, 71 and 107  $\mu\text{m}$  for the recycled powder. It can be seen that the bell curve of the recycled powder has shifted slightly inwards at the finer side of the size spectrum and

outwards at the coarser side (see the insets in Figure 4.3c). In terms of the PSD change with respect to locations in the powder bed, Figure 4.3d shows that the near-melt zone powder exhibits a wider PSD compared to the away-melt zone powder. The respective  $D_v(10)$ ,  $D_v(50)$  and  $D_v(90)$  values are 45, 78 and 135  $\mu\text{m}$  for the near-melt zone powder and 45, 69 and 105  $\mu\text{m}$  for the away-melt zone powder.

Virgin and recycled powders exhibited a flowability of  $26 \pm 0.02$  s/50g and  $25 \pm 0.02$  s/50g respectively. Both powders exhibited continuous flow without any interruptions. In terms of apparent and tap densities, virgin powder exhibited  $2.48 \pm 0.01$   $\text{gcm}^{-3}$  and  $3.03 \pm 0.02$   $\text{gcm}^{-3}$ , while recycled powders showed  $2.51 \pm 0.01$   $\text{gcm}^{-3}$  and  $3.09 \pm 0.02$   $\text{gcm}^{-3}$ . The Hausner ratio was found to be 1.22 for the virgin and 1.23 for the recycled powders. Any values less than 1.25 are indicative of 'free-flowing' [114], hence both the virgin and recycled powders is judged to have a good flowability.

#### 4.2.3 Powder cross-section analysis

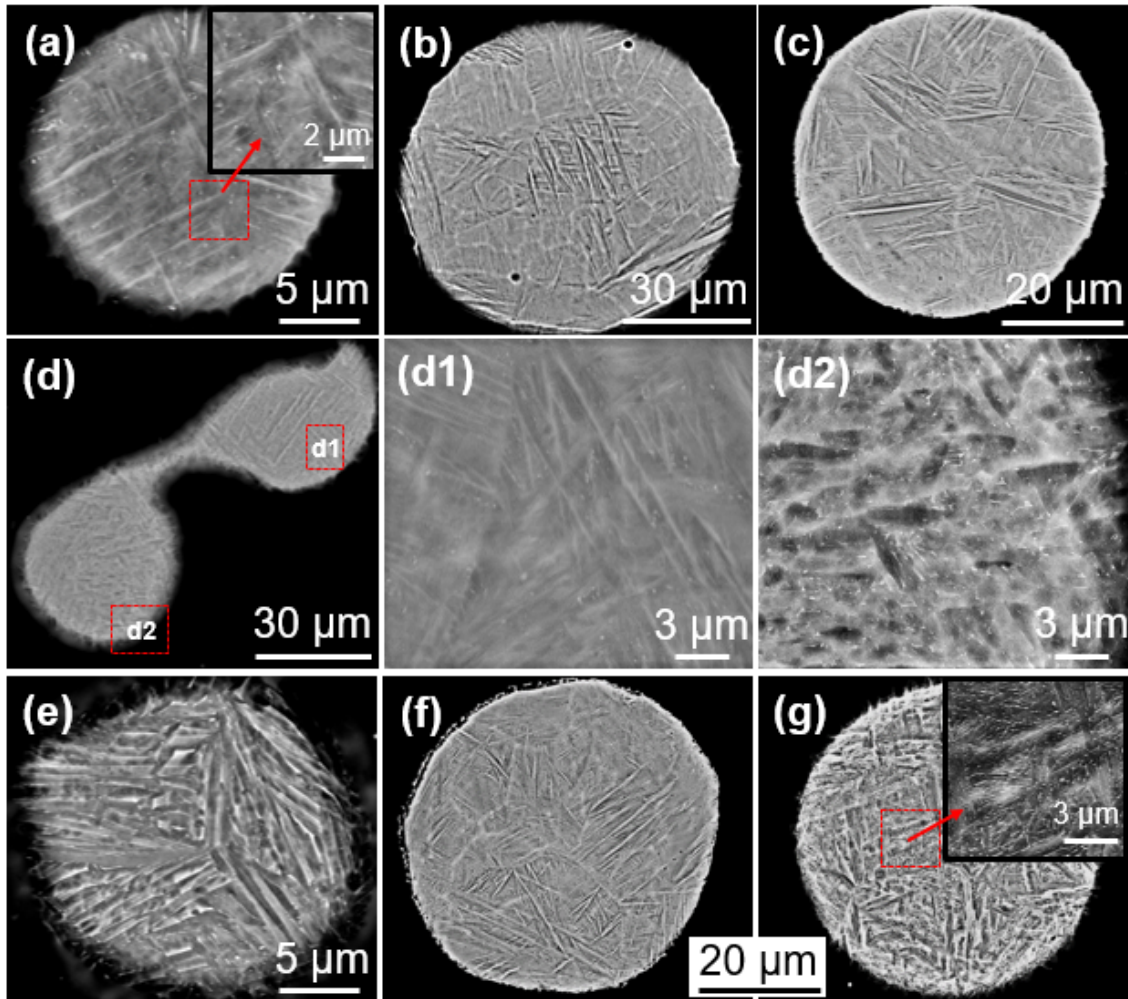
Figure 4.4 shows the optical and SEM images of virgin powder cross-section. It can be seen that the virgin powder consisted of entrapped gas porosity which is typical in the case of gas atomised powder. Furthermore, it can be seen qualitatively in Figure 4.4a that the coarser particles contained larger number of porosity than the relatively smaller particles. This similar to the observation reported in [100]. The sources of these porosity were reported to be inert gas entrapment during the atomisation process [103]. Powder porosity generally has a spherical morphology, possibly due to the high pressure inside the liquid droplet acting on the gas bubble.



**Figure 4.4** (a) Optical microscopy and (b) SEM BSE image of virgin powder cross-section revealing entrapped powder porosity.

Micrographs of the virgin, away-melt zone, near-melt zone and recycled powder microstructures are shown in Figure 4.5. In the virgin condition (Figure 4.5a and b), the powder particles predominantly consisted of  $\alpha'$  microstructure. However, the morphology of the  $\alpha'$  laths depended on the particle size due to differences in the cooling rate during atomisation. The fine particle (Figure 4.5a), comprised long  $\alpha'$  laths nucleated from particle edges and their growth continued until being interrupted by another  $\alpha'$  lath from a different nucleation site (the inset of Figure 4.5a). This is due to the larger surface-to-volume ratio leading to higher cooling rate. By comparison, the coarser particle (Figure 4.5b) consisted of a majority of  $\alpha'$  laths that were relatively short. This can be explained by the heterogeneous nucleation from several sites such as particle edges, material matrix and previously formed  $\alpha'$  laths. The presence of a few longer laths (Figure 4.5b) could be attributed to the complex thermal cycles experienced during atomisation. Similar microstructural features were observed in the away-melt zone powder (Figure 4.5c).

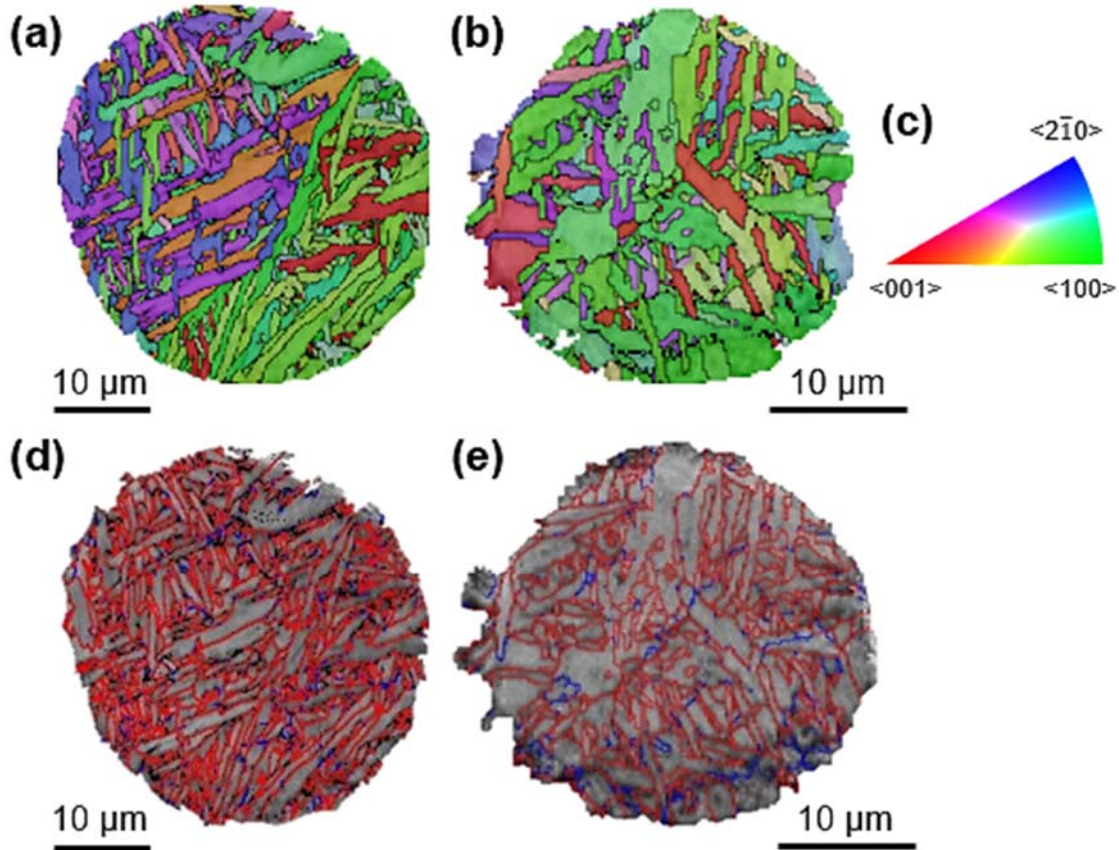
In the case of near-melt zone powder, the hard-sintered powder particle, Figure 4.5d, had a heterogeneous microstructure with  $\alpha'$  laths at one end (Figure 4.5d1) and coarser  $\alpha$  laths with semi-continuous  $\beta$  phase boundaries (bright regions) at the other (Figure 4.5d2). By comparison, the loose powder particle from the same region comprised  $\alpha+\beta$  microstructure (Figure 4.5e). The recycled powder contained particles with  $\alpha'$  laths (Figure 4.5f) and particles with semi-continuous  $\beta$  phase between  $\alpha$  laths (Figure 4.5g).



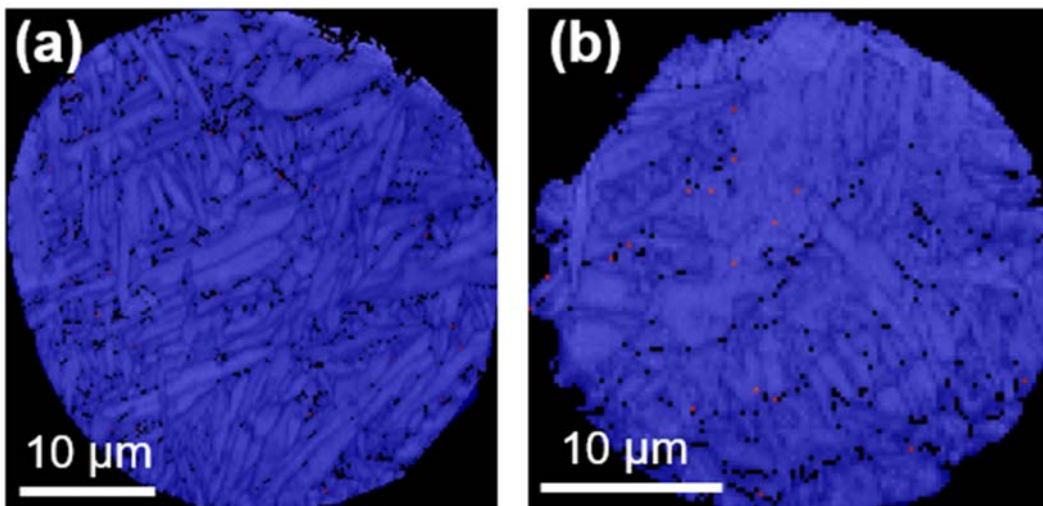
**Figure 4.5** SEM BSE image of EB-PBF Ti6Al4V (a and b) virgin, (c) away-melt zone, (d and e) near-melt zone and (f and g) recycled powder particle microstructure.

EBSD orientation maps were generated for virgin (Figure 4.6a) and near-melt zone (Figure 4.6b) powder particles based on the colour code in the inverse pole figure (IPF) (Figure 4.6c). The virgin powder particle consisted of randomly oriented  $\alpha'$  laths that were roughly 3 to 34  $\mu\text{m}$  in length. The  $\alpha'$  laths mainly nucleated from the particle edges and other  $\alpha'$  laths, supporting the SEM observations (Figure 4.5a and b). The near-melt zone powder particle, however, consisted of relatively thick  $\alpha$  laths, with the majority of  $\alpha$  laths oriented in the  $\langle 100 \rangle$  crystallographic direction. The HAGB (red lines,  $\theta > 15^\circ$ ) and LAGB (blue lines,  $1.5^\circ < \theta < 15^\circ$ ) overlaid on the band contrast map of the virgin (Figure 4.6d) and near-melt zone (Figure 4.6e) powder particle, show that the virgin powder particle had 19% LAGB and 81% HAGB while the near-melt zone powder particle contained 24% LAGB and 76% HAGB. The EBSD phase maps did not reveal any difference between the two powder particles (Figure 4.7). This could be due to the relatively large

step size of  $0.3 \mu\text{m}$  employed, considering the thickness of  $\beta$  phase in EB-PBF Ti6Al4V that was reported to be  $\sim 50 \text{ nm}$  [160].



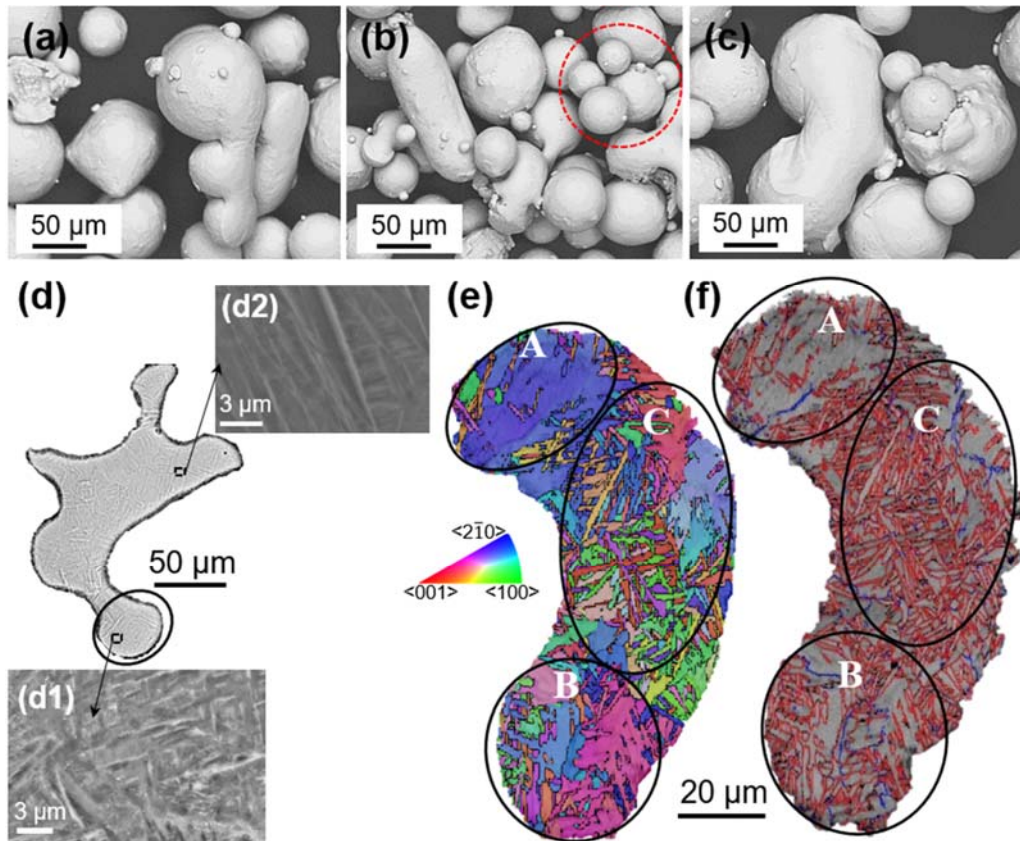
**Figure 4.6** Orientation maps of virgin (a) and near-melt zone (b) powder particles based on the IPF. (c) Band contrast map of the same virgin (d) and near-melt zone (e) powder particle with HAGB (red,  $\theta > 15^\circ$ ) and LAGB (blue,  $1.5^\circ < \theta < 15^\circ$ ).



**Figure 4.7** Phase maps of EB-PBF Ti6Al4V (a) virgin and (b) near-melt zone powder particles. Blue region- HCP; red region- BCC; black region- zero solutions.

#### 4.2.4 Sieve residue

Sieving was used to remove the undesired coarse particles (*i.e.* those larger than the mesh size of 150  $\mu\text{m}$ ) from entering into the subsequent builds and to maintain the PSD. The sieve residue powder consisted of severely process affected particles such as: (1) hard-sintered particles (Figure 4.8a), formed by excessive heat exposure; (2) soft-sintered particles (Figure 4.8b, red circle) that were not broken in the PRS; and (3) agglomerates caused by melt ejections falling back into the powder bed (Figure 4.8c).



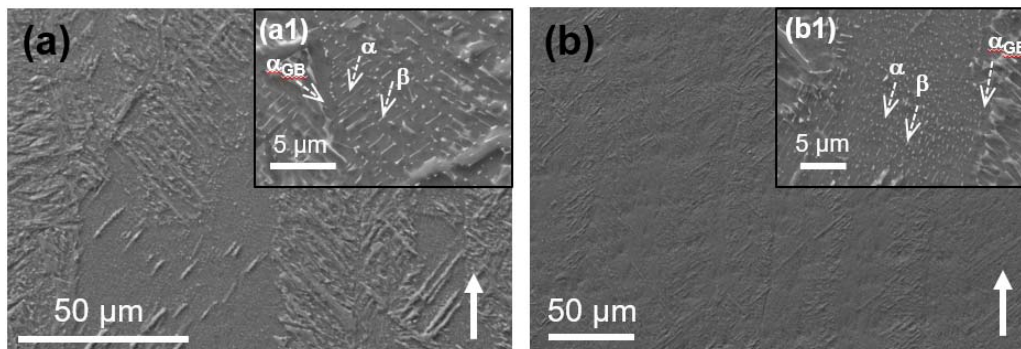
**Figure 4.8** Ti6Al4V EB-PBF sieve residue: SEM image of powder particles, (a) hard-sintered, (b) unbroken soft-sintered (red circle), and (c) agglomerated melt ejection; (d) the microstructure of a melt ejection that fell over a powder particle (indicated by the black circle); high magnification images of the (d1) powder particle and (d2) melt ejection regions; (e) orientation map with inset IPF and (f) band contrast map with HAGB (red) and LAGB (blue) of a melt ejection that fell over two powder particles.

Figure 4.8d shows the microstructure of a melt ejection that fell over a powder particle (indicated by the black circle) in the powder bed and solidified. The high magnification image (Figure 4.8d1) of the powder particle region shows the presence of  $\beta$  phase between  $\alpha$  laths while the melt ejection region has  $\alpha'$  laths with no  $\beta$  phase (Figure 4.8d2). EBSD data of a melt ejection which fell over two powder particles is

shown in Figure 4.8e and f. The selected particle for EBSD analysis appears to be similar to the particle shown in Figure 4.8c. It consists of three regions: two powder particle regions and one melt ejection region. The powder particle regions are designated as regions A and B while the melt ejection region corresponds to region C as indicated in the orientation (Figure 4.8e) and band contrast (Figure 4.8f) maps. Coarse  $\alpha$  laths mainly oriented in the  $\langle 2\bar{1}0 \rangle$  crystallographic direction was found in region A, while a few coarse  $\alpha$  laths with orientations one halfway between  $\langle 001 \rangle$  and  $\langle 2\bar{1}0 \rangle$  and another close to the  $\langle 2\bar{1}0 \rangle$  direction was found in region B. Region C corresponded to the melt ejection region that had a mixture of acicular and coarse  $\alpha$  laths with a size between 0.5- 2.0  $\mu\text{m}$  and 10-15  $\mu\text{m}$  respectively. No preferred orientation was found for the acicular  $\alpha$  laths, but the coarser  $\alpha$  laths had two preferred orientations of close to  $\langle 2\bar{1}0 \rangle$  and  $\langle 001 \rangle$ . The band contrast map with HAGB (red lines) and LAGB (blue lines) of each region in the particle is shown in Figure 4.8f. The melt ejection region with acicular  $\alpha$  laths had a slightly higher fraction of HAGB than the powder particle regions with coarse  $\alpha$  laths. Region A consisted of 24% LAGB and 76% HAGB, region B contained 22% LAGB and 78% HAGB and region C consisted of 15% LAGB and 85% HAGB.

### 4.3 Effects of recycling on build properties

Microstructure in the build direction of the virgin and recycled test coupons extracted from the same location are shown in Figure 4.9a and b. A typical EB-PBF Ti6Al4V microstructure can be seen; grain boundary  $\alpha$  ( $\alpha_{GB}$ ) and fine lamellar  $\alpha+\beta$  phases (inset of Figure 4.9a1 and b1). The width of the lamellar  $\alpha$  laths were measured as  $0.49 \pm 0.11 \mu\text{m}$  for the virgin and  $0.47 \pm 0.12 \mu\text{m}$  for the recycled test coupon.



**Figure 4.9** SEM SE image of (a) virgin and (b) recycled builds in build direction (note the difference in the scale bar length). Up-arrow indicates the build direction. The inset images show the presence of  $\alpha_{GB}$ ,  $\alpha$  and  $\beta$ .

Table 4.2 lists the tensile, Charpy impact, and Vickers hardness results of virgin and recycled EB-PBF test coupons together with as-cast Ti6Al4V material properties for comparison. The Vickers hardness values were the same for both the virgin and recycled builds. Similarly, the virgin and recycled builds had a similar value of Charpy impact energy. The tensile properties of both specimens were well above the minimum tensile property requirements mentioned in ASTM F3001. In addition, a marginal increase of 10 MPa in yield and tensile strength values of the recycled specimens was observed. However, the difference was marginal and therefore can also be regarded as an experimental scatter. Therefore, it can be said that there is no significant change in the tensile properties of the builds produced from virgin and recycled powder as also the EL% in both the specimens were similar.

**Table 4.2** Mechanical properties of virgin and recycled EB-PBF Ti6Al4V builds. ASTM F3001- minimum tensile properties of ELI Ti6Al4V specimen in X-Y direction (perpendicular to build direction) produced by powder bed fusion AM.

	Yield strength at 0.2% offset / MPa	Tensile strength / MPa	Elongation (EL) / %	Charpy impact energy/J	Vickers hardness / HV
Virgin	845 ± 0.5	918 ± 1	17 ± 1.05	47 ± 3.06	320 ± 7.57
Recycled	857 ± 1	928 ± 3.5	18 ± 0.68	45 ± 1.00	315 ± 5.20
ASTM F3001 (X-Y plane)	795 (minimum)	860 (minimum)	10 (minimum)	-	-
As-cast [161]	738±11	853±24	12±1	-	-

HCF results of virgin and recycled specimens tested normal to the build direction are shown in Figure 4.10. The average fatigue life was 121,384 ± 14,128 cycles for the virgin builds and 99,759 ± 8,287 cycles for the recycled builds. An example of the fatigue fracture surface from the specimens produced using virgin and recycled powder that failed at 101,773 and 90,419 cycles are shown in Figure 4.10b and e, respectively. For both cases, fatigue cracks initiated at a surface defect/pore (Figure 4.10d and g). The crack initiated from a lack-of-fusion defect in the recycled specimen, whereas it initiated from a spherical gas pore in the virgin test specimen. In addition, embedded pores were found in both specimens as shown in Figure 4.10c and f, with their equivalent diameter being coarser in the recycled (86 µm) than in the virgin specimen (26 µm). Although the

virgin specimen also contained larger embedded pores and larger lack-of-fusion defects like the recycled specimen (Figure 4.11), they were not located at the surface of the test specimens, hence being less detrimental to fatigue performance.

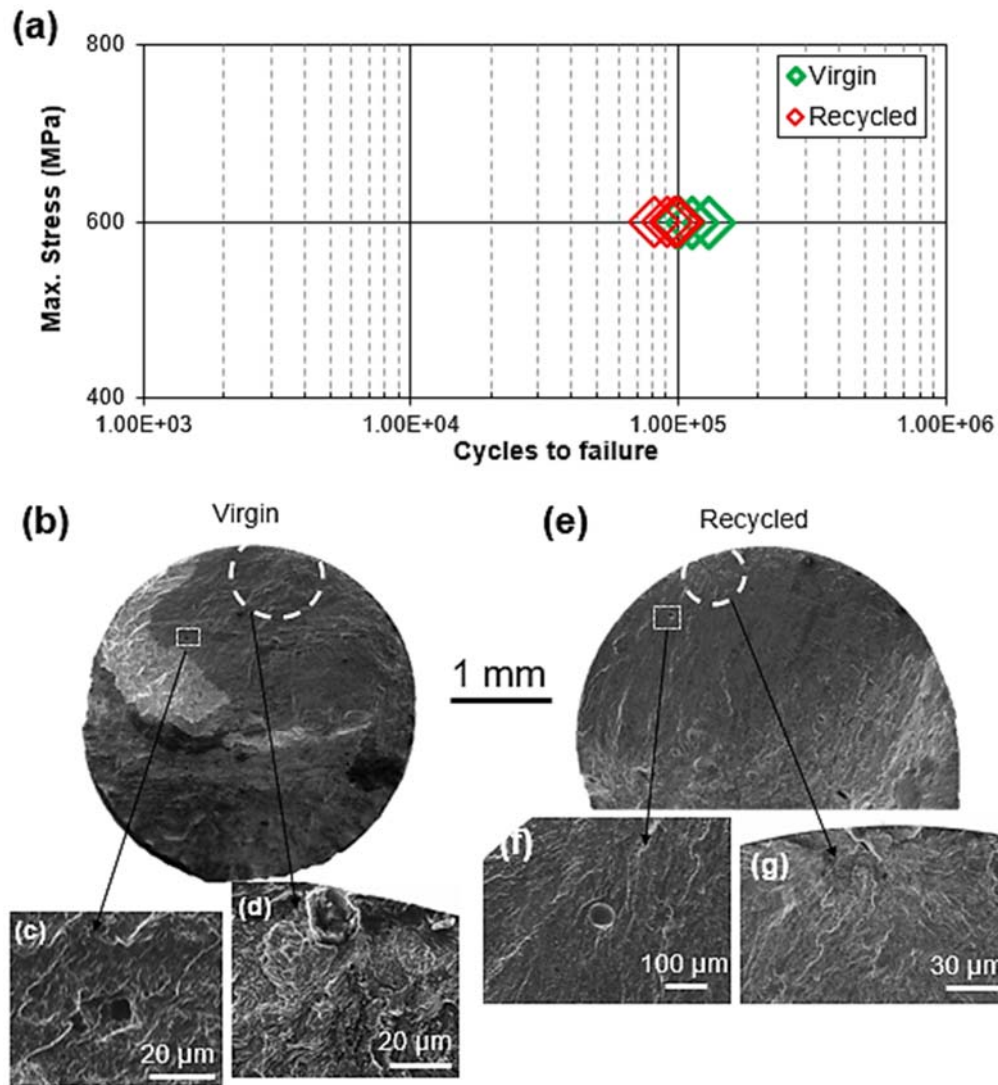


**Figure 4.10** Fatigue life and SEM images of example fracture surfaces of EB-PBF Ti6Al4V specimens produced from virgin and recycled powder: (a) HCF results, (b) macrograph of virgin specimen, (c) embedded small pores, (d) crack initiation from a surface pore; (e) macrograph of recycled specimen, (f) embedded large spherical pore, (g) crack initiation from a lack-of-fusion defect.

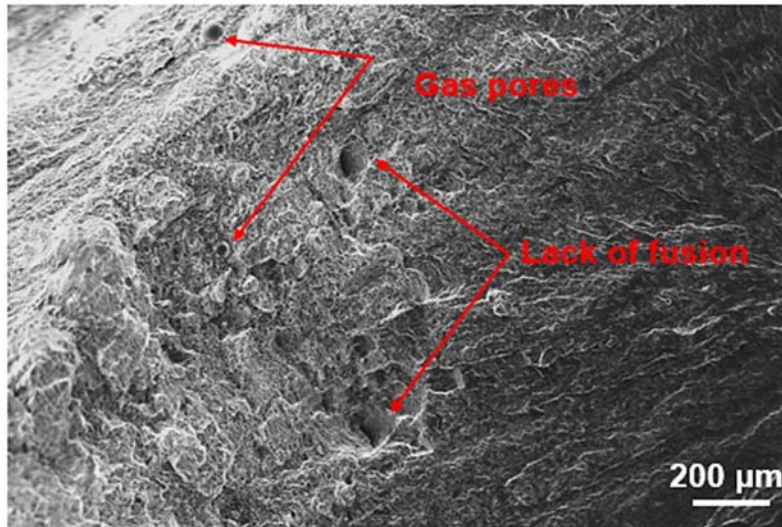


**Figure 4.11** Fatigue fracture surface of virgin EB-PBF Ti6Al4V specimen that failed after 114,111 cycles. Lack-of-fusion defects and gas pores embedded in the fracture surface are highlighted.

In order to quantify the pore size distribution, X-ray CT scanning was performed on virgin and recycled builds. Figure 4.12a and b show pores overlaid on volume rendered images of virgin and recycled specimens respectively with their corresponding equivalent diameters in the legend. The pores were randomly distributed in the samples, and their equivalent diameter ranged from 25 to 160  $\mu\text{m}$ . The volume and number fraction of the pores in virgin and recycled builds are shown in Figure 4.12c and d. Both samples had a similar defect size distribution, Figure 4.12c. The porosity plot (Figure 4.12d) shows that the recycled builds had a marginal increase in small pores (with an equivalent diameter of  $< 50 \mu\text{m}$ ). Meanwhile, there was a large increase (up to 50%) in large pores with an equivalent diameter from 50 to 160  $\mu\text{m}$  compared to the virgin specimens. The average sphericity plot (Figure 4.12e) shows that the pores were less spherical in the recycled specimen, especially for the large pores with sizes from 80 to 160  $\mu\text{m}$ . These irregular pores were likely to be lack-of-fusion defects. The SEM fractography (Figure 4.10e) of the recycled specimen shows that fatigue cracks initiated from lack-of-fusion defects with an equivalent diameter of 125  $\mu\text{m}$ . Therefore, the recycled specimens have a higher number/volume of lack-of-fusion defects/pores than that of the virgin specimens.

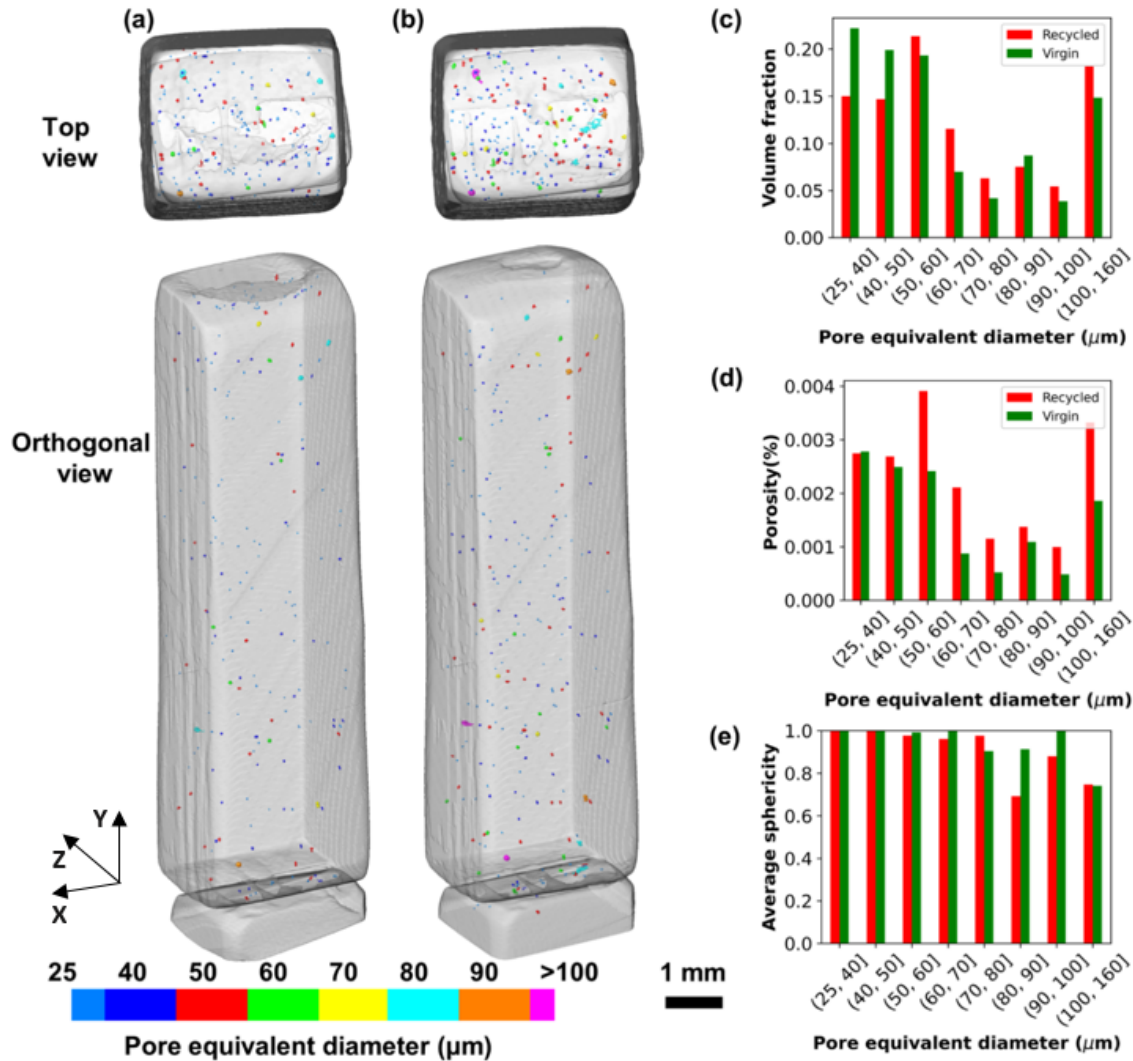


**Figure 4.12** Pore quantification in virgin and recycled Ti6Al4V test specimen using X-ray computed tomography. 3D rendered images of pores overlaid on (a) virgin and (b) recycled test specimens. Z axis corresponds to the build direction. Defect (c) volume fraction, (d) porosity percentage and (e) sphericity as a function of pore equivalent diameter.

## 4.4 Discussion

### 4.4.1 Evolution of powder characteristics

Compared to the virgin powder, the used powder showed significant changes in the O content, morphology, PSD and microstructure. Ti6Al4V alloy has a high affinity with oxygen [106]. During powder recovery and re-loading, the powder particles tend to absorb moisture on their surface upon exposure to humidity in the atmosphere, which then breaks down into oxygen inside the EB-PBF machine chamber due to high temperature processing conditions. Since the alloy is highly oxidising at high

temperatures (above 600°C), the dissociated oxygen can be picked up by the powder particles [4,128]. Therefore, an increase in the O content was observed in the recycled powder as shown in Table 4.1. Furthermore, due to the temperature gradient in the powder bed, the rate of powder oxidation varies at different areas in the powder bed. Powder particles at a higher temperature can oxidise more than particles at lower temperature in a given time [162]. Therefore, powder particles located closer to the melting area (near-melt zone), which gets exposed to both the preheat scans (preheat 1 and preheat 2) and latent heat from the melt pool exhibited a relatively higher O content than the away-melt zone particles. In addition, some fractions of light alloying elements like Al have also vaporised (Table 4.1) as the near-melt zone region was exposed to high temperature causing local powder particle melting (Figure 4.2). Nevertheless, the Al, V and O contents of all the powder samples stayed within the limit as specified in ASTM F3001.

Powder morphology and PSD play a vital role in determining the part density and surface roughness [95]. The virgin powder feedstock used in this study consisted of a significant number of fines, satellites and agglomerates, which are inherent features of the AGA powder [122], (Figure 4.1a-c, Figure 4.3b and c). After completion of each build cycle, the sintered powder bed was broken and recovered in the ARCAM PRS chamber using high velocity compressed air. This resulted in the formation of craters (shallow depressions) and concave sites (deeper depression) on the recycled powder surfaces (Figure 4.1e and f). It is speculated that the craters could be attributed to particle collisions and de-bonding of some strongly sintered particles as a result of multiple preheat scans. The concave sites could have been caused by the detachment of some satellite particles that had a weaker bond between the fine and coarse regions. Supporting evidence can be found from the quantitative shape analysis of the recycled powder (Figure 4.3b), which showed a significant reduction in the number of satellite particles. Therefore, the detached fine particles from satellites and other loose fine particles present in the virgin powder could have been blown-off by the compressed air flow to the powder collecting jug in PRS chamber. Hence a ~30% reduction in the number of fine particles and a marginal inward shift of the recycled powder PSD curve were observed (Figure 4.3b and c). The PSD curve shift appears to be marginal because the volume of a fine particle is low.

The formation of craters in the recycled powder would be unfavourable for a powder produced by plasma-based process, as they normally have higher sphericity in the as-manufactured condition [100]. However, in the case of AGA powder, the detachment of fine particles has increased powder sphericity (Figure 4.3b). In addition, the elimination of some fine particles with recycling has improved powder flowability by 4%, as fine particles have high surface energy and therefore are more cohesive [111]. Normally, a reduction in the number of fine particles tends to decrease the packing density of the powder bed, as the fine particles can fill the voids between the coarser particles [163]. On the contrary, there was only a marginal improvement in the packing density (2%). This could be due to the reduction in the number of satellite particles and improvement in powder sphericity which might have allowed the recycled powder to pack better.

The powder particles near the melt pool suffer maximum morphological degradation as shown in Figure 4.2a and b and Figure 4.3b and d. It is noteworthy that all the powder samples were sieved with 150  $\mu\text{m}$  sieve before PSD measurement but some of the high aspect ratio particles (hard-sintered) managed to pass through the sieves, resulting in a coarser PSD and a marginal shift at the coarser side of the recycled powder PSD curve, see the insets of Figure 4.3c and d. The other severely sintered particles and agglomerates were eliminated during sieving (Figure 4.8a and c). The minimal increase in the recycled powder flow, considering the significant increase in powder sphericity and reduction in the number of fine particles, could also be attributed to the presence of non-spherical high aspect ratio particles in the recycled powder. The away-melt zone powder which constitutes the majority of the recycled powder was only soft-sintered (Figure 4.2c). Therefore, it was easily broken in the PRS process and the unbroken soft-sintered particles were removed during sieving (Figure 4.8b, red circle). Hence, their PSD curve appeared similar to that of the virgin powder. It is noteworthy that the number of fine and satellite particles in the near-melt zone region is higher than the recycled powder (Figure 4.3b, c and d). This is because the samples collected from these regions were directly sieved without being taken to the PRS chamber as the sample volume was less. This further confirms that the loose fine particles and the fine particles detached from the satellite particles are removed from the subsequent builds by the air flow in the PRS chamber during recycling, as also confirmed by Tang *et al.* [50].

The degree of microstructural change in a powder particle with reference to the initial powder provides a clear indication of the changes in powder properties that occurred during the EB-PBF manufacturing process. In addition, studying powder microstructure can be useful to interrogate the thermal histories and the corresponding O pick-up at different regions in the powder bed. The difference in powder O content has a major impact on the part properties [5,69,164]. To further investigate the microstructural changes, as the lamellar structures seen in Figure 4.5 are not clearly distinguishable, detailed investigation of the powder cross-section was performed by EBSD analysis (Figure 4.6).

The virgin powder particles consist of  $\alpha'$  laths formed due to rapid cooling during the atomisation process. In the used powder, due to the high-temperature processing and temperature gradient in the powder bed, leading to complex thermal history in the powder particles during melting and repeated preheat scans, the particles at different regions of the powder bed are at different stages of  $\alpha' \rightarrow \alpha + \beta$  transformation. Although most of the powder particles retained their initial martensitic microstructure, some of them consisted of non-continuous  $\beta$  phase on the lamellar boundaries of coarse  $\alpha$  laths (Figure 4.5).

Any changes in the microstructure of the away-melt zone powder would have been caused by preheat 1 scan, which was applied to the entire build area. Given that the preheat 1 scan involves the electron beam scanning the bed with a series of parallel lines, it is possible that some of the powder particles which were in the vicinity of the preheat 1 scan lines might have experienced high local temperatures, that were greater than the  $\beta$ -transus temperature and underwent certain level of  $\alpha' \rightarrow \alpha + \beta$  transformation without reaching the melting point ( $\sim 1650^\circ\text{C}$ ) [165]. On the other hand, it is likely that the temperature at the away-melt zone region would be lower by  $\sim 70^\circ\text{C}$  of the set preheat temperature [166]. Nevertheless, since the analysed powder particles revealed no significant microstructural transformations, it is deduced that most of the powder particles that were away from the melting region were less affected by the EB-PBF processing conditions.

Due to the prolonged exposure of the near-melt zone powder particles to the heat from the melt pool and multiple preheat scans, significant changes were observed in their microstructure as illustrated in Figure 4.5d-e, and Figure 4.6b and e. Holding the material at high temperatures close to  $\beta$ -transus followed by slow cooling can lead to  $\alpha' \rightarrow \alpha + \beta$

transformation, due to dissociation of  $\beta$ -stabilizing elements such as vanadium rich elements from  $\alpha$  phase to their lamellar boundaries, forming  $\beta$  phase [167]. This dissociation is generally followed by the coarsening of  $\alpha$  laths in Ti6Al4V powders [106], which explains the formation of coarse  $\alpha$  laths in Figure 4.5d2, e and g. However, the transformed microstructure could be inhomogeneous like that shown in Figure 4.5d, where one region had  $\beta$  phase between the  $\alpha$  laths while the other had only  $\alpha'$  microstructure. This could be attributed either to partial exposure of the particle to the heat, or heat dissipation from the particle to the surrounding.

The recycled powder (Figure 4.5f and g) includes powder particles from both the near-melt zone and away-melt zone regions. Therefore, the recycled powder microstructure consists of particles with both  $\alpha'$  and particles with coarse  $\alpha$  laths that are at different stages of  $\alpha' \rightarrow \alpha + \beta$  phase transformation.

Montelione *et al.* [168] have shown that the powder particles with a coarser microstructure had thicker oxide layers, supporting that the near-melt zone powder, that consists of coarser microstructure (Figure 4.5 and Figure 4.6), had higher O content (Table 4.1). However, no intermetallic (Ti<sub>3</sub>Al) precipitates were found in any of the powder particles investigated. This is as expected because the O content needs to exceed  $\sim 0.35$  wt.% to trigger such phase transformation [29]. Hence, it is likely that no excessive local powder oxidation occurred due to high local temperatures caused by the temperature gradient during preheating and melting.

Investigation of the sieve residue provides a better understanding of powder degradation, as it contains the severely process affected particles that provide great potential for correlation between powder property changes to EB-PBF recycling methods: for example, hard sintered particles found in the near-melt zone due to high temperatures, unbroken soft-sintered particles found in the away-melt zone region, and melt ejections (Figure 4.8). Unlike laser additive manufacturing, melt ejections are seldom observed in electron beam additive manufacturing. Melt ejection in EB-PBF process can occur owing to the turbulence formed in the melt pool due to the interaction of various forces such as vapour pressure, beam to powder bed/substrate inconsistencies and charge interactions [169]. On the other hand, appearance of melt ejections indicates that the standard ARCAM process settings might need to be adjusted when using AGA powders.

Morphology and microstructure analysis of the melt ejections present in the sieve residue was performed (Figure 4.8). The melt ejection that exited the melt pool during fabrication, fell back into the powder bed and formed powder agglomerations (Figure 4.8c). As most of these agglomerates were relatively coarse (a few mm in size), they were removed by sieving. However, it is possible that ejection of certain volume of melt pool in the form of spatter, could lead to increased defects in the build parts. Anwar *et al.* [91] have reported that the distribution of ejections is higher at the near-melt zone region of the powder bed in the LB-PBF process. Since the EB-PBF process is performed in vacuum and there is no gas flow through the chamber during manufacturing as in the LB-PBF, it is speculated that these melt ejections were present in the near-melt zone region of the powder bed.

Microstructure and EBSD analysis performed on a melt ejection that fell over two powder particles revealed heterogeneity in phases and  $\alpha$  lath morphologies. The powder particle regions had coarse  $\alpha$  laths with reduced local misorientations (Figure 4.8d1, e, f). This might be due to the annealing effect associated with the heat transfer either from the deposited melt ejection to the powder particle regions or from the melt pool over that particular region. The melt ejection region (region C) had a high fraction of  $\alpha'$  laths and high local misorientations, which could be due to rapid cooling during of the melt ejection during the flight before falling into the powder bed. However, some parts of the melt ejection region had coarser  $\alpha$  laths that could have been caused by high temperature in the powder bed that resulted in slow cooling or the heat from the melt pool on that region of the melt ejection.

Therefore, the present study shows that Ti6Al4V powder microstructural changes do occur and depend on the location of the powder particles in the powder bed. However, it should be noted that the quantity of heat-affected powder particles that possess deformed powder morphology, transformed microstructure and high O level increases with the number of recycling iterations and when large build volume is utilised for processing. As the current study analysed only one particle in each condition, further statistical analysis is required to correlate the change in powder microstructure to chemical composition.

#### 4.4.2 Evolution of build properties

Test specimens were extracted in the same orientation (horizontal) from both the virgin and recycled test coupons to eliminate the effect of anisotropy. No obvious difference was

found in the microstructure (Figure 4.9) and the hardness values. Similarly, no reduction in Charpy impact values was observed in the recycled specimen.

The effects of EB-PBF powder recycling on the tensile properties of Ti6Al4V have been widely reported in several studies [23,50,170]. Most commonly reported phenomena were the increase in yield and tensile strength of the specimen with recycling. In the present work, no significant changes in the yield and tensile strength were observed with recycling (Table 4.2). Generally, an increase in the O content of Ti6Al4V material leads to an increase in material strength at the expense of ductility, as explained in Section 2.3.4. This is because oxygen in Ti6Al4V acts as  $\alpha$ -stabiliser [29] and provides strength by creating a solid-solution in the  $\alpha$  phase [5,34]. It occupies octahedral sites creating lattice strain in the  $c$  direction of the HCP structure and thereby affecting the interactions between dislocations [171]. Therefore, along with an increasing strength, a decrease in material elongation at high O content has been reported in some studies [23,172]. However, in the present work, the increase in O level was marginal (0.02 wt.%) and the total O content was well below the maximum O limit (0.13 wt.%) in contrast to the work by others, where the material O content exceeded 0.2 wt.% (which is the Ti6Al4V grade 5 O wt.% max.). Therefore, negligible impact was observed on the material tensile properties. However, with increased number of powder reuse, when the powder O content increases further, it is expected that the material yield and tensile strength would increase while the elongation will start to decline gradually.

The HCF testing on the virgin and recycled test specimens (Figure 4.10a) exhibited certain level of scatter due to the presence of pores of varied size and morphology. Only a marginal decrease in the average fatigue life occurred with recycling and hence could be considered as an experimental scatter. Therefore, it can be said that the fatigue life has not significantly changed with powder recycling. All the specimens in both the virgin and recycled conditions failed from surface pores/defects. In terms of pores/defect sizes, the fracture surface and XCT scan results show pore sizes of 25 to 160  $\mu\text{m}$  in both the virgin and recycled test specimens. This observation aligns with the previous work [136,144] where the increased number of large-sized pores were found with the powder reuse in LB-PBF process. Furthermore, with respect to defect morphology, a relatively larger fraction of lack-of-fusion defects were present in the recycled specimens (Figure 4.12c-e). Lack-of-fusion defects are more detrimental than spherical gas porosity [173]. Therefore, two out of four recycled specimens, which had the lowest fatigue life, failed

from the lack-of-fusion defects (Figure 4.10e), which reduced the average fatigue life of the recycled specimens marginally. However, the other two recycled specimens which failed from spherical defects had similar fatigue life as the virgin builds.

Therefore, although repetitive PRS treatment can improve powder sphericity and could provide better spreadability of a used powder during the build process, the presence of some heat-affected particles with high aspect ratio, coupled with reduction in the number of fine particles, can create more voids in a powder layer. This very likely promoted the higher fraction of lack-of-fusion defects as observed in the recycled test specimens. However, in the current study the number of lack-of-fusion defects were not significant enough to cause a steep decline in the fatigue life of the recycled builds. However, with increased number of powder reuse, it is expected that the fatigue life of the recycled specimens will start to decline due to increase in the volume fraction of lack-of fusion defects.

The current study provided fundamental insights into the different types of changes in individual powder particle properties, the related mechanisms which influence bulk powder behaviour and affect the build quality. However, there are some limitations worth commenting on. The current study employed a simulated method to recycle powder involving preheats alone. Although it was effective in demonstrating the effect of preheat cycles on powder properties, some of the effects of repetitive melting and post-heating were not accounted for. Therefore, it is expected that in the actual powder recycling process, the magnitude of changes in powder and build properties may be higher, depending on the number of reuse times, build volume, process parameters *etc.*

## 4.5 Chapter conclusions

The changes in powder physical and chemical properties during manufacturing and handling in electron-beam powder bed fusion process and its subsequent impact on Ti6Al4V build properties were investigated. The following conclusions can be drawn:

- (i) Powder particles at the near-melt zone region suffer maximum degradation. Results revealed powder morphological degradation such as hard-sintering, partial melting and agglomerations. The hard-sintered high aspect ratio particles managed to pass through the sieves affecting the recycled powder quality. Other powder physical property changes included larger particle size distribution,  $\alpha$  lath

coarsening and  $\beta$  precipitation. The near-melt zone powder particles had higher oxidation rate than the particles in the away-melt zone region.

- (ii) Powder particles at the away-melt zone region are soft-sintered due to powder bed preheating. A slight increase in O content with no change in microstructure was observed. The soft-sintered particles can be broken down and recycled.
- (iii) Virgin vs recycled powder: The recycled powder had better sphericity, improved flow and packing behaviour. The virgin powder had  $\alpha'$  microstructure while recycled powder had particles with  $\alpha'$  and particles being subjected to different stages of  $\alpha' \rightarrow \alpha + \beta$  microstructural transformation. O content in the recycled powder was found to be 25% higher than virgin powder.
- (iv) Virgin vs recycled build: There was no significant difference in the microstructure, Charpy impact energy, hardness, and tensile properties. The recycled builds consisted of relatively higher proportion of lack-of-fusion defects than the virgin builds. This is possibly because of the voids formed in the powder bed due to the coupled effect of reduced number of fines and presence of high aspect ratio powder particles in the used powder.
- (v) The increase in the volume fraction of lack-of-fusion defects after 10 times of simulated powder reuse was not significant enough to affect the fatigue life of the recycled builds.

\*\*\*\*\*

## 5 Response of virgin and recycled EB-PBF builds to post-thermal treatment

### 5.1 Introduction

The previous chapter concluded that the recycled builds had slightly higher fraction of lack-of-fusion defects with reference to the virgin condition. The objective of this Chapter is to evaluate the effect of post-thermal treatment on the mechanical and microstructural properties of the builds produced from recycled powder. Thereby, addressing Objective 3 laid out in Chapter 1.

Post-thermal treatment such as hot isostatic pressing has been realised as an attractive option to shrink the defects/pores in AM parts [103]. HIPed AM parts are widely used in aerospace applications. During HIPing, the yield strength of the material drops at high temperatures, the application of pressure results in high diffusion rates and plastic flow of the material helps to close voids or microcracks [174]. HIPing, has been reported to improve the ductility and fatigue properties of EB-PBF Ti6Al4V parts [139,175]. However, Hrabe *et al.* [141] and Zhao *et al.* [55] reported some reduction in strength of EB-PBF Ti6Al4V material due to coarsening of the  $\alpha$  laths after HIPing.

In Ti6Al4V powder recyclability studies, to the best of the author's knowledge, only Popov *et al.* [23] explored the effects post-thermal treatment on the recycled build properties. The authors found that in the HIPed-condition, the strength of the recycled builds dropped and high cycle fatigue life increased close to that of the as-built virgin part. Currently, no data is available in the open literature on the performance of Ti6Al4V EB-PBF recycled parts to post thermal treatments other than HIPing.

Therefore, there is a need to explore additional thermal treatment processes in line with HIPing to improve or retain the material strength. Formanoir *et al.* [171] investigated the evolution of EB-PBF Ti6Al4V microstructure after thermal treatment at subtransus and supertransus temperatures. It has been reported that the subtransus thermal treatment with furnace cooling caused marginal changes in the microstructure, like change in the thickness of the  $\alpha$  laths, while supertransus thermal treatment with similar furnace cooling led to a significant increase in  $\beta$  grain size up to  $\sim 1$  mm. Raghavan *et al.* [152] compared the hardness values of EB-PBF Ti6Al4V in subtransus heat treated condition with different holding times. It was found that the thickness of the

$\alpha$  laths increased with increasing holding time, which subsequently decreased material hardness. However, the effect of HIPing was not explored in conjunction with these thermal treatments. Therefore, it is essential to develop a heat treatment method to improve or retain the mechanical properties of HIPed EB-PBF Ti6Al4V without drastically modifying the microstructure of the material.

In this work, a standard thermal treatment practice followed on wrought Ti6Al4V material to improve material strength (solution treatment and ageing process), which has been reported to improve the strength of the material while maintaining its ductility [176], was used on both virgin and recycled EB-PBF Ti6Al4V parts after HIPing. The effect of post-thermal treatment on the microstructure and mechanical properties of the recycled parts with reference to the virgin part properties have been investigated. The data output from this basic investigation can be used as a platform to conduct further novel heat treatment practices on HIPed EB-PBF parts produced from recycled powder.

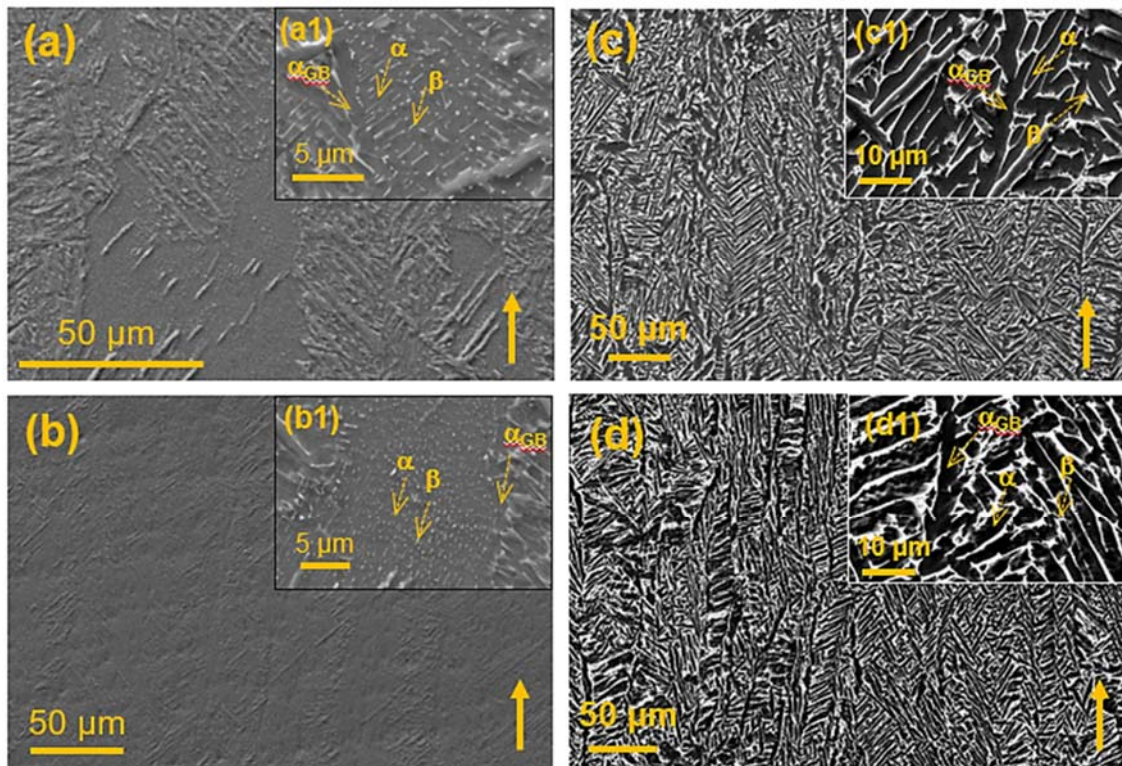
---

---

Some parts of this chapter has been published as a research article entitled, '*Effect of post-processing thermal treatments on electron-beam powder bed-fused Ti6Al4V*', Material Design & Processing Communications, 3(4):e168, Soundarapandiyan *et al.* 2020.

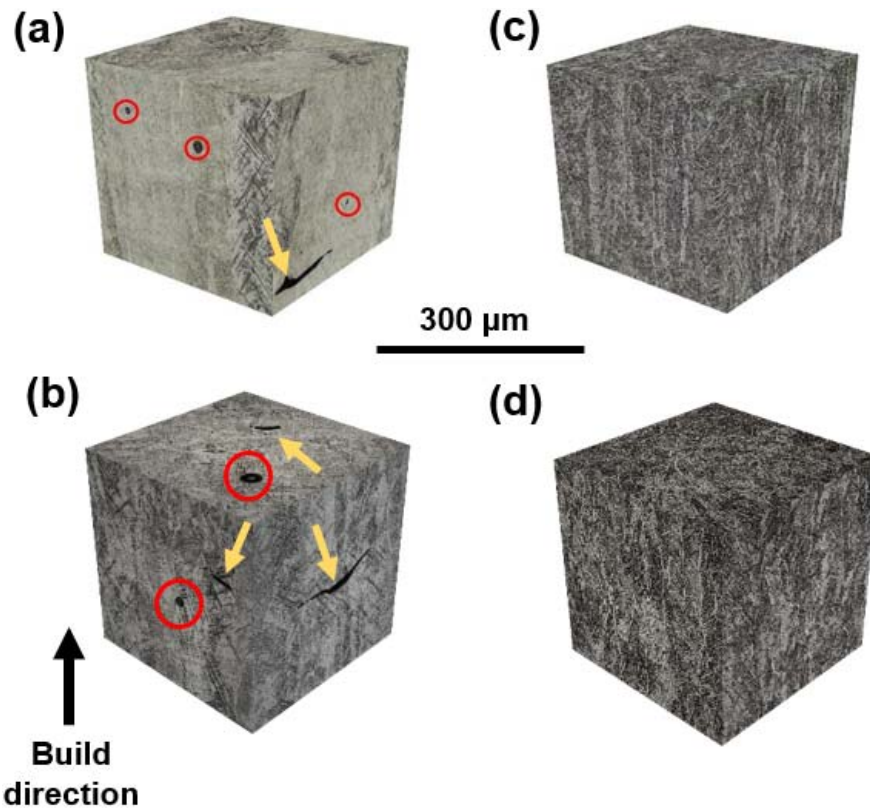
## 5.2 Effects of post-thermal treatment on the virgin and recycled build microstructure and defects

Figure 5.1a and b shows the microstructure of Ti6Al4V EB-PBF builds in the virgin and recycled as-built conditions respectively. As can be seen, no difference in the microstructural features were evident between the two as-built conditions. Both the builds consisted of typical EB-PBF Ti6Al4V microstructure. Figure 5.1c and d shows the microstructure of the virgin and recycled builds after post-thermal treatment respectively. It can be seen that significant coarsening of the  $\alpha$  laths have occurred in both the builds. The average thickness of the lamellae  $\alpha$  was  $2.9 \pm 0.5 \mu\text{m}$  for the virgin and  $3.1 \pm 0.3 \mu\text{m}$  for the recycled builds after post-thermal treatment. The microstructural changes ( $\alpha$  laths coarsening) of the recycled builds were the same as the virgin builds which accords with the observations reported by Popov *et al.* [23] after HIP-only treatment. Therefore, the subtransus heat treatment did not significantly alter the microstructural features present in the as-built conditions of the virgin and recycled builds.



**Figure 5.1** SEM micrograph of Ti6Al4V EB-PBF builds in SE mode: virgin specimen (a) as-built and (c) post-thermally treated condition; recycled specimen (b) as-built and (d) post-thermally treated condition (note the difference in the scale bar length).

Figure 5.2 shows the optical micrographs of the build and transverse direction of the virgin and recycled builds in the as-built and post-thermally treated condition. It can be seen that both the virgin and recycled builds in the as-built condition contains spherical (red circle) and irregularly shaped defects/pores (red arrow). The spherical pores attribute to the gas entrapments present in the powder particles [100]. These gas pores are generally  $<100\ \mu\text{m}$  in size while the irregular shaped pores are usually larger in size (several microns to a few millimetres). These could have formed due to lack-of-fusion between build layers and powder particles caused by insufficient energy density input [139]. After post-thermal treatment, in both the virgin and the recycled conditions, no pores/defects were detected. Therefore, HIP treatment seems to successfully reduced the size of the defects/pores present in the as-built virgin and recycled material below the resolution limit of the optical microscope.



**Figure 5.2** Optical micrograph of Ti6Al4V EB-PBF virgin build (a) as-built and (c) post-thermally treated condition; recycled build (b) as-built and (d) post-thermally treated condition. Red circles highlight spherical gas pores while yellow arrows point lack-of-fusion defects.

### 5.3 Effects of post-thermal treatment on the virgin and recycled build Mechanical properties

Table 5.1 summarises the static mechanical properties of the virgin and the recycled builds in the as-built and post-thermally treated condition. As can be seen, the Charpy impact energy values of both the virgin and recycled builds increased significantly after post-thermal treatment. Impact toughness is a crucial mechanical property which represents the energy absorbing capacity of the material before fracture when it is subjected to sudden loading condition. In the case of the aerospace, impact threats include bird strike, debris from runway, hail *etc.* exist. Therefore, the structural components of the aircraft should have high impact resistance. Current study shows that in the as-built condition, the failure mechanism was dominated by the defects/pores present in the build. As HIPing led to the closure of defects/pores present in the as-built material, the Charpy impact energy improved from 47 to 71 J in the virgin builds and from 45 to 64 J in the recycled builds. Furthermore, the virgin builds showed marginally higher Charpy impact energy values compared to the recycled builds after post-thermal treatment. The difference in the Charpy impact energy values between the virgin and recycled builds can be attributed to the difference in the O content in the builds. This is similar to the observations reported by Zhang *et al.* [158] in WAAM Ti6Al4V, where the fracture toughness of the material decreased with increase in the O content. Also, in EB-PBF Ti6Al4V builds, Grell *et al.* [155] demonstrated that the Charpy impact energy values of the material decreased with increasing O content in both the as-built and HIPed condition. Therefore, in the current study, the virgin builds with lower O content (0.08 wt.%) showed better impact toughness properties than the recycled builds (0.10 wt.%) after post-thermal treatment. Therefore, in applications demanding better impact resistance the EB-PBF Ti6Al4V material containing low O content in the HIPed condition can be employed.

A marginal decrease in the hardness values of both the Ti6Al4V virgin and recycled builds can be seen after post-thermal treatment. This could be attributed to the increase in the thickness of the  $\alpha$  laths which decreased the hardness values from 320 to 291 Hv in the virgin builds and from 315 to 300 Hv in the recycled builds as a result of slow cooling during HIPing. Similar phenomena of decrease in Ti6Al4V EB-PBF material hardness with increase in the  $\alpha$  lath thickness have been reported in [177,178]. However,

no discernible difference in the hardness properties between the virgin and recycled builds were observed in both the as-built and post-thermally treated conditions.

The yield strength and tensile strength after post-thermal treatment have decreased from 845 to 762 MPa and 917 to 857 MPa, respectively in the virgin builds, while the yield strength decreased from 857 to 780 MPa and the tensile strength decreased from 928 to 874 MPa in the recycled builds. The tensile stress-strain curves of each test specimen tested in each condition is shown in Figure 5.3. Greitemeier *et al.* [179] showed that the yield strength and the tensile strength values of the Ti6Al4V EB-PBF material decreased by 94 and 76 MPa, respectively, after HIPing. Although HIPing closed the pores, it also caused coarsening of  $\alpha$  laths, which due to the Hall-Petch effect, reduced the material strength. One of the limitations of the present study is that both the virgin and recycled builds were not tested in the HIP-only condition. Therefore, the effect of each post-thermal treatment could not be investigated separately. However, several studies conducted in the past few years explored as-built vs HIPed EB-PBF Ti6Al4V [139,141]. The tensile results obtained in this study are similar to the reports made from previous studies, *i.e.* HIP-only condition, such as decrease in yield and tensile strength, occurred in both the virgin and recycled builds.

Generally, when STA treatment was performed on wrought Ti6Al4V, the material strength increased. However, in this study, STA treatment failed to retain or improve the strength of the HIPed EB-PBF Ti6Al4V. This could be attributed to the relatively low interstitial oxygen content in both the builds. The effectiveness of the STA treatment is a function of heat treatment parameters and chemical composition of the alloy [176]. The virgin and recycled builds had only 0.08 wt% and 0.10 wt.% of oxygen respectively. As already mentioned, oxygen is an interstitial element and acts as an  $\alpha$  stabiliser and provides strength to the material by solid solution strengthening (SSS) (below the solubility limit). The presence of interstitial oxygen can affect the interactions between dislocations, which in turn can affect the material tensile behaviour [4]. Sufficient oxygen atoms are essential in the material to promote precipitation during the ageing process [1,176]. Since the material used in this work had low oxygen content, efficient precipitation was not created, and therefore, the STA treatment was not effective to retain the yield and tensile strength of the material. Increase in the O content of Ti6Al4V material causes degradation in material ductility [1]. Since the O content increased only slightly, the elongation of both the virgin and oxidised builds was retained after STA

treatment. Overall, the recycled builds showed better tensile properties than the virgin builds in both the as-built and post-thermally treated condition. Similar observations have been reported in Ti6Al4V recycled EB-PBF builds in HIP-only condition in [23].

**Table 5.1** Static mechanical properties of Ti6Al4V EB-PBF virgin and recycled material in the as-built and post-thermally treated condition.

	Yield strength at 0.2% offset (MPa)	Tensile strength (MPa)	Elongation (EL) [%]	Hardness (HV)	Charpy impact (J)
Virgin as-built	845	918	17	320 ( $\pm 7$ )	47 ( $\pm 3$ )
Recycled as-built	857	928	18	315 ( $\pm 5$ )	45 ( $\pm 1$ )
Virgin post-thermally treated	762	858	18	291 ( $\pm 8$ )	71 ( $\pm 5$ )
Recycled post-thermally treated	780	874	17	300 ( $\pm 9$ )	64 ( $\pm 4$ )

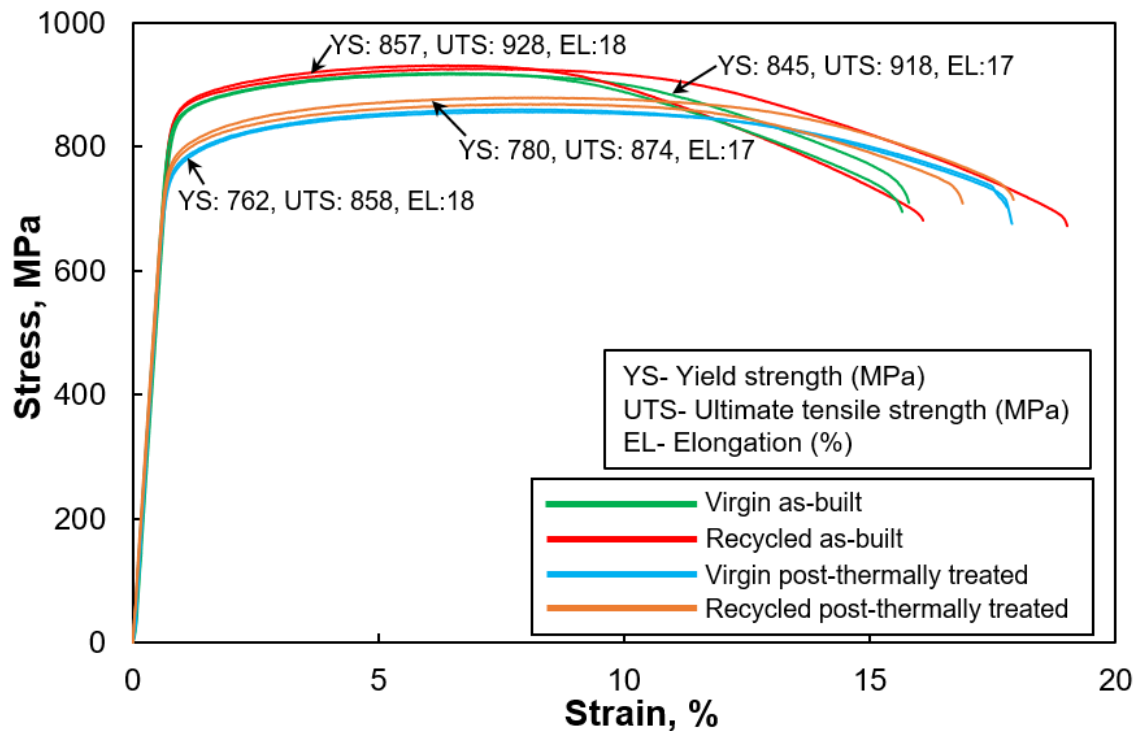


**Figure 5.3** Stress-strain plot of the virgin and recycled EB-PBF Ti6Al4V specimens in the as-built and post-thermally treated condition

As shown in Figure 5.4a, HCF tests performed on polished as-built virgin and recycled specimens found that the mean fatigue life was around  $10^5$  cycles, whereas the fatigue life of the post-thermally treated virgin and recycled builds improved drastically

to  $10^7$  cycles. This significant improvement in fatigue life of both the builds is likely to be attributed to the shrinkage or closure of defects/pores during HIPing. This is evident in the fatigue fracture surface shown in Figure 5.4b-e. In the as-built condition, the fatigue crack initiated from surface defects. However, after post-thermal treatments, since the material surface is free from defects/pores, the cracks initiated from the material microstructure in both the virgin and recycled builds.

In addition, it can be seen that the average HCF life of the recycled builds (11,438,516 cycles) were slightly higher than the virgin builds (9,442,993 cycles) after post-thermal treatment. This is contrary to the observations reported by Popov *et al.* [23], where the HCF tests conducted at  $R=0.1$  with maximum stress level of 675 MPa showed that the fatigue life of the recycled builds were lower than the virgin builds. These contradictory results could either be due to the effectiveness of the HIP process in this work, or the difference in the O content between the two studies. In the previous study, even after HIPing the recycled builds contained lack-of-fusion defects which acted as fatigue crack nucleation sites. Therefore, the HIP treatment employed by Popov *et al.* was not effective in closing the lack-of-fusion defects. Another reason could be that the recycled builds tested in the previous study had 0.33 wt.% O, which is significantly higher than the recycled builds tested in this study (0.10 wt.%). As mentioned earlier, elemental O is a strong alpha stabiliser that significantly enhances the strength of the  $\alpha$  phase in  $\alpha+\beta$  alloys like Ti6Al4V [1]. Supporting that, Tang *et al.* [180] observed an increase in the distance between the fatigue striations *i.e.* an increased crack growth rate, with increasing O content in Ti6Al4V wrought alloy with equiaxed microstructure.

The aforementioned studies had significantly higher O concentration compared to the current study where the O content of the recycled builds (0.10 wt.%) was well below the max. limit prescribed in ASTM F3001 standard (<0.13 wt.%). The recycled builds which comprised slightly enhanced  $\alpha$  phase due to relatively higher O content showed a slightly higher average fatigue life compared to the virgin builds. This is in line with findings reported by Lutjering *et al.* [1], where an increase in the O content (within the max. O limit mentioned in standards) improves the fatigue strength of the Ti6Al4V wrought material with fine lamellar structure.

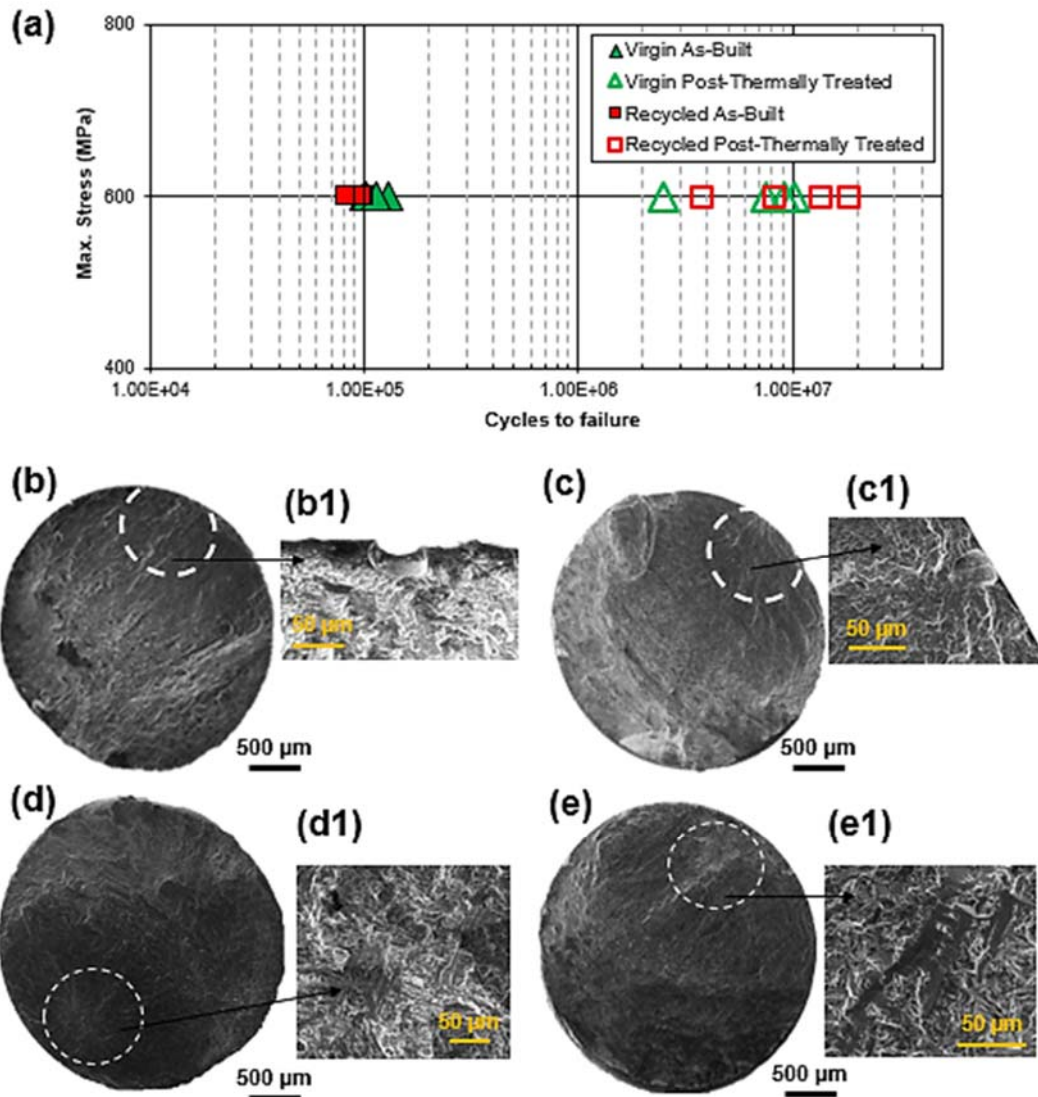


**Figure 5.4** High cycle fatigue properties of virgin and recycled builds in the as-built and post-thermally treated conditions. (a) Uniaxial HCF test; fatigue fracture surfaces of virgin (b) as-built and (d) post-thermally treated condition; fatigue fracture surfaces of recycled (c) as-built and (e) post-thermally treated condition.

## 5.4 Chapter conclusions

In the present study, the virgin and recycled builds produced from new and 10 times recycled AGA Ti6Al4V powders were post-thermally treated following HIPing + STA. The impact of post-thermal treatment on the microstructure and mechanical properties of the EB-PBF Ti6Al4V virgin and recycled builds was studied and the following conclusions can be drawn.

- (i) The  $\alpha$  lath thickness increased significantly after post-thermal treatment in both the virgin and recycled builds. However, no discernible differences were observed in

the microstructural features between the post-thermally treated virgin and recycled builds.

- (ii) In the as-built condition, both the virgin and recycled builds consisted of spherical and irregular shaped defects/pores. HIPing reduced the number of defects/pores in both the builds. However, further investigation is required to quantify the pore reduction and also to test the material in HIP-only condition to analyse pore regrowth during STA treatment. This is because previous studies have shown that pores regrow when additional post-thermal treatments were performed after HIPing [174,181,182].
- (iii) There is a marginal reduction in hardness and strength of the material caused by the increase in the thickness of  $\alpha$  laths after post-thermal treatments in both the virgin and recycled builds. The recycled builds exhibited slightly better tensile properties than the virgin builds after post-thermal treatment.
- (iv) It is postulated that the material did not possess a sufficient amount of oxygen (0.08 wt.% O in virgin and 0.10 wt.% in recycled builds) for the STA treatment to be effective at retaining the material strength after HIPing.
- (v) Post-thermal treatment significantly improved the Charpy impact energy values of both the virgin and recycled builds. The Charpy impact energy values increased by 24 J and 20 J in the virgin and recycled builds respectively. The fatigue life increased from  $10^5$  to  $10^7$  cycles in both the virgin and recycled builds after post-thermal treatments. The recycled builds with slightly higher O content exhibited marginally higher HCF life compared to the virgin builds. This is because HIPing reduced the number of defects/pores in both the builds.

\*\*\*\*\*

## 6 Effects of powder recycling in laser beam powder bed fusion

### 6.1 Introduction

In industry, the unfused powder that is left-out after EB-PBF and LB-PBF processes is generally recovered and recycled by blending or topping-up with virgin powder to maintain the build volume. The recycled powder particles present in the blend have slightly different physical and chemical properties compared to the virgin powder. In terms of powder physical properties, Chapter 4 has demonstrated that changes in powder physical properties led to an increase in the lack-of-fusion defects in the recycled builds. Chapter 5 has shown that the lack-of-fusion defects in the recycled builds can be eliminated by performing additional post-thermal treatments. On the other hand, the changes in powder chemical properties, particularly the increase in powder O content with recycling was unavoidable. Previous chapters revealed no detrimental effects due to the increase in powder O content except a slight increase in the strength of the recycled builds. This is because only a marginal increase in O content from 0.08 wt.% to 0.10 wt.% was observed after 10 simulated build cycles. However, some studies have reported decrease in material ductility [23], impact toughness [155] and fatigue life [180] at higher O levels of 0.33 wt.%, 0.46 wt.% and 0.20 wt.% O respectively. Hence, the increasing O content in the powder is realised as a major limiting factor in the number of times the Ti6Al4V powder can be recycled.

In industry, the high O content recycled powder is blended with low O content virgin powder to control the average O content of the powder and increase the number of possible recycling iterations. However, this can result in heterogeneity in powder layer chemistry, *i.e.* some regions of the powder bed will have high O content compared to the rest and thereby the part manufactured from those high O content regions may exhibit relatively different properties. Furthermore, it is also possible that heterogeneity in O content could occur within the same part, leading to an early failure in the areas with high O concentration. Although Ti6Al4V powder blending has been a common practice in most industries during recycling, to the best of the author's knowledge, no literature has investigated the effects of blending a high and low O content Ti6Al4V powder on the build

properties. This forms the objective of this Chapter and thereby, addressing Objective 4 laid out in Chapter 1 and knowledge gaps 4 and 5, highlighted in Chapter 2.

In this Chapter, the high O content Ti6Al4V powder was produced by artificial oxidation following the method described in Section 3.3, Chapter 3. The effects of powder blending were evaluated by conducting tensile, fatigue and Charpy impact tests on specimens produced from blended powder containing mixture of high O content (0.40 wt.%) powder with low O content (0.12 wt.%).

The effects of oxidised particles in the blend on the laser-matter interaction, molten pool dynamics, surface roughness and spatter behaviour were further investigated using a miniature LB-PBF process replicator on powders with two different O levels, 0.12 wt.% (virgin), and 0.40 wt.% (oxidised) using in situ X-ray imaging technique. Since no miniature or process monitoring facility which can study the physics of the molten pool in EB-PBF system is currently available, this study was performed in an LB-PBF system.

---

Some parts of this chapter will be submitted as a research article entitled, *Effect of Ti6Al4V powder oxidation on build properties during recycling in laser additive manufacturing process* in Scripta Materialia, Soundarapandiyam *et al*, 2021.

## 6.2 Powder characteristics

Powder morphology and PSD of the oxidised powder was analysed and compared with the virgin powder (Figure 6.1) to check for potential degradation in powder shape and size distribution caused by agglomeration or sintering due to powder heat treatment. Figure 6.1a and b show that both the powders look similar. Most particles were spherical with some common features generally found in AGA powders such as satellites, elongations, irregularly shaped particles and agglomerates.

Figure 6.1c shows the PSD bell curves of the virgin and oxidised powders. The respective  $D_v(10)$ ,  $D_v(50)$  and  $D_v(90)$  values were 26, 38 and 55  $\mu\text{m}$  for the virgin powder while 27, 38 and 54  $\mu\text{m}$  respectively for the oxidised powder. It can be seen that the PSD of both the powders were similar.

Virgin and oxidised powders exhibited a flowability of  $31 \pm 0.04$  s/50g and  $30 \pm 0.03$  s/50g respectively. Both powders exhibited continuous flow without any interruptions. The marginal improvement in the flow behaviour of the oxidised powder can be attributed to the reduction in the number of fine particles as revealed by a slight shift on the left side of the PSD bell curve (Figure 6.1c). Another reason could be the reduction in the moisture content of the virgin powder due to heat treatment which enabled the oxidised powder to flow better. Nevertheless, the changes in the powder physical properties were only marginal after artificial powder oxidation.

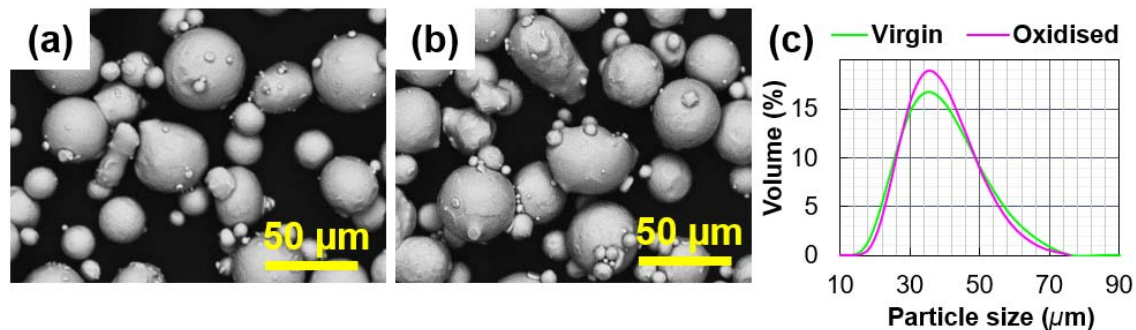


**Figure 6.1** SEM BSE image of (a) virgin and (b) oxidised powder; (c) PSD of virgin and oxidised powder.

SEM micrographs of virgin and oxidised powder particle cross-sections are shown in Figure 6.2a and b respectively. The heat treatment temperature ( $475^\circ\text{C}$ ) during artificial powder oxidation was maintained below the  $\beta$ -transus temperature ( $\sim 980^\circ\text{C}$ ), hence no significant changes in the microstructure occurred and both the powders consisted of  $\alpha'$  microstructure. Furthermore, it can be seen that the oxidised powder

particle had an oxide layer on its surface, in contrast to the virgin powder particle. The EDS line scan performed across the cross-section of both the particles further confirmed the presence of high concentration of oxygen on the surface of oxidised powder particle, in contrast to the virgin powder particle (Figure 6.2c and d). Furthermore, a small increase in the O concentration at the centre regions of the oxidised particle could mean that some concentration of O might have diffused through the oxide layer. This could have occurred due to the degradation of the oxide layer caused by collisions during the heat treatment process. Nevertheless, it is clear that the virgin powder has been oxidised after heat treatment and therefore, the oxidised powder was considered as a recycled powder having higher O content.

Quantitative measurement using the IGF technique revealed that the O content measured 0.40 wt.% for the oxidised powder, which is  $\sim 0.3$  wt.% higher than the virgin powder (0.12 wt.%). Since the powder oxidation was performed at relatively low temperature, it is less likely that vaporisation of light elements would occur. Therefore, remaining chemical elements such as Al and V contents in the oxidised powder were assumed to be same as the virgin powder (Table 3.2).

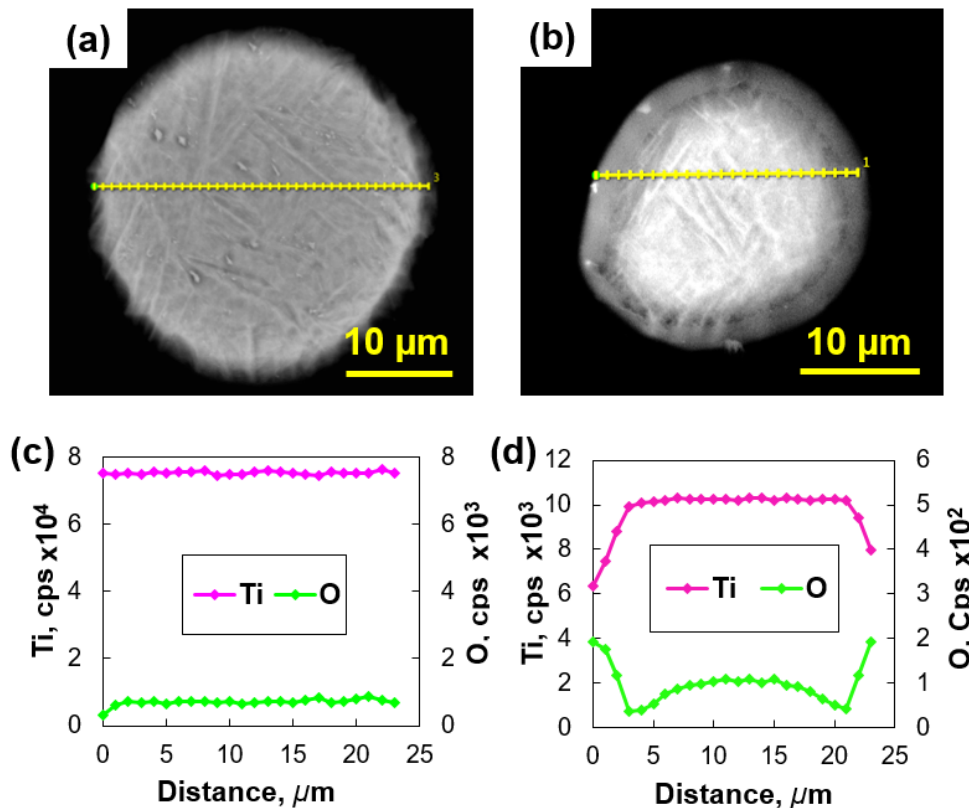


**Figure 6.2** SEM image of (a) virgin and (b) oxidised powder particle cross-sections with corresponding EDX/EDS line scan of (c) virgin and (d) oxidised powder particles.

### 6.3 Mechanical properties of builds produced from virgin and blended powder

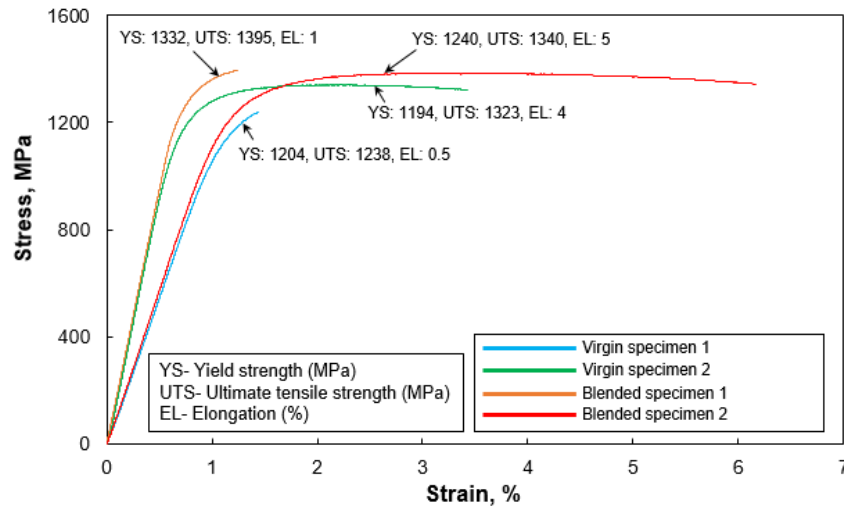
The Charpy impact values of the LB-PBF Ti6Al4V specimens built using virgin and blended powders were 8 J and 6 J respectively. The O content of the broken Charpy specimens measured  $0.17 \pm 0.005$  wt.% for the virgin and  $0.21 \pm 0.01$  wt.% for the blended builds. The decrease in the Charpy impact values of the blended builds can be attributed to the presence of a few fractions of high O content particles in the blended powder that increased the O content of the blended builds. Similar observation have been reported by Grell *et al.* [155] where the Charpy impact values of Ti6Al4V EB-PBF builds decreased with an increase in O content. No scatter in the Charpy impact values of the blended specimens occurred. Therefore, a homogenous blend of virgin and oxidised powder particles was achieved in the regions where the Charpy impact test coupons were built.

Table 6.1 lists the tensile test results of LB-PBF Ti6Al4V test coupons built using virgin and blended powder. It can be seen that the yield and tensile strength of the blended specimens were higher than the virgin specimens. However, no trend in EL% was observed between the virgin and blended specimens.

**Table 6.1** Tensile properties of virgin and blended LB-PBF Ti6Al4V builds.

		Yield strength at 0.2% offset/ MPa	Tensile strength/MPa	Elongation (EL)/%
Virgin	Specimen 1	1204	1238	0.5
	Specimen 2	1194	1323	4
Blended	Specimen 1	1332	1395	1
	Specimen 2	1240	1340	5

The slightly high yield and tensile strength values of the blended builds can be attributed to the slightly higher O content of the tensile specimen that measured  $0.23 \pm 0.01$  wt.% and  $0.17 \pm 0.005$  wt.% for the specimens manufactured from blended and virgin powder respectively. As discussed earlier, increase in the interstitial elements like oxygen in Ti6Al4V can hinder the movement of dislocations during plastic deformation and thereby increase the strength of the material [1].



**Figure 6.3** Tensile stress-strain curves of virgin and blended specimens.

The discrepancies in the elongation values can be explained using Figure 6.4 which shows that specimen that had relatively low EL% contained large lack-of-fusion defects. They had an equivalent diameter ( $D_{eq}$ ) of 790  $\mu\text{m}$  and 230  $\mu\text{m}$  in the virgin and blended builds respectively (Figure 6.4a and c). Whereas the virgin and blended specimens that contained fewer defects on the fracture surfaces (Figure 6.4b and d), exhibited higher EL% (4% and 5% elongation respectively), with values similar to the LB-PBF Ti6Al4V build properties reported in [183].

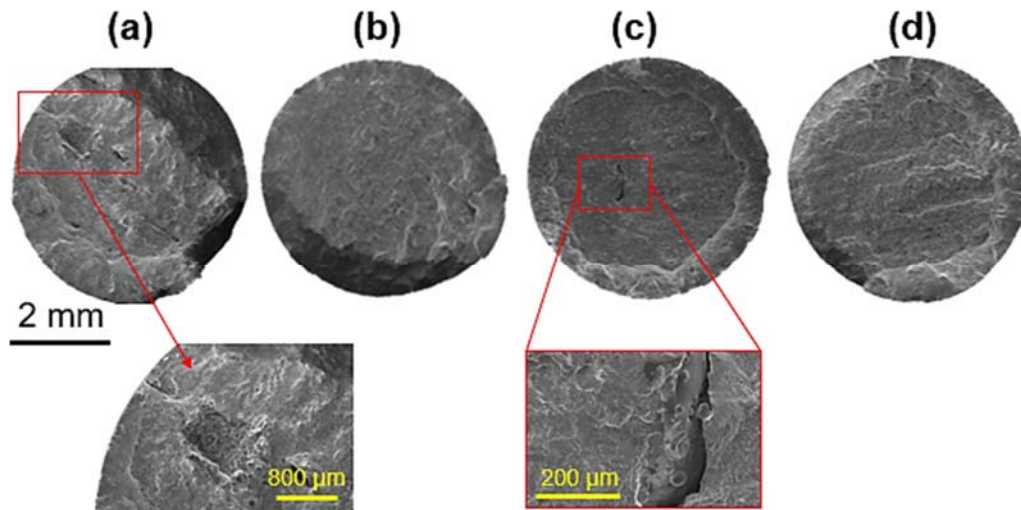


**Figure 6.4** SEM SE image of LB-PBF Ti6Al4V tensile fracture surfaces of virgin (a) specimen 1, (b) specimen 2 and blended (c) specimen 1, (d) specimen 2. The scale bars for all the macro surfaces are the same.

High cycle fatigue test results of the virgin and blended specimens tested normal to the build direction are shown in Figure 6.5. Overall, the fatigue life did not show any

trend between the virgin and blended builds. A large scatter in the fatigue life of both the specimens can be seen. The fatigue life ranged from 3,792 to 78,997 cycles for the virgin builds and from 6,522 to 99,481 cycles for the blended builds (Figure 6.5a). An example of the fatigue fracture surface of the specimens produced using virgin and blended powder are shown in Figure 6.5b-e. In the virgin builds, the specimen that failed at 78,997 cycles, had fatigue crack initiation from a near-spherical surface defect (Figure 6.5b), while for the specimen that failed at 3,792 cycles, the fatigue crack initiated from the lack-of-fusion defect (Figure 6.5c). Similarly, in the blended specimens, the specimen which had fatigue crack initiation from the spherical surface defect had relatively higher fatigue life of up to 99,481 cycles (Figure 6.5d) than the specimen in which the fatigue crack nucleated from the lack-of-fusion defect which sustained only 6,522 cycles (Figure 6.5e). It is known that lack-of-fusion defects caused by improper melting are more detrimental than spherical defects [173]. Therefore, specimens with lack-of-fusion defects had a shorter fatigue life.

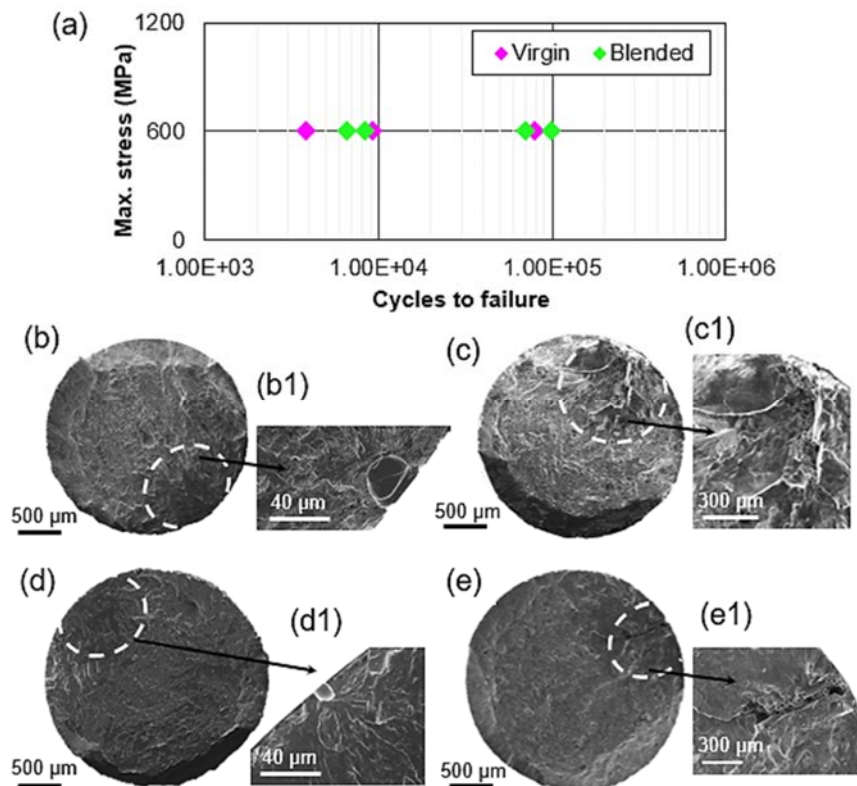


**Figure 6.5** Fatigue life and SEM images of fracture surfaces of LB-PBF Ti6Al4V specimens produced from virgin and blended powder: (a) HCF results; (b) virgin specimen that failed from a surface pore, (b1); (c) virgin specimen that failed from a lack-of-fusion defect, (c1); (d) blended specimen that failed from a surface pore, (d1); (e) blended specimen that failed from a lack-of-fusion defect, (e1).

Both the tensile and fatigue fracture surfaces revealed large lack-of-fusion defects which dominated the failure mechanism in both the conditions. During both the virgin and blended builds fabrication, several interruptions in the build occurred because the AM machine software and hardware were not synchronising well. Therefore, the software had to be rebooted a few times in-between the builds. Since the process parameters that were set were optimised for the Ti6Al4V powder, it is highly possible that the AM machine quality-related issues, caused improper melting of the powder particles that led to large lack-of-fusion defects in the builds. This caused discrepancies in the EL% and a large scatter in the HCF values of the virgin and oxidised builds.

Therefore, it is clear that process-related lack-of-fusion played a dominant role in determining the properties of the builds compared to the powder feedstock properties. Therefore, using optimised process parameters and good AM machine quality set up can have a more significant effect on mechanical properties than the powder feedstock properties.

Overall, the current study complies with previous literature and showed that an increase in Ti6Al4V powder O content increases material strength and reduces ductility and impact toughness. To further investigate the effects of those high O content particles in the blend during a build, the in situ X-ray imaging technique was performed using ISOPR [67].

## **6.4 Real-time monitoring of multi-layer build formation using virgin and oxidised powder in LB-PBF process**

### **6.4.1 Multilayer build formation**

Multi-layer builds that comprised 10 layers were manufactured with virgin and oxidised powder using a miniature entry-level LB-PBF machine. Figure 6.6 and Figure 6.7 shows the time-series X-ray radiographs of multi-layer melt track formation using virgin and oxidised powder feedstock respectively. The laser power and scan speed used was 150 W and 50 mms<sup>-1</sup> respectively for both the builds. Each row of the composite radiographs are labelled (a) to (d) which corresponds to layer 1, layer 2, layer 5 and layer 10 respectively. The scan direction and argon gas flow direction are indicated by purple and black arrows respectively. As can be seen, a bi-directional scan strategy was employed, *i.e.* the scan direction reversed after each powder layer was melted. The contour of the melt tracks and spatters are marked by red-dashed lines, the unmelted powder ahead of the laser

beam is indicated by blue-dashed line and the yellow-dashed line represents the local depression region that formed on the melt pool where laser beam was irradiated. In other words, the depression region indicated the position of the laser beam as schematically represented by red lines in the radiographs. Since the width of the substrate plate was larger than the deposited tracks, some of the powder particles deposited between the melt track and glassy carbon plate.

It is worth mentioning that the processing parameters used in the large scale LB-PBF builds is different compared to that employed during the real-time monitoring experiments. The scan speed was reduced, layer thickness was increased and the laser power had to be adjusted accordingly to suit the imaging conditions.

As explained earlier, keyhole mode of melting occurs during LB-PBF process that leads to metal vaporisation from the surface of the melt pool. Melt vaporisation could also lead to a marginal reduction in the concentration of light elements like Al in the builds as reported in [184]. Rapid vaporisation of melt creates a vapour cavity that leads to a strong recoil pressure acting normal to the surface of the melt pool [89]. This led to the formation of local depression regions as indicated by yellow-dashed line in Figure 6.6 and 6.7. The developed recoil pressure drives the melt pool to the bottom of the vapour channel, leading to a thin layer of liquid at the beam spot leading to the formation of a keyhole [75]. However, the keyhole is not evident in the radiographs due to the presence of powder particles between the melt track and glassy carbon. Furthermore, during laser-matter interaction, continuous ejection of powder particles and melt droplets occurred, as evident in the different stages of the radiographs.

#### **6.4.2 Spatter formation**

Several researchers have studied the spatter formation mechanism in LB-PBF process over the past few years [65,86,89,185]. Broadly, two types of spatters have been reported: solid spatter (powder particle ejection) and droplet spatter (melt ejections) [85]. Droplet spatters form at the melt pool surface due to strong exertion of recoil pressure on the melt pool surface, while powder spatters occur from the regions surrounding the melt pool due to entrainment of unfused powder particles in the metal vapour jet [65]. Spatter quantity, direction of flight, velocity, *etc.* are influenced by the processing parameters like input energy density, process environment and powder layer thickness [85,86,185]. In the current study, operating conditions used to produce both the virgin and oxidised builds were the same. However, comparing Figure 6.6 and

Figure 6.7, it can be seen qualitatively that the number of spatters produced in the virgin condition is significantly higher than the oxidised condition.

One of the limitations of the current study is that due to the high energy density of the X-ray beam (55 keV), only spatters with  $D_{eq} \geq 60 \mu\text{m}$  could be analysed because smaller spatters ( $D_{eq} < 60 \mu\text{m}$ ) appeared transparent to the X-rays providing negligible contrast difference with the background. Since majority of the powder spatters had  $D_{eq} < 60 \mu\text{m}$ , they were not included in the analysis. However, some fractions of agglomerated powder spatters ( $D_{eq} > 60 \mu\text{m}$ ) that formed at the laser front were also observed (Appendix C). To avoid discrepancies in the results and to confine the focus on the phenomena that occurs in the melt pool, only droplet spatters were analysed in this work.

Most of the droplet spatters ejected vertically from the melt pool without disturbing the unfused powder in the powder layer. However, some of the droplet spatters collided with the powder bed forming a larger spatter, which complies with the previous observation reported in [89]. Furthermore, although the droplet spatters were initially ejected in the vertical direction, after travelling some distance, they became entrained in the Ar gas flow and were carried along the Ar flow direction.

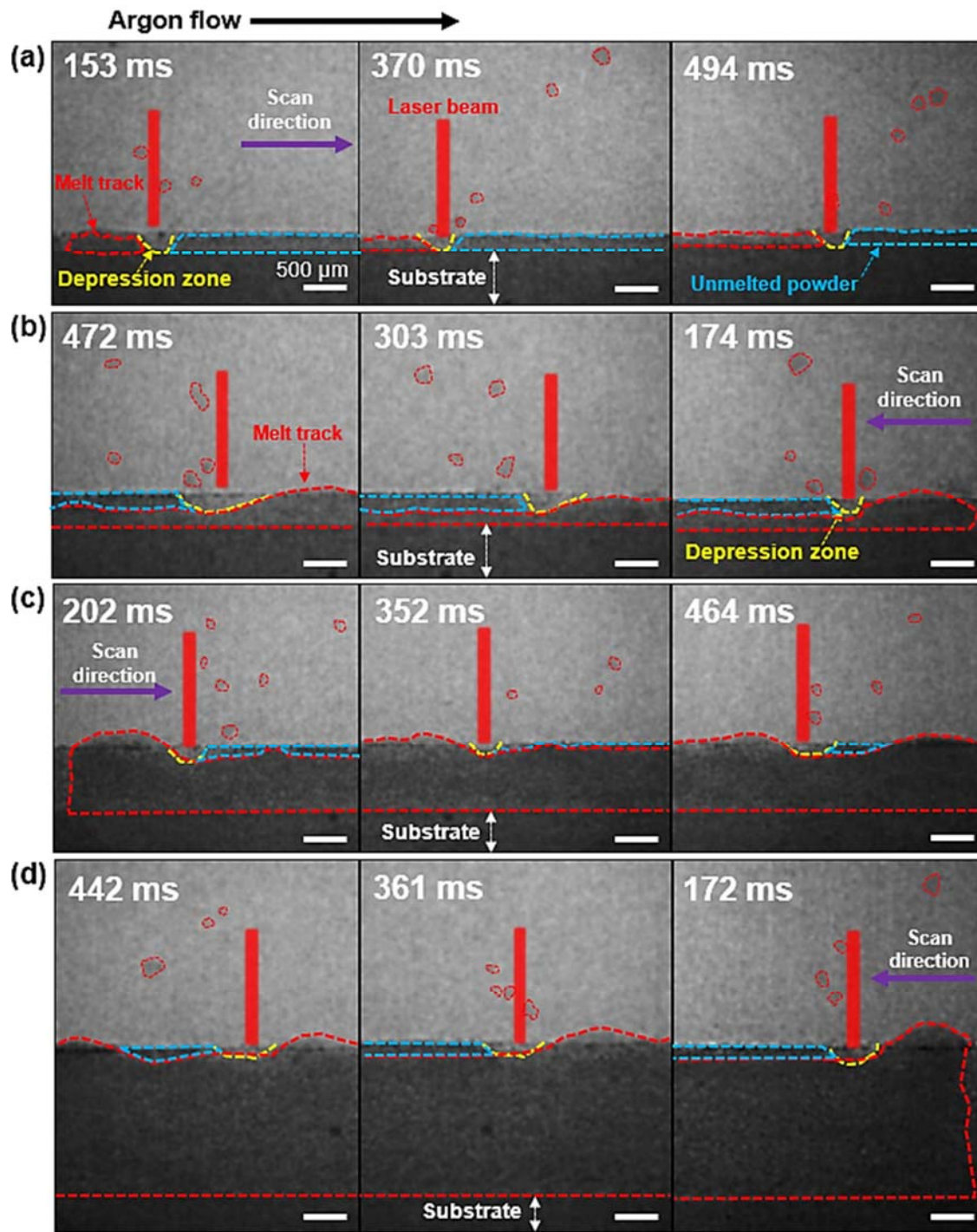


**Figure 6.6** Dynamic X-ray images showing laser-Ti6Al4V powder interaction and spatter formation at 150 W and 50  $\text{mm s}^{-1}$  in the virgin condition at (a) Layer 1, (b) Layer 2, (c) Layer 5 and (d) Layer 10. The scale bars in all the radiographs are 500  $\mu\text{m}$ . The spatter contours are marked by red-dashed circle; Contours of melt tracks, unmelted powder and the depression regions are marked by red, blue and yellow-dashed line respectively.

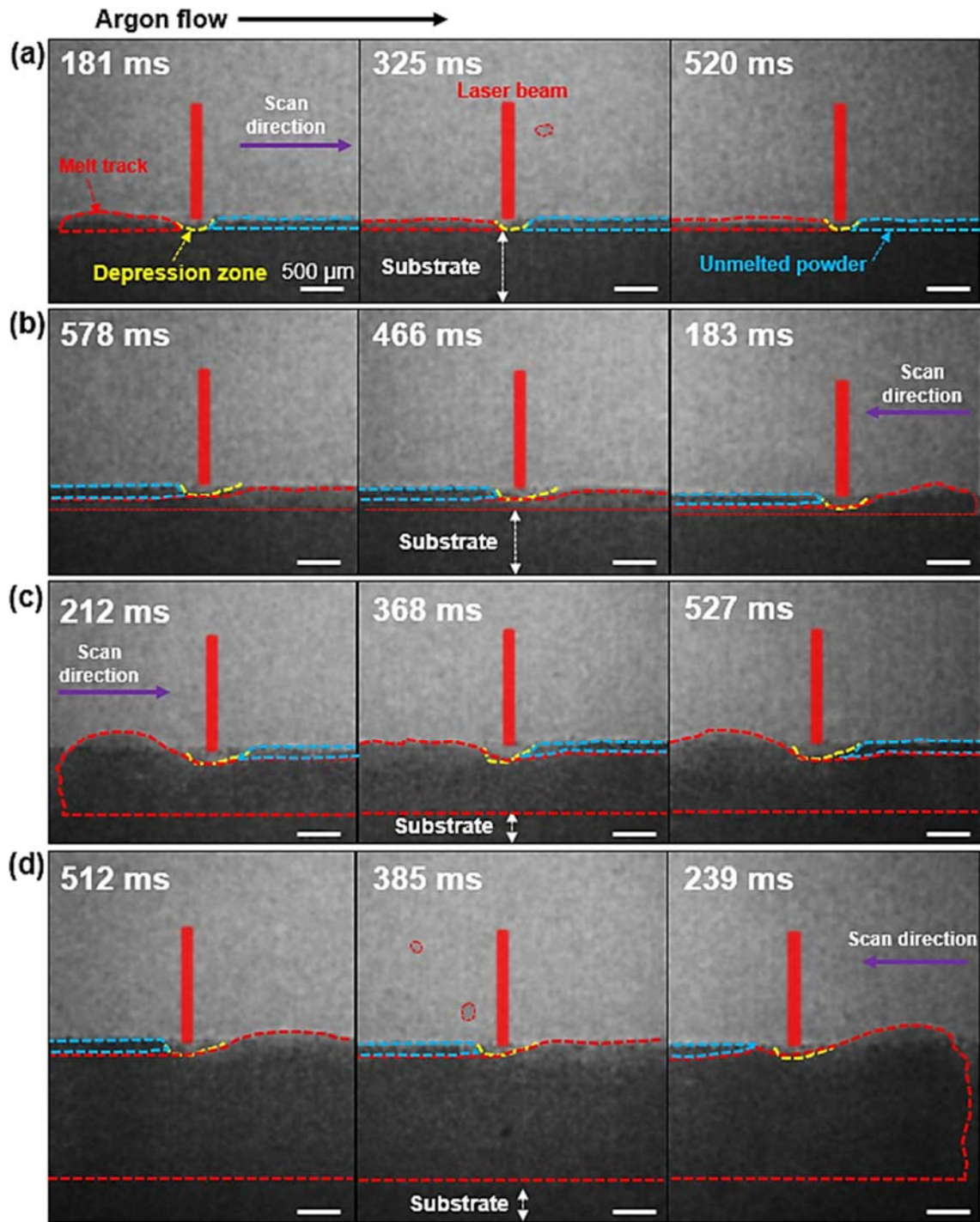


**Figure 6.7** Dynamic X-ray images showing laser-Ti6Al4V powder interaction and spatter formation at 150 W and 50 mm<sup>s</sup><sup>-1</sup> in the oxidised condition at (a) Layer 1, (b) Layer 2, (c) Layer 5 and (d) Layer 10. The scale bars in all the radiographs are 500 μm.

### 6.4.3 Spatter quantification

Figure 6.8 shows the number of droplet spatters produced during the virgin and oxidised build fabrication and their corresponding  $D_{eq}$  values. It can be seen that droplet spatters of all size ranges were ejected in both the virgin and oxidised conditions. It is evident that the virgin condition produced significantly more spatters compared to the oxidised condition. Furthermore, it can be seen that some of the spatters were three times larger than the size of the powder particles, 149  $\mu\text{m}$  compared to 15  $\mu\text{m}$ .

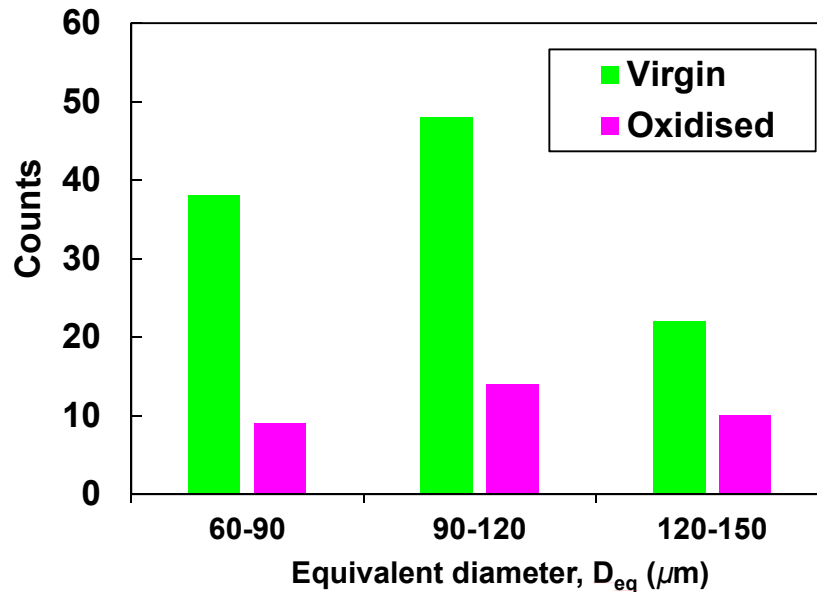


**Figure 6.8** Spatter quantity in virgin and oxidised condition.

The processing conditions employed for both the virgin and oxidised powders were the same. Therefore, the difference in the spatter quantity can be attributed to the variation in the powder O content. Since the oxidised powder had higher O content than the virgin powder, the subsequent melt pool that formed also contained higher concentration of oxygen. The increase in the O content of the melt pool affects the molten pool dynamics. In 316L stainless steel, Lu *et al.* [78] reported that the melt bead penetration increased in GMAW process due to the presence of surface active elements like oxygen. Similarly, Heiple *et al.* [80] during laser welding of stainless steel observed changes in the shape of the weld track due to the presence of surface active elements like oxygen and sulphur. The authors proposed that the presence of the surface active elements altered the surface tension gradient from negative to positive and thereby reversed the Marangoni convection from outward centrifugal to inward centripetal flow.

In LB-PBF process, Leung *et al.* [69] demonstrated similar change in melt flow direction with increase in the O content of the maraging steel powder.

However, in the above mentioned studies, the oxygen remained insoluble as oxides altering the Marangoni convection. As mentioned in Chapter 2, the solubility of oxygen in titanium is high. Therefore, the oxides present on the oxidised powder particle surfaces are likely to have broken down during laser irradiation to elemental oxygen, which subsequently dissolved in the melt pool. Mills *et al.* [121] reported that dissolved oxygen had minimal effect on the surface tension. Wunderlich [81] also demonstrated that the increase in the O content of Ti6Al4V melt had negligible effects on the surface tension. Furthermore, the author has shown that the viscosity of the Ti6Al4V melt increased with increase in O content. Similar conclusion was made by Skalon *et al.* [132] in LB-PBF process when Ti6Al4V reused powder with high O content was employed. Therefore, in this study the increase in the O content of the melt pool did not significantly affect the surface tension and the melting of oxidised powder produced a melt pool with higher viscosity compared to the virgin powder.

Increase in the viscosity of the melt pool reduces turbulence that forms during laser melting because viscous shear forces oppose the backward surge of the melt pool, reducing its flow inertia [66]. Since the flow inertia was greatly reduced and was not strong enough to overcome the surface tension force at the melt pool surface, molten droplets (droplet spatter) were not able to exit the melt pool surface. Therefore, the number of droplet spatters in oxidised condition was significantly lower than the virgin condition. Similar observation was reported in [186] during laser melting of bioactive glass powder, where the high viscous melt pool produced fewer spatters. Previous literature have correlated droplet spatter to process parameters, layer thickness and chamber pressure. The study shows that the O content of melt pool that depends on the powder O content, can also influence the number of droplet spatters that forms during LB-PBF process.

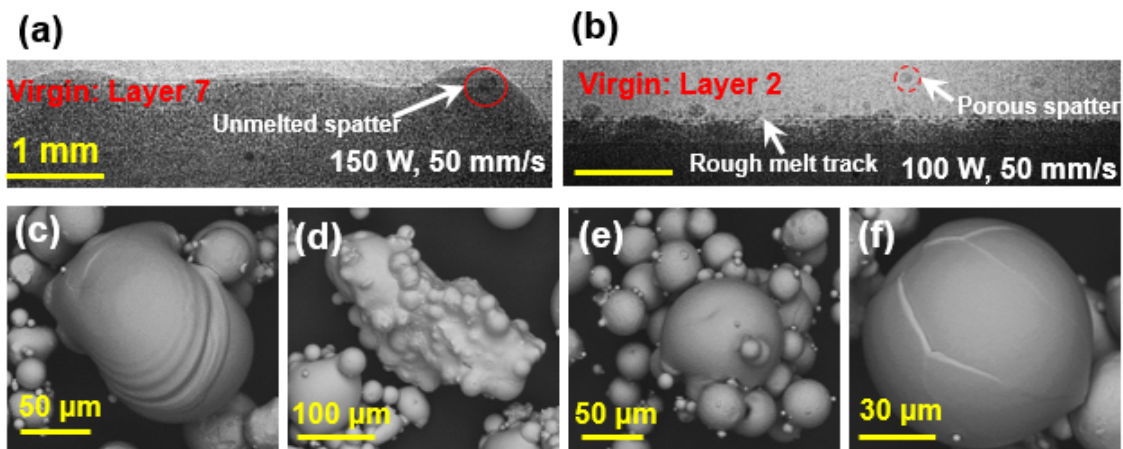
## 6.5 Effects of spatter on build properties and powder recycling

Figure 6.9a and b shows the effects of spatter when it falls back in the melting region. Spatters can remain unmelted as shown in Figure 6.9a (highlighted by red circle), acting as stress concentration sites for fatigue crack nucleation. Spatters can also be deposited over the previously formed melt track, increasing the melt track surface roughness and

also entrap gases present in the chamber during solidification that can lead to an increase in part porosity (highlighted by red-dashed circle) (Figure 6.9b).

Figure 6.9c-f shows the effects of spatter when it falls back in the unfused regions of the powder bed. Figure 6.9c shows a liquid spatter which landed on a powder particle and solidified. Figure 6.9d shows a liquid spatter that solidified over a cluster of powder particles creating an agglomerated high aspect ratio particle. Similarly, Figure 6.9e shows a spatter producing powder agglomerates but with a different morphology. Figure 6.9f shows a 'super-ball' spatter particle, *i.e.* a liquid spatter that became solidified during its flight into a large spherical particle, twice the size (92  $\mu\text{m}$ ) of the average virgin powder particle.

As can be seen in the micrographs, the spatter agglomerates are coarser than the virgin powder and can be eliminated from the subsequent builds during sieving when the powder is recycled. However, some high aspect ratio spatter agglomerates, like shown in Figure 6.9d can pass through the sieves in certain orientations and end up in the powder layer, affecting powder flow and packing density. In addition, oxidation of spatter particles have been reported in [94]. This can create chemical inhomogeneity of the powder layer when the spatter falls back into the powder bed.



**Figure 6.9** (a) Radiograph of Layer 7 virgin build produced using 150 W laser power and 50  $\text{mms}^{-1}$  scan speed showing unmelted spatter (red circle); (b) radiograph of Layer 2 virgin build formed using 100 W laser power and 50  $\text{mms}^{-1}$  scan speed showing spatter induced surface roughness and porous spatter. The scale bar in both a and b measured 1 mm. Powder bed contamination by droplet spatters: spatter solidified/sintered over (c) single powder particle, (d and e) cluster of particles to form agglomerates, and (f) spherical 'super-ball' spatter.

## 6.6 Morphology of melt tracks produced using virgin and oxidised powder

Top-surface of melt track boundaries of the first six layers of the builds produced from virgin and oxidised powders are shown in Figure 6.10a and b respectively. It can be seen that the melt track surfaces contained undulations along the track length in both the conditions, and the frequency and amplitude of those undulations were higher in the virgin condition compared to the oxidised condition. Furthermore, no trend in the evolution of track morphology with respect to the increasing layer numbers was observed in both the conditions.

In addition, it can be seen that the layer height was not uniform along the track length. The pre-set layer height was 100  $\mu\text{m}$ . However, the layer height increased up to 260  $\mu\text{m}$  and lowered up to 30  $\mu\text{m}$  in the virgin condition, while in the oxidised condition, the layer height increased up to 152  $\mu\text{m}$  and lowered up to 30  $\mu\text{m}$ . Therefore, the real layer height was not uniform as the pre-set layer height.

The average surface roughness ( $R_a$ ) of the top-surfaces of each melt tracks were measured using the X-Y coordinates of the melt track boundaries using image processing software. Figure 6.10c shows the  $R_a$  values of the 10 layers of the builds produced from virgin and oxidised powder. It is evident that the melt tracks formed from the virgin powder had higher surface roughness than oxidised builds in all the layers built. Furthermore, in both the conditions, the  $R_a$  value increased steeply in the first few layers and then stabilised with marginal fluctuations between each layers.

Since measuring surface roughness using image processing tools is neither a standard method nor a method followed commonly in industry, surface roughness of the final layer (10<sup>th</sup> layer) in the virgin and oxidised builds were measured according to ISO 4288 to validate the findings. The  $R_a$  value was 14  $\mu\text{m}$  for the virgin build and 3  $\mu\text{m}$  for the oxidised build. The corresponding  $R_a$  values measured using image processing technique were 29  $\mu\text{m}$  and 13  $\mu\text{m}$  for the virgin and oxidised builds respectively. The difference in the measured  $R_a$  values between the two techniques can be attributed to the deviation from the standard, as already mentioned in Section 3.3.10. Nevertheless, both methods demonstrate that the melt tracks produced from the virgin powder were relatively rougher than the oxidised builds.

The undulations, or commonly referred as 'humps' in welding metallurgy, that formed on the melt track surfaces are controlled by several factors including energy

density, surface tension, viscous force, capillary force, recoil pressure, *etc.* [66,187]. Similar type of undulations have also been observed in Ti6Al4V virgin melt tracks produced by LB-PBF process in [74]. Nguyen *et al.* [188] identified that the major factor for the initiation of hump was the strong backward momentum of the melt flow behind the energy source. Gunenthiram *et al.* [68] reported that the development of the hump is caused due to the large aspect ratio (length/width) of the melt tracks that promote Plateau-Rayleigh instability. Furthermore, simulation experiments performed by Tang *et al.* [66] have shown that the formation of first hump promotes the development of a more humps and thereby leading to the formation of periodic humps along the melt track length, as was observed in Figure 6.10a and b. In addition, the mathematical model developed by the authors demonstrated that the backward flow inertia of the melt pool significantly reduced with increase in viscous shear force. Therefore, the oxidised powder which produced a relatively more viscous melt pool than the virgin powder, had low melt backward flow momentum. This phenomenon possibly decreased the undulations in the melt tracks produced from oxidised powder.

The melt tracks produced in LB-PBF process using high O content Invar 36 powders contained higher number of humps compared to the virgin builds [69]. Possible reason for this phenomenon could be the change in the Marangoni convection from outward centrifugal to inward centripetal. Mills *et al.* [121] and Tang *et al.* [66] reported that the frequency of humps increases when the surface tension gradient changes from negative to positive using experimental analysis and mathematical model respectively. In the current study, the melt tracks produced from the oxidised powder had reduced number of humps compared to the virgin powder. This further confirms the hypothesis that the surface tension gradient remained unchanged and the oxides present in the powder dissolved into the melt pool upon laser irradiation.

Furthermore, the undulations present on the melt track surfaces can cause heterogeneity in powder layer thickness of the subsequent layer as shown schematically in Figure 6.10d and e. The red spheres illustrate powder particles laid on volume rendered XCT image of the virgin and oxidised builds. As can be seen, a higher volume of powder particles can be deposited in the valleys compared to the peak regions of the melt track. This leads to non-uniform powder particle distribution. Since the virgin builds consisted of a higher number of undulations compared to the oxidised builds, the unevenness in powder layer thickness would be more in the virgin compared to the

oxidised condition. The difference in powder layer thickness can lead to inhomogeneity in keyhole penetration depth and laser re-melting of the previous layer. Deeper re-melting is possible in the peak regions of the melt track with fewer powder particles covering their surface compared to the valley regions as shown in [74]. Improper laser penetration can lead to lack-of-fusion defects between the layers. Therefore, the valley regions of the undulations are more prone to lack-of-fusion defects compared to the peak regions of the melt track.

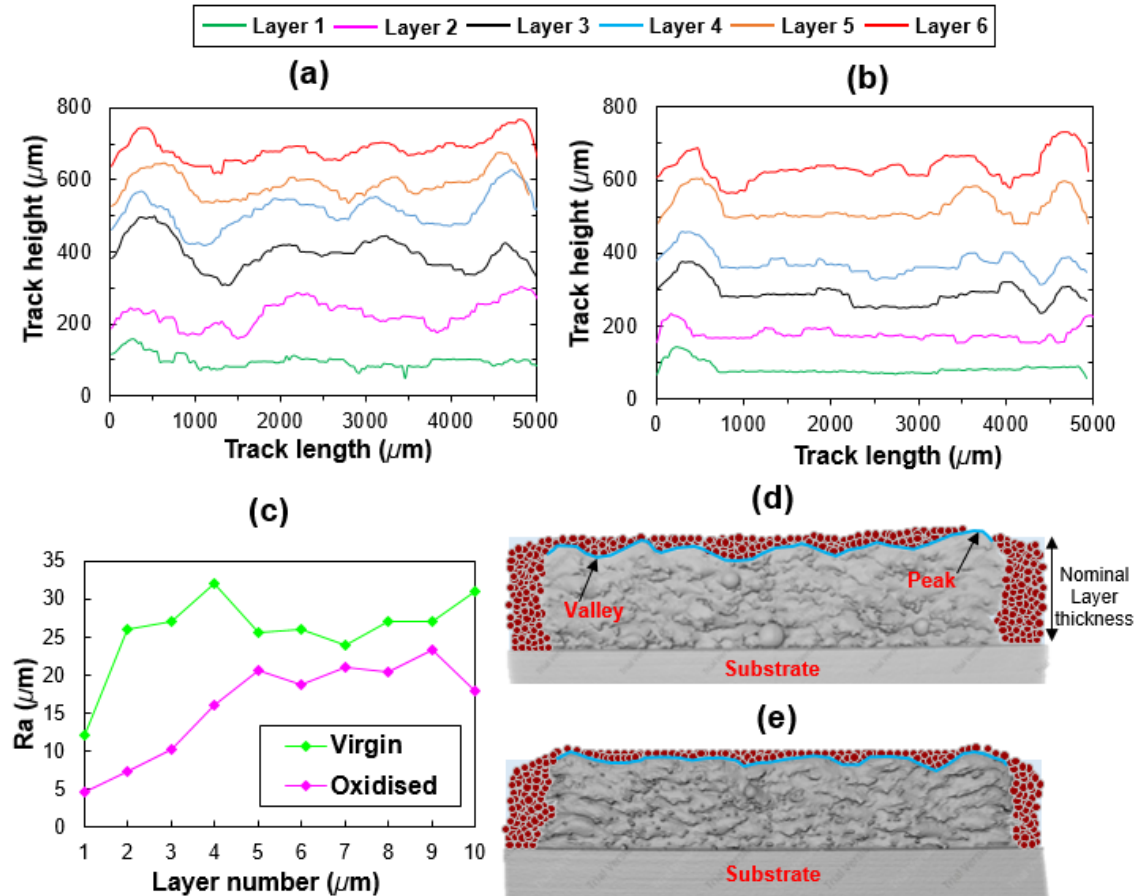


**Figure 6.10** Melt track surface profiles of builds produced by (a) virgin and (b) oxidised powder from layers 1 to 6; (c) average surface roughness in virgin and oxidised builds; effect of layer roughness on powder spreading in (d) virgin and (e) oxidised condition.

## 6.7 Analysis of defects in the builds produced from virgin and oxidised powder

XCT was used to analyse the overall trends in the defects present in virgin and oxidised builds. Figure 6.11a and b show pores overlaid on volume rendered image of the builds. The pores were randomly distributed in both the builds and their equivalent diameter ranged from 10 to 100  $\mu\text{m}$ . As shown in Figure 6.11c, the virgin builds contained larger

fraction of defects compared to the oxidised builds and Figure 6.11d shows that pores had spherical morphology. Therefore, mostly gas pores were present in both builds. The higher number of gas porosity in the virgin builds can be attributed to the relatively strong turbulence in the melt pool produced by the virgin powder compared to the oxidised powder. Furthermore, no correlation in defect distribution with respect to variations in powder layer thickness was evident. Therefore, although the powder layer thickness varied, the employed power density was sufficient to prevent lack fusion defects that could have occurred in the regions with larger track height.

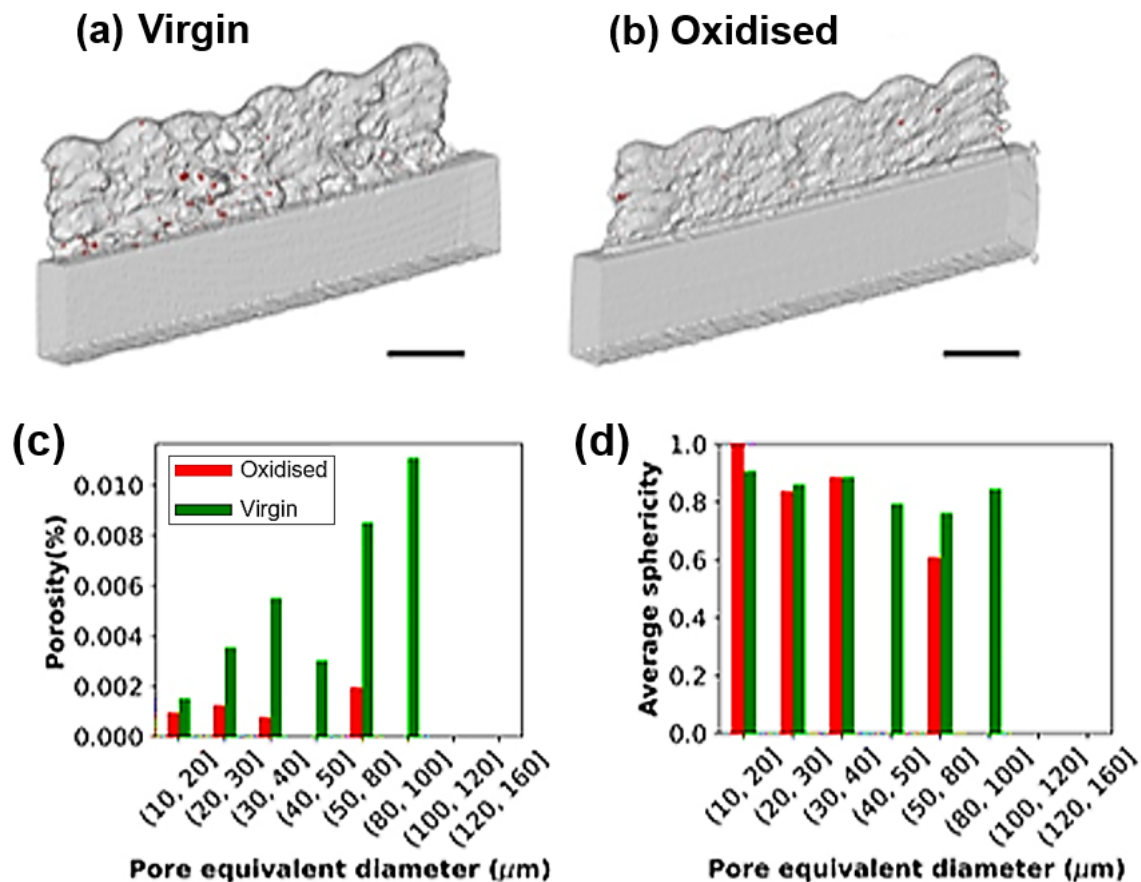


**Figure 6.11** Defect quantification in virgin and oxidised Ti6Al4V builds produced by ISOPR using XCT technique. 3D rendered images of pores overlaid on (a) virgin and (b) oxidised builds. (c) Percentage of porosity and its (d) sphericity as a function of pore equivalent diameter.

## 6.8 Microstructure and hardness of melt tracks produced from virgin and oxidised powder

Figure 6.12 shows the microstructure of virgin and oxidised builds in the build direction. Both the builds reveal a typical LB-PBF Ti6Al4V microstructure consisting of

predominantly  $\alpha'$ . Therefore, the difference in the powder O content had negligible impact on the build microstructure. As expected, the Vickers hardness values increased from  $393 \pm 9.8$  HV for the virgin to  $461 \pm 8.4$  HV for the oxidised builds. This is due to the high interstitial O content in the oxidised build. Interstitial O resists plastic deformation leading to an increase in material hardness, as explained in Section 2.3.4.

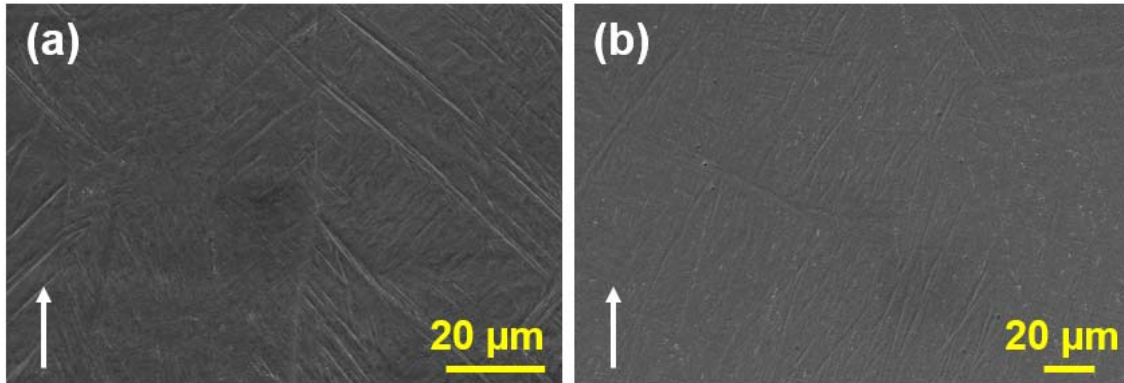


**Figure 6.12** SEM SE image of (a) virgin and (b) oxidised build microstructures. White arrow indicate build direction. Note the difference in scale bar length.

## 6.9 Chapter conclusions

This chapter investigated the effects of blending high and low O content Ti6Al4V powder on build properties in LB-PBF process using in situ and ex situ experiments. Ex situ analysis consisted of studying the mechanical properties of the builds produced from virgin and blended powder (virgin + oxidised). In situ study involved analysing the effect of high O content particles using real-time X-ray imaging of the LB-PBF process in a miniature LB-PBF process replicator. The following conclusions can be drawn from this study.

- (i) Mechanical properties: Failure mechanisms were dominated by the presence of build defects that decreased the fatigue life and EL% of both the virgin and blended builds. In the absence of defects, the virgin builds showed higher EL% and impact toughness, while the blended builds showed higher yield and tensile strength.
- (ii) Spatter: This study highlights that in addition to processing conditions, powder O content can influence spatter volume. Spatters of broad range of equivalent diameters formed in both the virgin and oxidised condition. However, virgin powder produced more spatters than the oxidised powder.
- (iii) Surface roughness: The surface roughness increased steeply at the start and then stabilised with slight fluctuations with increasing layer height. The melt tracks

produced from the oxidised powder were relatively smoother than the virgin condition. Presence of undulations on the melt track can lead to variations in powder layer thickness.

- (iv) Defects: The virgin builds contained a larger number of gas pores compared to the oxidised builds. No lack-of-fusion defects were observed in either build, showing that the input power density was suitable to fuse the layers.

\*\*\*\*\*

## 7 Conclusions and future work

### 7.1 Research summary

The present investigation aimed to determine the effects of recycling unmelted Ti6Al4V powder on the properties of parts manufactured by EB-PBF and LB-PBF processes. To begin with, a comprehensive review of the literature was conducted. It was revealed that powder feedstock properties, which play a crucial role in determining the build properties, undergo changes in their physical and chemical properties with reuse. This had subsequent impact on the part properties. The knowledge gaps that existed in this domain were then identified and a methodology was designed to address those knowledge gaps.

In the first facet, the Objectives 1 and 2 were addressed. The presented results demonstrated the nature, cause and mechanism of changes in Ti6Al4V powder characteristics and its subsequent impact on build properties as a consequence of recycling. The study was performed by recycling gas atomised Ti6Al4V powder in EB-PBF process following a simulated powder recycling strategy. This approach reduced powder consumption and powder top-up after each build cycle, and enabled analysis of the effects of preheat cycles on powder properties. In this study, the heterogeneity in powder property changes that occur within the same build cycle were also highlighted. The changes in powder properties due to manufacturing, powder recovery and handling were investigated by employing broad range of powder characterisation techniques and the changes that occur at the particle levels were correlated to the bulk powder behaviour. The impact of powder recycling on build properties were then investigated by conducting mechanical and metallurgical tests. The properties of the test specimens built from virgin and recycled powders were analysed at the micro scale using microscopy and XCT techniques to study the part microstructure and defect distribution respectively. The mechanical properties of the parts were studied by conducting Charpy impact, tensile, hardness and high cycle fatigue tests.

In the next facet, the Objective 3, the response of recycled Ti6Al4V EB-PBF builds to post-thermal treatments was investigated. The post-thermal treatment included hot isostatic pressing, solution treatment and ageing process. The metallurgical and mechanical properties of the recycled builds were tested and compared to the virgin build

properties after post-thermal treatments by conducting Charpy impact, tensile, hardness and high cycle fatigue tests.

Finally, the Objective 4, the effects of high O content particles in the blend of high and low O Ti6Al4V powder particles was studied in the LB-PBF process. The study consisted of both ex situ and in situ experiments. The ex situ experiments mainly involved Charpy impact, tensile and high cycle fatigue tests performed on builds produced from virgin and blended powder. In the in situ study, virgin and oxidised powders were used separately in the operando process replicator and the effects of powder O content on laser-matter interaction, molten pool dynamics, spatter, surface roughness and defect population were investigated using the high speed X-ray imaging technique. The microstructure and hardness of the virgin and oxidised builds were also investigated.

## 7.2 Key research findings

Understanding the nature, cause and mechanism of changes in powder properties and its corresponding impact on part characteristics is essential to predict and understand the properties of components produced from recycled powder. Based on this extensive research which covered different challenges in Ti6Al4V powder recycling, the following key findings can be drawn.

### 7.2.1 Evolution of powder properties with recycling in the EB-PBF process

- (i) Heterogeneity in powder degradation occurs within a build. The powder particles located closer to the melt-zone undergo the greatest changes in physical and chemical properties. These include particles sintering, partial melting, broader PSD, microstructural transformation ( $\alpha' \rightarrow \alpha + \beta$ ) and increase in powder O content (0.08  $\rightarrow$  0.12 wt.%).
- (ii) Compared to the virgin powder, the recycled powder showed better flow behaviour due to reduced number of fines and satellite particles, and improved powder sphericity. Particles with  $\alpha'$  and particles subjected to different stages of  $\alpha' \rightarrow \alpha + \beta$  microstructural transformation were found, and the recycled powder had slightly higher O content (0.10 wt.%) than the virgin powder (0.08 wt.%).
- (iii) Most of the severely process affected particles were eliminated during sieving which thereby caused only slight changes in bulk powder physical properties with recycling.

### 7.2.2 Evolution of build properties with recycling in the EB-PBF process

- (i) Negligible changes in microstructure, Charpy impact, hardness and tensile elongation were observed with recycling. Also no significant difference in the tensile properties of the virgin and recycled builds were observed.
- (ii) The recycled builds had higher fraction of lack-of-fusion defects in comparison to the virgin builds. However, no significant change in fatigue life was evident.
- (iii) The post-thermal treatment (HIPing+ Solution treatment and aging) improved the fatigue life of both the virgin and recycled builds by eliminating the lack-of-fusion defects. It also resulted in coarsening of the microstructure, causing a reduction in material strength of both the virgin and recycled builds.

### 7.2.3 Effects of high O Ti6Al4V powder particles in the LB-PBF process

- (i) The oxidised powder produced fewer melt ejections than the virgin powder during laser-powder melting. This is possibly due to the higher viscosity of the melt pool that formed when high O content oxidised powder was melted.
- (ii) In addition to processing conditions, Ti6Al4V powder O content plays a vital role in influencing spatter volume in LB-PBF process.
- (iii) Oxidised powder produced relatively smoother melt tracks with fewer defects compared to the virgin powder.
- (iv) The hardness values were higher for the oxidised builds than the virgin builds due to the relatively high O content.
- (v) The mechanical test specimens that contained large build defects caused by non-optimal processing conditions exhibited early fracture, irrespective of the powder O contents.

## 7.3 Limitations of the current study

- (i) A simulated powder recycling method was employed to elucidate the effects of powder reuse with 10 build cycles in the EB-PBF process. The changes in the powder properties were of lesser magnitude compared to the powder that went through 10 real build cycles because this involves melting of powder particles. In the actual build cycles, the following two phenomena are expected to escalate:
  - o Increase in powder O pick-up. Melting powder particles in each build cycle would have resulted in higher O pick-up by the particles in the vicinity of the melt pool due to the high temperatures experienced by those regions. Post-

heating was performed only in the first and final build cycle in which the test coupons were built. Therefore, the effect of post-heating on O pick-up in the intermediate cycles could not be considered in the evaluation of total O pick-up by the recycled powder.

- Increase in the fraction of agglomerated or sintered powder particles in the recycled powder.
- (ii) In the EB-PBF process, limited material was available and so only a limited number of test specimens could be manufactured for each condition (virgin as-built, recycled as-built, virgin post-thermally treated, recycled post-thermally treated). Only two tensile tests and four high cycle fatigue tests at a single stress range were conducted. This is because the aim of the study was to highlight the nature and mechanism of changes in powder characteristics and its subsequent effect on part properties with reuse rather than the magnitude of such changes. More tests would provide statistical rigour for particular industrial applications.
- (iii) Due to the limited amount of material available, the virgin and recycled Ti6Al4V EB-PBF builds could not be tested in the as-HIPed condition. Therefore, the effect of each post-thermal treatment on build microstructure, defect density and mechanical properties could not be investigated specifically.
- (iv) This study has shown that gas atomised Ti6Al4V powder can be used in an ARCAM EB-PBF machine, in addition to commonly employed plasma atomised powder. However, some melt ejections were observed, indicating that some fine tuning of the process parameters is necessary. Since this was outside the scope of this project, future research might need to adjust the default ARCAMQ10 plus process settings to suit the gas atomised powder.
- (v) Due to the build failures that occurred during the LB-PBF process, the results obtained in the current study are not significant enough to provide clarification on whether the isolated high O content particles in the blend can make the powder unusable. Therefore, a repeat of the build with less volume of defects and subsequent mechanical characterisation is needed.

#### **7.4 Outlook for future research**

The current study has shown that the changes in Ti6Al4V powder physical properties with reuse are small, and the impact on built properties, such as the increase in fraction

of lack-of-fusion defects in the builds produced from recycled powder, can be eliminated by employing additional post-thermal treatments. Therefore, the author suggests that future Ti6Al4V powder recycling studies should focus more on the effects of changes in powder chemical properties, especially the powder O content.

- (i) Firstly, it would be highly useful to generate a dataset on Ti6Al4V powder oxidation rate as a function of the thermal gradients that occur in the powder bed during part manufacturing.
- (ii) In the case of Ti6Al4V, this study has shown that there is an alternative route to increase the Ti6Al4V powder O content which otherwise would be tedious, time-consuming and expensive. Similar approach could be used to conduct further investigations related to powder blending, effects of heterogeneity in the powder layer chemistries, effects of powder oxidation on laser absorptivity *etc.*
- (iii) High O content particles exhibit a different colour in the optical microscope compared to the rest of the powder particles due to the increase in the oxide layer thickness, similar to that observed on wrought products with oxidation, as shown in [189]. Therefore, a suitable visualisation technique for particle level analysis to detect chemically out-of-spec powder particles in the recycled powder could be developed.
- (iv) Due to the high energy of the hard X-rays (55 keV) used in the current study (I12 JEEP beamline, Diamond), the powder spatters which had smaller diameter had negligible contrast difference with the background, hence, could not be quantified. Therefore, the author recommends that the future in situ X-ray imaging studies on spatter investigation in titanium LB-PBF process to be conducted in a lower energy beamline.
- (v) The phenomena that occur beneath the melt pool surface, like performed in [69], were not resolved in the current study. Therefore, follow-up research that explores these sub-surface phenomena can be conducted to demonstrate laser re-melting, keyhole penetration, molten pool convection, *etc.* in the oxidised condition with reference to the virgin condition.
- (vi) To further obtain a trend in the variation of melt pool behaviour with different O levels, more experiments can be conducted with varying Ti6Al4V powder O levels.
- (vii) All the mechanical tests in this work were performed on specimens manufactured in the horizontal orientation. The author proposes to investigate the recycled build

properties in other orientations such as vertical, 45° *etc.* due to the anisotropy that exists in the AM builds.

- (viii) Lastly, as mentioned in Section 2.6.2.5, powder cross-contamination can occur when the same machine or its accessories are used to handle different powder alloys. This problem is prevalent in SMEs, research institutes and Universities where dedicated machines are not allotted for a particular powder alloy. Surprisingly, to the best of the author's knowledge, no research has explored the effects of powder cross-contamination in neither EB-PBF nor LB-PBF processes. This is critical because a small fraction of cross-contaminant with different chemistry can cause a catastrophic failure of the components as demonstrated in an industrial report [190].

\*\*\*\*\*

## References

- [1] G. Lutjering, J.C. Williams, Titanium, Springer-Verlag Berlin Heidelberg, 2007. <https://doi.org/10.1007/978-3-540-73036-1>.
- [2] E. Uhlmann, R. Kersting, T. Borsoi, Additive Manufacturing of Titanium Alloy for Aircraft Components, *Procedia CIRP*. 35 (2015) 55–60. <https://doi.org/10.1016/j.procir.2015.08.061>.
- [3] D. Boruah, B. Ahmad, T.L. Lee, S. Kabra, A.K. Syed, P. McNutt, M. Doré, X. Zhang, Evaluation of residual stresses induced by cold spraying of Ti-6Al-4V on Ti-6Al-4V substrates, *Surf. Coatings Technol.* 374 (2019) 591–602. <https://doi.org/10.1016/j.surfcoat.2019.06.028>.
- [4] C. Leyens, M. Peters, Titanium and Titanium Alloys, Wiley, 2003. <https://doi.org/10.1002/3527602119>.
- [5] G. Soundarapandiyam, R. Khan, C. Johnston, B. Chen, M. Fitzpatrick, Effect of postprocessing thermal treatments on electron-beam powder bed-fused Ti6Al4V, *Mater. Des. Process. Commun.* (2020) 1–8. <https://doi.org/10.1002/mdp2.168>.
- [6] S. Liu, Y.C. Shin, Additive manufacturing of Ti6Al4V alloy : A review, *Mater. Des.* 164 (2019) 107552. <https://doi.org/10.1016/j.matdes.2018.107552>.
- [7] M. Hirsch, R. Patel, W. Li, G. Guan, R.K. Leach, S.D. Sharples, A.T. Clare, Assessing the capability of in-situ nondestructive analysis during layer based additive manufacture, *Addit. Manuf.* 13 (2017) 135–142. <https://doi.org/10.1016/j.addma.2016.10.004>.
- [8] T. DebRoy, H.L. Wei, J.S. Zuback, T. Mukherjee, J.W. Elmer, J.O. Milewski, A.M. Beese, A. Wilson-Heid, A. De, W. Zhang, Additive manufacturing of metallic components – Process, structure and properties, *Prog. Mater. Sci.* 92 (2018) 112–224. <https://doi.org/10.1016/j.pmatsci.2017.10.001>.
- [9] N.T. Aboulkhair, N.M. Everitt, I. Ashcroft, C. Tuck, Reducing porosity in AlSi10Mg parts processed by selective laser melting, *Addit. Manuf.* 1 (2014) 77–86. <https://doi.org/10.1016/j.addma.2014.08.001>.
- [10] K. V. Wong, A. Hernandez, A Review of Additive Manufacturing, *ISRN Mech. Eng.* 2012 (2012) 1–10. <https://doi.org/10.5402/2012/208760>.
- [11] K. Georgilas, R.H.U. Khan, M.E. Kartal, The influence of pulsed laser powder bed fusion process parameters on Inconel 718 material properties, *Mater. Sci. Eng. A.* 769 (2020). <https://doi.org/10.1016/j.msea.2019.138527>.
- [12] M.K. Thompson, G. Moroni, T. Vaneker, G. Fadel, R.I. Campbell, I. Gibson, A. Bernard, J. Schulz, P. Graf, B. Ahuja, F. Martina, Design for Additive Manufacturing: Trends, opportunities, considerations, and constraints, *CIRP Ann. - Manuf. Technol.* 65 (2016) 737–760. <https://doi.org/10.1016/j.cirp.2016.05.004>.
- [13] D. Herzog, V. Seyda, E. Wycisk, C. Emmelmann, Additive manufacturing of metals, *Acta Mater.* 117 (2016) 371–392. <https://doi.org/10.1016/j.actamat.2016.07.019>.
- [14] L. Loeber, S. Biamino, U. Ackelid, S. Sabbadini, P. Epicoco, P. Fino, J. Eckert,

- Comparison of selective laser and electron beam melted titanium aluminides, 22nd Annu. Int. Solid Free. Fabr. Symp. - An Addit. Manuf. Conf. SFF 2011. (2011) 547–556. <http://www.scopus.com/inward/record.url?eid=2-s2.0-84898402503&partnerID=tZOtx3y1>.
- [15] R.J. Hebert, Viewpoint: metallurgical aspects of powder bed metal additive manufacturing, *J. Mater. Sci.* 51 (2016) 1165–1175. <https://doi.org/10.1007/s10853-015-9479-x>.
- [16] A. Ferrigno, F. Di, R. Borrelli, F. Auricchio, A. Vigliotti, The mechanical strength of Ti-6Al-4V columns with regular octet microstructure manufactured by electron beam melting, *Materialia*. 5 (2019). <https://doi.org/10.1016/j.mtla.2019.100232>.
- [17] S. Chandrasekar, J.B. Coble, S. Yoder, P. Nandwana, R.R. Dehoff, V.C. Paquit, S.S. Babu, Investigating the effect of metal powder recycling in Electron beam Powder Bed Fusion using process log data, *Addit. Manuf.* 32 (2020). <https://doi.org/10.1016/j.addma.2019.100994>.
- [18] F. Calignano, Design optimization of supports for overhanging structures in aluminum and titanium alloys by selective laser melting, *Mater. Des.* 64 (2014) 203–213. <https://doi.org/10.1016/j.matdes.2014.07.043>.
- [19] Y. Bai, J. Zhang, C. Zhao, C. Li, H. Wang, Dual interfacial characterization and property in multi-material selective laser melting of 316L stainless steel and C52400 copper alloy, *Mater. Charact.* 167 (2020) 110489. <https://doi.org/10.1016/j.matchar.2020.110489>.
- [20] Q.B. Nguyen, M.L.S. Nai, Z. Zhu, C.N. Sun, J. Wei, W. Zhou, Characteristics of Inconel Powders for Powder-Bed Additive Manufacturing, *Engineering*. 3 (2017) 695–700. <https://doi.org/10.1016/J.ENG.2017.05.012>.
- [21] J. Clayton, R. Deffley, Optimising metal powders for additive manufacturing, *Met. Powder Rep.* 69 (2014) 14–17. [https://doi.org/10.1016/S0026-0657\(14\)70223-1](https://doi.org/10.1016/S0026-0657(14)70223-1).
- [22] M. Kamal, G. Rizza, 4-Design for metal additive manufacturing for aerospace applications, Elsevier Inc., 2019. <https://doi.org/10.1016/B978-0-12-814062-8.00005-4>.
- [23] M.B. Vladimir Popov, Alexander Katz-Demyanetz, Andrey Garkun, The effect of powder recycling on the mechanical properties and microstructure of electron beam melted Ti6Al4V specimens, *Addit. Manuf.* 22 (2018) 834–843. <https://doi.org/10.1016/j.addma.2018.06.003>.
- [24] C. Qiu, N.J.E. Adkins, M.M. Attallah, Microstructure and tensile properties of selectively laser-melted and of HIPed laser-melted Ti – 6Al – 4V, *Mater. Sci. Eng. A*. 578 (2013) 230–239. <https://doi.org/10.1016/j.msea.2013.04.099>.
- [25] I. Polmear, D. StJohn, J.F. Nie, M. Qian, *Light Alloys*, Butterworth-Heinemann, 2017.
- [26] M. Donachie J, *Titanium: A Technical Guide*, ASM International, 2000. <https://books.google.co.uk/books?id=HgzukknbNGAC>.
- [27] Q. Ma, Froes H. Francis, *Titanium Powder Metallurgy: Science, Technology and Applications*, 1st ed., Elsevier Inc., 2015.

- <https://doi.org/https://doi.org/10.1016/C2013-0-13619-7>.
- [28] T. Ahmed, H.J. Rack, Phase transformations during cooling in  $\alpha + \beta$  titanium alloys, *Mater. Sci. Eng. A.* 243 (1998) 206–211. [https://doi.org/10.1016/S0921-5093\(97\)00802-2](https://doi.org/10.1016/S0921-5093(97)00802-2).
- [29] M. Yan, M.S. Dargusch, T. Ebel, M. Qian, A transmission electron microscopy and three-dimensional atom probe study of the oxygen-induced fine microstructural features in as-sintered Ti-6Al-4V and their impacts on ductility, *Acta Mater.* 68 (2014) 196–206. <https://doi.org/10.1016/j.actamat.2014.01.015>.
- [30] D. Poquillon, C. Armand, J. Huez, Oxidation and oxygen diffusion in Ti-6Al-4V alloy: Improving measurements during SIMS analysis by rotating the sample, *Oxid. Met.* 79 (2013) 249–259. <https://doi.org/10.1007/s11085-013-9360-8>.
- [31] H. Guleryuz, H. Cimenoglu, Oxidation of Ti-6Al-4V alloy, *J. Alloys Compd.* 472 (2009) 241–246. <https://doi.org/10.1016/j.jallcom.2008.04.024>.
- [32] R. Gaddam, B. Sefer, R. Pederson, M.L. Antti, Study of alpha-case depth in Ti-6Al-2Sn-4Zr-2Mo and Ti-6Al-4V, *IOP Conf. Ser. Mater. Sci. Eng.* 48 (2013). <https://doi.org/10.1088/1757-899X/48/1/012002>.
- [33] R. Gaddam, M.L. Antti, R. Pederson, Influence of alpha-case layer on the low cycle fatigue properties of Ti-6Al-2Sn-4Zr-2Mo alloy, *Mater. Sci. Eng. A.* 599 (2014) 51–56. <https://doi.org/10.1016/j.msea.2014.01.059>.
- [34] J.M. Oh, B.G. Lee, S.W. Cho, S.W. Lee, G.S. Choi, J.W. Lim, Oxygen effects on the mechanical properties and lattice strain of Ti and Ti-6Al-4V, *Met. Mater. Int.* 17 (2011) 733–736. <https://doi.org/10.1007/s12540-011-1006-2>.
- [35] M. Yan, W. Xu, M.S. Dargusch, H.P. Tang, M. Brandt, M. Qian, Review of effect of oxygen on room temperature ductility of titanium and titanium alloys, *Powder Metall.* 57 (2014) 251–257. <https://doi.org/10.1179/1743290114Y.0000000108>.
- [36] S. Ford, M. Despeisse, Additive manufacturing and sustainability: an exploratory study of the advantages and challenges, *J. Clean. Prod.* 137 (2016) 1573–1587. <https://doi.org/10.1016/j.jclepro.2016.04.150>.
- [37] A. F2792-12, Standard terminology for additive manufacturing technologies, *ASTM Int.* (2012). <https://doi.org/10.1520/F2792-12A.2>.
- [38] I. Gibson, D.W. Rosen, B. Stucker, *Additive Manufacturing Technologies: Rapid Prototyping to Direct Digital Manufacturing*, 1st ed., Springer, Boston, MA, 2010. <https://doi.org/10.1007/978-1-4419-1120-9>.
- [39] A. Gomez-Gallegos, P. Mandal, D. Gonzalez, N. Zuelli, P. Blackwell, Studies on titanium alloys for aerospace application, *Defect Diffus. Forum.* 385 DDF (2018) 419–423. <https://doi.org/10.4028/www.scientific.net/DDF.385.419>.
- [40] R. Liu, Z. Wang, T. Sparks, F. Liou, J. Newkirk, Aerospace applications of laser additive manufacturing, in: *Laser Addit. Manuf.*, 2016: pp. 351–371. <https://doi.org/10.1016/B978-0-08-100433-3.00013-0>.
- [41] E. Hernández-Nava, A study on the mechanical properties of micro-truss Ti-6Al-4V materials fabricated by Electron Beam Melting, University of Sheffield, 2016.

- [42] W.E. Frazier, Metal additive manufacturing: A review, *J. Mater. Eng. Perform.* 23 (2014) 1917–1928. <https://doi.org/10.1007/s11665-014-0958-z>.
- [43] Y. Kok, X.P. Tan, P. Wang, M.L.S. Nai, N.H. Loh, E. Liu, S.B. Tor, Anisotropy and heterogeneity of microstructure and mechanical properties in metal additive manufacturing: A critical review, *Mater. Des.* 139 (2018) 565–586. <https://doi.org/10.1016/j.matdes.2017.11.021>.
- [44] K.S. Derekar, A review of wire arc additive manufacturing and advances in wire arc additive manufacturing of aluminium, *Mater. Sci. Technol.* 34 (2018) 895–916. <https://doi.org/10.1080/02670836.2018.1455012>.
- [45] S. Kumar, *Additive manufacturing processes*, 1st ed., Springer International Publishing, 2020. <https://doi.org/10.1007/978-3-030-45089-2>.
- [46] W.S.W. Harun, M.S.I.N. Kamariah, N. Muhamad, S.A.C. Ghani, F. Ahmad, Z. Mohamed, A review of powder additive manufacturing processes for metallic biomaterials, *Powder Technol.* 327 (2018) 128–151. <https://doi.org/10.1016/j.powtec.2017.12.058>.
- [47] C.A. Chatham, T.E. Long, C.B. Williams, A review of the process physics and material screening methods for polymer powder bed fusion additive manufacturing, *Prog. Polym. Sci.* 93 (2019) 68–95. <https://doi.org/10.1016/j.progpolymsci.2019.03.003>.
- [48] Z.C. Cordero, H.M. Meyer, P. Nandwana, R.R. Dehoff, Powder bed charging during electron-beam additive manufacturing, *Acta Mater.* 124 (2017) 437–445. <https://doi.org/10.1016/j.actamat.2016.11.012>.
- [49] E. Hernández-Nava, S. Tammam-Williams, C. Smith, F. Leonard, P.J. Withers, I. Todd, R. Goodall, X-ray Tomography Characterisation of Lattice Structures Processed by Selective Electron Beam Melting, *Metals (Basel)*. 7 (2017). <https://doi.org/10.3390/met7080300>.
- [50] H.P. Tang, M. Qian, N. Liu, X.Z. Zhang, G.Y. Yang, J. Wang, Effect of Powder Reuse Times on Additive Manufacturing of Ti-6Al-4V by Selective Electron Beam Melting, *Jom.* 67 (2015) 555–563. <https://doi.org/10.1007/s11837-015-1300-4>.
- [51] L.E. Murr, Metallurgy of additive manufacturing: Examples from electron beam melting, *Addit. Manuf.* 5 (2015) 40–53. <https://doi.org/10.1016/j.addma.2014.12.002>.
- [52] J. Raplee, A. Plotkowski, M.M. Kirka, R. Dinwiddie, A. Okello, R.R. Dehoff, S.S. Babu, Thermographic Microstructure Monitoring in Electron Beam Additive Manufacturing, *Sci. Rep.* 7 (2017) 1–16. <https://doi.org/10.1038/srep43554>.
- [53] C. Körner, Additive manufacturing of metallic components by selective electron beam melting - A review, *Int. Mater. Rev.* 61 (2016) 361–377. <https://doi.org/10.1080/09506608.2016.1176289>.
- [54] M. Galati, L. Iuliano, A literature review of powder-based electron beam melting focusing on numerical simulations, *Addit. Manuf.* 19 (2018) 1–20. <https://doi.org/10.1016/j.addma.2017.11.001>.
- [55] X. Zhao, S. Li, M. Zhang, Y. Liu, T.B. Sercombe, S. Wang, Y. Hao, R. Yang, L.E. Murr,

- Comparison of the microstructures and mechanical properties of Ti-6Al-4V fabricated by selective laser melting and electron beam melting, *Mater. Des.* 95 (2016) 21–31. <https://doi.org/10.1016/j.matdes.2015.12.135>.
- [56] C.L.A. Leung, R. Tosi, E. Muzangaza, S. Nonni, P.J. Withers, P.D. Lee, Effect of preheating on the thermal, microstructural and mechanical properties of selective electron beam melted Ti-6Al-4V components, *Mater. Des.* 174 (2019). <https://doi.org/10.1016/j.matdes.2019.107792>.
- [57] J. Karlsson, A. Snis, H. Engqvist, J. Lausmaa, Characterization and comparison of materials produced by Electron Beam Melting (EBM) of two different Ti-6Al-4V powder fractions, *J. Mater. Process. Technol.* 213 (2013) 2109–2118. <https://doi.org/10.1016/j.jmatprotec.2013.06.010>.
- [58] G. Soundarapandiyam, C. Johnston, R. Khan, B. Chen, M. Fitzpatrick, A technical review of the challenges of powder recycling in the laser powder bed fusion additive manufacturing process, *J. Eng.* (2021) 1–7. <https://doi.org/10.1049/tje2.12013>.
- [59] C. Zhao, K. Fezzaa, R.W. Cunningham, H. Wen, F. De Carlo, L. Chen, A.D. Rollett, T. Sun, Real-time monitoring of laser powder bed fusion process using high-speed X-ray imaging and diffraction, *Sci. Rep.* 7 (2017). <https://doi.org/10.1038/s41598-017-03761-2>.
- [60] H.K. Rafi, N. V. Karthik, H. Gong, T.L. Starr, B.E. Stucker, Microstructures and mechanical properties of Ti6Al4V parts fabricated by selective laser melting and electron beam melting, *J. Mater. Eng. Perform.* 22 (2013) 3872–3883. <https://doi.org/10.1007/s11665-013-0658-0>.
- [61] A.B. Spierings, N. Herres, G. Levy, Influence of the particle size distribution on surface quality and mechanical properties in AM steel parts, *Rapid Prototyp. J.* 17 (2011) 195–202. <https://doi.org/10.1108/13552541111124770>.
- [62] H. Lee, C.H.J. Lim, M.J. Low, N. Tham, V.M. Murukeshan, Y.J. Kim, Lasers in additive manufacturing: A review, *Int. J. Precis. Eng. Manuf. - Green Technol.* 4 (2017) 307–322. <https://doi.org/10.1007/s40684-017-0037-7>.
- [63] M. Saunders, Modulation matters - how to build all features great and small, 44 (2018) 1–7. <https://www.linkedin.com/pulse/modulation-matters-how-build-all-features-great-small-marc-saunders/#skip-link>.
- [64] M.J. Matthews, G. Guss, S.A. Khairallah, A.M. Rubenchik, P.J. Depond, W.E. King, Denudation of metal powder layers in laser powder bed fusion processes, *Acta Mater.* 114 (2016) 33–42. <https://doi.org/10.1016/j.actamat.2016.05.017>.
- [65] S.A. Khairallah, A.T. Anderson, A. Rubenchik, W.E. King, Laser powder-bed fusion additive manufacturing : Physics of complex melt flow and formation mechanisms of pores , spatter , and denudation zones, *Acta Mater.* 108 (2016) 36–45. <https://doi.org/10.1016/j.actamat.2016.02.014>.
- [66] C. Tang, K.Q. Le, C.H. Wong, Physics of humping formation in laser powder bed fusion, *Int. J. Heat Mass Transf.* 149 (2020). <https://doi.org/10.1016/j.ijheatmasstransfer.2019.119172>.

- [67] C.L.A. Leung, S. Marussi, R.C. Atwood, P.D. Lee, M. Towrie, P.J. Withers, In situ X-ray imaging of defect and molten pool dynamics in laser additive manufacturing, *Nat. Commun.* 9 (2018). <https://doi.org/10.1038/s41467-018-03734-7>.
- [68] V. Gunenthiram, P. Peyre, M. Schneider, M. Dal, F. Coste, I. Koutiri, R. Fabbro, Experimental analysis of spatter generation and melt-pool behavior during the powder bed laser beam melting process, *J. Mater. Process. Tech.* 251 (2018) 376–386. <https://doi.org/10.1016/j.jmatprotec.2017.08.012>.
- [69] C.L.A. Leung, S. Marussi, M. Towrie, R.C. Atwood, P.J. Withers, P.D. Lee, The effect of powder oxidation on defect formation in laser additive manufacturing, *Acta Mater.* 166 (2019) 294–305. <https://doi.org/10.1016/j.actamat.2018.12.027>.
- [70] Y.H. Zhou, Z.H. Zhang, Y.P. Wang, G. Liu, S.Y. Zhou, Y.L. Li, J. Shen, M. Yan, Selective laser melting of typical metallic materials: An effective process prediction model developed by energy absorption and consumption analysis, *Addit. Manuf.* 25 (2019) 204–217. <https://doi.org/10.1016/j.addma.2018.10.046>.
- [71] Y.H. Zhou, S.F. Lin, Y.H. Hou, D.W. Wang, P. Zhou, P.L. Han, Y.L. Li, M. Yan, Layered surface structure of gas-atomized high Nb-containing TiAl powder and its impact on laser energy absorption for selective laser melting, *Appl. Surf. Sci.* 441 (2018) 210–217. <https://doi.org/10.1016/j.apsusc.2018.01.296>.
- [72] W.E. King, H.D. Barth, V.M. Castillo, G.F. Gallegos, J.W. Gibbs, D.E. Hahn, C. Kamath, A.M. Rubenchik, Observation of keyhole-mode laser melting in laser powder-bed fusion additive manufacturing, *J. Mater. Process. Technol.* 214 (2014) 2915–2925. <https://doi.org/10.1016/j.jmatprotec.2014.06.005>.
- [73] R. Fabbro, Melt pool and keyhole behaviour analysis for deep penetration laser welding, *J. Phys. D. Appl. Phys.* 43 (2010). <https://doi.org/10.1088/0022-3727/43/44/445501>.
- [74] L. Sinclair, C.L.A. Leung, S. Marussi, S.J. Clark, Y. Chen, M.P. Olbinado, A. Rack, J. Gardy, G.J. Baxter, P.D. Lee, In situ radiographic and ex situ tomographic analysis of pore interactions during multilayer builds in laser powder bed fusion, *Addit. Manuf.* 36 (2020) 101512. <https://doi.org/10.1016/j.addma.2020.101512>.
- [75] P. Heinen, H. Wu, A. Olowinsky, A. Gillner, Helium-tight laser beam welding of aluminum with brilliant laser beam radiation, *Phys. Procedia.* 56 (2014) 554–565. <https://doi.org/10.1016/j.phpro.2014.08.043>.
- [76] X. Su, Y. Yang, Research on track overlapping during Selective Laser Melting of powders, *J. Mater. Process. Technol.* 212 (2012) 2074–2079. <https://doi.org/10.1016/j.jmatprotec.2012.05.012>.
- [77] L. Thijs, F. Verhaeghe, T. Craeghs, J. Van Humbeeck, J. Kruth, A study of the microstructural evolution during selective laser melting of Ti – 6Al – 4V, *Acta Mater.* 58 (2010) 3303–3312. <https://doi.org/10.1016/j.actamat.2010.02.004>.
- [78] S. Lu, H. Fujii, H. Sugiyama, M. Tanaka, K. Nogi, Weld penetration and Marangoni convection with oxide fluxes in GTA welding, *Mater. Trans.* 43 (2002) 2926–2931. <https://doi.org/10.2320/matertrans.43.2926>.
- [79] J. Shi, G. Song, J. Chi, Effect of active gas on weld appearance and performance in

- laser-TIG hybrid welded titanium alloy, *Int. J. Light. Mater. Manuf.* 1 (2018) 47–53. <https://doi.org/10.1016/j.ijlmm.2018.03.002>.
- [80] C.R. Heiple, J.R. Rope, R.T. Stagner, R.J. Aden, Surface Active Element Effects on the Shape of Gta, Laser, and Electron Beam Welds., *Weld. J. (Miami, Fla)*. 62 (1983) 72–77.
- [81] R.K. Wunderlich, Surface tension and viscosity of industrial Ti-alloys measured by the oscillating drop method on board parabolic flights, *High Temp. Mater. Process.* 27 (2008) 401–412. <https://doi.org/10.1515/HTMP.2008.27.6.401>.
- [82] H. Park, S. Rhee, Analysis of mechanism of plasma and spatter in CO2 laser welding of galvanized steel, *Opt. Laser Technol.* 31 (1999) 119–126.
- [83] K. Venkatakrisnan, B. Tan, B.K.A. Ngoi, Femtosecond pulsed laser ablation of thin gold film, *Opt. Laser Technol.* 34 (2002) 199–202.
- [84] D.K.Y. Low, L. Li, P.J. Byrd, Spatter prevention during the laser drilling of selected aerospace materials, *J. Mater. Process. Technol.* 139 (2003) 71–76. [https://doi.org/10.1016/S0924-0136\(03\)00184-5](https://doi.org/10.1016/S0924-0136(03)00184-5).
- [85] Y. Liu, Y. Yang, S. Mai, D. Wang, C. Song, Investigation into spatter behavior during selective laser melting of AISI 316L stainless steel powder, *JMADE*. 87 (2015) 797–806. <https://doi.org/10.1016/j.matdes.2015.08.086>.
- [86] Q. Guo, C. Zhao, L.I. Escano, Z. Young, L. Xiong, K. Fezzaa, W. Everhart, B. Brown, T. Sun, L. Chen, Transient dynamics of powder spattering in laser powder bed fusion additive manufacturing process revealed by in-situ high-speed high-energy x-ray imaging, *Acta Mater.* 151 (2018) 169–180. <https://doi.org/10.1016/j.actamat.2018.03.036>.
- [87] J. Yin, D. Wang, L. Yang, H. Wei, P. Dong, L. Ke, G. Wang, H. Zhu, X. Zeng, Correlation between forming quality and spatter dynamics in laser powder bed fusion, *Addit. Manuf.* 31 (2020) 100958. <https://doi.org/10.1016/j.addma.2019.100958>.
- [88] E. Santecchia, S. Spigarelli, M. Cabibbo, Material reuse in laser powder bed fusion: Side effects of the laser—metal powder interaction, *Metals (Basel)*. 10 (2020) 1–21. <https://doi.org/10.3390/met10030341>.
- [89] Z.A. Young, Q. Guo, N.D. Parab, C. Zhao, M. Qu, L.I. Escano, K. Fezzaa, W. Everhart, T. Sun, L. Chen, Types of spatter and their features and formation mechanisms in laser powder bed fusion additive manufacturing process, *Addit. Manuf.* 36 (2020) 101438. <https://doi.org/10.1016/j.addma.2020.101438>.
- [90] A.R. Nassar, M.A. Gundermann, E.W. Reutzel, P. Guerrier, M.H. Krane, M.J. Weldon, Formation processes for large ejecta and interactions with melt pool formation in powder bed fusion additive manufacturing, *Sci. Rep.* 9 (2019) 1–11. <https://doi.org/10.1038/s41598-019-41415-7>.
- [91] A. Bin Anwar, Q.C. Pham, Study of the spatter distribution on the powder bed during selective laser melting, *Addit. Manuf.* 22 (2018) 86–97. <https://doi.org/10.1016/j.addma.2018.04.036>.
- [92] D. Wang, S. Wu, F. Fu, S. Mai, Y. Yang, Y. Liu, C. Song, Mechanisms and characteristics of spatter generation in SLM processing and its effect on the properties, *Mater. Des.*

- 117 (2017) 121–130. <https://doi.org/10.1016/j.matdes.2016.12.060>.
- [93] J.W. Carson, B.H. Pittenger, Bulk Properties of Powders, *Powder Met. Technol. Appl. ASM Handb.* 7 (1998) 287–301. <https://doi.org/10.1361/asmhba0001530>.
- [94] A.T. Sutton, C.S. Kriewall, M.C. Leu, J.W. Newkirk, Powders for Additive Manufacturing Processes: Characterization Techniques and Effects on Part Properties, *Solid Free. Fabr. 2016 Proc. 26th Annu. Int. Solid Free. Fabr. Symp. – An Addit. Manuf. Conf.* (2016) 1004–1030. <https://doi.org/10.1080/17452759.2016.1250605>.
- [95] M.J. Heiden, L.A. Deibler, J.M. Rodelas, J.R. Koepke, D.J. Tung, D.J. Saiz, B.H. Jared, Evolution of 316L stainless steel feedstock due to laser powder bed fusion process, *Addit. Manuf.* 25 (2019) 84–103. <https://doi.org/10.1016/j.addma.2018.10.019>.
- [96] S. Pal, G. Lojen, R. Hudak, V. Rajtukova, T. Brajliah, V. Kokol, I. Drstvenšek, As-fabricated surface morphologies of Ti-6Al-4V samples fabricated by different laser processing parameters in selective laser melting, *Addit. Manuf.* 33 (2020) 101147. <https://doi.org/10.1016/j.addma.2020.101147>.
- [97] R. Esmaeilzadeh, U. Ali, A. Keshavarzkermani, Y. Mahmoodkhani, On the effect of spatter particles distribution on the quality of Hastelloy X parts made by laser powder-bed fusion additive manufacturing, *J. Manuf. Process.* 37 (2019) 11–20. <https://doi.org/10.1016/j.jmapro.2018.11.012>.
- [98] A. Ladewig, G. Schlick, M. Fisser, V. Schulze, U. Glatzel, Influence of the shielding gas flow on the removal of process by-products in the selective laser melting process, *Addit. Manuf.* 10 (2016) 1–9. <https://doi.org/10.1016/j.addma.2016.01.004>.
- [99] S.A. Khairallah, Spatter reduction laser scanning strategy in selective laser melting US 10,449,632, United States Pat. 2 (2019).
- [100] G. Chen, S.Y. Zhao, P. Tan, J. Wang, C.S. Xiang, H.P. Tang, A comparative study of Ti-6Al-4V powders for additive manufacturing by gas atomization, plasma rotating electrode process and plasma atomization, *Powder Technol.* 333 (2018) 38–46. <https://doi.org/10.1016/j.powtec.2018.04.013>.
- [101] S. Vock, B. Klöden, A. Kirchner, T. Weißgärber, B. Kieback, Powders for powder bed fusion: a review, *Prog. Addit. Manuf.* 4 (2019) 383–397. <https://doi.org/10.1007/s40964-019-00078-6>.
- [102] B.J. Dawes, R. Bowerman, Introduction to the Additive Manufacturing Powder Metallurgy Supply Chain Exploring the production and supply of metal powders for AM processes, *Johnson Matthey Technol. Rev.* 59 (2015) 243–256.
- [103] S. Tammas-Williams, P.J. Withers, I. Todd, P.B. Prangnell, The Effectiveness of Hot Isostatic Pressing for Closing Porosity in Titanium Parts Manufactured by Selective Electron Beam Melting, *Metall. Mater. Trans. A Phys. Metall. Mater. Sci.* 47 (2016) 1939–1946. <https://doi.org/10.1007/s11661-016-3429-3>.
- [104] Z.Z. Fang, J.D. Paramore, P. Sun, K.S.R. Chandran, Y. Zhang, Y. Xia, F. Cao, M. Koopman, M. Free, Powder metallurgy of titanium—past, present, and future, *Int. Mater. Rev.* 63 (2018) 407–459. <https://doi.org/10.1080/09506608.2017.1366003>.

- [105] A.T. Sutton, C.S. Kriewall, M.C. Leu, J.W. Newkirk, Powder characterisation techniques and effects of powder characteristics on part properties in powder-bed fusion processes, *Virtual Phys. Prototyp.* 12 (2017) 3–29. <https://doi.org/10.1080/17452759.2016.1250605>.
- [106] Y. Sun, M. Aindow, R.J. Hebert, The effect of recycling on the oxygen distribution in Ti-6Al-4V powder for additive manufacturing, *Mater. High Temp.* 35 (2017) 217–224. <https://doi.org/10.1080/09603409.2017.1389133>.
- [107] W. Nan, M. Pasha, T. Bonakdar, A. Lopez, U. Zafar, S. Nadimi, M. Ghadiri, Jamming during particle spreading in additive manufacturing, *Powder Technol.* 338 (2018) 253–262. <https://doi.org/10.1016/j.powtec.2018.07.030>.
- [108] M. Ahmed, M. Pasha, W. Nan, M. Ghadiri, A simple method for assessing powder spreadability for additive manufacturing, *Powder Technol.* 367 (2020) 671–679. <https://doi.org/10.1016/j.powtec.2020.04.033>.
- [109] ASTM B214, Standard Test Method for Sieve Analysis of Metal Powders, ASTM Int. (2015). <https://doi.org/10.1520/B0214-16.2>.
- [110] ASTM B822, Standard Test Method for Particle Size Distribution of Metal Powders and Related Compounds by Light Scattering, ASTM Int. (2017) 1–5. <https://doi.org/10.1520/B0822-17.2>.
- [111] C. Meier, R. Weissbach, J. Weinberg, W.A. Wall, A. John Hart, Modeling and characterization of cohesion in fine metal powders with a focus on additive manufacturing process simulations, *Powder Technol.* 343 (2019) 855–866. <https://doi.org/10.1016/j.powtec.2018.11.072>.
- [112] A. Averardi, C. Cola, S.E. Zeltmann, N. Gupta, Effect of particle size distribution on the packing of powder beds: A critical discussion relevant to additive manufacturing, *Mater. Today Commun.* 24 (2020) 100964. <https://doi.org/10.1016/j.mtcomm.2020.100964>.
- [113] P. Daniel, R.E.W. Allan, G. Louise, B. Neil, Understanding powder degradation in metal additive manufacturing to allow the upcycling of recycled powders, *J. Clean. Prod.* 268 (2020). <https://doi.org/10.1016/j.jclepro.2020.122077>.
- [114] A.B. Spierings, M. Voegtlin, T. Bauer, K. Wegener, Powder flowability characterisation methodology for powder-bed-based metal additive manufacturing, *Prog. Addit. Manuf.* 1 (2016) 9–20. <https://doi.org/10.1007/s40964-015-0001-4>.
- [115] Z. Snow, R. Martukanitz, S. Joshi, On the development of powder spreadability metrics and feedstock requirements for powder bed fusion additive manufacturing, *Addit. Manuf.* 28 (2019) 78–86. <https://doi.org/10.1016/j.addma.2019.04.017>.
- [116] S. Haeri, Y. Wang, O. Ghita, J. Sun, Discrete element simulation and experimental study of powder spreading process in additive manufacturing, *Powder Technol.* 306 (2017) 45–54. <https://doi.org/10.1016/j.powtec.2016.11.002>.
- [117] B. Liu, R. Wildman, C. Tuck, I. Ashcroft, R. Hague, Investigation the Effect of Particle Size Distribution on Processing Parameters Optimisation in Selective Laser Melting

- Process, in: 22nd Annu. Int. Solid Free. Fabr. Symp. - An Addit. Manuf. Conf., 2011: pp. 227–238.
- [118] D. Yao, X. An, H. Fu, H. Zhang, X. Yang, Q. Zou, K. Dong, Dynamic investigation on the powder spreading during selective laser melting additive manufacturing, *Addit. Manuf.* 37 (2021) 101707. <https://doi.org/10.1016/j.addma.2020.101707>.
- [119] H. Gruber, M. Henriksson, E. Hryha, L. Nyborg, Effect of Powder Recycling in Electron Beam Melting on the Surface Chemistry of Alloy 718 Powder, *Metall. Mater. Trans. A.* 50 (2019) 4410–4422. <https://doi.org/10.1007/s11661-019-05333-7>.
- [120] A.N.D. Gasper, B. Szost, X. Wang, D. Johns, S. Sharma, A.T. Clare, I.A. Ashcroft, Spatter and oxide formation in laser powder bed fusion of Inconel 718, *Addit. Manuf.* 24 (2018) 446–456. <https://doi.org/10.1016/j.addma.2018.09.032>.
- [121] K.C. Mills, B.J. Keene, R.F. Brooks, A. Shirali, Marangoni effects in welding, *Philos. Trans. R. Soc. A Math. Phys. Eng. Sci.* 356 (1998) 911–925. <https://doi.org/10.1098/rsta.1998.0196>.
- [122] I.E. Anderson, E.M.H. White, R. Dehoff, Feedstock powder processing research needs for additive manufacturing development, *Curr. Opin. Solid State Mater. Sci.* 22 (2018) 8–15. <https://doi.org/10.1016/j.cossms.2018.01.002>.
- [123] P. Sun, Z.Z. Fang, Y. Zhang, Y. Xia, Review of the Methods for Production of Spherical Ti and Ti Alloy Powder, *Jom.* 69 (2017) 1853–1860. <https://doi.org/10.1007/s11837-017-2513-5>.
- [124] Jackson Beau, Pyrogenesis Eliminates Tungsten Contamination in Metal Additive Powders, (2018). <https://3dprintingindustry.com/news/pyrogenesis-eliminates-tungsten-contamination-metal-additive-powders-130687/> (accessed May 19, 2020).
- [125] E. Santecchia, P. Mengucci, A. Gatto, E. Bassoli, S. Defanti, G. Barucca, Cross-Contamination Quantification in Powders for Additive Manufacturing: A Study on Ti-6Al-4V and Maraging steel, *Materials (Basel)*. 12 (2019). <https://doi.org/10.3390/ma12152342>.
- [126] V. Petrovic, R. Niñerola, Powder recyclability in electron beam melting for aeronautical use, *Aircr. Eng. Aerosp. Technol.* 87 (2015) 147–155. <https://doi.org/10.1108/AEAT-11-2013-0212>.
- [127] F. Le Bourhis, O. Kerbrat, L. Dembinski, J.Y. Hascoet, P. Mognol, Predictive model for environmental assessment in additive manufacturing process, *Procedia CIRP.* 15 (2014) 26–31. <https://doi.org/10.1016/j.procir.2014.06.031>.
- [128] P. Nandwana, W.H. Peter, R.R. Dehoff, L.E. Lowe, M.M. Kirka, F. Medina, S.S. Babu, Recyclability Study on Inconel 718 and Ti-6Al-4V Powders for Use in Electron Beam Melting, *Metall. Mater. Trans. B.* 47 (2016) 754–762. <https://doi.org/10.1007/s11663-015-0477-9>.
- [129] Y. Cao, M. Delin, F. Kullenberg, L. Nyborg, Surface modification of Ti-6Al-4V powder during recycling in EBM process, *Surf. Interface Anal.* 52 (2020) 1066–1070. <https://doi.org/10.1002/sia.6847>.

- [130] S. Ghods, E. Schultz, C. Wisdom, R. Schur, R. Pahuja, A. Montelione, D. Arola, M. Ramulu, Electron Beam Additive Manufacturing of Ti6Al4V: Evolution of Powder Morphology and Part Microstructure with Powder Reuse, *Materialia*. 9 (2020) 100631. <https://doi.org/10.1016/j.mtla.2020.100631>.
- [131] P.E. Carrion, A. Soltani-Tehrani, N. Phan, N. Shamsaei, Powder Recycling Effects on the Tensile and Fatigue Behavior of Additively Manufactured Ti-6Al-4V Parts, *Jom*. 71 (2019) 963–973. <https://doi.org/10.1007/s11837-018-3248-7>.
- [132] M. Skalon, B. Meier, T. Leitner, S. Arneitz, S.T. Amancio-Filho, C. Sommitsch, Reuse of Ti6Al4V Powder and Its Impact on Surface Tension, Melt Pool Behavior and Mechanical Properties of Additively Manufactured Components, *Materials (Basel)*. 14 (2021) 1251. <https://doi.org/10.3390/ma14051251>.
- [133] R. Harkin, H. Wu, S. Nikam, J. Quinn, S. McFadden, Reuse of grade 23 ti6al4v powder during the laser-based powder bed fusion process, *Metals (Basel)*. 10 (2020) 1–14. <https://doi.org/10.3390/met10121700>.
- [134] L. Denti, A. Sola, S. Defanti, C. Sciancalepore, F. Bondioli, Effect of powder recycling in laser-based powder bed fusion of Ti-6Al-4V, *Manuf. Technol.* 19 (2019) 190–196. <https://doi.org/10.21062/ujep/268.2019/a/1213-2489/mt/19/2/190>.
- [135] L. Cordova, M. Campos, T. Tinga, Revealing the Effects of Powder Reuse for Selective Laser Melting by Powder Characterization, *Jom*. 71 (2019) 1062–1072. <https://doi.org/10.1007/s11837-018-3305-2>.
- [136] V. Seyda, N. Kaufmann, C. Emmelmann, Investigation of aging processes of Ti-6Al-4V powder material in laser melting, *Phys. Procedia*. 39 (2012) 425–431. <https://doi.org/10.1016/j.phpro.2012.10.057>.
- [137] M.H. Farshidianfar, A. Khajepour, A.P. Gerlich, Effect of real-time cooling rate on microstructure in Laser Additive Manufacturing, *J. Mater. Process. Technol.* 231 (2016) 468–478. <https://doi.org/10.1016/j.jmatprotec.2016.01.017>.
- [138] H. Galarraga, D.A. Lados, R.R. Dehoff, M.M. Kirka, P. Nandwana, Effects of the microstructure and porosity on properties of Ti-6Al-4V ELI alloy fabricated by electron beam melting (EBM), *Addit. Manuf.* 10 (2016) 47–57. <https://doi.org/10.1016/j.addma.2016.02.003>.
- [139] M. Seifi, A. Salem, D. Satko, J. Shaffer, J.J. Lewandowski, Defect distribution and microstructure heterogeneity effects on fracture resistance and fatigue behavior of EBM Ti-6Al-4V, *Int. J. Fatigue*. 94 (2017) 263–287. <https://doi.org/10.1016/j.ijfatigue.2016.06.001>.
- [140] H. Gong, K. Rafi, H. Gu, G.D. Janaki Ram, T. Starr, B. Stucker, Influence of defects on mechanical properties of Ti-6Al-4V components produced by selective laser melting and electron beam melting, *Mater. Des.* 86 (2015) 545–554. <https://doi.org/10.1016/j.matdes.2015.07.147>.
- [141] N. Hrabe, T. Gnäupel-Herold, T. Quinn, Fatigue Properties of a Titanium Alloy (Ti-6Al-4V) Fabricated Via Electron Beam Melting (EBM): Effects of Internal Defects and Residual Stress, *Int. J. Fatigue*. 94 (2017) 202–210.
- [142] V. Chastand, P. Quaegebeur, W. Maia, E. Charkaluk, Comparative study of fatigue

- properties of Ti-6Al-4V specimens built by electron beam melting (EBM) and selective laser melting (SLM), *Mater. Charact.* 143 (2018) 76–81. <https://doi.org/10.1016/j.matchar.2018.03.028>.
- [143] F.J. Alamos, J. Schiltz, K. Kozlovsky, R. Attardo, C. Tomonto, T. Pelletiers, S.R. Schmid, Effect of powder reuse on mechanical properties of Ti-6Al-4V produced through selective laser melting, *Int. J. Refract. Met. Hard Mater.* 91 (2020) 105273. <https://doi.org/10.1016/j.ijrmhm.2020.105273>.
- [144] A. Farid, A. Usman, S. Dyuti, M. Ehsan, C. Kaylie, M. Yahya, T. Ehsan, Study of powder recycling and its effect on printed parts during laser powder-bed fusion of 17-4 PH stainless steel, *Jounal Mater. Process Tech.* 278 (2020) 116522. <https://doi.org/10.1016/j.jmatprotec.2019.116522>.
- [145] N. Hrabe, T. Quinn, Effects of processing on microstructure and mechanical properties of a titanium alloy (Ti-6Al-4V) fabricated using electron beam melting (EBM), Part 2: Energy input, orientation, and location, *Mater. Sci. Eng. A.* 573 (2013) 271–277. <https://doi.org/10.1016/j.msea.2013.02.065>.
- [146] A.M. Khorasani, I. Gibson, U.S. Awan, A. Ghaderi, The effect of SLM process parameters on density, hardness, tensile strength and surface quality of Ti-6Al-4V, *Addit. Manuf.* 25 (2019) 176–186. <https://doi.org/10.1016/j.addma.2018.09.002>.
- [147] Z.H. Jiao, R.D. Xu, H.C. Yu, X.R. Wu, Evaluation on Tensile and Fatigue Crack Growth Performances of Ti6Al4V Alloy Produced by Selective Laser Melting, *Procedia Struct. Integr.* 7 (2017) 124–132. <https://doi.org/10.1016/j.prostr.2017.11.069>.
- [148] B. Wysocki, P. Maj, R. Sitek, J. Buhagiar, K.J. Kurzydłowski, W. Świeszkowski, Laser and electron beam additive manufacturing methods of fabricating titanium bone implants, *Appl. Sci.* 7 (2017) 1–20. <https://doi.org/10.3390/app7070657>.
- [149] N. Hrabe, T. Quinn, Effects of processing on microstructure and mechanical properties of a titanium alloy (Ti-6Al-4V) fabricated using electron beam melting (EBM), part 1: Distance from build plate and part size, *Mater. Sci. Eng. A.* 573 (2013) 264–270. <https://doi.org/10.1016/j.msea.2013.02.064>.
- [150] J.K. Algardh, T. Horn, H. West, R. Aman, A. Snis, H. Engqvist, J. Lausmaa, O. Harrysson, Thickness dependency of mechanical properties for thin-walled titanium parts manufactured by Electron Beam Melting (EBM), *Addit. Manuf.* 12 (2016) 45–50. <https://doi.org/10.1016/j.addma.2016.06.009>.
- [151] V.S. Sufiiarov, A.A. Popovich, E. V. Borisov, I.A. Polozov, D. V. Masaylo, A. V. Orlov, The Effect of Layer Thickness at Selective Laser Melting, *Procedia Eng.* 174 (2017) 126–134. <https://doi.org/10.1016/j.proeng.2017.01.179>.
- [152] S. Raghavan, M.L.S. Nai, P. Wang, W.J. Sin, T. Li, J. Wei, Heat treatment of electron beam melted (EBM) Ti-6Al-4V: microstructure to mechanical property correlations, *Rapid Prototyp. J.* 24 (2018) 774–783. <https://doi.org/10.1108/RPJ-05-2016-0070>.
- [153] X. Yan, S. Yin, C. Chen, C. Huang, R. Bolot, R. Lupoi, M. Kuang, W. Ma, C. Coddet, H. Liao, M. Liu, Effect of heat treatment on the phase transformation and mechanical properties of Ti6Al4V fabricated by selective laser melting, *J. Alloys Compd.* 764 (2018) 1056–1071. <https://doi.org/10.1016/j.jallcom.2018.06.076>.

- [154] V. Seyda, D. Herzog, C. Emmelmann, Relationship between powder characteristics and part properties in laser beam melting of Ti-6Al-4V, and implications on quality, *J. Laser Appl.* 29 (2017) 022311. <https://doi.org/10.2351/1.4983240>.
- [155] W.A. Grell, E. Solis-Ramos, E. Clark, E. Lucon, E.J. Garboczi, P.K. Predecki, Z. Loftus, M. Kumosa, Effect of powder oxidation on the impact toughness of electron beam melting Ti-6Al-4V, *Addit. Manuf.* 17 (2017) 123–134. <https://doi.org/10.1016/j.addma.2017.08.002>.
- [156] E. Olson, Particle shape factors and their use in image analysis-part 1: theory, *J. GxP Compliance.* 15 (2011) 85–96.
- [157] G. Soundarapandiyam, C. Johnston, R.H.U. Khan, C.L.A. Leung, P.D. Lee, E. Hernández-Nava, B. Chen, M.E. Fitzpatrick, The effects of powder reuse on the mechanical response of electron beam additively manufactured Ti6Al4V parts, *Addit. Manuf.* 46 (2021) 102101. <https://doi.org/10.1016/j.addma.2021.102101>.
- [158] X. Zhang, F. Martina, J. Ding, X. Wang, S.W. Williams, Fracture toughness and fatigue crack growth rate properties in wire + arc additive manufactured Ti-6Al-4V, *Fatigue Fract. Eng. Mater. Struct.* 40 (2017) 790–803. <https://doi.org/10.1111/ffe.12547>.
- [159] C.L.A. Leung, X-ray imaging of powder consolidation during laser additive manufacturing, University of Manchester, 2017.
- [160] C. Dharmendra, R. Alaghmandfard, A. Hadadzadeh, B.S. Amirkhiz, M. Mohammadi, Influence of build orientation on small-scale properties of electron beam melted Ti-6Al-4V, *Mater. Lett.* 266 (2020) 126970. <https://doi.org/10.1016/j.matlet.2019.126970>.
- [161] M. Koike, P. Greer, K. Owen, G. Lilly, L.E. Murr, S.M. Gaytan, E. Martinez, T. Okabe, Evaluation of titanium alloys fabricated using rapid prototyping technologies-electron beam melting and laser beam melting, *Materials (Basel)*. 4 (2011) 1776–1792. <https://doi.org/10.3390/ma4101776>.
- [162] E. Baril, L.P. Lefebvre, Y. Thomas, Interstitial elements in titanium powder metallurgy: Sources and control, *Powder Metall.* 54 (2011) 183–186. <https://doi.org/10.1179/174329011X13045076771759>.
- [163] L.C. Ardila, F. Garciandia, J.B. González-Díaz, P. Álvarez, A. Echeverria, M.M. Petite, R. Deffley, J. Ochoa, Effect of IN718 recycled powder reuse on properties of parts manufactured by means of Selective Laser Melting, *Phys. Procedia.* 56 (2014) 99–107. <https://doi.org/10.1016/j.phpro.2014.08.152>.
- [164] B. Gao, H. Peng, Y. Liang, J. Lin, B. Chen, Electron beam melted TiC/high Nb-TiAl nanocomposite: Microstructure and mechanical property, *Mater. Sci. Eng. A.* 811 (2021). <https://doi.org/10.1016/j.msea.2021.141059>.
- [165] N. Shen, K. Chou, Numerical Thermal Analysis in Electron Beam Additive Manufacturing with Preheating Effects, *Proc. ASME 2012 Int. Manuf. Sci. Eng. Conf.* (2012) 774–784.
- [166] E. Landau, E. Tiferet, Y.I. Ganor, R.K. Ganeriwala, M.J. Matthews, D. Braun, M. Chonin, G. Ziskind, Thermal characterization of the build chamber in electron beam

- melting, *Addit. Manuf.* 36 (2020) 101535. <https://doi.org/10.1016/j.addma.2020.101535>.
- [167] K. Zhang, J. Mei, N. Wain, X. Wu, Effect of Hot-Isostatic-Pressing Parameters on the Microstructure and Properties of Powder Ti-6Al-4V Hot-Isostatically-Pressed Samples, *Metall. Mater. Trans. A.* 41 (2010) 1033–1045. <https://doi.org/10.1007/s11661-009-0149-y>.
- [168] A. Montelione, S. Ghods, R. Schur, C. Wisdom, D. Arola, M. Ramulu, Powder Reuse in Electron Beam Melting Additive Manufacturing of Ti6Al4V: Particle Microstructure, Oxygen Content and Mechanical Properties, *Addit. Manuf.* 35 (2020) 101216. <https://doi.org/10.1016/j.addma.2020.101216>.
- [169] C. Ledford, M. Tung, C. Rock, T. Horn, Real time monitoring of electron emissions during electron beam powder bed fusion for arbitrary geometries and toolpaths, *Addit. Manuf.* 34 (2020) 101365. <https://doi.org/10.1016/j.addma.2020.101365>.
- [170] C. Wei, X. Ma, X. Yang, M. Zhou, C. Wang, Y. Zheng, W. Zhang, Z. Li, Microstructural and property evolution of Ti6Al4V powders with the number of usage in additive manufacturing by electron beam melting, *Mater. Lett.* 221 (2018) 111–114. <https://doi.org/10.1016/j.matlet.2018.03.124>.
- [171] C. de Formanoir, S. Michotte, O. Rigo, L. Germain, S. Godet, Electron beam melted Ti-6Al-4V: Microstructure, texture and mechanical behavior of the as-built and heat-treated material, *Mater. Sci. Eng. A.* 652 (2016) 105–119. <https://doi.org/10.1016/j.msea.2015.11.052>.
- [172] Y. Kim, E. Kim, Y. Song, S. Ho, Y. Kwon, Microstructure and mechanical properties of hot isostatically pressed Ti – 6Al – 4V alloy, *J. Alloys Compd.* 603 (2014) 207–212. <https://doi.org/10.1016/j.jallcom.2014.03.022>.
- [173] H. Masuo, Y. Tanaka, S. Morokoshi, H. Yagura, T. Uchida, Y. Yamamoto, Y. Murakami, Influence of defects, surface roughness and HIP on the fatigue strength of Ti-6Al-4V manufactured by additive manufacturing, *Int. J. Fatigue.* 117 (2018) 163–179. <https://doi.org/10.1016/j.ijfatigue.2018.07.020>.
- [174] A. du Plessis, E. Macdonald, Hot isostatic pressing in metal additive manufacturing: X-ray tomography reveals details of pore closure, *Addit. Manuf.* 34 (2020) 101191. <https://doi.org/10.1016/j.addma.2020.101191>.
- [175] J. Günther, D. Krewerth, T. Lippmann, S. Leuders, T. Tröster, A. Weidner, H. Biermann, T. Niendorf, Fatigue life of additively manufactured Ti-6Al-4V in the very high cycle fatigue regime, *Int. J. Fatigue.* 94 (2017) 236–245. <https://doi.org/10.1016/j.ijfatigue.2016.05.018>.
- [176] R.K. Gupta, V.A. Kumar, S. Chhangani, Study on Variants of Solution Treatment and Aging Cycle of Titanium Alloy Ti6Al4V, *J. Mater. Eng. Perform.* (2016). <https://doi.org/10.1007/s11665-016-1993-8>.
- [177] H. Sharma, D. Parfitt, A.K. Syed, D. Wimpenny, E. Muzangaza, G. Baxter, B. Chen, A critical evaluation of the microstructural gradient along the build direction in electron beam melted Ti-6Al-4V alloy, *Mater. Sci. Eng. A.* 744 (2019) 182–194. <https://doi.org/10.1016/j.msea.2018.12.016>.

- [178] H. Galarraga, R.J. Warren, D.A. Lados, R.R. Deho, M.M. Kirka, P. Nandwana, Effects of heat treatments on microstructure and properties of Ti-6Al-4V ELI alloy fabricated by electron beam melting (EBM), *Addit. Manuf.* 685 (2016) 417–428. <https://doi.org/10.1016/j.msea.2017.01.019>.
- [179] D. Greitemeier, F. Palm, F. Syassen, T. Melz, Fatigue performance of additive manufactured TiAl6V4 using electron and laser beam melting, *Int. J. Fatigue.* 94 (2017) 211–217. <https://doi.org/10.1016/j.ijfatigue.2016.05.001>.
- [180] L. Tang, J. Fan, H. Kou, B. Tang, J. Li, Effect of oxygen variation on high cycle fatigue behavior of Ti-6Al-4V titanium alloy, *Materials (Basel)*. 13 (2020) 1–16. <https://doi.org/10.3390/ma13173858>.
- [181] R. Cunningham, A. Nicolas, J. Madsen, E. Fodran, E. Anagnostou, M.D. Sangid, A.D. Rollett, Analyzing the effects of powder and post-processing on porosity and properties of electron beam melted Ti-6Al-4V, *Mater. Res. Lett.* 5 (2017) 516–525. <https://doi.org/10.1080/21663831.2017.1340911>.
- [182] S. Tammas-Williams, P.J. Withers, I. Todd, P.B. Prangnell, Porosity regrowth during heat treatment of hot isostatically pressed additively manufactured titanium components, *Scr. Mater.* 122 (2016) 72–76. <https://doi.org/10.1016/j.scriptamat.2016.05.002>.
- [183] M. Simonelli, Y.Y. Tse, C. Tuck, Effect of the build orientation on the mechanical properties and fracture modes of SLM Ti-6Al-4V, *Mater. Sci. Eng. A.* 616 (2014) 1–11. <https://doi.org/10.1016/j.msea.2014.07.086>.
- [184] G. Zhang, J. Chen, M. Zheng, Z. Yan, X. Lu, X. Lin, W. Huang, Element vaporization of Ti-6Al-4V alloy during selective laser melting, *Metals (Basel)*. 10 (2020) 1–14. <https://doi.org/10.3390/met10040435>.
- [185] C. Qiu, C. Panwisawas, M. Ward, H.C. Basoalto, J.W. Brooks, M.M. Attallah, On the role of melt flow into the surface structure and porosity development during selective laser melting, *Acta Mater.* 96 (2015) 72–79. <https://doi.org/10.1016/j.actamat.2015.06.004>.
- [186] C.L.A. Leung, S. Marussi, M. Towrie, J. del Val Garcia, R.C. Atwood, A.J. Bodey, J.R. Jones, P.J. Withers, P.D. Lee, Laser-matter interactions in additive manufacturing of stainless steel SS316L and 13-93 bioactive glass revealed by in situ X-ray imaging, *Addit. Manuf.* 24 (2018) 647–657. <https://doi.org/10.1016/j.addma.2018.08.025>.
- [187] D. Wu, X. Hua, D. Ye, F. Li, Understanding of humping formation and suppression mechanisms using the numerical simulation, *Int. J. Heat Mass Transf.* 104 (2017) 634–643. <https://doi.org/10.1016/j.ijheatmasstransfer.2016.08.110>.
- [188] T.C. Nguyen, D.C. Weckman, D.A. Johnson, H.W. Kerr, The humping phenomenon during high speed gas metal arc welding, *Sci. Technol. Weld. Join.* 10 (2005) 447–459. <https://doi.org/10.1179/174329305X44134>.
- [189] M. V. Diamanti, B. Del Curto, M.P. Pedferri, Interference colors of thin oxide layers on titanium, *Color Res. Appl.* 33 (2008) 221–228. <https://doi.org/10.1002/col.20403>.
- [190] P. Carroll, To understand Additive Manufacturing from the perspective of the

Powder, LPW Technol. (2017).  
[https://mapp.ac.uk/uploads/files/Launch\\_310117\\_Phil\\_Carroll\\_LPW\\_Technology.pdf](https://mapp.ac.uk/uploads/files/Launch_310117_Phil_Carroll_LPW_Technology.pdf) (accessed January 27, 2019).

\*\*\*\*\*

## Appendix A

**Table A.1.** Previous literature on Ti6Al4V powder recycling in EB-PBF and LB-PBF processes.

<b>Process</b>	<b>Reuse times</b>	<b>Impact on powder properties</b>	<b>Impact on part properties</b>	<b>Reference</b>
EB-PBF	16	<ul style="list-style-type: none"> <li>• O content increased and Al content decreased.</li> <li>• No change in PSD and particle shape.</li> </ul>	No change in microstructure.	[126]
EB-PBF	30	<ul style="list-style-type: none"> <li>• Coarsening of <math>\alpha</math> laths.</li> <li>• Fractured particle surface.</li> <li>• Surface hardening due to oxidation.</li> </ul>	Not reported	[168]
EB-PBF	30	<ul style="list-style-type: none"> <li>• Increase in O and Fe contents.</li> <li>• Narrow PSD- number of fine particles decreased while number of sintered particles increased.</li> <li>• Dimples on surface of recycled powder.</li> </ul>	No change in microstructure.	[130]
EB-PBF	69	<ul style="list-style-type: none"> <li>• Increase in O and C content.</li> <li>• Surface deformation of recycled powder.</li> <li>• Increase in number of agglomerated particles.</li> </ul>	<ul style="list-style-type: none"> <li>• No change in microstructure.</li> <li>• Increase in YS and UTS and decrease in elongation.</li> <li>• Decrease in high cycle fatigue life.</li> </ul>	[23]
EB-PBF	21	<ul style="list-style-type: none"> <li>• Increase in O content and decrease in Al and V content.</li> <li>• Narrower PSD.</li> <li>• Increase in powder surface roughness.</li> <li>• Increase in powder flow.</li> <li>• No change in apparent density</li> </ul>	<ul style="list-style-type: none"> <li>• Decrease in material density.</li> <li>• Increase in YS and UTS with no change in elongation.</li> </ul>	[50]

EB-PBF	30	<ul style="list-style-type: none"> <li>• Increase in O content.</li> <li>• Decrease in number of fine particles.</li> <li>• Increase in powder surface roughness.</li> <li>• Increase in number of agglomerated particles.</li> <li>• Narrower PSD.</li> <li>• Coarsening of <math>\alpha</math>-plates with precipitated <math>\beta</math>-phase boundaries.</li> </ul>	Not reported	[106]
EB-PBF	6	<ul style="list-style-type: none"> <li>• Increase in O content.</li> <li>• No significant change in powder morphology.</li> <li>• No change in PSD.</li> <li>• Flowability increased initially and then remained steady.</li> </ul>	Not reported	[128]
EB-PBF	10	<ul style="list-style-type: none"> <li>• Thicker oxide layer in recycled powder.</li> <li>• Increase in powder surface roughness.</li> </ul>	Not reported.	[129]
LB-PBF	12	<ul style="list-style-type: none"> <li>• Widening of PSD.</li> <li>• Increase in number of coarser particles.</li> <li>• Decrease in number of fine particles.</li> <li>• Increase in flowability and apparent density.</li> </ul>	<ul style="list-style-type: none"> <li>• Number of pores decreased while the pore size decreased.</li> <li>• Increase in hardness, YS and UTS.</li> </ul>	[136]
LB-PBF	15	<ul style="list-style-type: none"> <li>• Narrowing of PSD.</li> <li>• Increase in powder flow.</li> <li>• Decrease in number of satellite particles.</li> <li>• Increase in O content with no change in N content.</li> </ul>	<ul style="list-style-type: none"> <li>• No change in microstructure.</li> <li>• Decrease in pore size.</li> <li>• Increase in high cycle fatigue life.</li> <li>• Increase in YS and UTS with no change in elongation.</li> </ul>	[131]

LB-PBF	11	<ul style="list-style-type: none"> <li>• Negligible change in powder morphology.</li> <li>• Decrease in number of fine particles.</li> <li>• No change in O content.</li> <li>• No change in powder particle microstructure.</li> <li>• Increase in powder flow.</li> <li>• No change in powder packing ratio.</li> </ul>	Not reported.	[135]
LB-PBF	12	<ul style="list-style-type: none"> <li>• Marginal change in powder PSD.</li> <li>• Decrease in powder sphericity.</li> <li>• Increase in O content.</li> <li>• Increase in N content.</li> </ul>	<ul style="list-style-type: none"> <li>• No change in microstructure.</li> <li>• Increase in lack-of-fusion defects.</li> <li>• Decrease in Charpy impact values.</li> <li>• Slight increase YS and UTS with no change in elongation values.</li> </ul>	[132]
LB-PBF	9	<ul style="list-style-type: none"> <li>• Increase in O content.</li> <li>• No change in powder morphology.</li> <li>• No change in PSD.</li> <li>• Improvement in powder flow.</li> </ul>	Not reported.	[133]
LB-PBF	100	<ul style="list-style-type: none"> <li>• Slight increase in O content.</li> <li>• Narrowing of PSD.</li> <li>• Increase in powder flow.</li> <li>• Marginal degradation in powder morphology.</li> </ul>	<ul style="list-style-type: none"> <li>• No change in part density.</li> <li>• No change in YS and UTS.</li> </ul>	[134]
LB-PBF	8	Not reported	<ul style="list-style-type: none"> <li>• No significant change tensile properties</li> <li>• No change in part density.</li> <li>• Slight increase in O content.</li> </ul>	[143]

## Appendix B

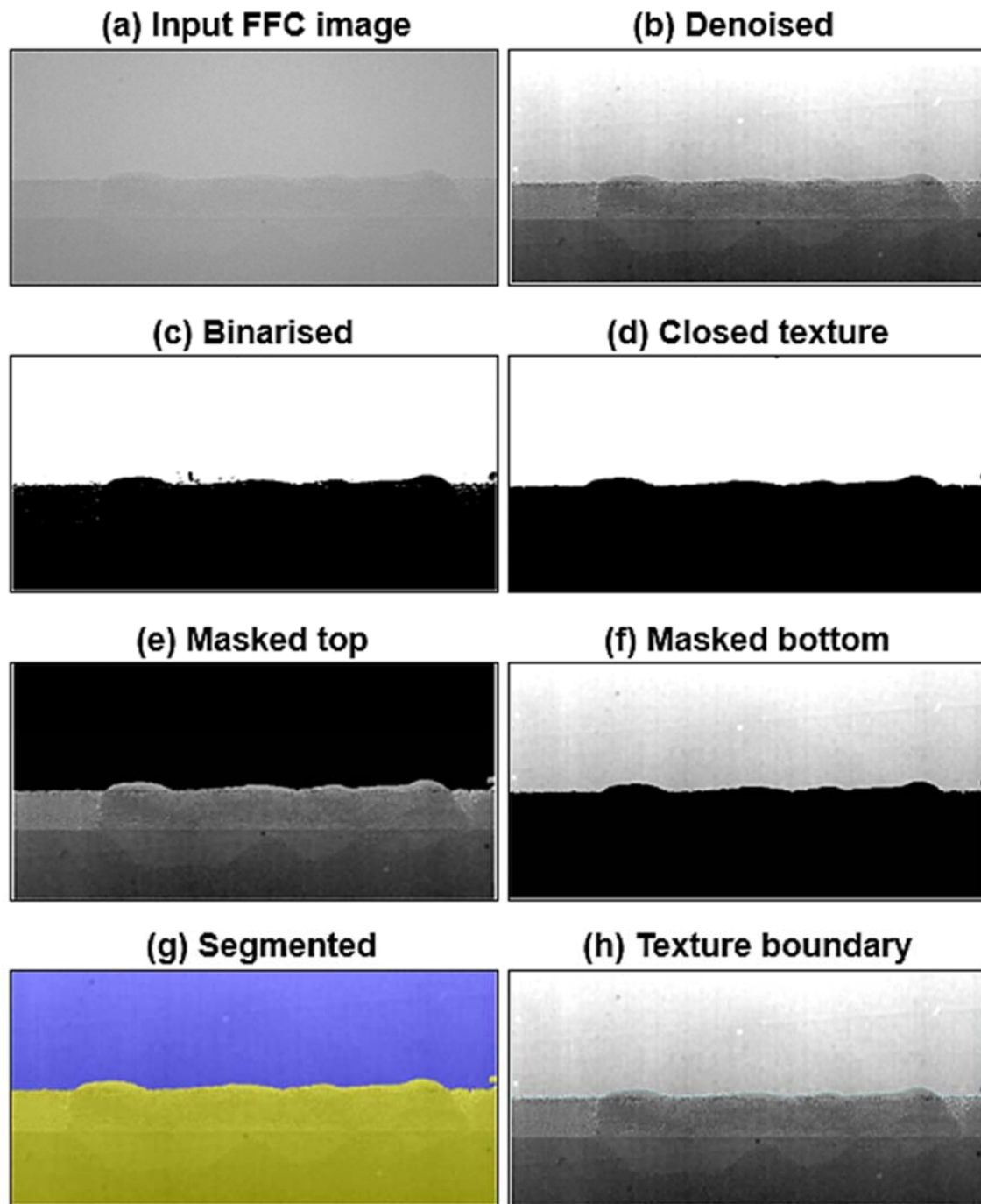


**Figure B.1** (a-h) Image processing stages to evaluate melt track surface roughness. The X-Y coordinates of the texture boundary was used to calculate the surface roughness.

## Appendix C

### Agglomerated powder spatter

X-ray radiographs of agglomerated powder particles ejected as a hot spatter is shown in Figure C.1. The cluster of powder particles (red-dotted circle) initially got entrained in the vapour plume at the laser front (Figure C.1a). The entrained particles interacted with the laser beam and formed a molten droplet (Figure C.1b) which then later got entrained in the Ar flow and got carried in the direction of flow (Figure C.1c).

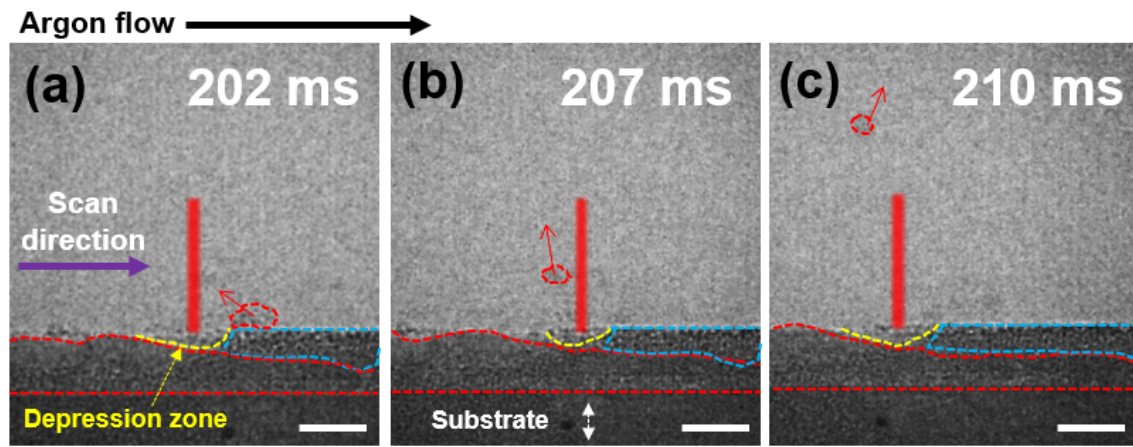


**Figure C.1 (a-c)** Dynamic X-ray images showing the formation of agglomerated hot powder spatter at 150 W 50  $\text{mms}^{-1}$  in virgin condition at Layer 3. The scale bars in all the radiographs are 500  $\mu\text{m}$ .

### Powder and droplet spatter

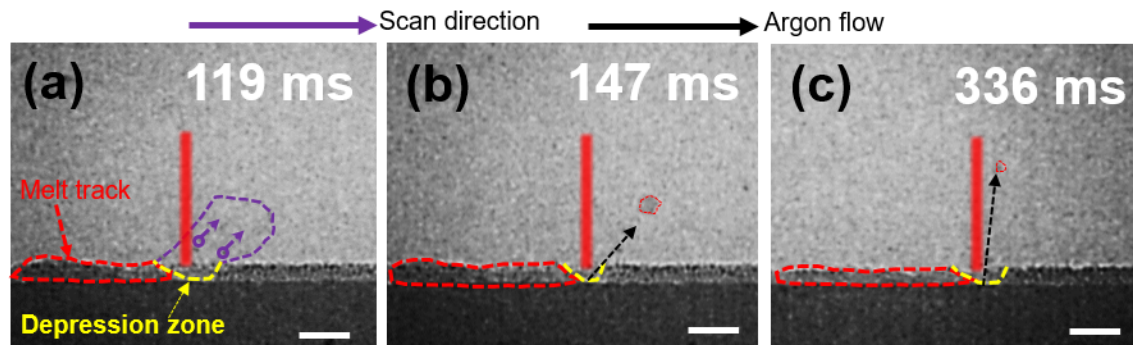


**Figure C.2** X-ray radiographs showing (a) powder spatter (purple area), (b) droplet spatter that collided with unfused particles in the powder layer during ejection, (c) droplet spatter that ejected vertically without any collisions in virgin condition at Layer 1 with 150 W 50  $\text{mms}^{-1}$ . The scale bars in all the radiographs are 500  $\mu\text{m}$ .

### Spatter-spatter interaction

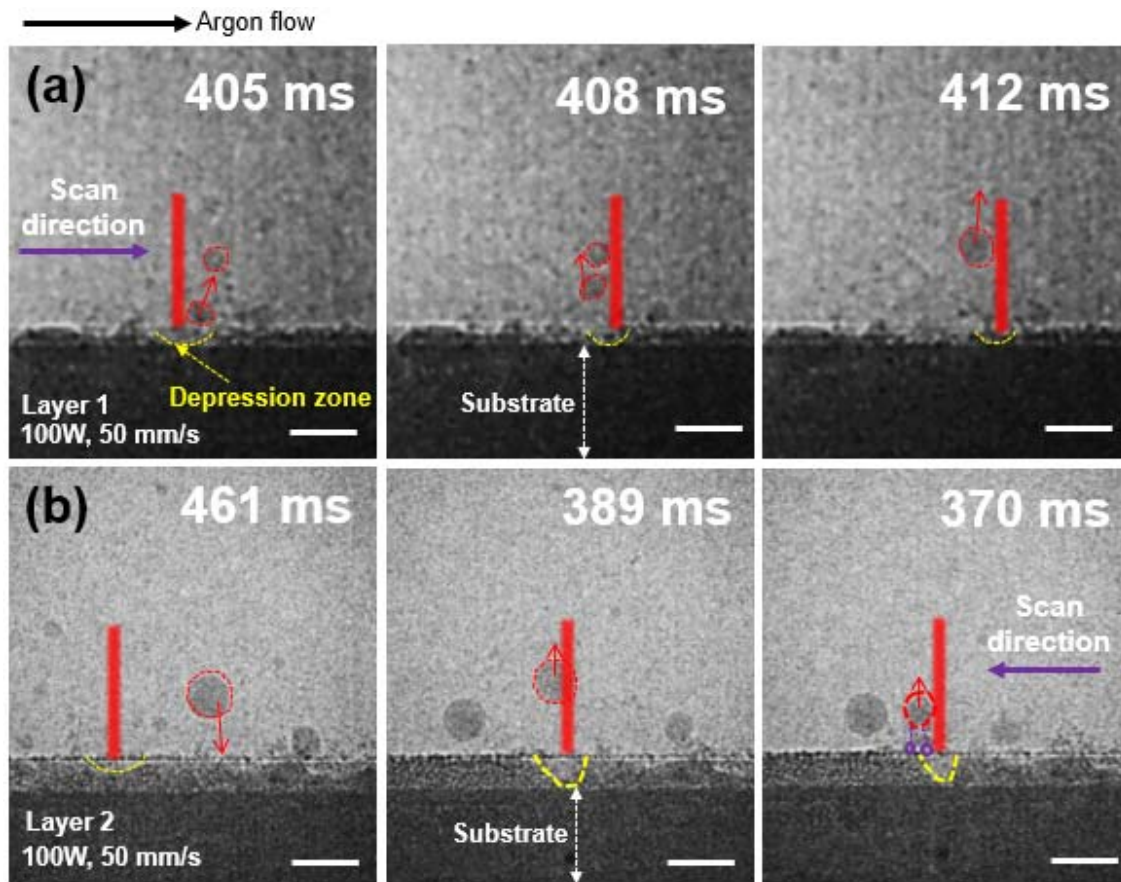


**Figure C.3** Dynamic X-ray images showing Layer 1 and 2 in virgin condition at 100W and 50  $\text{mm s}^{-1}$ . (a) Coalescence of one droplet spatter with another to form a large spatter at Layer 1 and (b) coalescence of powder spatters with a droplet spatter to form a large spatter. The droplet spatters are indicated by red-dotted circles while powder spatters are indicated shown by violet circles. The scale bars in all the radiographs are 500  $\mu\text{m}$ .

\*\*\*\*\*